



Alberta CO₂ Purity Project

Final Report

May 30, 2014

Acknowledgement

This report was prepared by PTAC, with major contributions from the Integrated CO₂ Network (ICO₂N), Carbon Management Canada, Chevron Corporation, ConocoPhillips Canada and TransCanada Corporation.

Financial support was received from Alberta Energy, Alberta Innovates – Energy and Environment Solutions, the Canadian Energy Pipeline Association, the CO₂ Capture Project, the Electric Power Research Institute, IPAC CO₂, the Global CCS Institute, ICO₂N, Natural Resources Canada, ARC Resources, Barrick Energy, Cenovus Energy, the Computer Modelling Group, Enhance Energy, Harvest Operations, Pengrowth Energy, Penn West Exploration, Praxair, Stantec, Technosol Engineering, Uhde Corporation, Upside Engineering, and WorleyParsons.

The report was edited by Marc Godin. Section authors are Kamal Botros and John Geerligs, NOVA Chemicals, Weixing Chen, University of Alberta, Kelly Edwards, Andrew McGoey-Smith, WorleyParsons, Jean-Philippe Nicot, University of Texas, and David Sinton, University of Toronto. The authors and sponsors wish to express their appreciation for the invaluable contributions, insight and comments received during the course of this work from Steering Committee members Soheil Asgarpour, Katie Blanchett, Rob Craig, Kelly Edwards, Scott Imbus, Amrita Lall Atwal, David LaMont, Richard Luhning, Duncan Meade and Thomas Robinson.

Disclaimer

PTAC does not warrant or make any representations or claims as to the validity, accuracy, currency, timeliness, completeness or otherwise of the information contained in this report, nor shall it be liable or responsible for any claim or damage, direct, indirect, special, consequential or otherwise arising out of the interpretation, use or reliance upon, authorized or unauthorized, of such information.

The material and information in this report are being made available only under the conditions set out herein. PTAC reserves rights to the intellectual property presented in this report, which includes, but is not limited to, our copyrights, trademarks and corporate logos. No material from this report may be copied, reproduced, republished, uploaded, posted, transmitted or distributed in any way, unless otherwise indicated on this report, except for your own personal or internal company use.

Executive Summary

Carbon capture and storage (CCS) has emerged as one of the few technologies available to achieve the dramatic reductions in carbon dioxide (CO₂) emissions that will be necessary to mitigate global climate change. CCS is composed of the following elements:

- Capture of CO₂ emissions from large industrial facilities;
- Transportation of the CO₂ through pipelines; and
- Permanent storage of the CO₂ in deep underground formations:
 - Oil reservoirs where CO₂ is utilized for Enhanced Oil Recovery (EOR);
 - Deep saline aquifers (sequestration).

However, CO₂ that is captured from industrial sources is not pure and can contain many impurities. The Alberta CO₂ Purity Project (ACPP) examined the effect of CO₂ purity and contaminants on the above 4 elements of CCS systems. A key result of ACPP is a globally unique techno-economic model that balances technical and economic considerations and derives a purity guideline that is optimal to all components in the CCS value chain. The model can be used by government and industry to develop purity guidelines across the CCS chain.

Phase 1

Phase 1 was a scoping exercise designed to canvass literature and industry knowledge, aggregate the suite of contaminants that need to be evaluated, and to screen and rank each contaminant. This was done to ensure that future technical analysis would be focused on the appropriate contaminants; i.e. those that are present in larger quantities or greatly affect any one component of the value chain.

Phase 1 provided the ACPP with some important interim conclusions. The current industrial experience with CO₂ purity is based on geologic CO₂ supply where contaminants are few and generally well understood. As the world moves to capture and utilization of anthropogenic CO₂, the number of potential contaminants increases, including compounds that are poorly understood from the point of view of their impact on CCS.

There are a large number of discrete carbon capture technologies, and each technology has a unique CO₂ purity and contaminants profile. In addition, the contaminants profile of each carbon capture technology is affected by the industrial process and feedstock to which it is applied, from steel manufacturing to electricity generation. ACPP assembled a list of 21 contaminants based on all major capture processes by collecting data from 17 energy companies. Subsequently, ACPP identified the contaminants that occur in a significant concentration and that have the greatest effect on each of the four elements of the value chain: capture, transportation, EOR and sequestration. This analysis was done using existing literature and knowledge, and culminated in the selection of six impure CO₂ compositions typical of the capture and utilization scenarios most likely to take place in a Canadian context (See table on the following page.) These six compositions were the basis for the physical and modeling analyses conducted during Phase 2.

| Impure CO₂ Compositions | | | | | | |
|---|-----------------------|-------------------|-------------|------------------------|--------------------|---------------------------|
| | Base Case | Low Purity | | Mid Purity | High Purity | |
| Composition Number | 1 | 2 | 3 | 4 | 5 | 6 |
| Feedstock | Heavy Fuel | Heavy Fuel | Natural Gas | Heavy Fuel | Natural Gas | Natural Gas |
| Process | Amine Post Combustion | Oxy Fuel | Oxy Fuel | IGCC* Partial Shift | Various | SMR** Physical Solvent |
| | (mol %) | (mol %) | (mol %) | (mol %) | (mol %) | (mol %) |
| CO₂ | 99.8 | 91.8 | 96.2 | 95.0 | 97.4 | 99.4 |
| N₂ | 0.2 | 2.0 | 1.9 | - | 0.2 | 0.3 |
| O₂ | - | 2.3 | 1.9 | - | - | - |
| Ar | - | 3.9 | - | - | - | - |
| CO | - | - | - | 0.5 | - | - |
| H₂ | - | - | - | 4.0 | - | 0.3 |
| CH₄ | - | - | - | 0.5 | 2.4 | - |
| Total | 100.0 | 100.0 | - | 100.0 | 100.0 | 100.0 |

*Integrated Gasification Combined Cycle

**Steam Methane Reforming

Phase 2

The purpose of Phase 2 was to fill critical knowledge gaps about the impact of anticipated anthropogenic CO₂ compositions on each element of the CCS value chain.

CO₂ Capture Technologies

Phase 2 focused on understanding water solubility and dew point in supercritical CO₂ mixtures because as long as water remains in the supercritical phase, corrosion and hydrate formation are minimized. There is much literature with references to the solubility of water in pure supercritical CO₂ and supercritical CO₂ with CH₄ and H₂S impurities, over the critical range of temperatures and pressures. However there is little knowledge regarding water solubility and dew point in CO₂ with the types and quantities of impurities typically found in anthropogenic CO₂. These impurities can have a significant impact on the water carrying capacity of the supercritical fluid.

The solubility of CO₂ in water is determined by the dew point which is determined by changing temperature and pressure and identifying the point at which free water begins to form or at which corrosion takes place. ACPP and Carbon Management Canada engaged two Canadian research groups to undertake complementary studies:

- The microfluidics technology of Dr. David Sinton (University of Toronto) used a novel microfluidics technology which required adaptation and validation for use in supercritical CO₂.
- Dr. Weixing Chen (University of Alberta) used more conventional technology to undertake corrosion assessments.

Microfluidic experiments were conducted for pressures up to 2500 psi and temperatures between 31 and 50°C. Droplet formation and growth was observed within seconds of pressure reduction below the dew point pressure. Images were taken at a fixed location over time to track droplet formation and droplet size evolution. For validation, the method was first applied to the well-studied CO₂-water system. The microfluidic results were shown to correspond closely to both previous experimental and theoretical results.

The method was then applied to determine the dew point conditions of water in industrially relevant CO₂ mixtures. The dew point conditions for some industrial mixtures remained very similar to that of pure CO₂ and water, while impurities in other mixtures reduced the mixtures' overall solubility for water, indicating a potential increase in pressure requirements for safe transportation.

Corrosion assessments were conducted on X-65 pipeline steel in various moisture-containing supercritical CO₂ gas mixture environments. This corrosion approach to determine the dew point is very reliable and highly sensitive.

The microfluidic and corrosion methods yielded similar outcomes on an overall basis: the impure CO₂ composition tested would not result in a separate water phase or corrosion if the temperature is maintained above 35°C and the pressure above 1250 psi when water concentration is at or below the industrially important value of 500 ppm (weight).

CO₂ Transmission Pipeline Transportation

Key issues related to pipeline transportation of CO₂ are (i) the impact of impurities and (ii) wave speed and crack propagation. The latter concerns the possibility of catastrophic running ductile fractures in CO₂ pipelines due to the difference in speed between the decompression wave and crack propagation. Steel with increased toughness or crack arresters are used to mitigate this concern and much research has been done in understanding the phenomena, particularly by TransCanada Corporation and NOVA Chemicals. Thus, the ACPP work program was focused on obtaining a better understanding of the effect of anthropogenic impurities on transportation capacity so that unnecessary overdesign parameters could be reduced in order to optimize design, reduce material, and lower construction and operation costs.

The literature review found that indeed the presence of impurities affect pipeline transportation flow capacity. The general effect is that the higher the level of impurities, the higher the reduction in the flow capacity given same pipeline inlet pressures and flow temperatures. Furthermore, according to the literature, impurities with much lower molecular weight than CO₂ (e.g. H₂ and CH₄) result in higher reductions in flow capacity. It was determined that a typical impurity level of 5% in anthropogenic CO₂ would result in a reduction in transportation flow capacity by approximately 3 to 6%, and that an impurity level of 11% would cause reductions in flow capacity in the order of 7 to 17.5%. However, the literature review did not discover experimental data to substantiate the theoretical work. In addition, published theoretical results were not directly comparable due to variations in equation of state used, as well as temperature and pressure conditions.

Validation of the outcomes of the literature review was needed and done via numerical analysis and actual tests in a small pipeline loop. The Phase 2 investigation was aimed at obtaining experimental data from actual flow loop testing and was conducted at TransCanada's Gas Dynamic Test Facility in Didsbury, Alberta. The flow loop is 178 m long, NPS 2 in size and rated up to 22 MPa operating pressure. It incorporates a special pump suitable for CO₂ application, along with necessary mixing and filling capabilities of any mixture of CO₂ including impurities.

The results of flow loop testing on the six impure CO₂ compositions as well as numerical analysis on these mixtures indicated that impurities investigated in this study (namely, N₂, O₂, Ar, CO, H₂ and CH₄) impact the flow capacity of a pipeline transporting these mixtures in a negative way. That is, these impurities result in a reduction in pipeline flow capacity relative to pure CO₂ fluid. The degree of flow capacity reduction in terms of the relative reduction in mass flow rate is directly proportional to ½ (one-half) of the relative reduction in the mixture density as compared to pure CO₂ fluid, at the same flow condition of pressure and temperature. For example, if the reduction in density of a CO₂+impurity mixture is 6%, the resulting reduction in flow capacity in terms of mass flow rate is 3% at the same condition. Flow capacity is not directly related to the mixture molecular weight as may have been commonly perceived. Both molecular weight and compressibility factor at the prevailing condition of pressure and temperature affect the mixture density, which in turn affects the flow capacity of a pipeline. Hydrogen as an impurity component has the most negative effect on flow capacity. This is primarily due to its effects on dramatically reducing the mixture density at the same flow condition relative to pure CO₂. Impurities were shown to have little effect on the pressure loss coefficients (e.g. friction factor) via the Reynolds number, and hence on flow capacity of a pipeline under the same conditions.

CO₂ Enhanced Oil Recovery

The EOR work program focused on understanding the effects that impurities in CO₂ have on Minimum Miscibility Pressure (MMP) which is the minimum pressure at which the injected gas and oil combine to form a single, uniform mixture. A miscible flood operating at or above this pressure should maximize oil recovery, while floods operating below this pressure will leave unrecovered oil in the reservoir. Most impurities found in anthropogenic CO₂ have a negative

impact on the oil recovery process by increasing the MMP. Laboratory testing was undertaken to gain a better understanding of the magnitude of these impacts, especially with mixtures involving multiple impurities. MMP was tested on one representative oil sample from the Cardium formation in Alberta using two different types of equipment: rising bubble apparatus (RBA) and slimtube. Using these tests the MMP and the recovery factor slope were determined for Cardium oil for CO₂ containing key anthropogenic impurities. The experimental results compared favorably with the literature.

With the experimental results, ACPP was able to estimate the negative oil recovery impact of impurities by applying a standard workflow of reservoir engineering calculations. The workflow allowed the estimation of loss reserves and production from the presence of impurities as compared to industry experience in Alberta and in the Permian Basin. These outputs were then translated into economic impact in the techno-economic model.

CO₂ Sequestration in Deep Saline Aquifers

The sequestration work program was mostly concerned with the performance of the storage formation and was focused on better understanding the effect that impurities have on a sequestration scheme's containment, pore space use efficiency and capacity, plume extent, trapping capability, and injection scheme performance.

A parametric study was conducted on impact of impurities on plume dynamics and rate and extent of trapping mechanisms in saline aquifers. The task was mostly a desktop numerical study performed with synthetic simplified cases and generalized models of actual reservoirs. An important observation controlling all study results was that viscosity and density of the mixtures considered were lower than those of pure CO₂ at the same temperatures and pressures. It follows that a plume of CO₂ with impurities, moving updip with no barrier, will therefore migrate farther from the point of injection but will be trapped through residual saturation sooner than will a plume of pure CO₂ and possibly enhance dissolution, primarily because it is exposed to more rock / brine volume. A larger plume, however, means that a larger area must be defined and monitored for leakage pathways, such as faults and wells, but the faster trapping translates into a shorter monitoring period.

Equally important is that contrasts of viscosity and density between pure CO₂ and a CO₂ mixture decrease with depth, suggesting that differences in flow behavior and storage capacity are proportionally reduced with depth.

Experimental rock-fluid interaction studies, including modeling and autoclave experiments were also performed using samples from siliciclastic and carbonate rocks. Batch experiments were conducted in high-pressure, high-temperature autoclaves with rock samples immersed in synthetic brine and exposed to supercritical CO₂ with and without admixed O₂. Tests of 3 siliciclastic rocks show that O₂ is likely to alter the geochemistry of subsurface systems in ways that the pure CO₂ case does not, in particular when ferrous-iron bearing minerals are present. One carbonate rock (not containing ferrous minerals) was also tested and it was observed that carbonate grains

dissolved unevenly. In all of the autoclave experiments runs, mineral precipitation remained minor because the precursor minerals that supply component ions are not abundant. This suggests that as long as a precursor reactive mineral fraction is a small portion of the rock, O₂ will not have a large geochemical effect on mineral precipitation and therefore on rock stability or fluid flow.

Phase 3

The techno-economic model was developed to tie technical parameters to economic costs in order to quantify impact. Technical data collected in Phase 2 of the study were linked to economic implications that quantified (as a dollar amount) the effects of impurities on an integrated CCS system. For transportation, the data collected helped to define the design parameters that directly affect cost. For EOR, the data collected on the effect that impurities have on MMP was used to determine potential changes in oil recovery, and thus, changes in revenue that results from injecting impure CO₂. For sequestration, the behaviour of impure CO₂ in a geologic formation determined the design of the injection scheme (number of wells, failures, etc.) as well as the measurement, monitoring and verification (MMV) requirements and the required pore space, all of which have cost implications.

The techno-economic model allows the user to input system parameters such as capture process, pipeline length and EOR / sequestration allocation and understand the effect of these inputs throughout the system. The tool's scenario structure ensures that it is relevant to many diverse users and applications. The user defines input parameters, including capture technologies or combinations of technologies, pipeline length and end market choice (EOR or sequestration). The model derives a combined CO₂ stream and purity which are linked to cost factors for each value chain component. These factors are used to calculate cost impacts to each value chain component and to the CCS system in its entirety. The model directly compares the impure CO₂ scenario to a 100% pure CO₂ scenario and determines how the total system and individual components are affected by the presence of impurities. For example, the user is able to input lower purity capture streams, and observe the trade-off of these lower capture costs against resulting higher pipeline costs.

The model was designed to be flexible for multiple users with varying interests and objectives. It was designed to clearly illustrate the trade-offs between scenarios. This will allow any user to define their own assumptions and run scenarios to see the impacts they are most concerned with.

Phase 4

The purpose of Phase 4 is knowledge mobilization and it is now taking place with the publication of ACP's Final Report, the distribution of the techno-economic model to ACP participants and presentations at selected industry and academic gatherings. In particular, the techno-economic model will allow individual companies and government jurisdictions to apply proprietary or regional data in reaching conclusions relevant to their situation.

Table of Contents

| | |
|---|----|
| Executive Summary | 3 |
| Table of Contents | 9 |
| List of Figures | 12 |
| List of Tables | 15 |
| 1. Project Overview | 17 |
| 1.1. Introduction | 17 |
| 1.2. Purpose | 17 |
| 1.3. Project Benefits | 19 |
| 1.4. Project Overview | 20 |
| 1.4.1. Phase 1 - Understanding Purity | 20 |
| 1.4.2. Phase 2 - Evaluating Technical Effects of Impurities | 22 |
| 1.4.3. Phase 3 - Quantifying Economic Implications | 27 |
| 1.4.4. Phase 4 - Prepare and Share Project Deliverables | 27 |
| 2. CO ₂ Capture Technologies | 28 |
| 2.1. Phase 1 Outcomes | 28 |
| 2.2. Phase 2 Research Needs | 29 |
| 2.3. Phase 2 Research Program | 29 |
| 2.4. Research Outcomes | 30 |
| 2.4.1. Dew Point Determination using Microfluids Technology | 30 |
| 2.4.2. Dew Point Determination using Onset of Corrosion | 37 |
| 3. CO ₂ Transmission Pipeline Transportation | 41 |
| 3.1. Phase 1 Outcomes | 41 |
| 3.2. Phase 2 Research Needs | 42 |
| 3.3. Experimental Setup of the Flow Loop at Didsbury, Alberta | 43 |
| 3.3.1. Close Loop Piping System | 43 |
| 3.3.2. Auxiliary System | 43 |
| 3.3.3. Special CO ₂ Pump | 44 |
| 3.3.4. Measurement Instrumentation | 44 |
| 3.3.5. Costs | 45 |
| 3.4. Test Procedure | 45 |
| 3.5. Uncertainty Analysis | 46 |
| 3.6. Test Program | 47 |
| 3.7. Numerical Simulation of the Test Loop Configuration | 48 |

| | | |
|---------------|---|-----------|
| 3.8. | Test results..... | 53 |
| 3.8.1. | Flow Test Compositions..... | 53 |
| 3.8.2. | Loop Calibration..... | 54 |
| 3.8.3. | Reference Tests..... | 57 |
| 3.8.4. | CO ₂ Mixtures with Impurities | 59 |
| 3.9. | Summary and Conclusions..... | 66 |
| 4. | CO ₂ Enhanced Oil Recovery | 69 |
| 4.1. | Phase 1 Outcomes | 69 |
| 4.2. | The Need for Phase 2 Research..... | 69 |
| 4.3. | Methodology | 71 |
| 4.3.1. | Pressure, Composition and Recovery Factor..... | 71 |
| 4.3.2. | Calculation of Increase in MMP..... | 72 |
| 4.4. | Laboratory Program | 73 |
| 4.4.1. | Oil Sampling and Recombination..... | 74 |
| 4.4.2. | Compositional Comparison to Other Cardium Wells..... | 78 |
| 4.4.3. | Experimental Apparatus | 80 |
| 4.5. | Experimental Results..... | 84 |
| 4.5.1. | RBA Program | 84 |
| 4.5.2. | Slimtube Program | 85 |
| 4.6. | Technical/Economic Model..... | 88 |
| 4.6.1. | Example Calculations of Economic Impact..... | 91 |
| 4.7. | Conclusions..... | 92 |
| 5. | CO ₂ Sequestration in Deep Saline Aquifers | 94 |
| 5.1. | Phase 1 Outcomes | 94 |
| 5.2. | Phase 2 Research Needs..... | 94 |
| 5.3. | Research Program | 94 |
| 5.4. | Research Outcomes | 95 |
| 5.4.1. | Plume Dynamics..... | 95 |
| 5.4.2. | Geochemistry..... | 112 |
| 5.5. | Conclusion..... | 115 |
| 6. | Phase 3 Quantifying Economic Implications with the Cost Optimization Model..... | 118 |
| 6.1. | Model Scope..... | 118 |
| 6.2. | Model Objectives | 118 |
| 6.3. | Conceptual Model | 119 |

| | | |
|--------|---|-----|
| 6.3.1. | Conceptual Model for Capture | 120 |
| 6.3.2. | Conceptual Model for Pipelines | 120 |
| 6.3.3. | Conceptual Model Enhanced Oil Recovery | 120 |
| 6.3.4. | Conceptual Model for Geologic Sequestration | 121 |
| 6.4. | Mathematical Model | 122 |
| 6.4.1. | Chemical Composition of Impure Stream | 123 |
| 6.4.2. | Mathematical Model for Capture | 124 |
| 6.4.3. | Mathematical Model for Transport..... | 125 |
| 6.4.4. | Mathematical Model for EOR | 126 |
| 6.4.5. | Mathematical Model for Geologic Sequestration..... | 128 |
| 6.5. | Input Data..... | 130 |
| 6.5.1. | Capture Input Data..... | 130 |
| 6.5.2. | Pipeline Input Data | 130 |
| 6.5.3. | Enhanced Oil Recovery Input Data..... | 130 |
| 6.5.4. | Geological Sequestration Input Data..... | 133 |
| 6.6. | Software Implementation | 137 |
| 6.7. | Results | 144 |
| 6.8. | Conclusions | 151 |
| 7. | Phase 4 – Preparing and Sharing Project Outcomes..... | 153 |
| 8. | Conclusion | 154 |
| 9. | References..... | 156 |

List of Figures

| | |
|---|----|
| Figure 1. Overview of Carbon Capture and Storage..... | 18 |
| Figure 2. Alberta CO ₂ Purity Project Elements | 23 |
| Figure 3. Schematic of Microfluidic Approach | 32 |
| Figure 4. Experimental Setup for Sample Preparation | 32 |
| Figure 5. Microfluidic Detection of the Dew Point | 34 |
| Figure 6. Dew Point Data..... | 35 |
| Figure 7. Schematic Illustration of the Corrosion and Dew Point Test Facility..... | 38 |
| Figure 8. Corrosion Observation..... | 39 |
| Figure 9. Dew Points of Mixture 3 with Water Content of 10,000 ppm | 40 |
| Figure 10. Comparison of Pipeline Capacity | 42 |
| Figure 11. Schematic of the CO ₂ Flow Loop Setup..... | 44 |
| Figure 12. Steady Flow Simulation Results of Isothermal Flow | 51 |
| Figure 13. Steady Flow Simulation Results of Isothermal Flow | 51 |
| Figure 14. Simulation Results of Flow Rates for a Given Pressure Drop | 52 |
| Figure 15. Mixture Density at the Inlet of the 70 m Long Test Section..... | 52 |
| Figure 16. Simulation Results of Decrease of Flow Rates | 53 |
| Figure 17. Example Test Results from RefA Mixture the Mass Flow Rate..... | 55 |
| Figure 18. Measured Static Pressure and Average Temperature..... | 56 |
| Figure 19. Deviation of the Measured Pressure Gradient..... | 56 |
| Figure 20. Test RefA Measured Pressure Gradient vs. Flow Rate..... | 58 |
| Figure 21. Error in Density Prediction based on GERG-2008 EOS of Test RefA..... | 58 |
| Figure 22. Pressure Gradient vs. Mass Flow Rates of the Tested Mixtures | 62 |
| Figure 23. Experimental Results of the Reduction in Flow Rates Compared to Test RefA..... | 63 |
| Figure 24. Average Density Measurements by the Coriolis Flow Meter | 63 |
| Figure 25. Deviation of Measured Density by the Coriolis Flow Meter | 64 |
| Figure 26. Experimental Results of the Reduction in Flow Rates..... | 65 |
| Figure 27. Comparison between the Numerical Results and the Experimental Results..... | 65 |
| Figure 28. Relative Effect of Impurities on MMP | 71 |
| Figure 29. Correlation Used to Calculate $MMP_{\text{impure}}/MMP_{\text{pure}}^{16}$ | 73 |
| Figure 30. Map of Alberta with the Location of the Pembina Oilfield..... | 75 |
| Figure 31. Historical Production of Cardium Well 100/12-24-047-10W5/0..... | 76 |
| Figure 32. Compositional Comparison of Cardium Oils to Well 12-24..... | 78 |
| Figure 33. Bubble Point Pressure Comparison of Cardium Oils to Well 12-24..... | 79 |

| | |
|---|-----|
| Figure 34. Rising Bubble of CO ₂ in Reservoir Oil in an RBA - Immiscible Conditions | 81 |
| Figure 35. Streaming CO ₂ in Reservoir Oil in an RBA - Miscible Conditions | 81 |
| Figure 36. Photograph of a Slimtube Apparatus..... | 82 |
| Figure 37. Schematic Showing the Process of Calculating MMP | 83 |
| Figure 38. Schematic for Calculating the Decrease in Recovery with Impure CO ₂ | 83 |
| Figure 39. Original RBA Program..... | 84 |
| Figure 40. Original Slimtube Program..... | 85 |
| Figure 41. Net Efficiency of CO ₂ , (tonne CO ₂ /sm ³ oil) ¹⁷ | 90 |
| Figure 42. Estimated CO ₂ Utilization for 10 Alberta Reservoirs ¹⁸ | 91 |
| Figure 43. Density (a), Viscosity (b), and Solubility (c) at 100,000 mg/L..... | 96 |
| Figure 44. Cross Section of Generic Model Displaying Homogeneous Field..... | 99 |
| Figure 45. Mixture Density (a) and Density to Viscosity Relative to Neat CO ₂ (b) | 100 |
| Figure 46. Illustration of how maximum extent and time to reach the top are extracted. | 102 |
| Figure 47. Plume-Extent-Increase for Binary CO ₂ Systems vs. Pure CO ₂ Plume Extent | 103 |
| Figure 48. 3D view of the Carbonate Reservoir Model Showing Cell Depth | 106 |
| Figure 49. Permeability and Rock Type Distributions for Carbonate Aquifer Model | 106 |
| Figure 50. Normalized Porosity vs. Reservoir Quality Index..... | 107 |
| Figure 51. Permeability Histogram from Downloaded Petrel Model for Carbonate Aquifer | 108 |
| Figure 52. Gas Saturation Cross-Section | 109 |
| Figure 53. Impact on Injection Stream Composition on Parametric Study for Nisku Aquifer .. | 110 |
| Figure 54. Impact on Injection Stream Composition (95% CO ₂) for Carbonate Aquifer | 110 |
| Figure 55. Impact on Injection Stream Composition (85% CO ₂) for Carbonate Aquifer | 111 |
| Figure 56. Impact on Injection Stream Composition (75% CO ₂) for Carbonate Aquifer | 111 |
| Figure 57. Conceptual Model Showing Capture, Pipeline EOR and Sequestration..... | 119 |
| Figure 58. Conceptual Model of Sequestration | 121 |
| Figure 59. Base and Scaled Capture Cost for 10MT IGCC Plant | 125 |
| Figure 60. Top level System Model..... | 138 |
| Figure 61. Capture Model..... | 138 |
| Figure 62. Pipeline Model..... | 139 |
| Figure 63. Pipeline Diameter Calculations | 139 |
| Figure 64. Enhanced Oil Recovery Model | 140 |
| Figure 65. EOR Software: Impure Recovery..... | 140 |
| Figure 66. Calculations involving Critical Temperatures..... | 141 |
| Figure 67. Calculations involving Critical Pressures..... | 141 |

| | |
|---|-----|
| Figure 68. Sequestration Model | 142 |
| Figure 69. Plume Area Calculations | 142 |
| Figure 70. Spatial Well Density Calculations..... | 143 |
| Figure 71. Number of Injection Wells Calculations | 143 |
| Figure 72. Overall Sequestration Cost Calculation..... | 144 |
| Figure 73. Input Dashboard for Techno-economic Model | 145 |
| Figure 74. Output Results Dashboard for Techno-economic Model..... | 145 |
| Figure 75. 10MT Heavy Amine Post - combustion..... | 146 |
| Figure 76. 10MT Heavy Oxy..... | 146 |
| Figure 77. 10MT Natural Gas Oxy | 146 |
| Figure 78. 10MT IGCC Partial Shift | 147 |
| Figure 79. 10MT Various Natural Gas Processing Plant..... | 147 |
| Figure 80. 10MT Natural Gas Steam Methane Reforming (SMR) | 147 |
| Figure 81. All Costs vs. Capture Rate: Pure CO ₂ | 148 |
| Figure 82. All Costs vs. Capture Rate: Impure CO ₂ | 148 |
| Figure 83. Pipeline Dashboard..... | 150 |
| Figure 84. EOR Dashboard..... | 150 |
| Figure 85. Sequestration Dashboard | 151 |

List of Tables

| | |
|--|-----|
| Table 1. Phase I Analysis Summary | 21 |
| Table 2. Impure CO ₂ Compositions..... | 22 |
| Table 3. Overview of Phase 2 Research Needs | 23 |
| Table 4. CO ₂ Compositions for Dew Point and Corrosion Measurements | 30 |
| Table 5. Dew Points of CO ₂ Compositions (psi) using Microfluids | 36 |
| Table 6. Dew Points of CO ₂ Compositions (°C) using Onset of Corrosion | 39 |
| Table 7. GDTF Flow Loop Modification and Testing Costs..... | 46 |
| Table 8. Uncertainty Analysis in Determining the Mass Flow Rate | 48 |
| Table 9. Target Compositions of the Six CO ₂ +Impurities Mixtures | 49 |
| Table 10. GC Analysis of Gas Samples Drawn from the Flow after Two Hours of Mixing | 54 |
| Table 11. Values of the Semi-empirical Coefficients..... | 61 |
| Table 12. Physical Properties of the Recombined Oil Sample | 77 |
| Table 13. RBA Results | 85 |
| Table 14. Summary of Slimtube Results | 86 |
| Table 15. Summary of MMP and Recovery Slopes | 87 |
| Table 16. Comparison of MMP increases..... | 88 |
| Table 17. Molar Composition of Base Cases..... | 98 |
| Table 18. Characteristics of Shallow and Deep Generic Models | 98 |
| Table 19. Comparison of Stream A, Stream C, and Neat CO ₂ Plume Extent | 101 |
| Table 20. Base-case characteristics of the Canadian Carbonate model..... | 105 |
| Table 21. Summary of Sample Mineralogical Composition | 112 |
| Table 22. Summary of Geochemical Runs | 113 |
| Table 23. Standard Mass Flow Rates Q_j s for each Capture Technology | 123 |
| Table 24. Base Cost Values for Capture..... | 131 |
| Table 25. Pipeline Model Input Parameters..... | 131 |
| Table 26. EOR Model Parameters | 132 |
| Table 27. Critical Parameters for Components..... | 132 |
| Table 28. Coefficients in Polynomial Expansions..... | 132 |
| Table 29. Pressure Recovery and MF Factors | 133 |
| Table 30. Plume Areas for CO ₂ plus N ₂ | 133 |
| Table 31. Plume Areas for CO ₂ plus Ar | 134 |
| Table 32. Plume Areas for CO ₂ plus O ₂ | 134 |
| Table 33. Plume Areas for CO ₂ plus CH ₄ | 135 |

| | |
|---|-----|
| Table 34. Plume Areas for CO ₂ plus H ₂ | 135 |
| Table 35. Plume Areas for CO ₂ plus CO | 136 |
| Table 36. Well and Monitoring Costs..... | 136 |
| Table 37. Abandoned Well Spatial Densities in Central Alberta | 137 |

1. Project Overview

1.1.Introduction

Carbon capture and storage (CCS) has emerged as one of the few technologies available to achieve the dramatic reductions in carbon dioxide (CO₂) emissions that will be necessary to mitigate global climate change. CCS is an emerging industrial process that is composed of the following elements (Figure 1):

- Capture of CO₂ emissions from large industrial facilities such as coal, oil and gas facilities and other industrial operations before the CO₂ is emitted to the atmosphere;
- Transportation of the CO₂ through pipelines; and
- Permanent storage of the CO₂ in deep underground formations which generally can be:
 - Oil reservoirs where CO₂ is utilized for Enhanced Oil Recovery (EOR) and then permanently stored in the space vacated by the oil;
 - Deep saline aquifers where the CO₂ occupies available space and eventually dissolves in formation water and may be mineralized in formation rock.

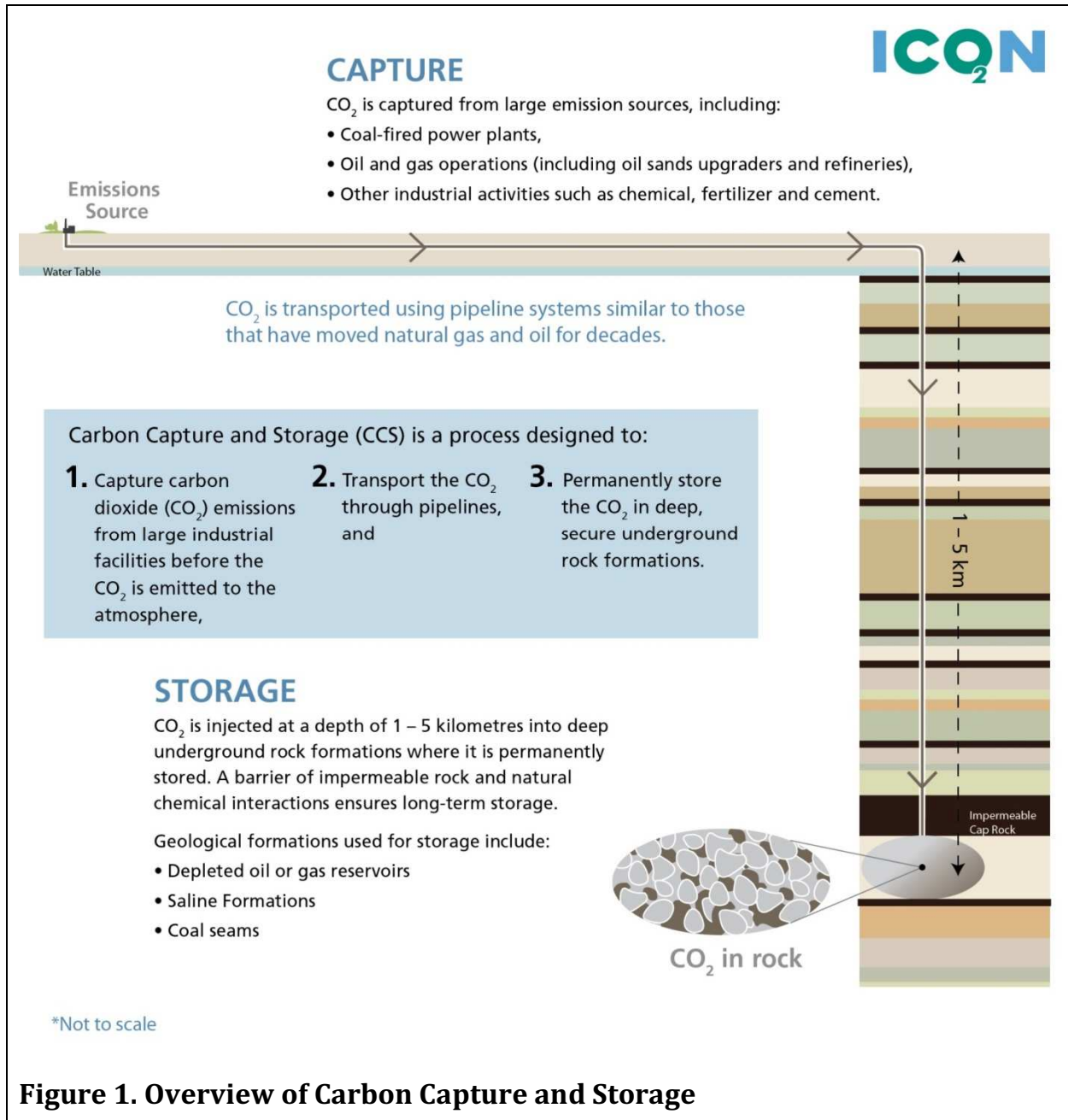
However, CCS is challenged by high costs and by limited offsetting revenues and uptake by industry and government has been slow due to these high costs. Approximate purity standards and onerous regulation could contribute to yet higher CCS costs and result in reduced overall system efficiency. The development of purity guidelines and standards that are grounded in technical and economic analysis will allow CCS design to be optimized, will drive down overall costs and will influence development of new technologies and front-end design for projects. Building integrated CCS infrastructure aligned on an optimum CO₂ specification would result in greater efficiency across the CCS value chain. Thus, it is crucial that the implications of the impurities found in anthropogenic CO₂ emissions be more deeply understood to optimize CCS implementation.

In addition, although some components of CCS (e.g. pipeline transportation of pure CO₂) are relatively well understood, significant work is required for the development, adoption and deployment of regulations and best practices to manage the implementation of CO₂ capture, EOR and sequestration, particularly for anthropogenic (impure) CO₂. The determination of optimized CO₂ purity levels is a critical step in the management of regulated and commercial transactions across the CCS chain.

1.2.Purpose

The Alberta CO₂ Purity Project (ACPP) brought together industry experts and stakeholders to evaluate the effect of CO₂ purity and numerous contaminants on the main elements of CCS systems: capture, pipeline, EOR and sequestration. One of the original desired outcomes was a “made in Alberta” purity specification to support the development of a multi-user CO₂ network. However, it soon became clear that there could not be one single specification for all projects, and ACPP designed a techno-economic a model that optimizes any particular project. This key ACPP

outcome is a globally unique techno-economic model that balances technical and economic considerations and derives a purity guideline that is optimal to all components of a particular CCS chain. It allows the user to input system parameters such as capture process, pipeline length and EOR / sequestration allocation and understand the effect of these inputs on the overall system. The model can be used by government and industry to develop purity guidelines across the CCS chain.



The ACPP will also assist with the understanding of the safety implications of CO₂ purity from the perspectives of industry and the public, and provide technical and economic information, based on the collective findings of the project, to regulators governments and stakeholders to enhance their understanding of CO₂ purity issues.

It is understood that a tremendous amount of effort has been placed on CCS by Canadian governments and by multiple parties and groups over the years. The Project was intended to complement and consolidate this work as opposed to duplicate it, since past work was not necessarily informed by an understanding of optimum purity standards. One of the outcomes of the Project is to enable users of the ACPP model to quantify the benefits, costs, and technical trade-offs between all of the components in the CCS chain depending on the CO₂ purity specifications brought forward for consideration.

1.3. Project Benefits

The ACPP tackled a key knowledge gap for advancing CCS: how CO₂ purity could be optimized for an integrated CCS project. This work was unique in seeking a comprehensive purity solution that is sensitive to the four industrial sectors involved across the CCS chain. Integration is a key success factor for the accelerated deployment of CCS technology and it is important that there is a complete understanding of how CO₂ purity affects an entire CCS system. Optimizing the trade-offs between purity and the operational costs of each element of the CCS chain will allow for more efficient and effective CCS deployment. The results of the ACPP Project will be essential to ensuring purity standards are technically sound and economically efficient.

The ACPP was a first-of-its-kind assessment of CO₂ purity that incorporated the broad perspectives of capture, pipeline transportation, EOR markets, and sequestration. The Project developed a detailed techno-economic model that can be run to optimize purity levels across an integrated CCS infrastructure. This work will enable the development of project specific purity recommendations using a tool that could be adopted by regulators and industry in Alberta, Canada and jurisdictions across the globe.

ACPP will also help to influence the development of new technologies and the front-end design of CCS projects. This acceleration of the overall CCS deployment will result in increased reductions in CO₂ emissions at a quicker rate than otherwise would be achieved.

CCS has tremendous potential to support Canada's energy future, and is expected to be the single largest GHG reduction technology in Canada. ACPP will help ensure that CCS deployment achieves its potential by promoting operational efficiency and cost effective decision making. Purity standards based on the in-depth analysis undertaken through ACPP will help foster safety of integrated CCS systems and increase public confidence in CCS. ACPP will position Canada to be a leader in large-scale CCS deployment.

1.4. Project Overview

The Project was composed of four Phases as follows:

- Phase 1 - Understanding Purity
- Phase 2 - Evaluating Technical Effects of Impurities
- Phase 3 - Quantifying Economic Implications
- Phase 4 - Prepare and Share Project Deliverables

1.4.1. Phase 1 - Understanding Purity

Phase 1 of the project was comprised of understanding purity issues at a summary level, reviewing publically available literature, and determining the scope of technical work that will make up subsequent phases of work.

Phase 1 was a scoping exercise designed to canvass literature and industry knowledge, aggregate the suite of contaminants that need to be evaluated, and to screen and rank each contaminant. This was done to ensure that future technical analysis would be focused on the appropriate contaminants; i.e. those that are present in larger quantities or greatly affect any one component of the value chain.

Phase 1 provided the ACPP with some important interim conclusions. There are a large number of discrete carbon capture technologies, and each technology has a unique CO₂ purity and contaminants profile. In addition, the contaminants profile of each carbon capture technology is affected by the industrial process and feedstock to which it is applied, from steel manufacturing to electricity generation. The Project assembled a list of 21 contaminants based on all major capture processes by collecting data from 17 energy companies. Subsequently, the contaminants that occur in a significant concentration and have the greatest effect were identified in each of the four elements of the value chain: capture, transportation, EOR and sequestration. This analysis was done using existing literature and knowledge, and culminated in a workshop where findings were presented and a shortened list of contaminants was agreed upon for further analysis.

Table 1 summarizes the parameters evaluated and the overall conclusions. Phase 1 resulted in a short list of 9 key contaminants of interest (O₂, H₂S, SO₂, H₂O, H₂, Ar, CH₄, N₂, CO) as well as some acid species.

Subsequently, energy companies were asked to supply process data that was used to derived purity compositions. There were over 18 independent streams submitted. Each combination of fuel source and capture technology resulted in a discrete data point of purity. The six resulting impure CO₂ compositions (shown in Table 2) were chosen to effectively cover the range of technologies, and purities that would most likely be encountered, and thus provide appropriate process, and purity data to the techno-economic model. These six impure CO₂ compositions were then evaluated in Phase 2. The scenarios are broken into 3 categories low (~90% CO₂ purity), mid (~95% CO₂ purity) and high purity (~98% CO₂ purity).

| Table 1. Phase I Analysis Summary | | | |
|--|---|--|---|
| Value Chain Component | Evaluated effects of impurities on | Analysis Used | Contaminants Ranked by Importance |
| Capture | Compression, i.e. CO ₂ to super critical phase | Information collection exercise (from companies with expertise in CO ₂ capture) | O ₂ , H ₂ S, SO ₂ , H ₂ O |
| Pipeline Transportation | Phase behaviour, capacity, safety, and compression requirements | Internal Literature Review | H ₂ , CH ₄ , H ₂ S, H ₂ O, O ₂ , SO ₂ |
| EOR | Minimum miscibility pressure (MMP), and enhanced (incremental) oil recovery | Literature review (completed by Petroleum Technology Resource Centre) | O ₂ , Ar, N ₂ |
| Sequestration | Sub-surface plume migration, capacity, and injectivity | PVT and parametric flow studies | N ₂ , O ₂ , Ar, CH ₄ , and acid species |

ACPP is unique in that analysis included multi-contaminant mixtures rather than simplified binary compositions as is available in the current academic and industrial literature.

CCS capture technologies are not widely deployed at large scale and therefore capital and operating data is only selectively available. For ACPP, energy companies who have proprietary expertise in various capture processes were asked to provide cost data for these CO₂ capture processes. These costs were broken out into categories of capture, subsequent cleaning, if any, and drying and compression. By looking at the full spectrum of capture processes, ACPP was able to assess if companies add process steps to increase purity and whether those steps could be eliminated. Most processes did not include dedicated back-end steps to increase the purity from its raw captured state. It was found that there was little or no ability to adjust the minimum CO₂ purity by removing existing process steps and that the minimum purity is largely determined by capture process.

| Table 2. Impure CO₂ Compositions | | | | | | |
|--|-----------------------|-------------------|-------------|------------------------|--------------------|---------------------------|
| | Base Case | Low Purity | | Mid Purity | High Purity | |
| Composition Number | 1 | 2 | 3 | 4 | 5 | 6 |
| Feedstock | Heavy Fuel | Heavy Fuel | Natural Gas | Heavy Fuel | Natural Gas | Natural Gas |
| Process | Amine Post Combustion | Oxy Fuel | Oxy Fuel | IGCC* Partial Shift | Various | SMR** Physical Solvent |
| | (mol %) | (mol %) | (mol %) | (mol %) | (mol %) | (mol %) |
| CO₂ | 99.8 | 91.8 | 96.2 | 95.0 | 97.4 | 99.4 |
| N₂ | 0.2 | 2.0 | 1.9 | - | 0.2 | 0.3 |
| O₂ | - | 2.3 | 1.9 | - | - | - |
| Ar | - | 3.9 | - | - | - | - |
| CO | - | - | - | 0.5 | - | - |
| H₂ | - | - | - | 4.0 | - | 0.3 |
| CH₄ | - | - | - | 0.5 | 2.4 | - |
| Total | 100.0 | 100.0 | - | 100.0 | 100.0 | 100.0 |

*Integrated Gasification Combined Cycle

**Steam Methane Reforming

1.4.2. Phase 2 - Evaluating Technical Effects of Impurities

ACPP is the first internationally recognized project to incorporate all four components of CCS into a science-based project on purity and contamination. The four components, as illustrated in Figure 2 are:

- 1) Capture – CO₂ capture, cleanup and compression,
- 2) Transportation – pipeline and pumping,
- 3) EOR - incremental oil recovery, and
- 4) Sequestration - long-term storage in saline formations.



Figure 2. Alberta CO₂ Purity Project Elements

Based on the results of Phase 1, a comprehensive Phase 2 research work program was developed to properly define and source data to populate the ACPP techno-economic model. Table 3 summarizes the work that was planned to fill knowledge gaps. The overall goal was to derive technical information that could be tied to financial costs or revenues and could inform the techno-economic model.

| Table 3. Overview of Phase 2 Research Needs | | | |
|--|--|--|---|
| Value Chain Component | Key Considerations | Uncertainties and Knowledge Gaps | Research Tasks |
| Capture | <ul style="list-style-type: none"> • Fuel source • Capture process • Drying and compression | <ul style="list-style-type: none"> • Impurities, process steps and costs • Water viewpoint and corrosion | <ul style="list-style-type: none"> • Capture process and cost data gathering • Dew point in presence of impurities |
| Pipeline Transportation | <ul style="list-style-type: none"> • Capacity • Materials • Pressure profile • Safeguards • Dew point and corrosion | <ul style="list-style-type: none"> • Compression, flow behavior, corrosion • Material toughness, equation of state • Impact of impurities on capacity | <ul style="list-style-type: none"> • Literature review • Capacity validation • Flow loop testing |
| EOR | <ul style="list-style-type: none"> • MMP | <ul style="list-style-type: none"> • Multi—contaminant mixture effect on MMP and recovery | <ul style="list-style-type: none"> • Literature review • Laboratory testing |
| Sequestration | <ul style="list-style-type: none"> • Plume extent • Injected that he and well scheme • Monitoring, measurement and validation (MMV) | <ul style="list-style-type: none"> • Fluid properties, geochemical reactions, porosity, and permeability changes | <ul style="list-style-type: none"> • PVT and parametric flow studies • Autoclave experiments for geological modeling and acid species analysis • Reactive transport modeling |

The following sections summarize the scope of the Phase 2 work programs.

1.4.2.1. CO₂ Capture Technologies

The technical feasibility of capture processes and overall costs are greatly affected by the amount of clean up required for any given process as specifications become more stringent. Impurities from the capture process will impact the efficiency of pipeline transportation and the work program was focused mainly on determining the effects impurities have on compressing CO₂ to supercritical state and a pressure of 2200 psi. Key issues under discussion were as follows:

Dew Point and Corrosion Program – Understanding water solubility and dew point in supercritical CO₂ mixtures is important because as long as water remains in the supercritical phase, corrosion and hydrate formation are minimized. There is much literature with references to the solubility of water in pure supercritical CO₂ and supercritical CO₂ with CH₄ and H₂S impurities, over the critical range of temperatures and pressures. However there is little knowledge regarding water solubility in CO₂ with the types and quantities of impurities typically found in anthropogenic CO₂. These impurities can have a significant impact on the water carrying capacity of the supercritical fluid. There are several analytical techniques for measuring solubility and dew point that generally involve combining CO₂, the desired impurities and water into a closed vessel whose internal conditions can be controlled, and then looking for the point at which free water begins to form. In Phase 2, an innovative technique was applied to measuring dew point in various CO₂ compositions.

Hydrate formation was excluded from Phase 2 as there is already a large body of public literature on hydrates, including all of the impurities found in anthropogenic CO₂. Additionally, unlike natural gas that is commonly transported in a water-saturated condition through gathering systems, anthropogenic CO₂ is always treated at the capture facility to meet a dew point specification. Thus, hydrate formation conditions will be rare in CCS infrastructure. Lastly, should hydrate conditions be encountered, mitigation strategies for CO₂ transport systems would not be significantly different from those used in the natural gas industry.

1.4.2.2. CO₂ Transmission Pipeline Transportation

The transportation of CO₂ using pipelines is well understood but experience to date is limited to either pure CO₂ streams or CO₂ with single contaminants (binary mixtures). As the amount and complexity of impurities increase, costs, operability and safety of pipelines are impacted; particularly by the levels of impurities typically found in anthropogenic sources of captured CO₂ streams.

Key issues related to pipeline transportation of CO₂ are (i) the impact of impurities and (ii) wave speed and crack propagation.

The issue of crack propagation relates to the possibility of catastrophic running ductile fractures in CO₂ pipelines due to the difference in speed of crack propagation as compared to the decompression wave. Steel with increased toughness or crack arresters are used to mitigate this concern (at a high cost) and much research has been done in understanding the phenomena,

particularly by TransCanada Corporation and NOVA Chemicals. Thus, the ACPD work program did not address this issue because other active research programs were.

As determined by the literature review, there was a need to gain a better understanding of the effect of anthropogenic impurities on transportation capacity. Therefore, the transportation work program was focused around obtaining a better understanding of the flow properties of various CO₂ compositions so that unnecessary overdesign parameters could be reduced and in turn lead to optimization of design, reduction in materials, and decreases in construction and operation costs.

The two main components of the work program were:

1) Capacity Validation - The impact of impurities on pipeline capacity and pump/compressor requirements and performance were evaluated through a comprehensive literature review and analysis of work that has already been published. Literature indicates that some impurities at levels as low as 5 – 10% can decrease the physical capacity of a pipeline by as much as 25%. However, most empirical work in this area appears to be using binary mixtures (i.e. CO₂ plus just one impurity). Understanding the effect of multiple impurities, their interaction and the impact on capacity and pump/compressor selection is critical to the economic and safe design of a supercritical CO₂ pipeline. The analysis used existing software to conduct an investigation of the effects of impurities on flow capacity and the various system design parameters.

2) Flow Loop Testing - Flow loop testing was undertaken to test the six compositions defined in Table 2. Flow loop testing consisted of a lab-scale pipeline segment that was tested in a controlled environment. The purpose of this testing was to help gain a better understanding of the effects of operating conditions in terms of ranges of pressure and temperatures on pipeline operability in the supercritical and dense regions and closeness to the respective phase envelopes. A high pressure loop (NPS 2 pipe, rated up to 22 MPa operating pressure) located at the TransCanada Gas Dynamic Test Facility (GTDF) in Didsbury, Alberta was used. It was modified to allow testing and validation of the flow characteristics of anthropogenic CO₂ mixtures. The GTDF is an internationally recognized high pressure facility that has been in operation since 1984. Testing and analysis was conducted by NOVA Research and Technology Corporation (NRTC) on behalf of TransCanada.

1.4.2.3. CO₂ Enhanced Oil Recovery

The EOR work program focused on understanding the effects that impurities in CO₂ have on MMP which is the minimum pressure at which the injected gas and oil combine to form a single, uniform mixture. A miscible flood operating at or above this pressure should maximize oil recovery, while floods operating below this pressure will leave unrecovered oil in the reservoir. Most impurities found in anthropogenic CO₂ have a negative impact on the oil recovery process by increasing the MMP. Laboratory testing was undertaken to gain a better understanding of the magnitude of these impacts, especially with mixtures involving multiple impurities. MMP was tested on one representative oil sample from Alberta using two different types of equipment: rising bubble

apparatus (RBA) and slimtube. Using these tests the Project was able to estimate the negative oil recovery impact of impurities.

1.4.2.4. CO₂ Sequestration in Deep Saline Aquifers

The sequestration work program was mostly concerned with the performance of the storage formation and was focused on better understanding the effect that impurities have on a sequestration scheme's containment, pore space use efficiency and capacity, plume extent, trapping capability, and injection scheme performance. The three major elements of the work program were as follows:

Numerical Modeling and Autoclave Experiments - Computer geological modeling was completed on a modified version of a carbonate rock reservoir model obtained from the University of Calgary's Wabamun Area Sequestration Project (WASP; <http://www.ucalgary.ca/wasp/>). Physical testing was done by exposing actual Western Canada Sedimentary Basin rock to supercritical fluid reservoir conditions in an autoclave. The purpose of this element was to help gauge changes, if any, in the mineralogy of rock samples and their likely impact on porosity, permeability and injectivity.

Acid Species Analysis - Geochemical modeling was completed to estimate the impact of minor and trace reactive gas species such as HCl, SO₂, NO₂ and other trace gases, particularly the concentration threshold below which the species can be neglected. The analysis relied on modeling because the acid species were not dealt with in laboratory experiments. These tests helped to determine the rate at which wells could potentially fail or be abandoned.

Reactive Transport Modeling – This modeling combined chemical reaction and flow behaviour models to help determine chemical reactions, and permeability and porosity changes that could be expected through the system. The modeling also included two related but distinct analyses: far-field and near-field. In the far-field analysis, away from the injection well, the modeling used a range of reservoir types (carbonate, siliciclastic with various levels of clays and feldspars) calibrated to the autoclave geochemical experiments to test the sensitivity of each reservoir type to various CO₂ purity streams. Previous modeling had shown that contrast in dissolved amount of supercritical phase components changes the composition of the supercritical phase and thus viscosity and density of the phase as it flows. Chemical interactions of the components with minerals and other solid phases will either moderate or enhance the change. This has bearing on cost because a potentially larger plume will require geological characterization and post-injection monitoring of a larger area. The near-field analysis is similar but focused on the potential for a sharp decrease in porosity, permeability, and injectivity which could impair wells, decrease their availability for injection (that is, more wells would be needed), and increase costs through multiple remedial workovers.

1.4.3. Phase 3 - Quantifying Economic Implications

One of the ground-breaking attributes of ACPP is that it tied economic costs to technical parameters in order to quantify impact. A techno-economic model was built in order to do this.

Creating Economic Factors – All the technical data collected in Phase 2 of the study were linked to economic implications that quantified (as a dollar amount) the effects of impurities on an integrated CCS system. For capture and pipeline, the data collected helped to define the design parameters that directly affect cost. For EOR, the data collected on the effect that impurities have on MMP was used to determine potential changes in oil recovery, and thus, changes in revenue that results from injecting impure CO₂. For sequestration, the behaviour of impure CO₂ in a geologic formation determined the design of the injection scheme (number of wells, failures, etc.) as well as the measurement, monitoring and verification (MMV) requirements and the required pore space, all of which have cost implications.

Building the Techno-Economic Model – Based on our knowledge of the public literature, the techno-economic model will be the first of its kind in the world. It allows the user to input system parameters such as capture process, pipeline length and EOR / sequestration allocation and understand the effect of these inputs throughout the system. This tool's scenario structure ensures that it is relevant to many diverse users and applications. The user defines input parameters, including capture technologies or combinations of technologies, pipeline length and end market choice (EOR or sequestration). The model derives a combined CO₂ stream and purity which are linked to cost factors for each value chain component. These factors are used to calculate cost impacts to each value chain component and to the CCS system in its entirety. The model directly compares the impure CO₂ scenario to a 100% pure CO₂ scenario and determines how the total system and individual components are affected by the presence of impurities. For example, the user is able to input lower purity capture streams, and observe the trade-off of these lower capture costs against resulting higher pipeline costs.

The model was designed to be flexible for multiple users with varying interests and objectives. It was designed to clearly illustrate the trade-offs between scenarios. This will allow any user to define their own assumptions and run scenarios to see the impacts they are most concerned with.

1.4.4. Phase 4 - Prepare and Share Project Deliverables

The key deliverables of the ACPP Project were a working techno-economic model and this comprehensive final report detailing the findings of the Project. The ACPP model was provided to each Project participant so that it can be used in individual circumstances using proprietary or regional data.

2. CO₂ Capture Technologies

2.1.Phase 1 Outcomes

During Phase 1, an internal review was conducted by the capture technologies team of stream composition data related to CO₂ capture. The review involved not only gathering stream composition data from several companies, but also aggregating and synthesizing these data into a common working format.

Requests for information were made to more than 20 companies and included industrial processes such as natural gas treatment, reforming and combustion, and oil (including bitumen) production, upgrading and refining, as well as coal gasification and combustion. More than 50% of companies surveyed responded. The information provided ranged from compositions of actual and estimated flue gas and process streams to actual and estimated high pressure CO₂ streams (including some impurities) ready for transportation from plant sites.

In total, 19 different raw “pre-CO₂ extraction” streams and 29 different “pipeline ready CO₂” streams were provided. Additionally, 18 intermediate stream compositions were provided, several of which did not appear to be materially different in CO₂ composition when compared to their corresponding “pre-CO₂ extraction” stream, although impurity levels varied. Several other intermediate stream compositions did not appear to be significantly different in overall CO₂ or impurity compositions when compared to their corresponding “pipeline ready CO₂” stream except for water content.

“Pre-CO₂ extraction” streams showed a very wide range of CO₂ and impurity concentrations depending on the fuel, feedstock and the industrial process. Within some industrial processes, there were different potential “pre-CO₂ extraction” streams targeted for CO₂ capture. For instance, potential capture scenarios were presented for flue gas streams, tail gas streams, syngas streams and mixtures of flue gas and tail gas streams for different steam methane reforming facilities. As well, within the various industrial processes, significant deviation existed in CO₂ and impurity concentrations, as well as CO₂ mass flow rates and other process parameters such as the target stream flowing temperature and pressure. Nearly all reported streams were actual compositions or estimates of actual compositions.

“Pipeline ready CO₂” streams showed a fairly narrow range of CO₂ and impurity concentrations, generally irrespective of the CO₂ capture technology used. With a few notable exceptions, natural gas fired or natural gas fed industrial processes tended to show CO₂ concentrations in “pipeline ready CO₂” streams in excess of 98.75 mole% and typically in excess of 99.75%. Coal fired or coal fed industrial processes tended to show results within the same range, although not typically exceeding a CO₂ concentration of 99.75%. Predominantly, the reported pressures for these streams were fairly consistent near 2,200 psig and reflected highly concentrated CO₂ streams in a dense phase. A few reports indicated pressures as low as ~1500 psig or as high as ~2600 psig. Not all

reported streams were actual compositions. Rather, some reported streams were from studies of varying depth and rigor.

Given the wide range of impurities within the “pre-CO₂ extraction” streams, there were some important stream by stream variations with respect to residual impurities within the more narrow range of “pipeline ready CO₂” streams. In particular, depending on whether the data set included certain specific industrial processes or not, the maximum concentration of certain impurities could vary significantly even though the high concentration of CO₂ in the “pipeline ready CO₂” streams remained relatively constant.

This work informed the ACPP workshop that took place during Phase 1 which led to the development of the CO₂ composition scenarios presented in Table 2.

2.2.Phase 2 Research Needs

An understanding of water solubility and dew point in supercritical CO₂ mixtures is important because as long as water remains in the supercritical phase, corrosion and hydrate formation are suppressed. Studies of the solubility of water in pure supercritical CO₂ and in supercritical CO₂ with CH₄ and H₂S impurities are reported in the scientific literature over the critical range of temperatures and pressures. However, there is little knowledge regarding water solubility in supercritical CO₂ containing the types and quantities of impurities found in anthropogenic CO₂. These impurities could have significant impact on the water carrying capacity of the supercritical phase. Therefore, a study of the impact of anthropogenic impurities on water solubility, the dew point and the onset of corrosion in supercritical CO₂ mixtures is required to assist the design of pipeline and other facilities.

2.3.Phase 2 Research Program

There are several analytical techniques for measuring solubility, dew point and onset of corrosion that generally involve combining CO₂, the desired impurities and water into a closed vessel whose internal conditions can be controlled. The dew point is then determined by changing temperature and pressure and identifying the point at which free water begins to form or at which corrosion takes place.

ACPP and Carbon Management Canada (CMC) engaged two Canadian research groups to undertake complementary studies:

- The microfluidics technology of Dr. David Sinton (University of Toronto) provides fast and accurate dew point determinations but is not be able to address corrosion. This novel microfluidics technology however required adaptation and validation for use in supercritical CO₂.
- Dr. Weixing Chen (University of Alberta) uses more conventional technology to undertake corrosion assessments. His method also gives indirect dew point estimates from the onset of corrosion, an independent method which would be used to validate the microfluidics technology.

Thus, the objectives of the research program were to:

- Adapt the microfluidics chip technology for the determination of dew points in supercritical CO₂;
- Validate the microfluidics technology by comparing results to the literature for a defined set of characteristic compositions and pressure and temperature values;
- Perform dew point measurements for specified CO₂ compositions using the microfluidics technology; and
- Perform dew point assessments using corrosion onset determinations for the same specified CO₂ compositions.

The CO₂ compositions that were used are shown in Table 4.

| Table 4. CO₂ Compositions for Dew Point and Corrosion Measurements | | | | |
|--|---------|---------|---------|---------|
| Gas Mixture Number | 1 | 3 | 4 | 7 |
| | (mol %) | (mol %) | (mol %) | (mol %) |
| CO₂ | 82.5 | 91.7 | 95.0 | 99.8 |
| N₂ | 3.4 | 2.5 | | 0.2 |
| O₂ | 5.2 | 5.8 | | - |
| Ar | 8.9 | | - | - |
| CO | - | - | 0.5 | |
| H₂ | - | - | 4.0 | |
| CH₄ | - | - | 0.5 | |
| Total | 100.0 | 100.0 | 100.0 | 100.0 |

2.4. Research Outcomes

2.4.1. Dew Point Determination using Microfluids Technology

(Edited summary)

Section author: Dr. David Sinton, University of Toronto

Overview

Dew point conditions for pure and impure CO₂ mixtures were measured using a novel microfluidic method which is based on the direct visualization of liquid phase (dew) formation in a microchannel at specific pressures and temperatures. To apply this new technique for detecting the

dew point in impure CO₂ mixtures, the first step was to validate the method for the pure CO₂ and water system, a well-studied mixture for which comparison with the available literature data is possible. After the validation, the dew point for each of the impure mixtures in Table 4 was determined.

Method Description

A microfluidic chip was fabricated by etching a straight channel onto a piece of borosilicate float glass (S.I. Howard Glass, Worcester, MA, USA) using photolithography and wet etching. These techniques were previously demonstrated in-house. A glass substrate was chosen due to its water-wettability, pressure and temperature tolerance, and imperviousness to supercritical CO₂. The channel (6cm×100µm) was etched to the center of the chip and square hatches were created around the channel to enhance bonding quality, resulting in improved pressure resistance.

A stainless steel chip holder, as shown in Figure 3, was fabricated to enable the microfluidic chip for operation at pressures beyond the critical pressure of CO₂. Two 50W miniature high temperature cartridge heaters (McMaster Carr #8376T22) were used to heat the holder and the chip such that on-chip visualization could be realized at the desired temperatures. The cartridges were inserted into two grooves on the top surface of the chip holder which were symmetrically placed about the microchannel. The heaters were regulated using an Omega CNi 1643-DC temperature controller (Omega Engineering Inc., Laval, QC, Canada). A thermocouple connected to the controller was adhered on the top surface of the chip 1mm away from the center of the microchannel. An inlet and an outlet port were created on the steel holder to load the chip with high pressure fluids. O-rings (Double seal BUNA-N 004, McMaster Carr #90025K119) were used to create a leak-free interface between the steel manifold and the glass chip.

The experimental setup is shown in Figure 4. Water was first added to pure and impure CO₂ (purchased from Praxair), to create the wet mixture. De-ionized water was injected using a 50µL glass syringe (Hamilton syringe, luer tip 80501) into a sealed steel cylinder (150mL, Swagelok 316L-50DF4-150) initially filled with CO₂ at atmospheric conditions to create the specific water content.

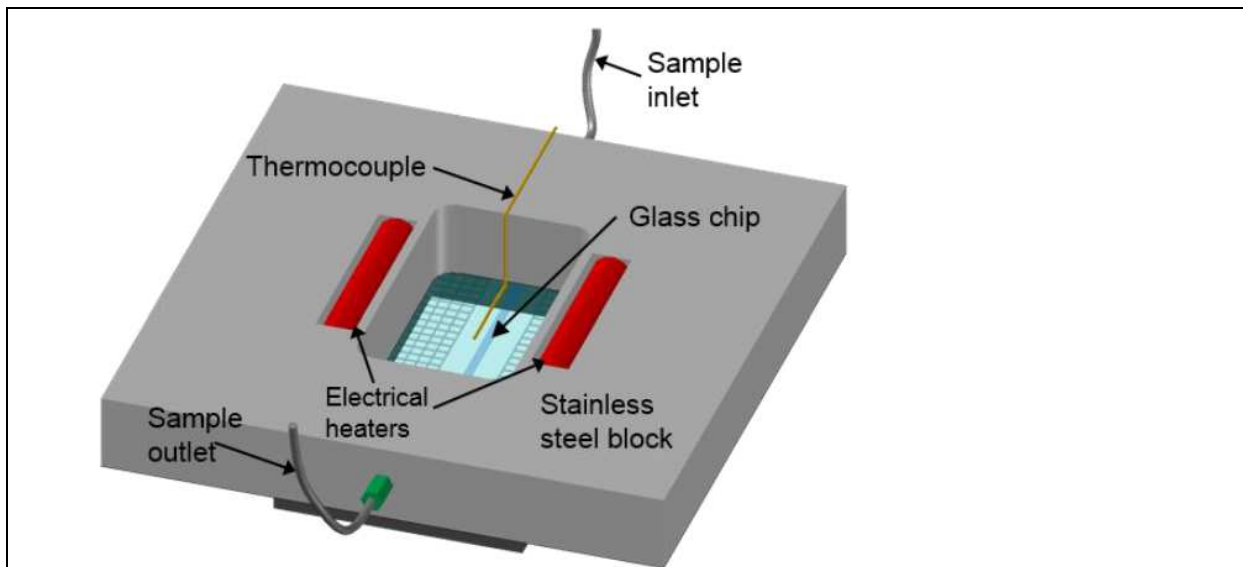


Figure 3. Schematic of Microfluidic Approach with high pressure, high temperature stainless steel chip holder and a 1"x3" glass chip

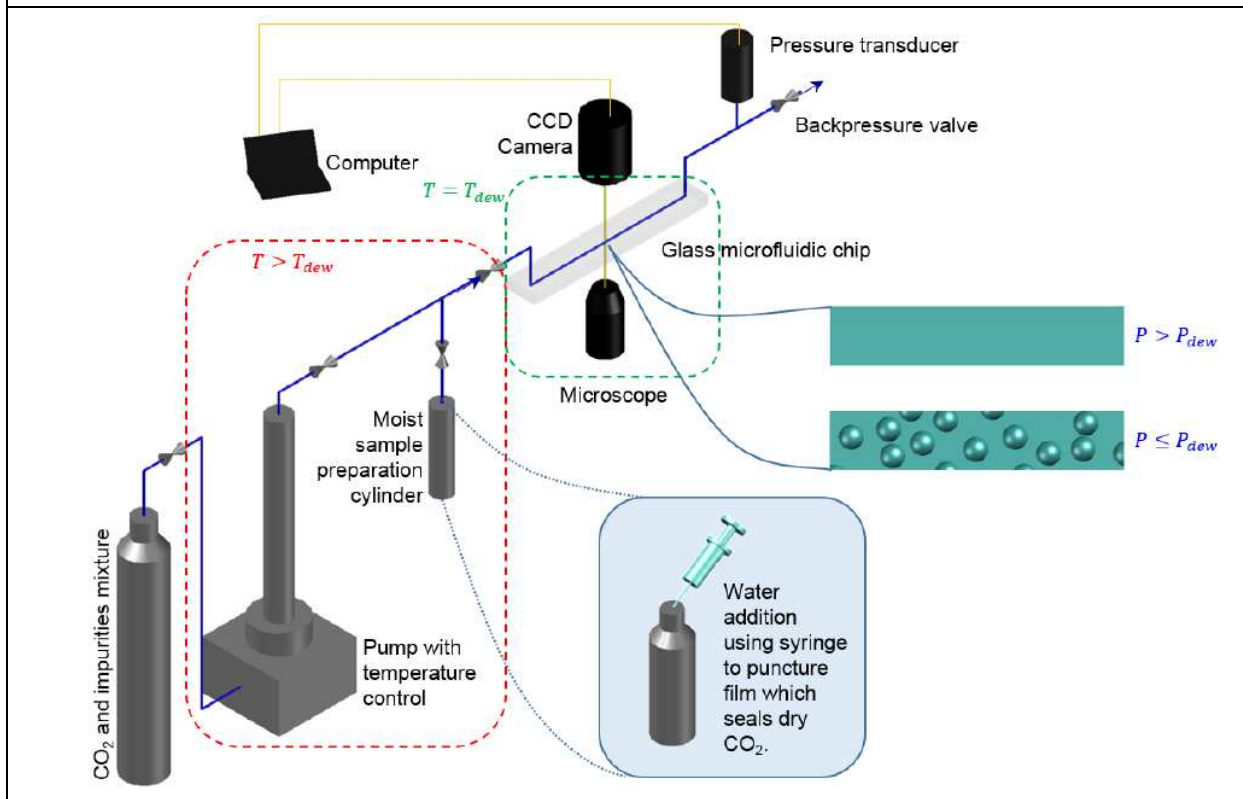


Figure 4. Experimental Setup for Sample Preparation and high pressure, high temperature dew point testing

The cylinder with water and CO₂ (at initial low pressure) was then submerged in a 75°C water bath (Thermo SCIENTIFIC HAAKE SC150) and pressurized in a step-wise fashion using a syringe pump (TELEDYNE ISCO model 260) to 3000psi. The pressurized sample was left to equilibrate. The preparation conditions (75°C and 3000psi) were well above the expected dew points for all water contents used in the present study and were thus chosen to generate a well-mixed, single-phase fluid sample with the desired concentrations. The moist sample was then loaded into the syringe pump, after which the moisture-addition cylinder was isolated from the experiment. All connections between the pump, moisture-addition cylinder, and the visualization platform were made with stainless steel tubing which was encased in water jackets to prevent premature condensation. A small circulation pump (Hydor Pico II Mini Pump) was used to flow water from the 75°C water bath through each water jacket. The minimum measured temperature at the flow outlet was 72.2°C, well above the required temperature to prevent such untimely condensation.

Single phase, moist CO₂ was initially introduced to the microfluidic visualization platform by incrementally releasing the upstream needle valve (McMaster Carr #4800K62) while keeping the downstream microvalve (UpChurch Micro-Splitter Valve 10-32 Grad - P-470) fully closed to maintain backpressure. Chip pressure was monitored with a downstream pressure transducer (Swagelok PTI-S-NG5000-15AO). Sudden transitions during pressurization were avoided to prevent rapid gas expansion and possible channel rupturing.

Fresh sample was introduced to the microchannel by allowing ultra-low flow (~1μL/min), sufficient to fill the chip with fresh uniform test sample while maintaining the pressure safely above the expected dew point pressure. Specifically, the pressure drop at this flow rate was estimated to be ~ 5psi, whereas the chip pressure exceeded the expected dew point pressure by more than 600psi. The backpressure valve was then closed, isolating the test sample within the confines of the microchannel. The chip temperature was held constant while system pressure was incrementally decreased (via the pump) until the droplets were observed. System pressure was reduced gradually, with maximum expansion rates of 5mL/min to minimize transient effects. The phase condition was monitored for 15 minutes at each pressure to allow sufficient time for potential droplet formation. Once the first droplets formed (indicating system pressure had dropped below the dew point pressure), the pressure was tuned at small increments in the vicinity to delineate the particular dew point pressure.

The dew point was determined using the following criterion:

- i. If no droplets are observed, or if the observed droplets shrink, then $P > P_{\text{dew}}(T, W_{\text{H}_2\text{O}})$;
- ii. If droplets are observed to grow, then $P < P_{\text{dew}}(T, W_{\text{H}_2\text{O}})$; and
- iii. If droplets remain unchanged, then $P = P_{\text{dew}}(T, W_{\text{H}_2\text{O}})$.

The dew point was determined as the point at which droplet sizes stayed constant, i.e., rates of condensation and evaporation were equal. For each dew point collected, the pressure was increased again to reach single phase and the dew detection procedure was repeated to ensure consistent

data. The microchannel was imaged by a digital camera (COOLSNAP MYO), and the images were automatically transferred to a computer for analysis.

Results

Experiments were conducted for pressures up to 2500 psi and temperatures between 31 and 50°C. Droplet formation and growth was observed within seconds of pressure reduction below the dew point pressure. Images were taken at a fixed location over time to track droplet formation and droplet size evolution. Droplet growth due to both condensation and coalescence were observed.

For validation, the method was first applied to the well-studied CO₂-water system. The images in Figure 5 show the observed field of view for the CO₂-water system prior to dew formation ($P > P_{\text{dew}}$, Figure 3a) and after initially dropping below the dew point pressure ($P < P_{\text{dew}}$, Figure 3b). As shown, droplets on the order of $D = 1\text{-}2\mu\text{m}$ are sharply visible using brightfield microscopy, in part due to the strong contrast in refractive index ($n_{\text{CO}_2} = 1.00$, $n_{\text{H}_2\text{O}} = 1.33$) and associated lensing at the high-curvature (small radius) droplets. With visible dew formation, the pressure was increased to reduce droplet size and subsequently finely tuned to determine the pressure at which the droplet size remained constant with time ($P = P_{\text{dew}}$).

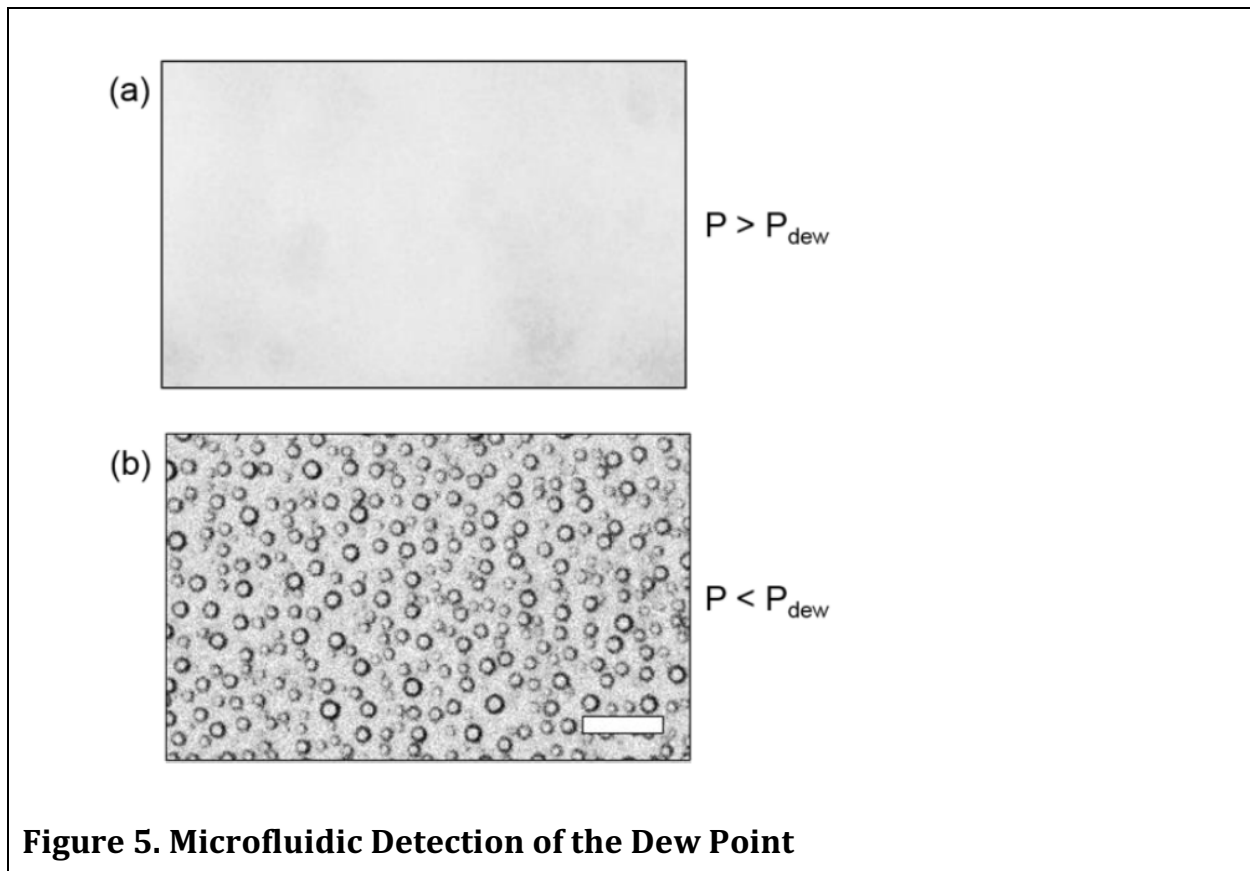


Figure 5. Microfluidic Detection of the Dew Point

Figure 6 shows measured dew point data for pure CO₂ and water mixtures plotted with both experimental results and theoretical predictions from literature data. (See references 1, 2, 3, 4, 5, 6, 7, 8, 9, 10). Dew point pressures were obtained using the microfluidic approach for different water contents on the 31, 35, 40, and 50°C isotherms. As shown, the microfluidic results correspond closely to both previous experimental and theoretical results. The slope of the water solubility diagram near the critical pressure ($P \sim 1070$ psi) is very high for the 31°C isotherm case (Figure 6), due to the proximity of the critical point. Notably, the predicted sharp slope in this case is reproduced well by the microfluidic approach, an area for which there is insufficient previous data. The more gradual transitions for higher temperature cases are also well reproduced and in good agreement with previous measurements where available.

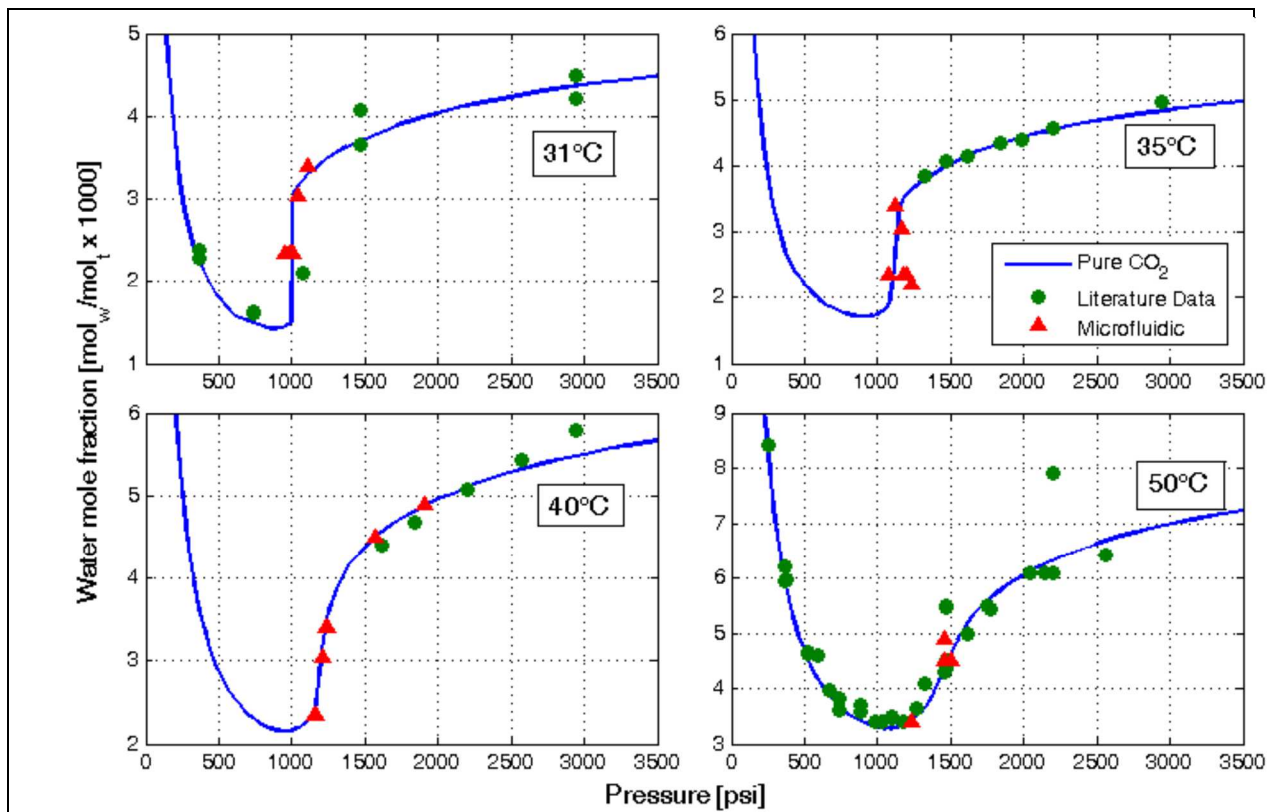


Figure 6. Dew Point Data obtained using the proposed microfluidic method plotted against theoretical values and experimental results found in the literature

Water solubility in mole fractions is shown as a function of pressure along the 31, 35, 40, and 50°C isotherms

The CO₂ compositions in Table 4 were then tested to determine their dew point. The dew point conditions for water in Mixtures 1 and 7 were similar to those of water in pure CO₂. In particular,

for Mixture 1 and 7, no dew was detected at the industrially important water concentration of 500 ppm (weight) for temperatures of 35°C and above over the experimental pressure range (1000 to 2000 psi); at 31°C and 500 ppm (weight) water, the dew point for Mixture 7 was 1065 psi. While the composition of Mixture 7 is close to pure CO₂, Mixture 1 had the lowest CO₂ content and the highest amount of impurities.

The water solubility of Mixtures 3 and 4 were much lower than that of pure CO₂ and higher pressures were required to remain in single phase compared to pure CO₂, indicating that these impurity compositions may require higher pressures for safe transportation. Results for a water concentration of 500 ppm (weight) are shown in Table 5.

| Table 5. Dew Points of CO₂ Compositions (psi) using Microfluids at Water Concentration of 500 ppm (weight) | | | | |
|--|------------------|------------------|------------------|------------------|
| Temperature (°C) | Mixture 1 | Mixture 3 | Mixture 4 | Mixture 7 |
| 31 | | 1005 | 1020 | 1065 |
| 35 | No dew | 1050 | 1060 | No dew |
| 40 | No dew | 1100 | 1000 | No dew |
| 50 | No dew | No dew | 1200 | No dew |
| Measured water concentration (ppm weight) | 472 | 467 | 486 | 501 |

In conclusion, the microfluidic approach for dew point measurements was successfully validated using the pure CO₂ – water system. The method was then applied to determine the dew point conditions of water in industrially relevant CO₂ mixtures. The dew point conditions for Mixtures 1 and 7 remained very similar to that of pure CO₂ and water, while impurities in Mixtures 3 and 4 reduced the mixtures' overall solubility for water, indicating a potential increase in pressure requirements for safe transportation.

However, for the water contents generally required by industry, at 500 ppm (mass-based, or equivalently $1.1-1.2 \times 10^{-3}$ molwater/moltotal), no dew was detected for pressures above 1250 psi and temperatures above 35°C for the 4 compositions tested. These results indicate that no liquid water is expected in these gas streams with this (relatively low) water content, when transported at pressures above 1250 psi and temperatures above 35°C.

2.4.2. Dew Point Determination using Onset of Corrosion

(Edited summary)

Section author: Dr. Weixing Chen, University of Alberta

Overview

All four gas mixtures in Table 4 were tested to determine their dew points with water contents at 500 and 1,000 ppm (weight).

Method Description

The determination of dew points performed by the group at the University of Alberta was based on corrosion assessments of X-65 pipeline in various moisture-containing supercritical CO₂ gas mixture environments. As all the gas mixtures evaluated contain very high level of CO₂, any condensation of water on the steel surface could lead to the dissolution of CO₂ and the subsequent CO₂ corrosion of the steel. Fe⁺² ions or its compounds could be formed due to the corrosion in the environments that are free of oxygen and Fe⁺² could further be oxidized to Fe⁺³ ions when oxygen is present. This corrosion approach to determine the dew point is very reliable and highly sensitive because of the high concentration of CO₂ and the high susceptibility of the carbon steel (X-65) to CO₂ corrosion.

The test setup for the dew point measurements is illustrated in Figure 7. It consists of three main sections:

- 1) Gas cylinder (Praxair, Canada), which contains a dry gas mixture that has the required gas composition. The gas mixture is pressurized to a high constant pressure using a Maximator gas booster system (High Pressure Technologies, USA). Moisture is added separately into the gas mixture.
- 2) Moisture mixing capsule is placed in a pre-heat water bath, which is for the purpose of adding water to the system and producing the required moisture levels in the gas environments. The water is injected after the entire system is purged with the dry gas mixture to remove air in the loop. After injection of water, this capsule is heated to transform water into moisture and then injected with the gas mixture to pressurize the system as required.
- 3) The test capsules are placed in two Refrigerated/Heated Water Baths (Fisher Scientific, USA), which consists of 4 individual capsules connected and immersed in the water baths. The temperature of the two water baths can be adjusted from -20 °C to +100 °C. The gas mixture in the moisture mixing unit is released to the test capsules to start the test. The pressure in the test capsules can be controlled by operating the gas booster that builds the gas pressure in the moisture mixing unit and monitored by reading the pressure gauge connected to the testing capsules. The moisture mixing capsule has a much larger volume than the test capsules so that the drop of pressure after gas release to the test capsule can

be minimized. The temperature in the test water baths should be lower than that in the pre-heat water bath.

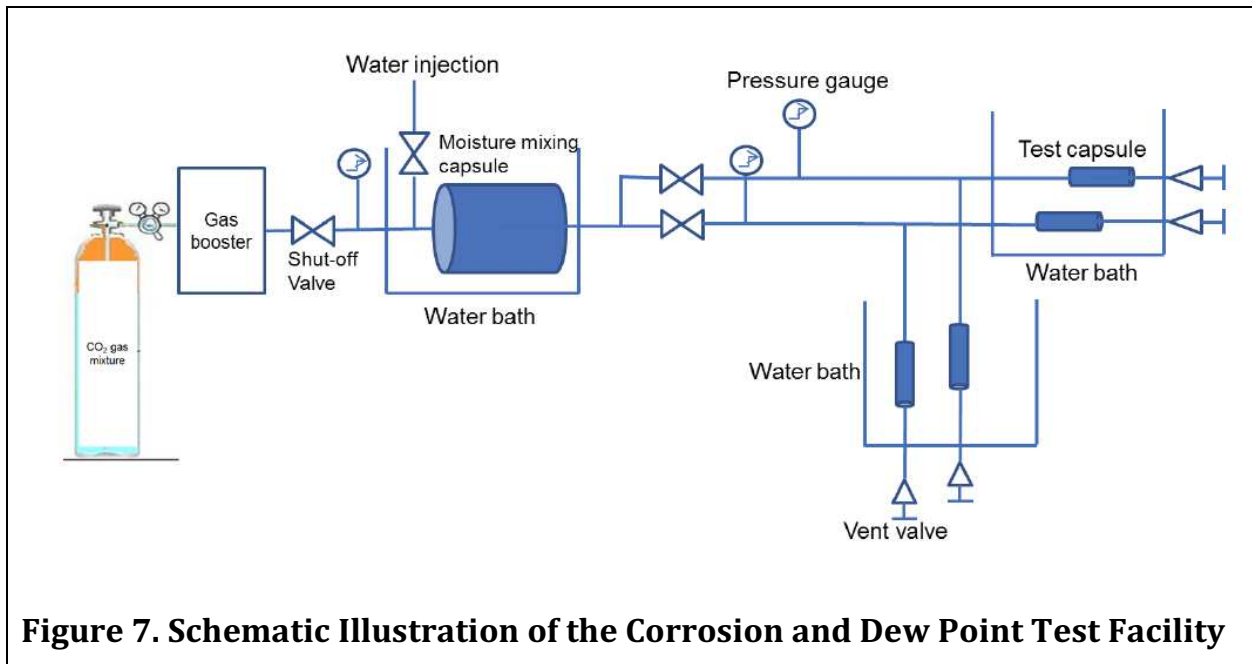


Figure 7. Schematic Illustration of the Corrosion and Dew Point Test Facility

Rectangular coupons with a dimension of 10 mm x 4 mm x 2 mm were cut from the X-65 pipeline steel. All the coupons were ground using emery paper from 400# to 1200# grit finish. The coupons were then washed in an acetone ultrasonic bath prior to the tests. The dew point measurements in the gas mixture with a water content of 500 ppm were required to be tested in the project. However, tests were also conducted in the gas environments at higher water contents in order to validate the system. All the corrosion exposure tests were conducted for about 24 hours. The coupons after exposure were examined by an optical microscopy and a high-resolution JEOL (JSM-6301FXV) field emission scanning electron microscopy (FESEM) and ZEISS (EVO-MA 15) scanning electron microscopy (SEM), respectively.

Results

Method validation was necessary because no similar research could be found in literature. Initial efforts were made to determine typical features of corrosion caused by water condensation at a water concentration of 10,000 ppm (weight). These measurements were conducted with Mixture 3 in Table 4. A typical morphology of the corrosion observed on the coupons exposed to the gas mixture at 1250 psi and 45°C is shown in Figure 8. The corrosion pits have a circular shape, which should be the replication of the water drops condensed on coupon surface when the testing temperature was below the dew point. Corrosion products were observed along the circular edge as well as inside the circular pits.

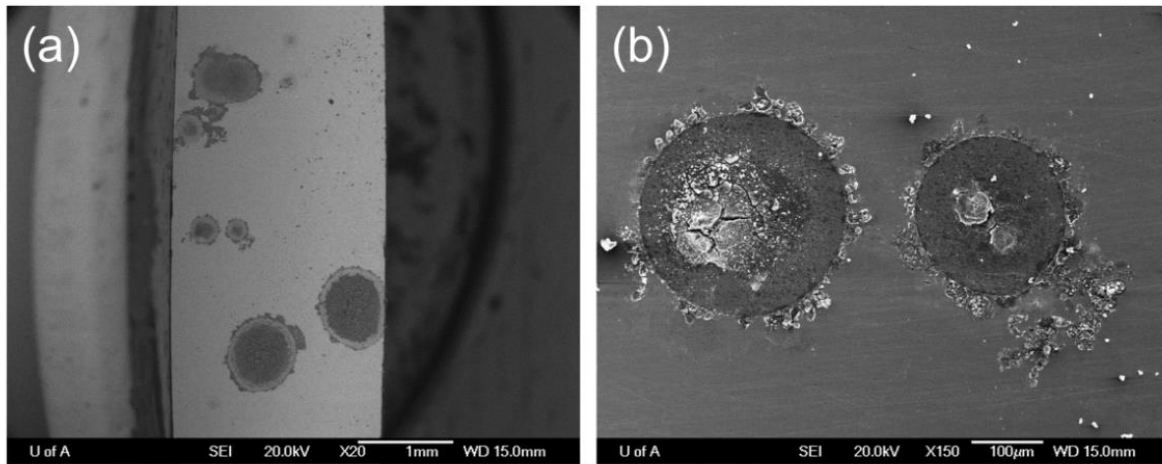


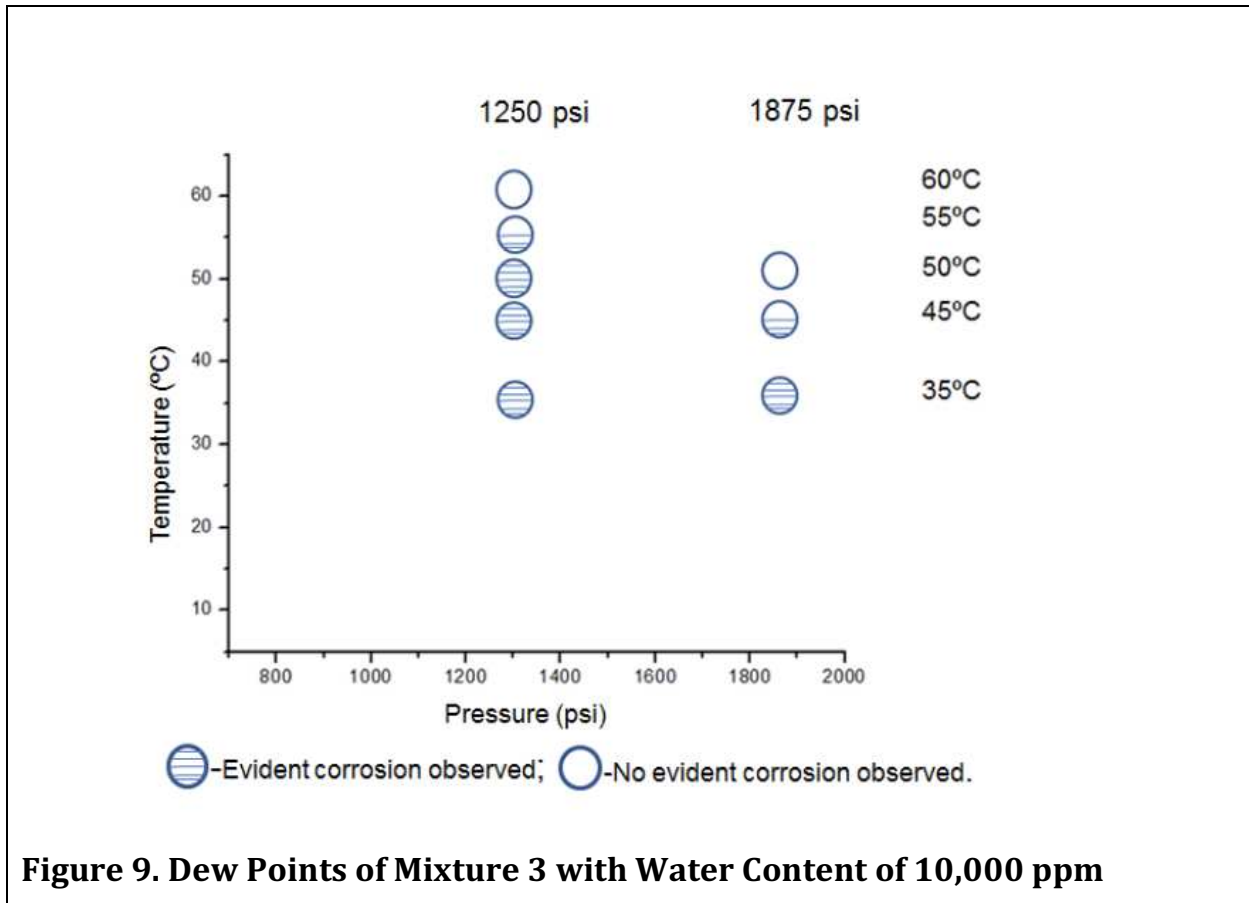
Figure 8. Corrosion Observation on (a) the coupon tested at 1250 psi and 45 °C in Mixture 3 containing 10,000 ppm water; (b) image in high magnification

The pitting corrosion could be observed on the coupons tested in the gas mixture with a water concentration of 10,000 ppm (weight) at temperatures up to 55°C at 1250 psi and to 45°C at 1875 psi. When the temperature increased above those temperatures, no evident corrosion was observed. Therefore, based on the corrosion observed under different conditions (See Figure 9), the dew point for gas Mixture 3 with the water content of 10,000 ppm is at around 55°C at the pressure of 1250 psi, and at around 45°C at 1875 psi.

The CO₂ compositions in Table 4 were then tested at concentrations of 500 and 1000 ppm (weight) water and pressures of 1250 and 1875 psi. The highest temperature at which corrosion was detected on the coupons was taken as the dew point and is shown in Table 6.

Table 6. Dew Points of CO₂ Compositions (°C) using Onset of Corrosion at Water Concentration of 500 ppm (weight)

| Pressure (psi) | Mixture 1 | Mixture 3 | Mixture 4 | Mixture 7 |
|----------------|-----------|-----------|-----------|-----------|
| 1250 | 25 | 35 | 35 | 35 |
| 1875 | 20 | <35 | <35 | 35 |



In conclusion, the dew point, as determined by the onset of corrosion was found to be similar for Mixtures 3, 4 and 7 over the experiment range and given the chosen temperature increments. Mixture 1 exhibited lower dew points and thus an apparent higher ability to keep water in the dense phase despite its high impurity content.

The microfluidic and corrosion methods yields similar outcomes on an overall basis: the impure CO₂ composition tested would not result in a separate water phase or corrosion if the temperature is maintained above 35°C and the pressure above 1250 psi when water concentration is at the industrially important value of 500 ppm (weight).

3. CO₂ Transmission Pipeline Transportation

(Edited summary)

Section authors: Dr. Kamal Botros and John Geerligs, NOVA Chemicals

3.1. Phase 1 Outcomes

The effects of impurities in anthropogenic CO₂ on pipeline transportation flow capacity was first evaluated by a literature survey and fundamental analysis based on flow calculations with different mixtures of CO₂ with various impurities which was conducted by the NOVA Research and Technology Centre. While there are CO₂ pipelines in commercial service worldwide, the majority of these pipelines transport relatively pure CO₂ from geological sources to oilfields for use in EOR. Anthropogenic CO₂ is less pure than geological CO₂ and may contain a variety of impurities that may materially affect the gas properties of the CO₂ (impacting the rate of crack propagation), and negatively impact transportation flow capacity.

The literature review found that indeed the presence of impurities affect pipeline transportation flow capacity. The general effect is that the higher the level of impurities, the higher the reduction in the flow capacity given same pipeline inlet pressures and flow temperatures. Furthermore, impurities with much lower molecular weight than CO₂ (e.g. H₂ and CH₄) result in higher reductions in flow capacity. It was determined that a typical impurity level of 5% in anthropogenic CO₂ would result in a reduction in transportation flow capacity by approximately 3 to 6%, and that an impurity level of 11% would cause reductions in flow capacity in the order of 7 to 17.5%.

Studies published in the literature predominantly are concerned with investigations of binary mixtures rather than the more complex impurity mixtures of anthropogenic CO₂. By and large, the literature was found to be very scarce with very little information available on flow capacities of pipelines carrying anthropogenic CO₂ mixtures either from actual pipeline systems or numerical simulations. Only few papers presented results of numerical simulations showing the effects of impurities on flow capacity for CO₂ compositions typical of the three main CCS technologies namely oxyfuel, pre-combustion and post combustion.

For example, CO₂ with impurities such as argon and oxygen has not been transported before by pipeline and therefore their effects on pipeline design parameters are not fully understood. Furthermore, due to CO₂'s unique properties and operating parameters, careful consideration needs to be given to the interrelationship of the impurities, in particular how they interact with each other and consequently how they change along the pipe length. For example, Figure 1 shows an example from the literature of the relationship between pipeline capacity and pipe diameter for a given pressure drop of 20 kPa/km¹¹.

In general, the information uncovered by the literature review was based on theoretical analyses and on numerical simulations of simple binary systems mostly with impurities found in geologic CO₂, such as methane. In addition results were not consistent due to the use of different equation

of state, and temperature and pressure conditions. No experimental data based on flow in a pipeline was found. This outcome clearly supported the need for physical testing in a pipeline loop.

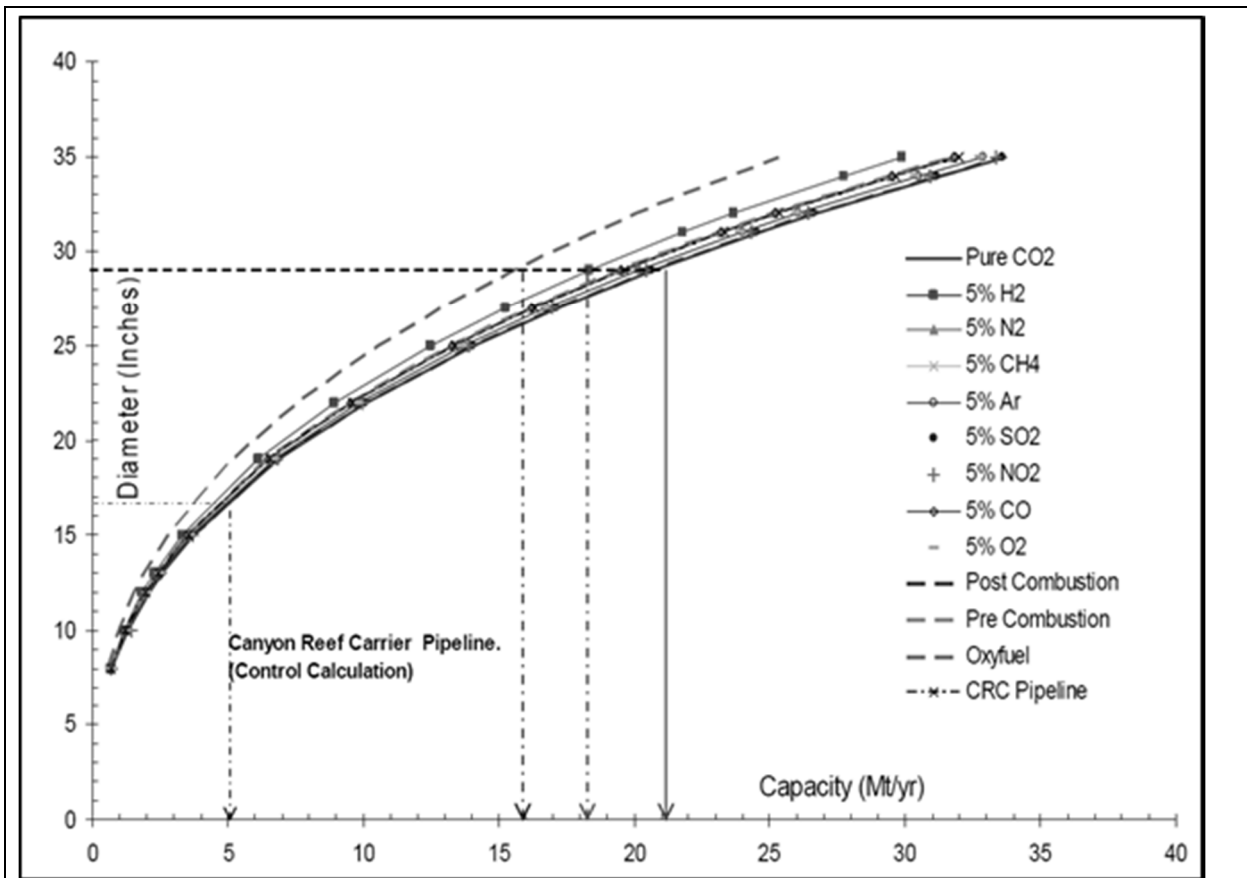


Figure 10. Comparison of Pipeline Capacity (operating at a pressure drop of 20 kPa/km) for Different Combination of Impurities and Capture Technologies¹¹.

3.2.Phase 2 Research Needs

Although the analysis performed during Phase 1 was based on fundamental flow capacity determination, validation of the results was still needed via numerical analysis and actual tests in a small loop of the same mixture compositions analyzed. The Phase 2 investigation was aimed at obtaining experimental data from actual flow loop testing conducted at TransCanada’s Gas Dynamic Test Facility in Didsbury, Alberta. The flow loop is 178 m long, NPS 2 in size and rated up to 22 MPa operating pressure. To minimize cost, this existing facility (which included mixing and filling capabilities for the required mixtures of CO₂ and impurities) was modified by the addition of a special CO₂ pump and necessary additional instrumentation.

The following sections provide a description of this flow loop and details of the test setup, instrumentations and data acquisition system, results from testing six different CO₂ mixtures with

impurities typical of different CO₂ capture technologies and sources, as well as numerical results of simulated test conditions of the flow loop geometry. The simulated analysis was based on the most applicable and accurate equation of state (EOS) suitable for CO₂+impurities, namely GERG-2008 EOS.¹²

3.3. Experimental Setup of the Flow Loop at Didsbury, Alberta

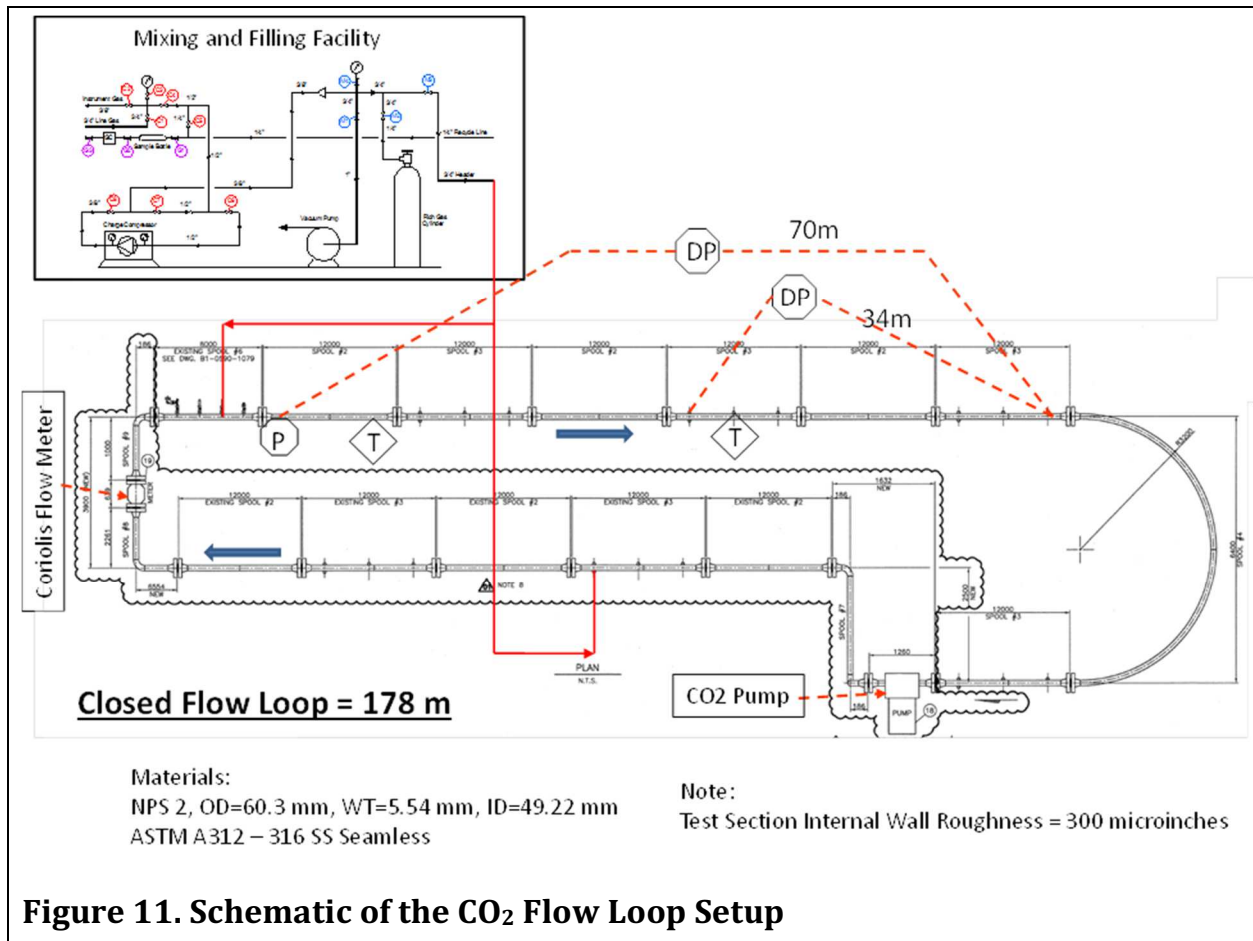
3.3.1. Close Loop Piping System

Figure 11 shows a schematic of the existing flow loop at the TransCanada Gas Dynamic Test Facility (GDTF) in Didsbury, Alberta, Canada. It consists of spool pieces of NPS 2 stainless steel pipe making up a total length of 178 meters. All these spool pieces existed at the Test Facility prior to the project with the exception of additional three spools specially made to accommodate the introduction of a new and specialized CO₂ pump. All spool pieces are made of NPS 2 x WT 5.54 mm, ASTM A312 – 316 SS seamless tube (O.D. = 60.3 mm, I.D. = 49.22 mm), designed for 22 MPag. ANSI 1500 RTJ flanges (material specification ASTM A182 - 316 SS) connect the pipe spools together. One pipe spool is equipped with an automated ESD valve for station emergencies, and a certified pressure relief valve for operating pressure safety. The automated ESD valve also functions as a manual blowdown valve to prepare the pipe loop for injection of a new gas mixture. A static pressure transmitter measures the pressure at this location. Differential pressure transmitters and temperature transmitters measure the pressure drop and fluid temperature along the length of the loop. The flow loop features a straight test section, 70m in length, which is used to accurately measure pressure drop.

The internal wall surface roughness parameters of the test section spool pieces were measured using a Mitutoyo Model #SJ-210 surface texture profiler, according to DIN (4777) and ISO (4287;1997). The internal pipe surface measurement followed a procedure detailed by Botros et al¹³. All spool pieces showed similar values of the roughness parameter. The average surface roughness (Rz), was found to be ~ 12 μm. The Nikuradse equivalent sand grain roughness parameter (ks) in use for the determination of the friction factor correlates to Rz via a factor of 1.244, hence the absolute roughness parameter for the test section is established at ~ 15 μm.

3.3.2. Auxiliary System

To fill the flow loop, with the 12 MPa CO₂ gas mixture, an auxiliary system inside a heated building is employed. The auxiliary system includes a vacuum pump, a charge compressor, as well as gas cylinders of CO₂ and gas cylinders of pure gases used as impurities required for mixing. The vacuum pump is an Edwards Model # E2M30, which consists of a direct drive, rotary vane, double stage vacuum pump. The charge compressor is a Haskel Gas booster model AGT-30/75 which consists of a large area reciprocating air driven piston directly coupled by a connecting rod to a small area gas piston. The compressor is capable of a discharge pressure up to 110 MPa (pressure ratio of 60:1. All of the components in this auxiliary system existed and were in operation at TCPL test facility prior to the commencement of the present project.



3.3.3. Special CO₂ Pump

A special three-plunger pump driven by a 25 HP electric motor via a pulley-belt system controls the fluid flow through the loop. To protect against high suction pressure, there are three unique cross over tubes connecting the pump discharge to the backside of each plunger to balance the forces on the plunger primary piston. The pump is capable of maximum flow of 600 L/min at pump speed = 182 rpm. A Toshiba AS1 25 HP Variable Frequency Drive (VFD) controls the electric motor speed. The VFD is used to control the speed of the pump from 182 rpm max to a desired speed for lower flow rates below 600 L/min. There is a pulsation dampener (2.5 gallons) mounted on the discharge side of the pump.

3.3.4. Measurement Instrumentation

Two Rosemount differential pressure (DP) transmitters (3051S3CD), mounted on the flow test section, measure the pressure drop along 70m and 34m segments of the test section as shown in Figure 11. The 3051S3 ultra, with pressure range 3 (250 kPa), has uncertainty specification of $\pm 0.025\%$ of span, which translates to ± 25 Pa of reading for span of 100 kPa.

The static pressure transducer is a Yokogawa model EJA440 with uncertainty specification of $\pm 0.12\%$ of span, which translates to ± 20 kPa for 17 MPa span. The temperature transmitters equipped with TC probes are Yokogawa Model YTA110A, capable of $\pm 0.5^\circ\text{C}$ of measurement uncertainty. All pressure and temperature transducers were available at TCPL test facility prior to the commencement of this project.

The flow meter is a Micro-Motion Model CMF200H Coriolis mass flow meter, equipped with ANSI 1500# RTJ Flanges. Flow accuracy is $\pm 0.1\%$ of mass flow rate for CO_2 at 15 MPa because it is behaving more like a liquid than a gas. This flow meter is also capable of measuring the fluid density to ± 0.5 kg/m^3 uncertainty.

The data acquisition system is a HP VXI E1413B high speed scanning A/D. Data is collected in a block of 100 data points; hence, for a window of 64 seconds, the data resolution is exactly 0.64 second. The data is averaged over a number of measurement blocks to match the desired total test time for the flow test.

3.3.5. Costs

Auxiliary facilities and data acquisition system that the majority of the components and in particular the straight spool pieces of the test loop pre-dated the Project. Purchased specifically for the Project were: the special CO_2 pump, two Rosemount differential pressure transmitters and a new flow meter. This rendered the actual cost of modifying the test loop to suit the current test program relatively low. The actual cost by major cost element and task are shown in Table 7

3.4. Test Procedure

The test program (Section 3.6) lists the required gas component mixtures. Gas is injected into the flow loop from supply cylinders, starting with the heavier gases, and then topped off with CO_2 . A simple mass balance calculation is performed to determine the amount and composition of the supplementary gas required, based on the main loop gas composition, the desired final composition, the volume of the test section together with the connecting system, and the final pressure. The test procedure involves nine main steps starting from evacuating the main flow loop, associated header and tubing, up to the final steady flow of the CO_2 +impurities around the loop.

These are:

1. Purging with N_2 gas;
2. Evacuation;
3. Impurity gas charges from heaviest to lightest;
4. Topping off with pure CO_2 , and charging with the Haskel compressor up to the desired loop pressure (e.g. 15 MPag);
5. Operate the CO_2 pump to cycle the flow around the loop to ensure good mixing;

6. After sufficient mixing time, confirmed by stable density and temperature, measurements of static pressure and temperatures, two differential pressures, mass flow rate and fluid density are acquired;
7. The flow rate is then changed to the next desired value using the VFD drive on the pump and the measurements are repeated;
8. After all the flow tests for the current mixture are complete, two gas samples are taken from the loop for mixture analysis in the lab using standard gas chromatography analysis to accurately determine the final gas component mixture; and
9. The flow loop is then prepared for the next gas mixture to test.

| Table 7. GDTF Flow Loop Modification and Testing Costs | |
|--|------------------|
| Description | CAS |
| CO ₂ and impurities gases (from Praxair) | \$16,000 |
| Coriolis flow meter (2,200 psig) | \$28,000 |
| Design and fabrication of additional spool pieces to connect to the existing 172 m NPS 2 loop, and construction activities | \$36,000 |
| Instrumentation (DP transmitters), DAS and calibration | \$18,000 |
| Special CO ₂ pump (100 GPM and 2,200 psig rating) | \$65,750 |
| Conduct a total of 6 mixture composition flow tests at various flow rates (The actual number of tests was 8.) | \$63,000 |
| Final report | \$8,000 |
| Total | \$234,750 |

3.5. Uncertainty Analysis

As mentioned above, the objective of present testing program is to quantify the effects of various impurities on the flow capacity of a pipeline system. Stated differently, the aim is to quantify the effect on the effects of various CO₂+impurty mixtures on the flow throughput (mass flow rate) for a given pressure drop along a given pipe length, diameter, static pressure and temperature. The mass flow rate (\dot{m}) is related to these parameters via:

$$\dot{m}^2 \propto \frac{\rho \Delta P D_i^5}{f L} \quad (1)$$

Where:

- \dot{m} - mass flow rate
- ρ - fluid density flow rate
- ΔP - pressure drop along the pipe section
- D_i - internal diameter of the pipe
- f - Darcy friction factor
- L - section length

The uncertainty in the determination of the mass flow rate can thus be estimated based on the uncertainty of all of the dependent parameters in Eq. 1. This can be expressed as:

$$2 \frac{\delta \dot{m}}{\dot{m}} = \sqrt{\left(\frac{\delta \rho}{\rho}\right)^2 + \left(\frac{\delta \Delta P}{\Delta P}\right)^2 + \left(5 \frac{\delta D_i}{D_i}\right)^2 + \left(\frac{\delta L}{L}\right)^2 + \left(\frac{\delta f}{f}\right)^2} \quad (2)$$

Table 8 gives estimated values for the above individual uncertainties. It is shown that the uncertainty in the mass flow rate determined from the present test setup and instrumentation is estimated at +1%, and the main contributor to it is the uncertainty in the internal diameter of the loop. This is expected due to the relatively small diameter of the test loop being NPS 2.

3.6. Test Program

The flow loop test program involves a total of 6 different CO₂+impurities mixture compositions which were selected by the ACPD project team to represent different CO₂ capture technologies. These six compositions are given in Table 9 (same as in Table 2). The reference test (PTAC-Test-Ref) is almost pure CO₂ with a small amount of N₂ (0.2% by mole), which represents the post-combustion capture technology. Two compositions are identified as ‘low purity’ mixtures which primarily come from oxycombustion type technologies with typical impurities involving N₂, O₂ and Ar. These are labeled PTAC-Test-1 and PTAC-Test-2 in Table 9. One mid-purity mixture composition is identified as a typical mixture from IGCC (post-combustion technology), which would contain a relatively high content of H₂ in addition to CO and CH₄. This mixture is labeled PTAC-Test-3. The last two mixtures are characterized as ‘high purity’ mixtures with CO₂ being above 97% by mole. These are labeled PTAC-Test-4 and PTAC-Test-5 in Table 9.

Table 8. Uncertainty Analysis in Determining the Mass Flow Rate from the Flow Loop

| Parameter | Value | Units |
|---|--------------|----------------------|
| <i>Mixture Density (ρ)</i> | 980 | (kg/m ³) |
| <i>Pressure Drop (ΔP)</i> | 100 | (kPa) |
| <i>Length (L)</i> | 70 | (m) |
| <i>Internal Diameter (D_i)</i> | 49.22 | (mm) |
| <i>Friction Factor</i> | 0.015 | |
| <i>Uncertainty in Mixture Density ($d\rho/\rho$)</i> | 0.2 | (%) |
| <i>Uncertainty in Pressure Drop ($d\Delta P/DP$)</i> | 0.25 | (%) |
| <i>Uncertainty in Length (dL/L)</i> | 0.015 | (%) |
| <i>Uncertainty in Internal Diameter (dD_i/D_i)</i> | 0.4 | (%) |
| <i>Uncertainty in Friction factor (df/f)</i> | 0.2 | (%) |
| Uncertainty in Mass Flow Rate | 1.018 | (%) |

In each test, the flow loop is pressurized to approximately 15 MPa, and then flow circulates for enough time to reach equilibrium in terms of temperature and mixing of the impurities with CO₂. Measurements are taken of static pressure, static temperature, differential pressures along the 34m and 70m sections, as well as flow rates and density from the Coriolis flow meters. The flow rate is then changed to the next desired flow by changing the pump speed using the VFD on the driver motor. After data for all flow rates are collected, at this point, two samples are withdrawn for lab analysis to establish the exact mixture composition. Section 3.8 summarizes the results obtained from all of the tests conducted.

3.7. Numerical Simulation of the Test Loop Configuration

Steady flow simulations of the six CO₂+impurities mixtures of Table 9 were conducted using mixture properties (primarily density and viscosity) based on GERG-2008 EOS¹². In these simulations, the length of the test section was taken as the 70 m long section shown in Figure 11, I.D. = 49.22 mm and internal wall absolute surface roughness = 15 μ m. For each mixture composition, six mass flow rates were considered; namely 1 kg/s to 6 kg/s at a step of 1 kg/s. Inlet static pressure at the test section is assumed to be 15 MPa-a and temperature = 10°C.

Table 9. Target Compositions of the Six CO₂+Impurities Mixtures

| | Category | | | | | |
|-----------------|---------------|---------------------|-------------|-------------|-------------|-------------------------|
| | "Pure" Case | Low Purity | | Mid Purity | High Purity | |
| Fuel | Heavy | Heavy | Gas | Heavy | Gas | Gas |
| Process | Post Comb. | Oxy (Partial Shift) | Oxy | IGCC | Sour | Steam Methane Reforming |
| | (mol%) | (mol%) | (mol%) | (mol%) | (mol%) | |
| CO ₂ | 99.8 | 91.8 | 96.2 | 95.0 | 97.4 | 99.4 |
| N ₂ | 0.2 | 2.0 | 1.9 | - | 0.2 | 0.3 |
| O ₂ | - | 2.3 | 1.9 | - | - | - |
| Ar | - | 3.9 | - | - | - | - |
| CO | - | - | - | 0.5 | - | - |
| H ₂ | - | - | - | 4.0 | - | 0.3 |
| CH ₄ | - | - | - | 0.5 | 2.4 | - |
| Total | 100.0 | 100.0 | 100.0 | 100.0 | 100.0 | 100.0 |
| Mixture ID | PTAC-Test-Ref | PTAC-Test-1 | PTAC-Test-2 | PTAC-Test-3 | PTAC-Test-4 | PTAC-Test-5 |

Flow is assumed isothermal. Under this assumption, the pressure drop along the 70 m long test section can be expressed as:

$$\Delta P = \int_0^L \frac{f}{D_i} (0.5 \rho u^2) dx \quad (3)$$

Where:

u - local mean flow velocity

ρ - fluid density flow rate

ΔP - pressure drop along the pipe section

D_i - internal diameter of the pipe

f - Darcy friction factor

L - total section length

Note that f , ρ , u and P are all function of the location x , and are determined based on mass flow rate and the local pressure calculated at every increment (dx). Colebrook implicit expression for the Darcy friction factor¹⁴ is used in this calculation, which is a function of Reynolds number (Re) and the relative roughness (k_s/D_i) as follows:

$$f^{-1/2} = -2 \log \left(\frac{k_s/D_i}{3.7} + \frac{2.51}{Re f^{1/2}} \right) \quad (4)$$

Figure 12 shows a compilation of the results in terms of the pressure drop along the 70 m long test section vs. flow rate for each of the mixture compositions. Figure 13 shows detailed results (zoom-in) for the range of flow rates between 5 and 6 kg/s. It is shown that the PTAC-Test-3 mixture (which has a high H₂ content) exhibits the highest pressure-drop among all other mixtures. Stated differently, the PTAC-Test-3 mixture composition will result in the least flow capacity for a given pressure drop along a given section of the pipeline. This is demonstrated in Figure 14, where the flow rates for a given pressure drop of 110 kPa along the 70 m long test section are compared among the six CO₂+impurities mixtures. As can be seen, PTAC-Test-3 shows the minimum flow rate, followed by PTAC-Test-1 mixture. These reductions in mass flow rates are related to the relative mixture densities as shown in Figure 15. Figure 16 shows the relative flow rate reduction of five PTAC mixture compositions relative to the reference mixture (PTAC-Test-Ref). It is shown that PTAC-Test-3 mixture composition results in approx. 4.7% reduction in mass flow for the same pressure drop. This is primarily to the relatively high content of H₂ in this mixture, which results in lower density and hence lower flow (cf. Eq. 1 and Figure 15).

PTAC-Test-1 mixture composition results also in a reduction in the flow rate by 3.5% compared to the reference or pure CO₂ (see Figure 16). This mixture is the least pure among all mixtures with only 91.8% CO₂, which also resulted in relatively lower density than pure CO₂ (or PTAC-Test-Ref composition), as shown in Figure 15. Although molecular weight of the mixture has a direct impact on the mixture density, however, it is important to note that PTAC-Test-2 and PTAC-Test-4 have very similar molecular weights, 43.255 and 43.307, respectively, i.e. a ratio of almost 1.0, yet these two mixtures have different densities as shown in Figure 15. Here, PTAC-Test-1 has a density of 883.49 kg/m³ vs. PTAC-Test-4 which has a density of 920.99 kg/m³, i.e. a ratio of 1.042 (that is 4.2% higher). This is because of the variance in the compressibility factor due to the difference in the components (impurities) in the mixture, even though the molecular weights are the same. It is therefore the density (rather than strictly the molecular weight) that influence the flow capacity of a given a pipeline containing specific CO₂+impurities.

Another observation is the effects of the mixture composition on viscosity, which is reflected on the friction factor via the Reynolds number. These data indicate that the viscosity varies between 85-106 μPa.s, yet the friction factors is almost the same, averaging around 0.0155 (at the high flow rate of 6 kg/s). Therefore, one can conclude that the viscosity of the CO₂+impurities has little effects on the flowability of the mixtures in a pipeline.

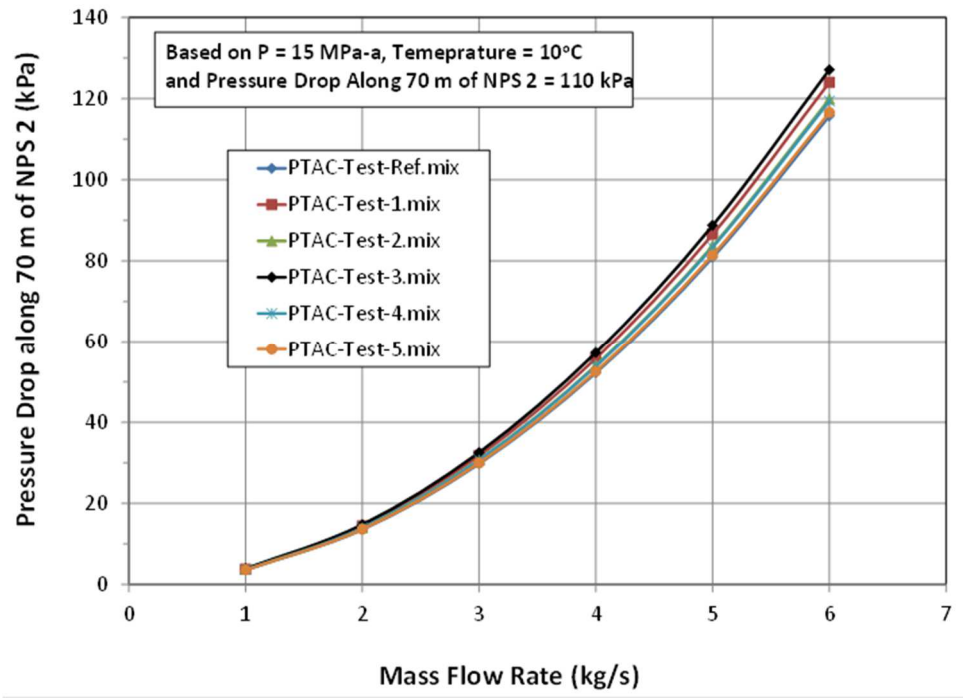


Figure 12. Steady Flow Simulation Results of Isothermal Flow through the Test Section of the NPS 2 Test Loop

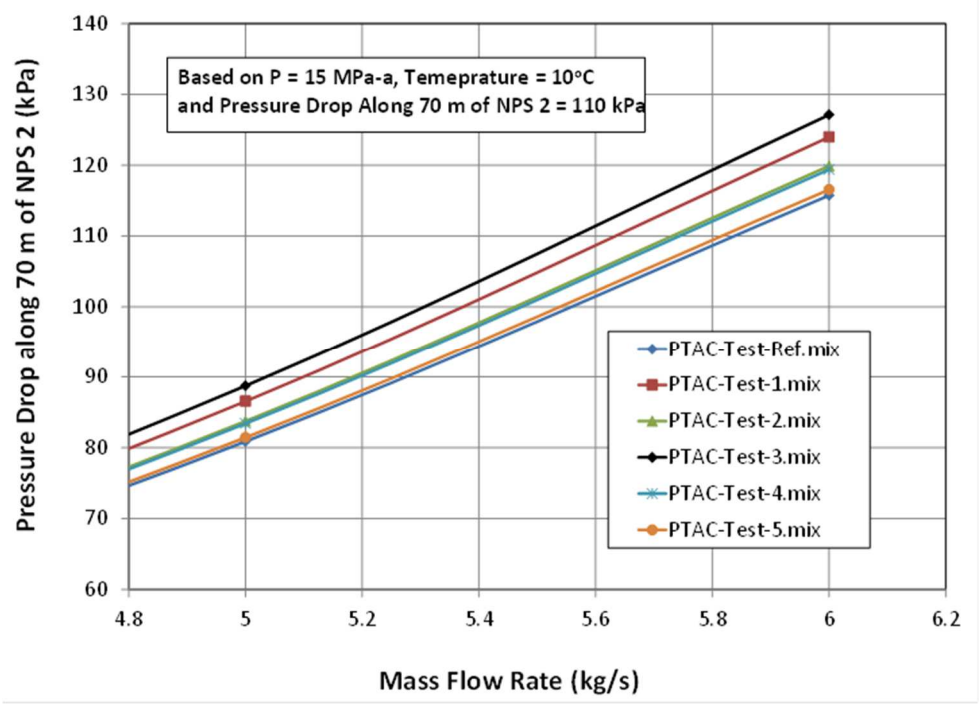


Figure 13. Steady Flow Simulation Results of Isothermal Flow through the Test Section of the NPS 2 Test Loop (details for flow rates between 5 and 6 kg/s)

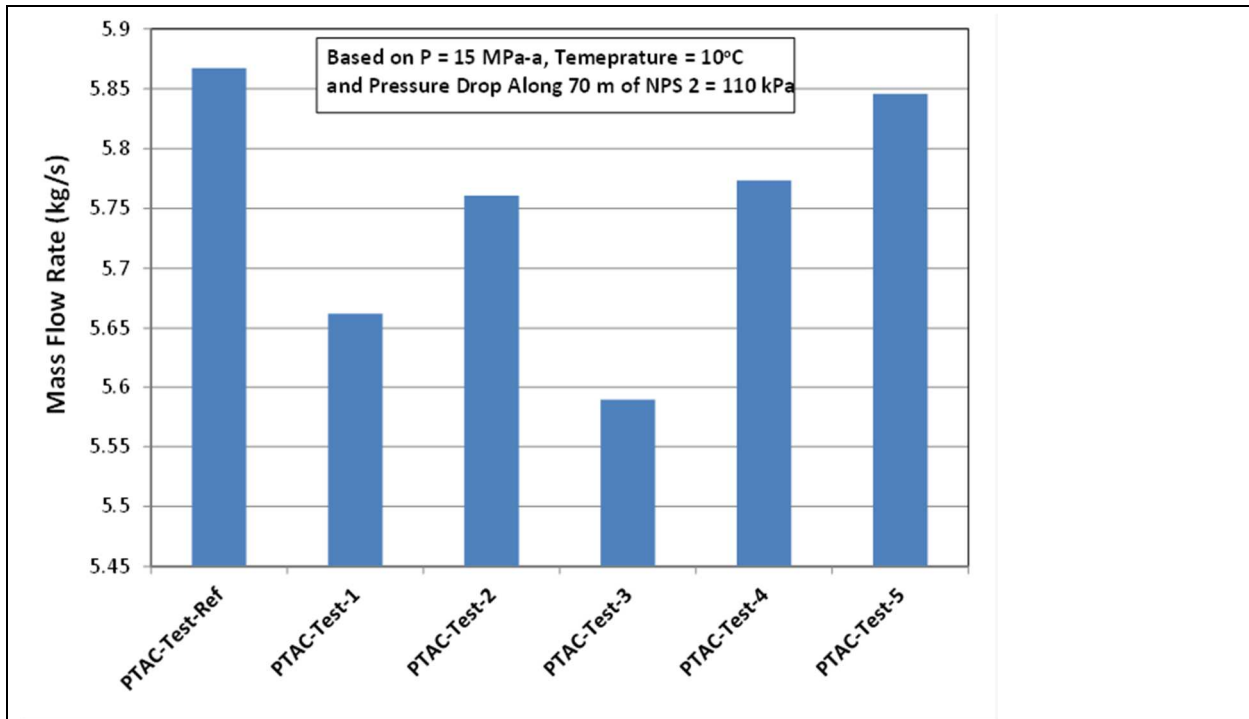


Figure 14. Simulation Results of Flow Rates for a Given Pressure Drop of 110 kPa along the 70 m long Test Section of the NPS 2 Test Loop

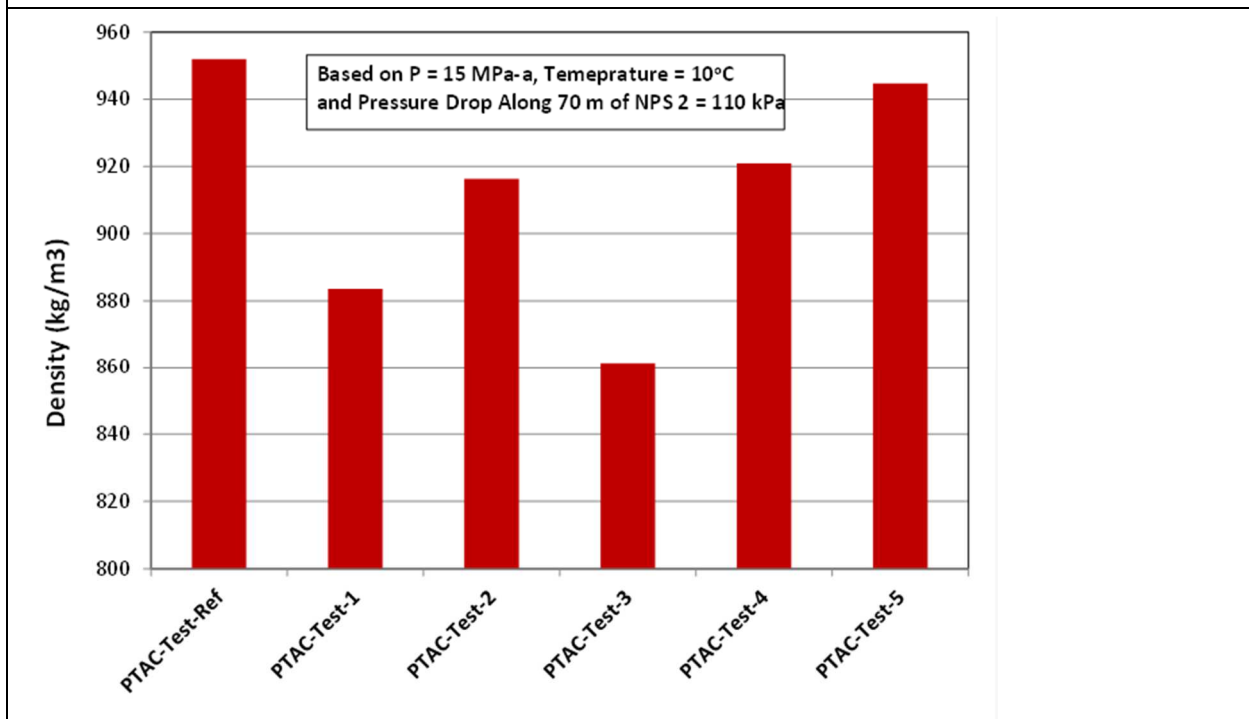


Figure 15. Mixture Density at the Inlet of the 70 m Long Test Section of the NPS 2 Test Loop

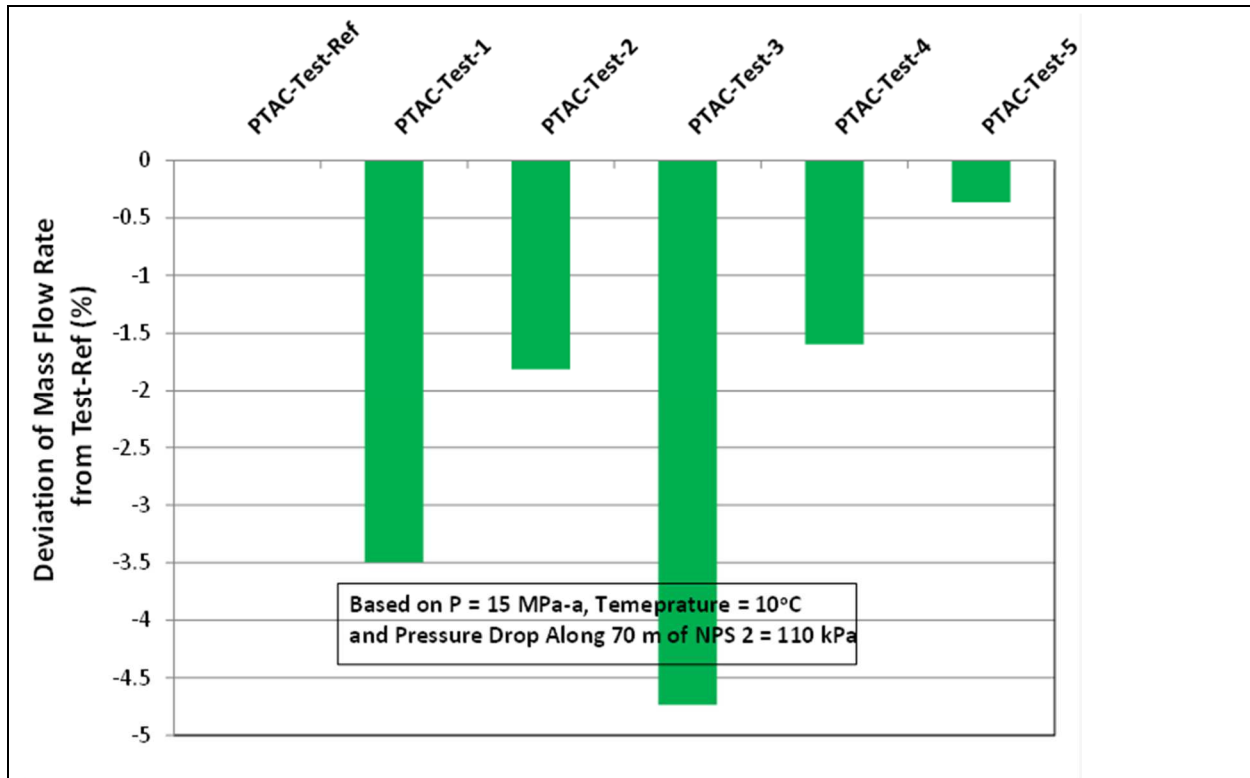


Figure 16. Simulation Results of Decrease of Flow Rates (in %) Compared to PTAC-Test-Ref Mixture Composition for a Given Pressure Drop of 110 kPa along the 70 m long Test Section of the NPS 2 Test Loop

3.8. Test results

3.8.1. Flow Test Compositions

Flow tests were conducted for the six cases described in Table 9, using compositions that were as close as could be practically attained. As discussed earlier, the amount by mass of each component is pre-calculated based on the holding volume capacity of the flow loop (which is approx. 0.335 m³), pressure of 15 MPa-a and temperature of 10°C. This calculation is based on the GERG-2008 EOS. After injecting the required mass of each component in the flow loop, the mixture is circulated through the loop for at least 40-50 minutes. This amounts to approximately 40-50 complete cycles of the mixture around the loop (based on 178 m long loop and circulation velocity of approximately 3 m/s). The flow test starts by slowly varying the CO₂ pump speed in small increments so as to allow data acquisition of the measured parameters, namely flow rate, Ps, T1, T2, DP1 and DP2. Data were collected every 0.64 seconds. In some instances, the pump had to be stopped to allow the gas to cool; otherwise the pressure could reach the maximum operating pressure of the loop (22 MPag).

After data for all flow rates are collected, two small gas samples are drawn in two separate sample bottles and sent to the analytical lab for gas analysis using a standard gas chromatograph. Table 10 gives the gas analysis results received from the analytical lab averaged over the two samples (one from each sample bottle). It should be emphasized that the exact desired mixture composition cannot be achieved to the first decimal point due to the uncertainty in the pre-estimated mass of each component injected. However, the resulting actual mixture compositions shown in Table 10 are representative, to some degree, of the desired mixture compositions shown in Table 9. The reference test was repeated since this is the first time this type of pump was used in CO₂ application. The test loop was therefore depressurized to allow disconnection of the pump and inspect its internals. The DP's gaugelines were also inspected for any potential pluggage as well as all other charging and mixing small diameter tubes around the Haskel charge compressor. The test loop was then charged with the reference test mixture to check repeatability of the test procedure and measurement data. Test-3 was also repeated as the first test (Test-3A) was found to have H₂ concentration lower than the desired value. The repeated test (Test-3B) turned out to have overcharged H₂ concentration. Nevertheless, the two Test-3A and Test-3B spans the desired ACPD desired H₂ concentration.

Table 10. GC Analysis of Gas Samples Drawn from the Flow after Two Hours of Mixing

| Component | RefA | RefB | Test 1 | Test 2 | Test 3A | Test 3B | Test 4 | Test 5 |
|-------------------------|----------|----------|----------|----------|----------|----------|----------|----------|
| CO ₂ | 99.8950 | 99.8760 | 89.4430 | 96.0920 | 96.2830 | 90.4010 | 97.7795 | 99.5035 |
| N ₂ | 0.0845 | 0.1210 | 2.1000 | 1.9350 | 0.1865 | - | 0.1320 | 0.1955 |
| O ₂ | 0.0010 | 0.0030 | 2.5350 | 1.9600 | 0.0035 | - | 0.0025 | 0.0015 |
| Ar | - | - | 5.9200 | 0.0130 | - | - | - | - |
| CO | - | - | - | - | 0.2110 | 0.4165 | - | - |
| H ₂ | - | - | - | - | 2.9550 | 8.6250 | 0.0010 | 0.2975 |
| CH ₄ | 0.0195 | - | 0.0020 | - | 0.3610 | 0.5575 | 2.0850 | 0.0020 |
| Total | 100.0000 | 100.0000 | 100.0000 | 100.0000 | 100.0000 | 100.0000 | 100.0000 | 100.0000 |
| M.W. | 43.990 | 43.990 | 43.128 | 43.464 | 42.604 | 40.165 | 43.405 | 43.853 |
| M.W. (Diff % from RefA) | 0.000 | -0.001 | -1.960 | -1.196 | -3.152 | -8.696 | -1.331 | -0.314 |

3.8.2. Loop Calibration

Figure 17 shows a sample test result (for Test RefA mixture) of the flow rate measured by the Coriolis flow meter and the corresponding pressure gradient (dP/dx) along the test section, averaged over the measurements by the two differential pressure transducers DP1 and DP2. The measured flow rates and the corresponding measured static pressure (Ps) and static temperature (averaged over T1 and T2), shown in Figure 18, are also used to predict the theoretical dP/dx at the same conditions. In this calculation, the internal absolute wall surface roughness was taken as

15 μm which was the average roughness measured at each end of each spool of the 70 m test section before construction and assembly of the entire loop.

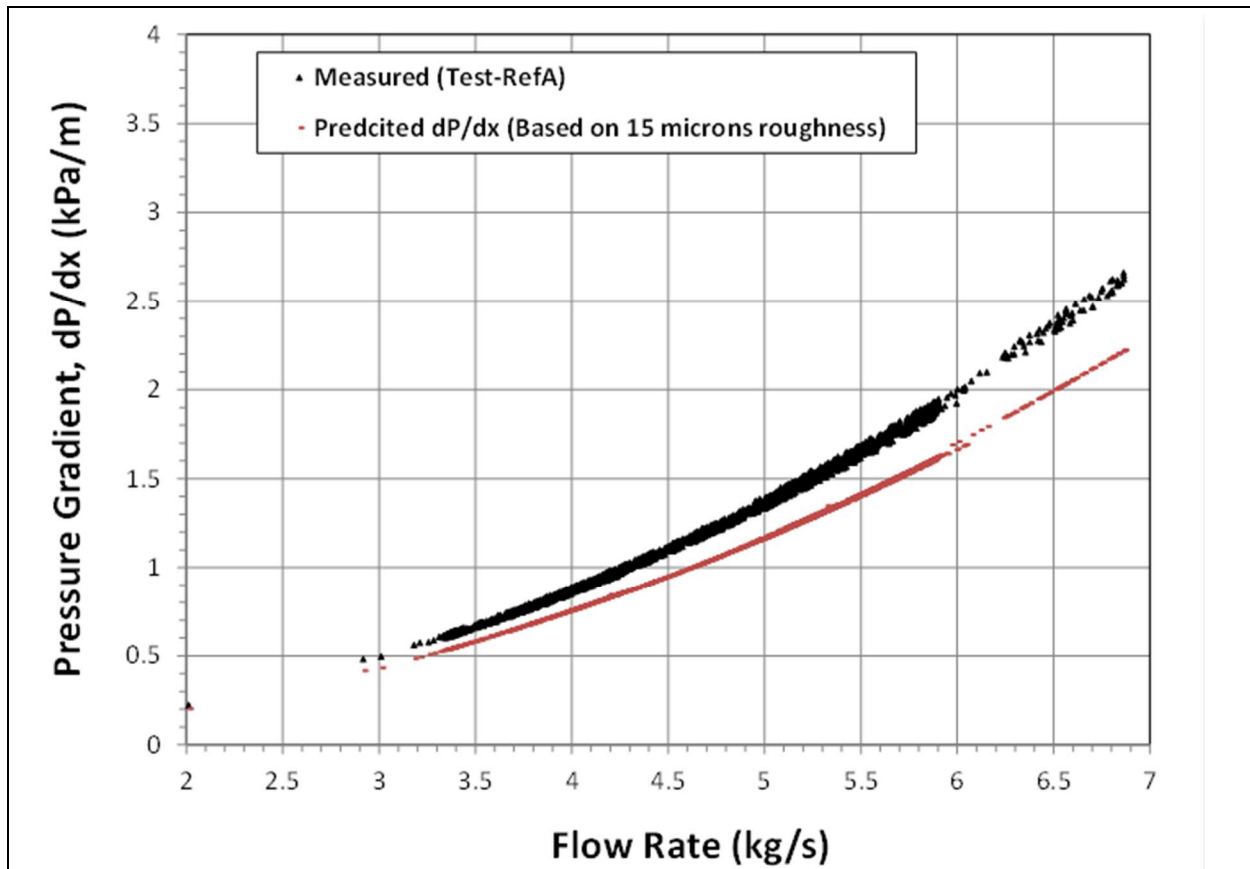


Figure 17. Example Test Results from RefA Mixture the Mass Flow Rate (Measured by the Coriolis Flow Meter), and the Average Pressure Gradient Measured by the two Differential Pressure Transducers DP1 and DP2

The results of the numerical calculation based on the measured flow rate, pressure and temperature are also plotted in Figure 17. It is shown that the measured dP/dx is higher than the predicted dP/dx based on tube internal wall surface roughness of 15 μm . Figure 19 shows the difference between the measured vs. the predicted pressure gradients for the same flow rate, pressure and temperature over a record period of 80 seconds. It is shown that the measured dP/dx is approximately 15-20% (average of 17.2%) higher than the predicted values. This can be attributed to two factors:

- The tube roughness farther inside each spool piece is likely higher than that at both ends. Before roughness measurements were taken with the Mitutoyo stylus at both ends of each spool, the tube wall surfaces were thoroughly cleaned from any sticking debris, grease or fine dusts. Farther inside each spool, the wall surface condition could be rougher as it was difficult to reach far enough into the NPS 2 spools to ensure cleanliness.

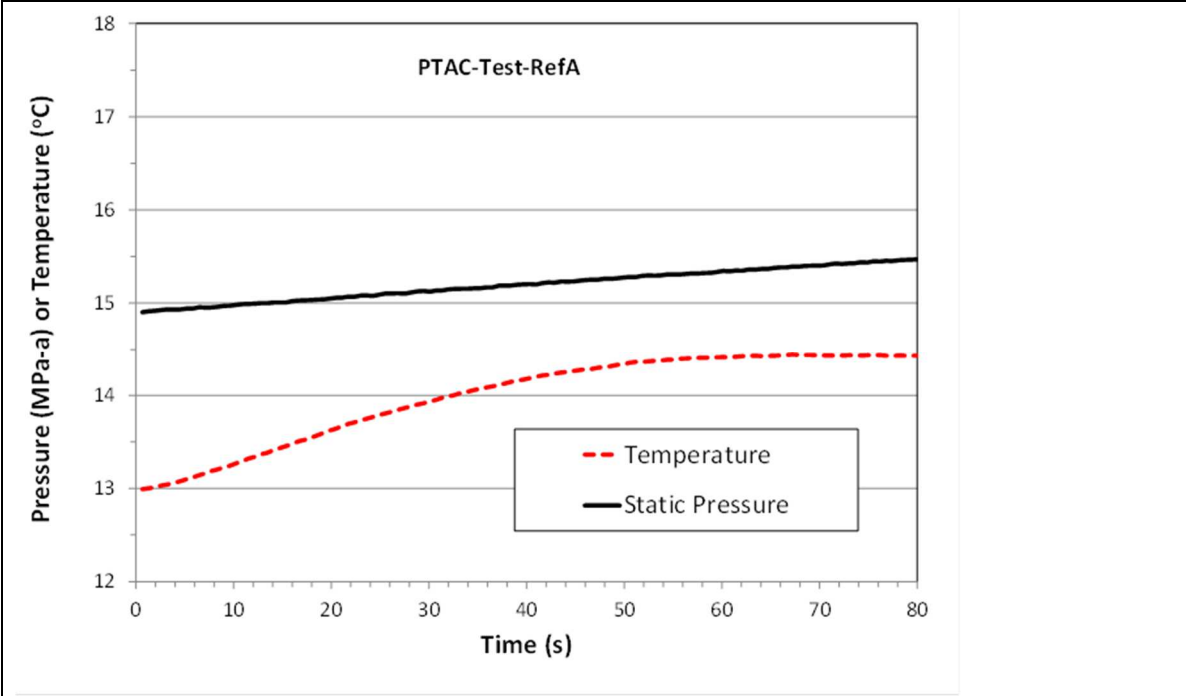


Figure 18. Measured Static Pressure and Average Temperature (between T1 and T2) Along the Test Section over the 80 Seconds Record of Figure 17

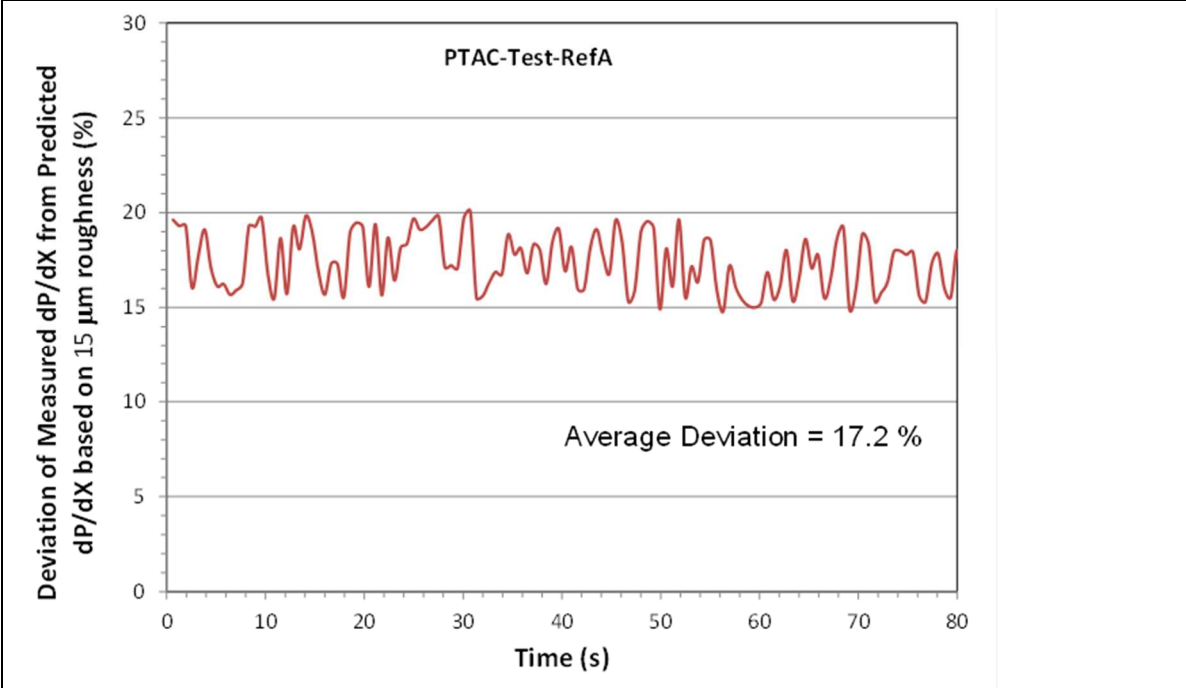


Figure 19. Deviation of the Measured Pressure Gradient from the Numerical Calculation Based on Tube Internal Wall Surface Roughness of 15 μm

- The ring gaskets used between flanges typically have a larger I.D. than the I.D. of the tube. This gives rise to a small narrow gap (approx. 3 mm) which the axial flow encounters at each flange location.

Therefore, it is not surprising that the 70 m encounters ~17.2% higher pressure drop than that calculated based on measured internal wall roughness of 15 μm at spool ends. This is reasonable given the aforementioned two factors. Another way to look at these results is that the friction factor based on the measured internal wall roughness of 15 μm at spool ends, which is approx. 0.0155 for the range of Reynolds numbers considered, ought to be increased to an effective friction factor of approx. 0.018 (i.e. 17% higher). Whatever effective friction factor or flow resistance coefficient that characterizes the test section is, the various CO₂+impurity mixtures will be flowing through the same test section and subjected to the same flow resistance, whether it be the one corresponding to an internal wall surface roughness of 15 μm or higher, the main purpose is to determine and quantify directionally the effects of impurities on the flow capacity (or dP/dx for a given flow). In the end, it is the comparative assessment of the effects of the different component of impurities and their respective mole fractions on the flow capacity, regardless of the section resistance since they all flow through the same test section.

3.8.3. Reference Tests

The mixtures RefA and RefB were the purest CO₂ compositions tested and are representative of CO₂ from an amine capture process. They were evaluated first to provide a reference for the flow loop. GC analysis of Test RefA mixture is given in Table 10. There appears a small trace of methane (CH₄) remained trapped in the test loop which amounts to 0.0195% (mole). This came about from the purging and cleaning procedure of the flow loop with pipeline natural gas during commissioning, followed by CO₂ purging. However, it is considered to be too small an amount to be of any concern. As mentioned earlier, the temperature was averaged between T1 and T2 measurements, and the pressure gradient was averaged between DP1 and DP2 over their respective section lengths. The results are presented in Figure 20 in terms of the average pressure gradient dP/dx vs. flow rates. The measured dP/dx vs. flow is fitted to a power trend line in the form $dP/dx = C_1 (\dot{m})^{C_2}$ imbedded in Figure 20. Here the coefficient $C_2 = 2.0084$ is consistent with the fluid dynamics principle of flows in pipe being the pressure drop is proportional to the square of the mass flow rate. The measured pressure gradient (dP/dx) is also compared to the predicted dP/dx based on the internal wall surface roughness of 15 μm . Note that the measured dP/dx is approx. 17% higher than the predicted dP/dx due to the other contributions to the flow resistance mentioned earlier.

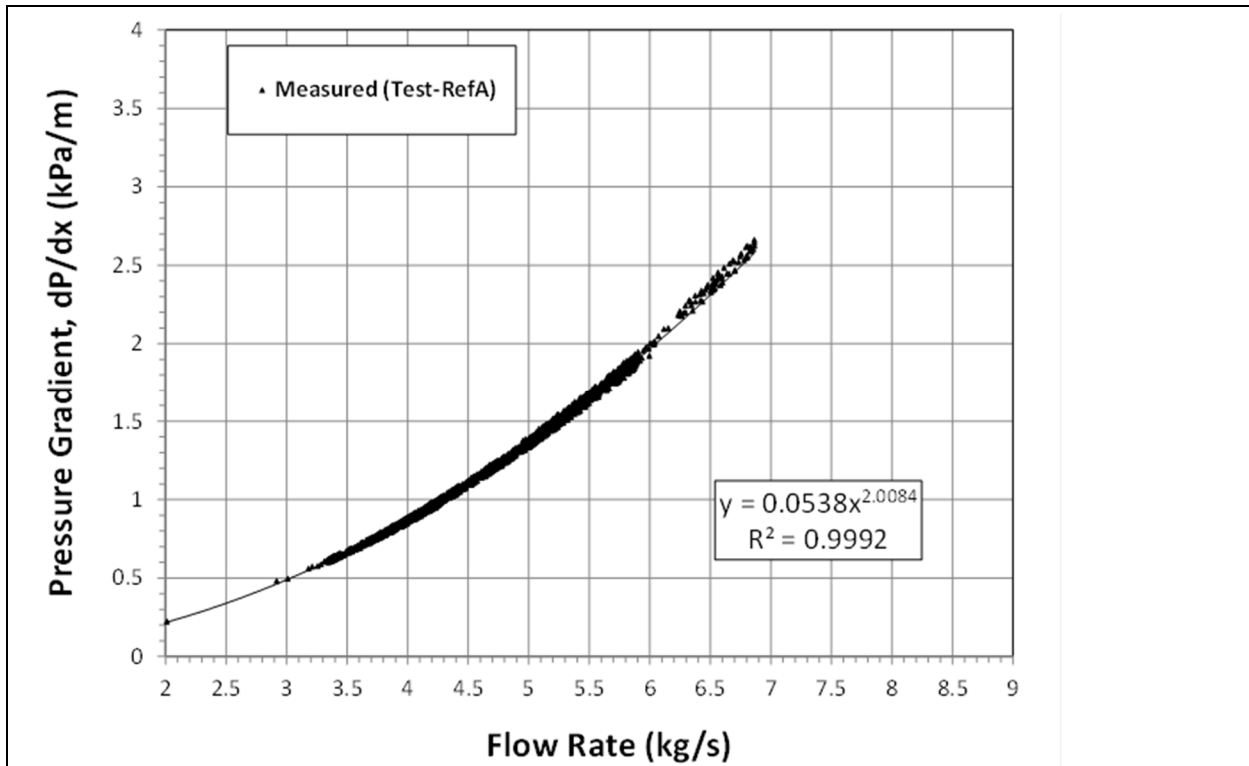


Figure 20. Test RefA Measured Pressure Gradient vs. Flow Rate

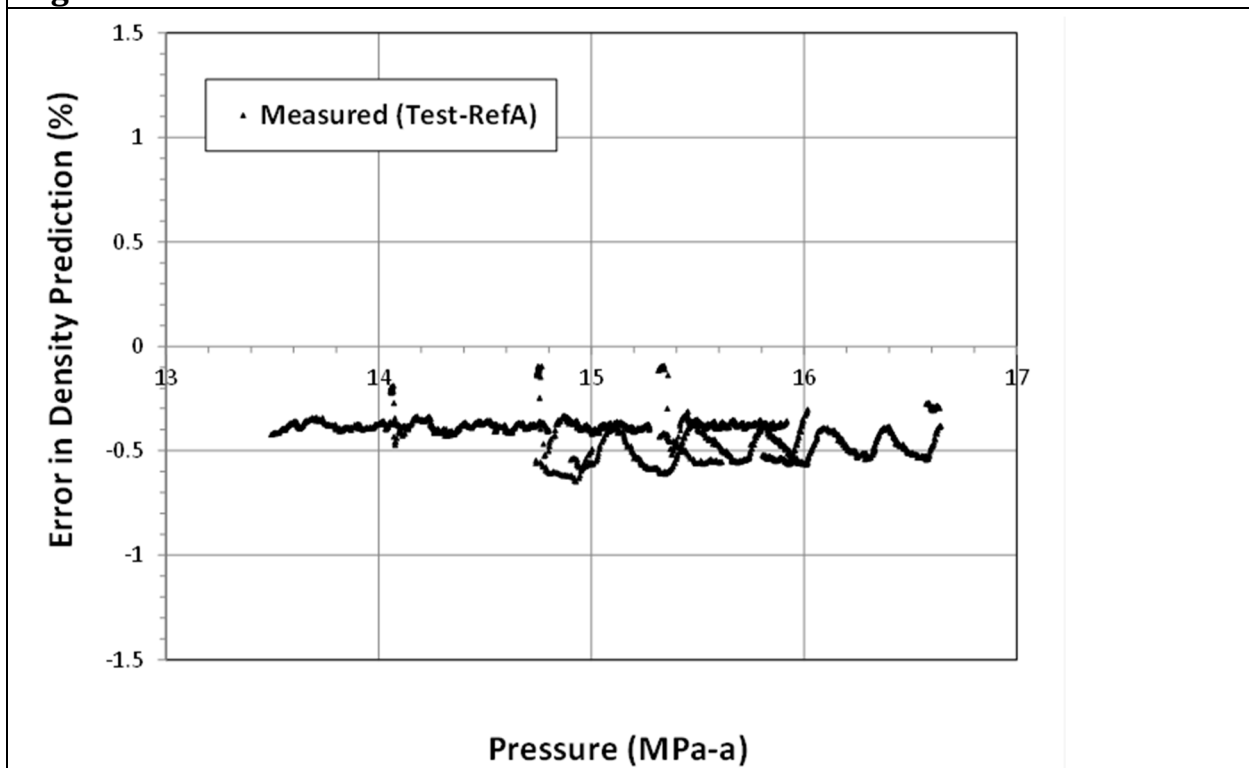


Figure 21. Error in Density Prediction based on GERG-2008 EOS of Test RefA

A by-product from the flow loop test is the density measurements by the Coriolis flow meter. Density predictions using GERG-2008 EOS were also carried out at the corresponding measured pressure and temperature at each measured data point. Figure 21 shows the resulting deviation of the density predictions as compared to measurements. It is shown that GERG-2008 EOS under-predicts density by approx. -0.4% for this mixture composition, which is close to being pure CO₂, and at the pressure and temperature range for this test.

As mentioned earlier, the reference test was to inspect the CO₂ pump internals for cleanliness, integrity and free of water, contaminants or debris. It was important to ensure that the pump is clean and clear at this stage before proceeding with all other tests. The test procedure was then repeated and the average mixture composition from the two samples drawn was obtained from the GC analysis is shown in Table 10 (Test RefB). Note that there is no trace of CH₄ in this test indicating that the purge process was successful. Again, the CO₂ pump speed was varied in slow increments so as to allow data acquisition of the measured parameters (flow rate, Ps, T1, T2, DP1 and DP2) as in the previous test. In this test, the upper limit of the pump speed was increased over the previous the test, extending the upper flow range from 6.85 kg/s in Test RefA to 8.3 kg/s in this test. The measured pressure gradient (dP/dx) is calculated and compared to the predicted dP/dx based on internal wall surface roughness of 15 μm , and again, the measured dP/dx is approx. 17% higher than the predicted dP/dx due to the other contributions to the flow resistance mentioned above. The density measurements by the Coriolis flow meter are also compared to predictions using GERG-2008 EOS and the corresponding measured pressure and temperature at each measured density data point. The result was that GERG-2008 EOS also under-predicts density by approx. -0.4%.

3.8.4. CO₂ Mixtures with Impurities

The procedure and calculations described above are then repeated for the five test compositions shown in Table 10. Highlights of the experimental report for each composition are as follows:

Test 1

This mixture is representative of oxy-combustion a heavy fuel. The desired composition is 91.8% (CO₂), 2.0% (N₂), 2.3% (O₂) and 3.9% (Ar). The actual composition of the injected components in the flow loop was very close in terms of N₂ and O₂, but the Argon concentration was actually 5.92% (mole) as measured by the GC, which is higher than the desired level of 3.9%. However, this was deemed conservative which will still represent an oxy-combustion process with partial shift and an air separation unit that generates higher concentration of Argon.

Test 2

This mixture is representative of oxy-combustion natural gas. The desired composition for this test is 96.2% (CO₂), 1.9% (N₂) and 1.9% (O₂). The actual mixture composition of the injected components in the flow loop was very close.

Test 3

This mixture is representative of an IGCC process using a heavy fuel. The desired composition is 95.0% (CO₂), 0.5% (CO), 4.0% (H₂), and 0.5% (CH₄). The actual composition of the injected components in the flow loop as measured by the GC from the two samples drawn was very close, with the exception of H₂ being 2.955% (mole) instead of the desired 4.0%. It was therefore, decided to repeat this test with higher concentration of H₂. Test 3B is a repeat of Test-3A but with more hydrogen injected into the flow loop to increase its concentration. The resulting composition was 8.625% (H₂), 0.4165% (CO) and 0.5575% (CH₄). The H₂ concentration came out much higher than the desired value of 4%. This was later found to be caused by a significant loss of mass inventory in the flow loop through the pump seal as the loop was left pressurized with Test-3A mixture for two days until new H₂ cylinders were delivered to site to complete this test. However, this test was considered valuable because it will accentuate the effects of hydrogen, which is known to be the impurity that has the most impact on flow capacity reduction in CO₂ pipeline transportation.

Test 4

This mixture is representative of various natural gas processing plants. The desired composition contains 2.4% CH₄ and 0.2% N₂. However the actual mixture composition of the injected components in the flow loop as measured by the GC from the two samples drawn were slightly below target at 2.085% CH₄ and 0.132% N₂,

Test 5

This mixture is representative of natural gas SMR. The desired composition is N₂ (0.3%) and H₂ (also 0.3%). The actual composition of the injected components in the flow loop as measured by the GC was very close in terms of H₂, but N₂ was around 0.2%.

Flow Loop Results

For each test and as per the references tests, the CO₂ pump speed was varied in slow increments to allow data acquisition of the measured parameters (flow rate, Ps, T1, T2, DP1 and DP2) to be taken. The average pressure gradient dP/dx vs. flow rates was calculated and compared to the predicted dP/dx based on internal wall surface roughness of 15 μm . Density measurements by the Coriolis flow meter were also compared to predictions using GERG-2008 EOS.

Results are presented in Table 11 which shows a summary of the two dP/dx coefficients C_1 and C_2 , and density results. It should be noted that the pressures and temperatures varied during any one test, and these coefficients were the results of fitting all the data in one single test, despite the slight variation in pressure and temperature. The measured pressure gradient (dP/dx) is approx. 17% higher in all cases than the predicted dP/dx based on the internal wall surface roughness of 15 μm .

GERG-2008 EOS was found to under-predict density by 0.1 to 1.0% except for Test 1 where the under-prediction was approx. -2.4%. It was determined that GERG-2008 had to extrapolate to the concentration of Argon of Test 1, which was slightly outside its range.

Table 11. Values of the Semi-empirical Coefficients in the Fitted Experimental Data of all Tests and the Corresponding Average Measured Pressure, Temperature and Density

| Test ID | Coefficients | | Measured Parameters | | | Density Predictions | Error |
|---------|----------------|----------------|--------------------------|--------------------------|---|---|---|
| | C ₁ | C ₂ | Average Pressure (MPa-a) | Average Temperature (°C) | Average Measured Density (kg/m ³) | Based on Avg P and Avg T (kg/m ³) | In Density Predictions by GERG-2008 (%) |
| Ref A | 0.0538 | 2.0084 | 15.188 | 13.2 | 942.43 | 938.51 | -0.42 |
| Test 1 | 0.0573 | 2.015 | 13.085 | 9.0 | 871.14 | 850.11 | -2.41 |
| Test 2 | 0.0589 | 1.9893 | 15.870 | 16.8 | 890.86 | 885.85 | -0.56 |
| Test 3A | 0.0567 | 2.0179 | 15.463 | 14.9 | 872.27 | 863.81 | -0.97 |
| Test 3B | 0.0734 | 1.9875 | 16.205 | 22.8 | 713.10 | 707.32 | -0.81 |
| Test 4 | 0.0574 | 2.0006 | 14.582 | 15.8 | 894.63 | 893.66 | -0.11 |
| Test 5 | 0.0564 | 1.9998 | 11.924 | 13.4 | 911.71 | 907.03 | -0.51 |

Based on these semi-empirical relationships, the pressure gradients (dP/dx) vs. mass flow rates are plotted in Figure 22. Note that Test-3B stands out as being the least flow capacity mixture for the same dP/dx . This clearly due to the relatively high concentration of H₂ in this particular test that exceeded the initial desired concentration as discussed earlier.

It is now possible to quantify the reduction in flow capacity due to the different components and their respective concentration of impurities in the various tests, all compared to Test RefA. The reduction in the flow capacities for all tests relative to Test RefA capacity is shown in Figure 23. The trend in these experimental results compares well to that of the numerical simulation of Figure 16, at least directionally. The exact percentage of capacity reduction is slightly different in Figure 23 from Figure 16. This is due to the variations in the test pressures and temperatures.

Fundamentally, the reduction in the measured flow capacity of CO₂+impurity mixtures for the different tests relative to Test RefA flow capacity shown in Figure 23 can be correlated to the relative mixture densities as shown in Figure 24. Note that, according Eq. 1 (Section 0), for a given pressure gradient (or pressure difference between upstream and downstream points along a pipeline), the flow capacity in terms of mass flow rate of the CO₂ mixture is proportional to square root of the density. This means that, the change in flow capacity (in %) is directly proportional to ½ (one-half) the change in the density (in %). This is manifested in the density deviation plot of Figure 25. Compare Figure 23 to Figure 25 to arrive at the ½ rule of capacity reduction vs. density reduction for all of the test mixture compositions relative to Test RefA mixture.

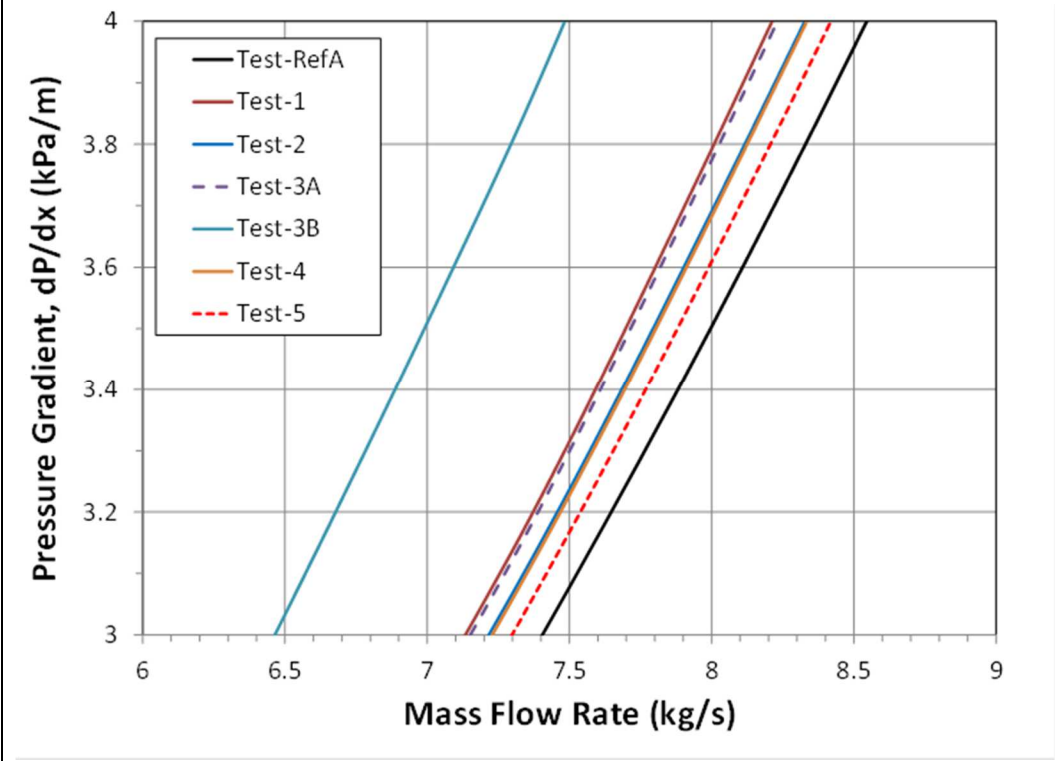
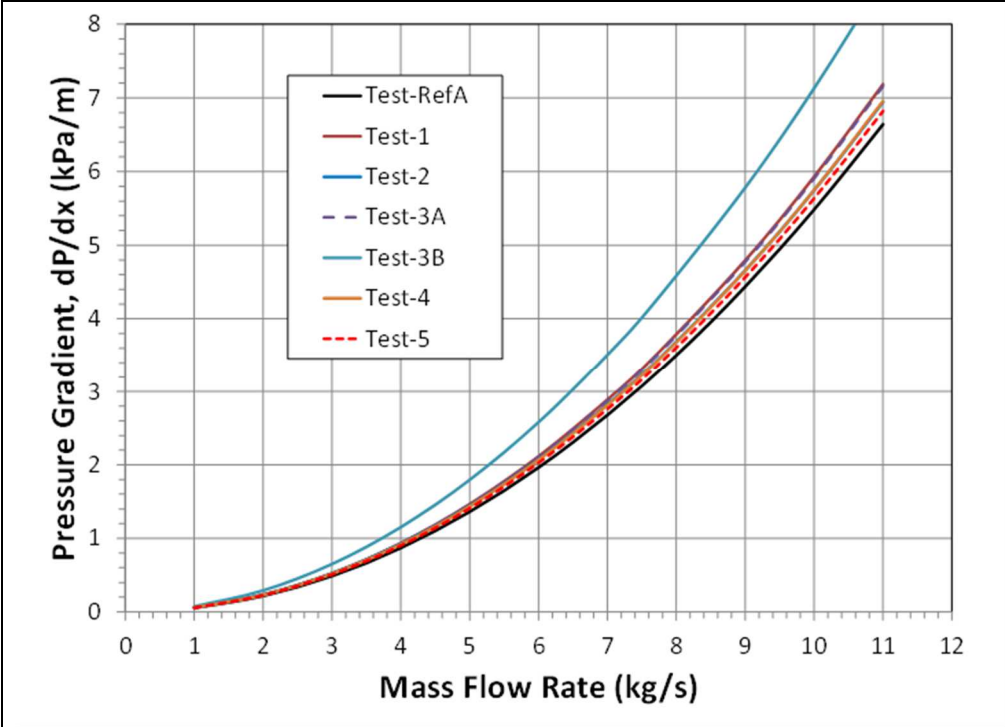


Figure 22. Pressure Gradient vs. Mass Flow Rates of the Tested Mixtures Based on the Experimentally Determined Coefficients C1 and C2 (bottom graph is details of the top graph)

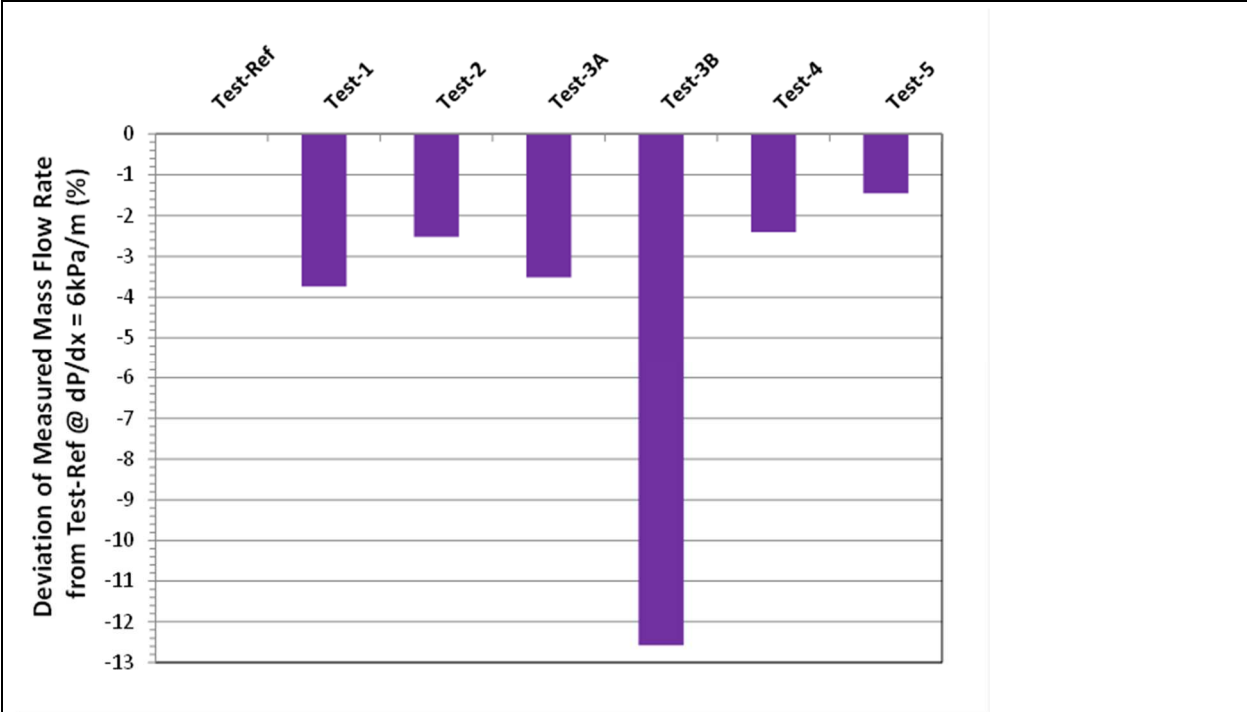


Figure 23. Experimental Results of the Reduction in Flow Rates Compared to Test RefA

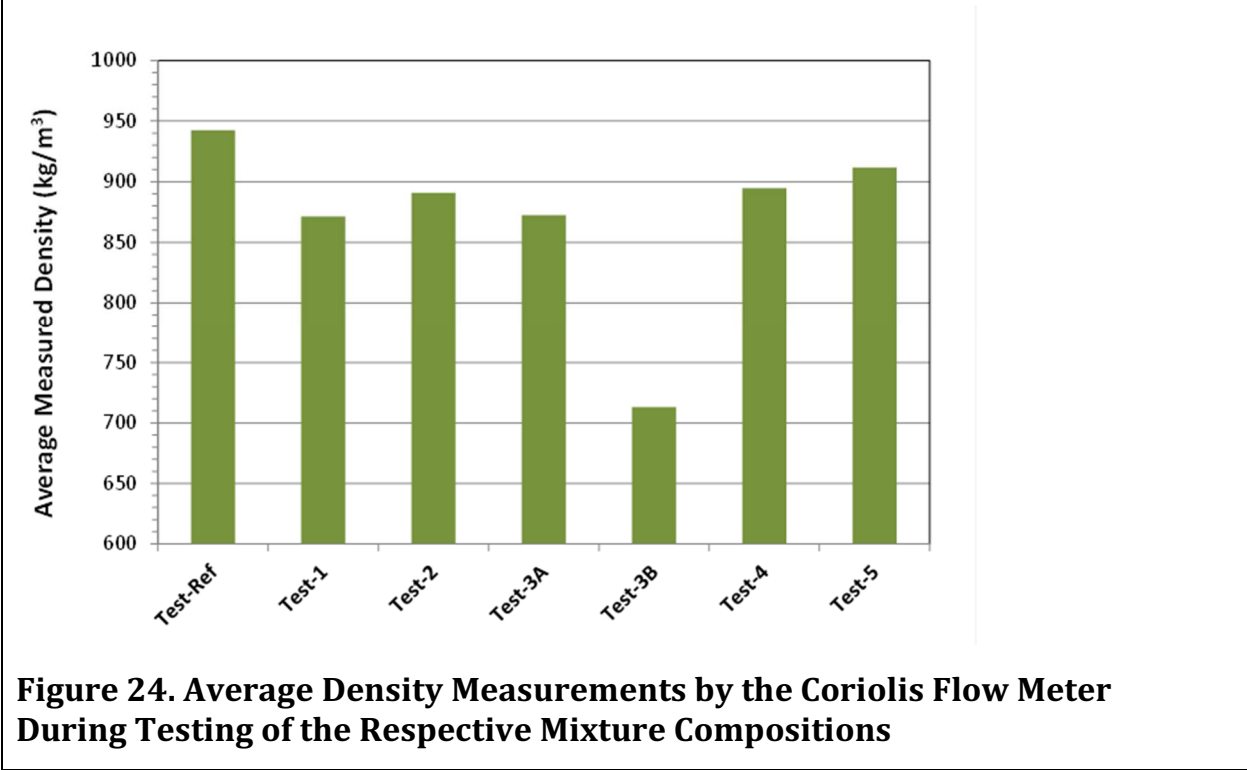


Figure 24. Average Density Measurements by the Coriolis Flow Meter During Testing of the Respective Mixture Compositions

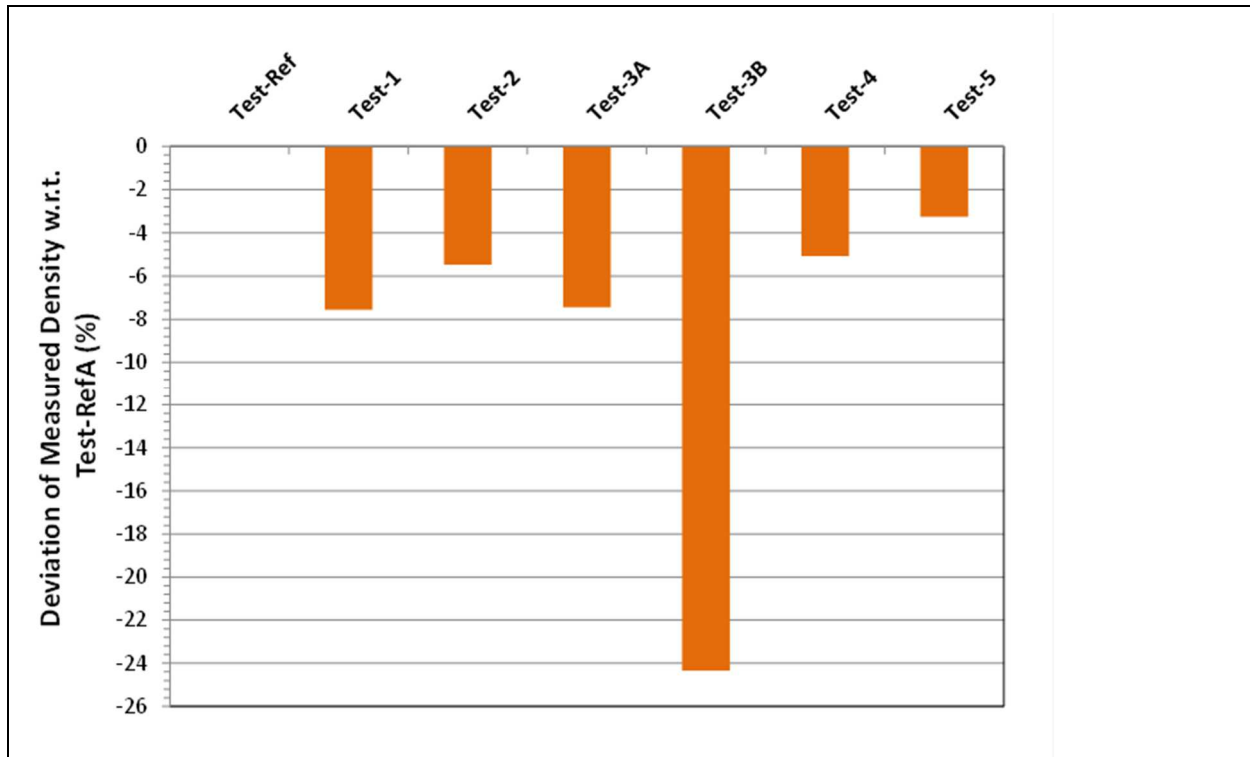


Figure 25. Deviation of Measured Density by the Coriolis Flow Meter Relative to Test RefA Density

It is important to recognize, however, that the change in density is not only attributed to the concentration and type of impurities (which is the subject of the present work), but also to the flow conditions in terms of the average pressure and temperature along the pipeline. This is why the literatures appear to give a wide range of data in terms of the flow capacity reduction even for the same concentration of an impurity. Turning back to the comparison between the numerical results of Figure 16 vs. the experimental results of Figure 23, it is important to recognize that the experimental tests were not conducted at the same average pressure and temperature (see Table 11). Despite that the trend of Figure 23 is comparable to that of Figure 16 (with the exception of Test-3B due to its high concentration of H₂, as discussed earlier), it is possible to show a better comparison if the flow capacity reduction in Tests 1 through 5, are compared to RefA test but with adjustment to the coefficient C₁ for the RefA test by the density ratio of RefA mixture *at the average P and T of each other test* to the density of still RefA mixture at its test condition of P = 15.188 MPa-a, T = 13.2°C and its calculated density = 938.51 kg/m³. This adjustment was made for each comparison between all of the tests relative to the (now) adjusted RefA test C₁'s. For example, when Test-5 is compared to Test-RefA to determine the relative capacity reduction for the mixture composition of Test-5 relative to Test-RefA, the coefficient C₁ for the RefA test is multiplied by the ratio: 914.69 kg/m³ / 938.51 kg/m³, i.e. 0.9746. The value of 914.69 kg/m³ is the calculated density of the RefA mixture at P = 11.924 MPa-a and T = 13.4°C, which is the average P and T of Test-5.

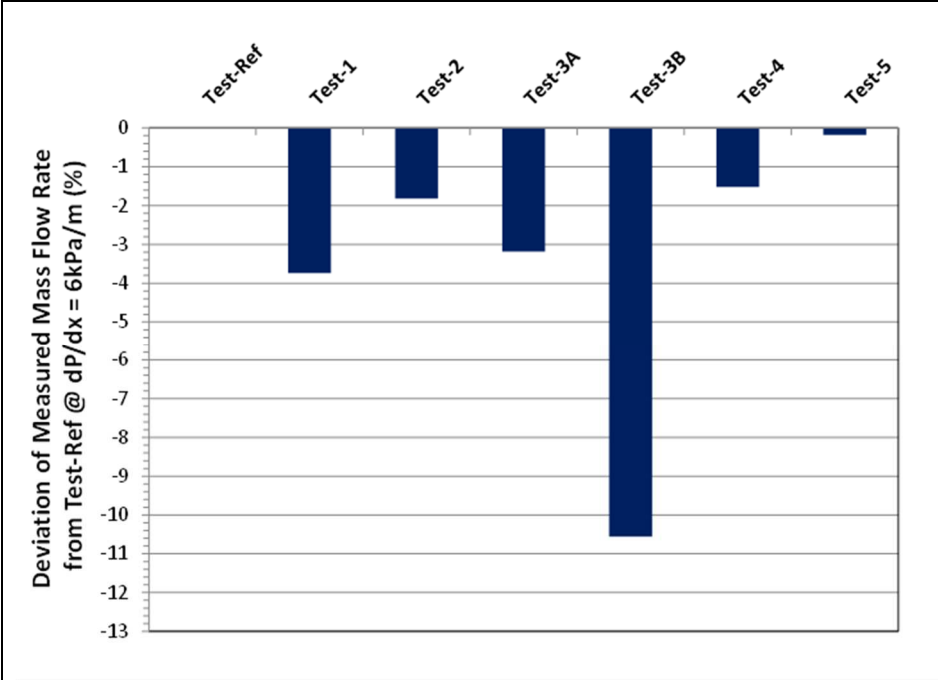


Figure 26. Experimental Results of the Reduction in Flow Rates Compared to Test RefA, where RefA Was Adjusted to the Same Condition of P and T of Each Other Tests

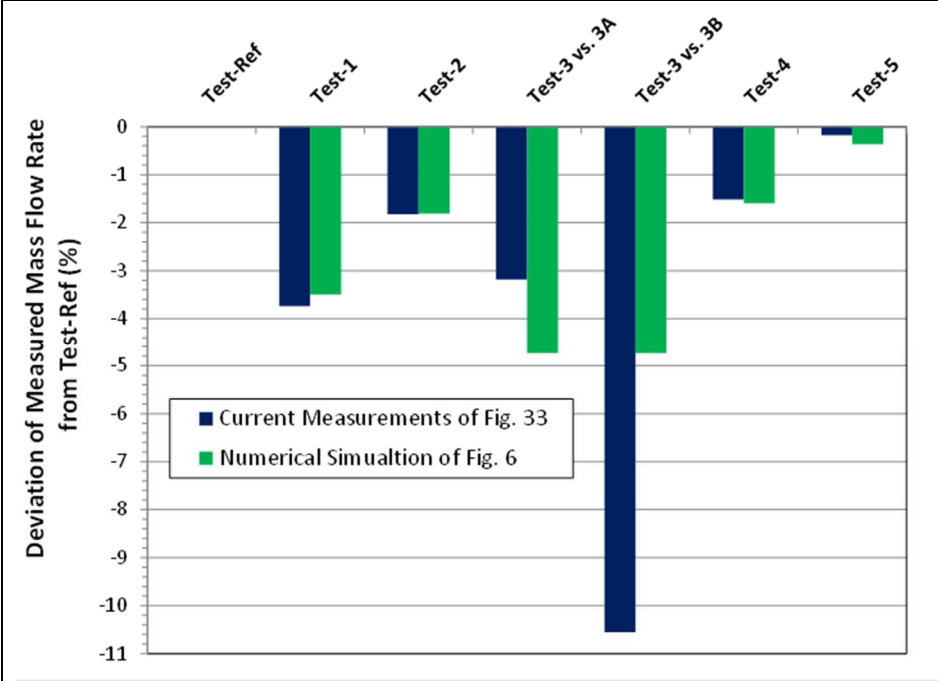


Figure 27. Comparison between the Numerical Results and the Experimental Results Figure 16 vs.

When these adjustments are done to all of the tests, a fair comparison between all of the experimental test results relative to Test-RefA is shown in Figure 26. Now, Figure 26 compares much better to the numerical results of Figure 16, because in both Figures, the comparison between the various mixtures to that of the pure CO₂ (or RefA test mixture) are made based on the same conditions of P and T. Figure 27 combines Figure 16 and Figure 26 to allow easy comparison between the test results and the numerical results.

3.9. Summary and Conclusions

The following summary and conclusions can be drawn from the above numerical and experimental data:

1. Impurities in predominantly CO₂ mixtures investigated in this study (namely, N₂, O₂, Ar, CO, H₂ and CH₄) impact the flow capacity of a pipeline transporting these mixtures in a negative way. That is, these impurities result in a reduction in pipeline flow capacity relative to pure CO₂ fluid.
2. The degree of flow capacity reduction in terms of the relative reduction in mass flow rate is directly proportional to $\frac{1}{2}$ (one-half) of the relative reduction in the mixture density as compared to pure CO₂ fluid, at the same flow condition of pressure and temperature. For example, if the reduction in density of a CO₂+impurity mixture is 6%, the resulting reduction in flow capacity in terms of mass flow rate is 3% at the same condition.
3. Hydrogen as an impurity component has the most negative effect on flow capacity. This is primarily due to its effects on dramatically reducing the mixture density at the same flow condition relative to pure CO₂.
4. The literature quotes a wide range of flow capacity reduction for various types and concentrations of impurities in predominantly CO₂ mixtures. Even at the same concentration level of a binary system of CO₂+impurity, there are different values quoted for flow capacity reduction. For example, 95% CO₂ + 5% H₂ mixture is shown to have an effect on capacity reduction by 11.3% to 18.3% relative to pure CO₂. This was found to be primarily due to differences in flow condition of pressure and temperature, among other factors such as the choice of the appropriate EOS and hydraulic model. The present work pointed to the fundamental relationship between flow capacity being directly proportional to square root of the mixture density, hence capacity reduction (in %) is proportional to $\frac{1}{2}$ density reduction (in %), as stated above.
5. Flow capacity is not directly related to the mixture molecular weight as may have been commonly perceived. Both molecular weight and compressibility factor at the prevailing condition of pressure and temperature affect the mixture density, which in turn affects the flow capacity of a pipeline.
6. The experimental data collected in the present investigation agreed very well with the results obtained from numerical simulations of the flow conditions through the test section,

despite the scatter of the experimental data in terms of dP/dx around the trend line in each test. The scatter was limited to only +2% at the same flow rate, with 1σ standard deviation of 1.23%. This, along with the good agreement with the numerical results, point to the good quality of the experimental data collected.

7. Predictions of density of the CO_2 +impurity mixtures considered in the present work by GERG-2008 EOS showed acceptable results compared to those measured by the Coriolis flow meter. It was shown that GERG-2008 EOS under-predicted density for the most mixtures by 0.2 to 0.5% which is quite good. This is with the exception of the mixture containing H_2 where GERG-2008 under-predicted density by 0.8-1.0%, and for the mixture containing Ar, it under-predicted density by 2.5%. This under-prediction by GERG-2008 would result in a conservative estimate of a pipeline capacity containing these mixtures by $\frac{1}{2}$ of these stated under-prediction percentage (i.e. 0.4-0.5% and 1.25% respectively).
8. The tested mixture viscosities varied between 85-106 $\mu\text{Pa}\cdot\text{s}$ between at the stated range of pressures and temperatures. This is shown to have little effect on the pressure loss coefficients (e.g. friction factor) via the Reynolds number, and hence on flow capacity.
9. The 70 m long, NPS 2 test section, with average Reynolds number of approximately 1.3×10^6 , and effective friction factor of 0.0184, represents 1,280 m long, NPS 20 pipeline section, with internal surface roughness such that at the prevailing Reynolds number of approximately 13×10^6 , is approximately 0.010 at the same average pressure and temperature.
10. The experimental data collected in the present test campaign should be useful in three aspects: a) It provides validation and a 'reality-check' of the large variation in the open literature of the effects of various impurities of flow capacities of CO_2 mixtures; b) It validated the fundamental concept of the flow capacity relationship to the square root of density; and c) It generated density measurements at a good range of pressure and temperature for the CO_2 +impurity mixtures tested.
11. Suggestions for future work includes:
 - a. Conduct other tests in a relatively higher range of temperature (e.g. 30-60°C), which corresponds to the supercritical region of CO_2 mixtures. The present testing program covered a temperature range in the liquid regions of the tested mixtures. Testing at higher temperature would benefit pipeline conditions downstream of compression and pumping stations. The test loop currently does not have heating capability (via heat tracing) and hence is not controlled on temperature.
 - b. Study the effects of impurities on other aspects of pipeline design and operation aspects, such as effects of metering accuracy, valve throttling, blowdown and depressurization.

- c. The flow capacity can also be determined from flow vs. pressure drop across a throttling element, such as an orifice and a control valve. This will eliminate the long gauge lines between the pressure measurement ports.
- d. Study the effects of CO₂-binary mixtures, i.e. one impurity at a time at different levels, e.g. 3%, 5%, 7% by mole of each impurity, to represent medium, high and relatively high levels. This will provide a database of the effects of each impurity component rather than a mixture of several combined.

4. CO₂ Enhanced Oil Recovery

(Edited summary)

Section author: Kelly Edwards

4.1. Phase 1 Outcomes

Phase 1 involved a literature review jointly conducted by the Petroleum Technology Research Centre, the Saskatchewan Research Council and the University of Regina. The purpose of the literature review was to identify published knowledge about the effect of impurities in CO₂ used for EOR.

The literature review found that the type and level of impurities may differ significantly in post-combustion and pre-combustion CO₂ capture processes. In post-combustion processes, components and impurities of flue gases may be captured along with the CO₂ and become CO₂ impurities. In general, CO₂ capture from flue gases may contain the following impurities: CO₂, N₂, O₂, and H₂O, as well as some air pollutants, such as SO_x, NO_x, particulates, HCl, HF, mercury, other metals and other organic and inorganic contaminants. In pre-combustion processes, synthesis gas is produced from the gasification of coal or the reforming of natural gas. The captured CO₂ may contain impurities such as N₂, O₂, H₂, CH₄, CO, and sulfur compounds such as H₂S. Pre-combustion CO₂ does not contain SO_x or NO_x.

It is well known that the performance of CO₂ EOR will strongly depend on the presence of impurities in the CO₂. Impurities generally reduce the solubility of CO₂ in oil and thus raise the minimum miscibility pressure (MMP) which is a key factor in determining EOR performance. The literature review summarized information from theoretical considerations, laboratory studies and field EOR projects. Maximum impurity levels established by various information sources were listed for 19 CO₂ impurities. CO₂ specifications used in EOR projects were also identified as well as the impact on EOR performance.

4.2. The Need for Phase 2 Research

EOR is accomplished through a number of different processes, one of which is miscible gas injection. Miscible gas injection involves the injection of a gas into the reservoir under such conditions that it is able to displace oil left behind by other processes such as primary production or waterflooding. The most common injectant currently used for miscible gas injection is carbon dioxide (CO₂), although in the past many miscible projects operated in Alberta used hydrocarbon solvents, a combination of methane and natural gas liquids mixed in proper proportions to achieve miscibility.

Pressure plays an important role in miscible projects. The oil recovery measured in the laboratory generally increases with increasing pressure to a certain value at which maximum recovery is achieved. Beyond this point no further oil recovery is realized. The minimum pressure at which

maximum oil recovery is achieved is called the minimum miscibility pressure (MMP). A miscible flood operated at or above this pressure should maximize oil recovery, while floods operated below this pressure will leave unrecovered oil in the reservoir.

All industrial sources of CO₂ contain impurities. The impurities in the CO₂ stream can either positively or negatively impact oil recovery when CO₂ is injected for EOR. Most of the impurities have a negative impact on the oil recovery process, either by reducing the amount of oil recovered when the oil is contacted by CO₂ or by increasing the MMP.

In order to optimize the CO₂ purity specification over the full value chain, it is important to estimate and model the impact of impurities on EOR. The impure CO₂ stream compositions and associated industrial processes that are the focus of the technical-economic model of the Project are detailed in Table 2. The objective of this element of the Project will thus be to generate the information and data required to model the impact of the impurities shown in Table 2 on EOR recovery.

Ideally, the effects of impurities are evaluated in the laboratory. However, each reservoir is unique, and lab work is expensive and time consuming. Therefore, it is not practical to conduct laboratory work on every reservoir to determine the effects of impurities on MMP. To overcome this limitation, correlations have been developed as a means to provide first-order estimates of the effects of impurities on oil recovery and MMP.

There are a number of published correlations that estimate the MMP of pure CO₂ given various reservoir parameters and various characteristics of the reservoir oil. Other correlations have been developed to predict the effect on MMP of impurities mixed with CO₂. Figure 28 shows the results calculated using the correlation used in this study prior to adjustment based on the experimental results, which plots the ratio of the MMP of impure CO₂ compared to the MMP of pure CO₂ for various impurities included in this study.

While these correlations are handy and easy to use, it is prudent to confirm them with laboratory data. Thus, the research program was designed to confirm the inputs for the correlation used in this study for the particular oil that was sampled and characterized for this study. The laboratory data also provided key data required in the technical economic model.

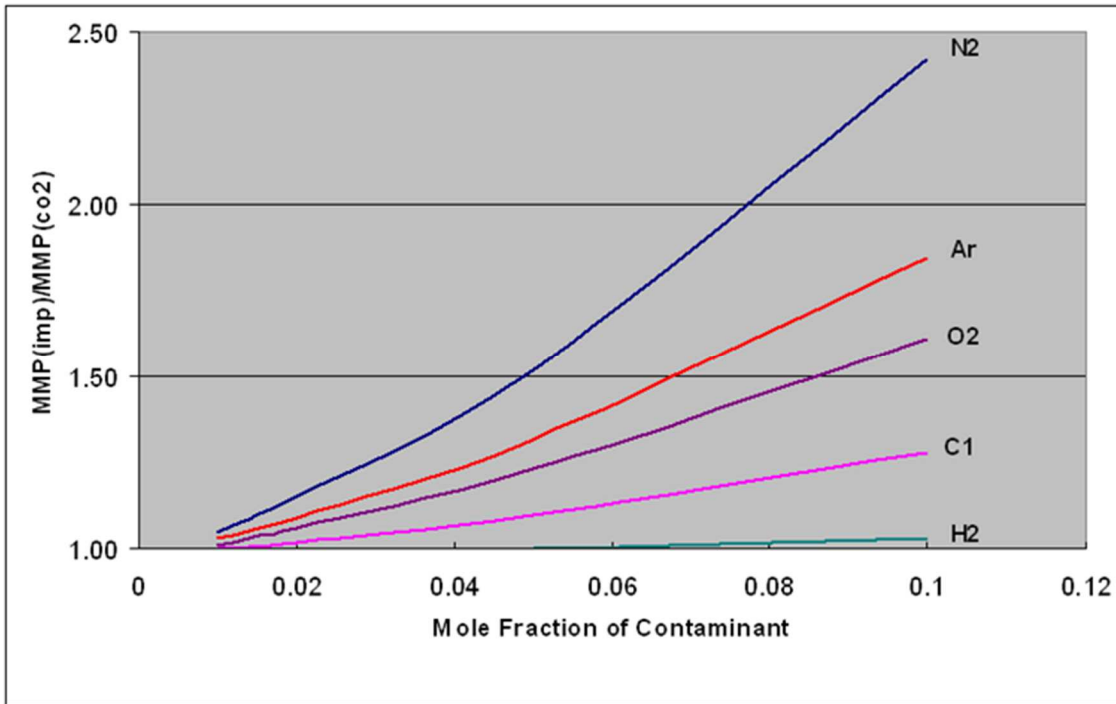


Figure 28. Relative Effect of Impurities on MMP

4.3. Methodology

4.3.1. Pressure, Composition and Recovery Factor

The recovery factor of a gas injection process can be estimated as follows:

$$RF = \eta_{displacement} * \eta_{areal} * \eta_{vertical}$$

Where:

$$\eta_{displacement} = displacement\ efficiency$$

$$\eta_{areal} = areal\ sweep\ efficiency$$

$$\eta_{vertical} = vertical\ sweep\ efficiency$$

Thus, the recovery factor of the 3-dimensional system is assumed to be the combination of three 1-dimensional efficiencies. The displacement efficiency is typically measured experimentally in either a slimtube or coreflood. Corefloods are expensive, involved, and reservoir specific, so slimtube experiments, being cheaper and a more general means to determine the effects of different contaminants in the CO₂ stream, were used in this study. The areal and vertical sweep efficiencies are assumed to remain unaffected by changes in gas composition. If gas composition does change areal and vertical sweep, it is expected to be, at most, a minor effect.

The increase in displacement efficiency of a CO₂ EOR scheme is achieved through a reduction in the oil/gas interfacial tension. This allows oil that would otherwise remain trapped in the pore system, to be mobilized and produced with the CO₂. In order to maximize oil recovery, the gas injection process must be operated at, or above, the pressure where maximum displacement efficiency occurs. This point occurs when the gas/oil IFT approaches zero, at which point the oil and CO₂ become miscible. The corresponding pressure is called the minimum miscibility pressure (MMP).

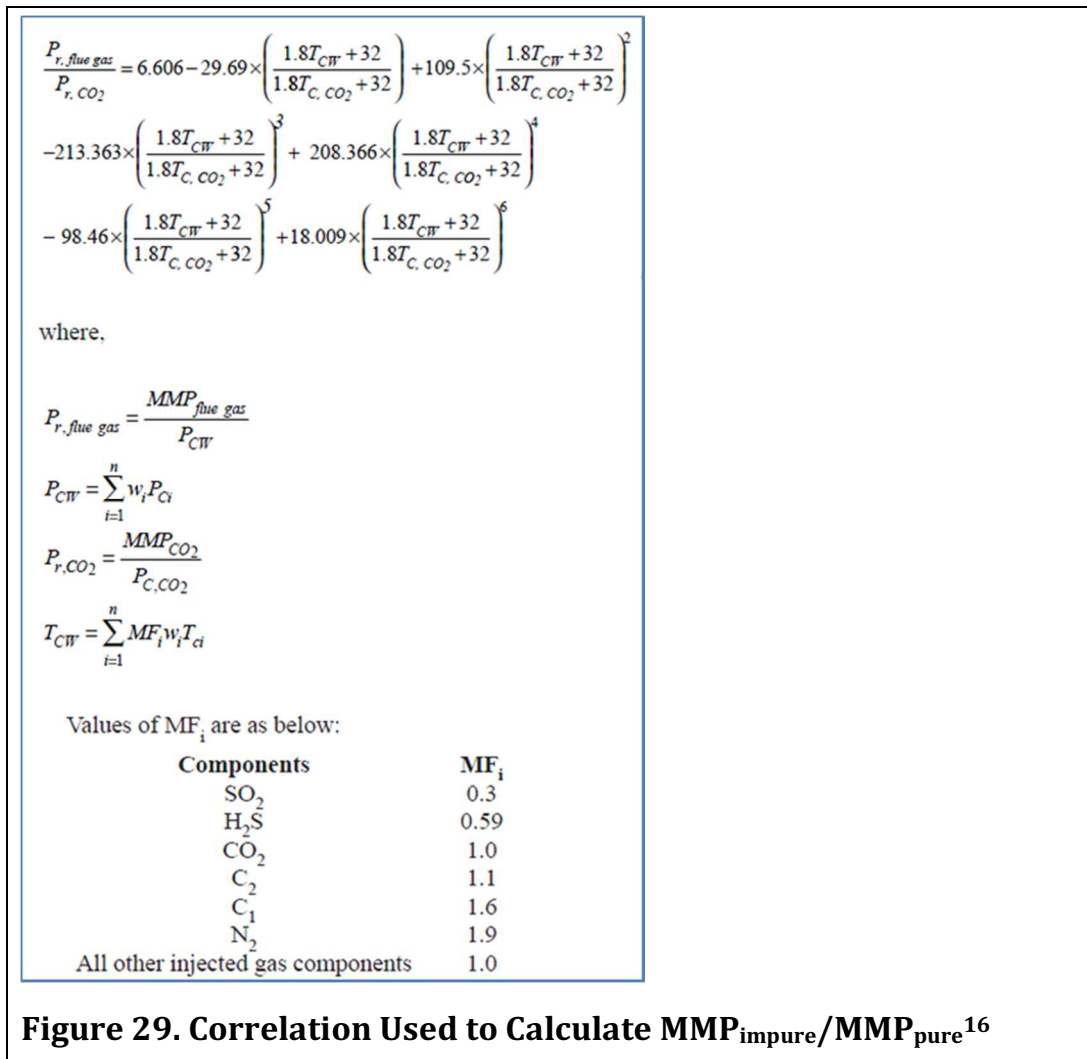
The economic impact of contaminants is evaluated through their effect on the MMP, which in turn is indicative of their effect on displacement efficiency. Most contaminants have the effect of increasing the MMP. However, the ability to raise the pressure to the MMP required for an impure CO₂ stream is not a given in every reservoir. If the reservoir is connected to a strong aquifer, the pressure cannot be increased beyond the pressure in the aquifer, and a lower recovery factor will result from injection of impure CO₂. In other reservoirs, the geomechanical conditions may be such that the reservoir pressure cannot be increased. In other reservoirs, the pressure increase required to reach the MMP of the impure CO₂ stream might be possible. What this indicates is that every reservoir requires an in-depth study to know whether the pressure could be increased enough to achieve the MMP of the impure CO₂ stream. In order to simplify the analysis for this study, **the conservative assumption was made that the maximum reservoir pressure that could be achieved was the MMP of pure CO₂**. Because the MMP of the impure CO₂ stream will typically be greater than that for pure CO₂, and given the assumption that pressure cannot be raised above the MMP of pure CO₂, reduced oil recovery results from the injection of an impure CO₂ stream.

Thus, in order to calculate the effects of impurities on recovery, one must first estimate the increase in MMP due to the impurities. This, along with two assumptions (areal and vertical sweep efficiency remain unchanged with the change in gas composition, and reservoir pressure cannot be increased above the MMP for pure CO₂), allows the loss in displacement efficiency to be estimated using combined data from the experimental program and correlations.

4.3.2. Calculation of Increase in MMP

There are many correlations that can be used to predict the increase in MMP for a CO₂ stream with contaminants compared to that for pure CO₂.¹⁵ These correlations are all based on one or more parameters which include reservoir temperature, oil molecular weight and density, C₇₊ properties, mole percentages of light ends, mole percentages of intermediates, etc. The correlation chosen for this work is by Emera and Sarma.¹⁶ Their work has three advantages for this study. The first is that it more accurately fits the experimental data considered in its development. The second is its ability to handle the specific impurities that are under consideration in this work. In fact, their research dealt specifically with SO₂, H₂S, CO₂, C₂, C₁, and N₂. The third is that they also include a formula for the calculation of MMP for pure CO₂.

The correlation for the ratio of $MMP_{\text{impure}}/MMP_{\text{pure}}$ from the work of Emera and Sarma is shown in Figure 29.



The specific factors that are included in this correlation are: T_{ci} (component critical temperature), P_{ci} (component critical pressure), weight fractions of each component, and a component-specific Multiplication Factor (MF_i). Because the effects of the impurities are based on mass percent, H₂ is predicted to have little effect on MMP because it is such a light molecule and has a negligible impact on the overall mass of the gas mixture. The laboratory program was designed to validate the Emera and Sarma correlation, and where necessary, provide the data for changes in the values of the Multiplication Factors so that the correlation would match the experimental work carried out in this study.

4.4. Laboratory Program

An extensive laboratory program was undertaken using an oil sample from the Pembina Cardium formation to provide fundamental data required to calculate the impact of impurities on recovery

factor, and to verify the correlation used to estimate the effects of impurities on MMP. The following work was carried out:

1. Sampling of well 100/12-24-047-10W5/0, which produces from the Cardium formation;
2. Recombination of gas and oil samples to yield a recombined reservoir oil sample;
3. Rising Bubble Apparatus tests to determine MMP of various CO₂/impurity mixtures;
4. Slimtube tests to verify the RBA MMP estimates. The slimtube tests also provided the recovery vs. pressure correlation required to estimate the recovery impact of impurities in the technical economic model.

Each of these will be covered in detail in the sections below. The decisions around which well to sample and the recombination process are discussed first. Then, the experimental program will be covered. A short description of the experimental equipment is followed by the specific experimental program and results.

4.4.1. Oil Sampling and Recombination

The Pembina Cardium formation was chosen as the reservoir upon which to base the laboratory evaluation for a number of reasons:

1. **Size.** The Pembina Cardium formation forms the largest oil field in Alberta with an original oil in place of more than 9 billion barrels. The significant extent of the Pembina Cardium field within the province of Alberta is shown in Figure 30.
2. **Advantages.** It is an attractive EOR target due to location, existing infrastructure, and its sheer size. Committee members also operate wells in the Pembina Cardium, facilitating the work of obtaining samples.
3. **Economic Impact.** A 5% increase in recovery factor would mean production of an additional 450 million barrels of oil. At today's oil prices of approximately \$100/bbl, additional revenues of \$45 billion would be realized due to EOR.

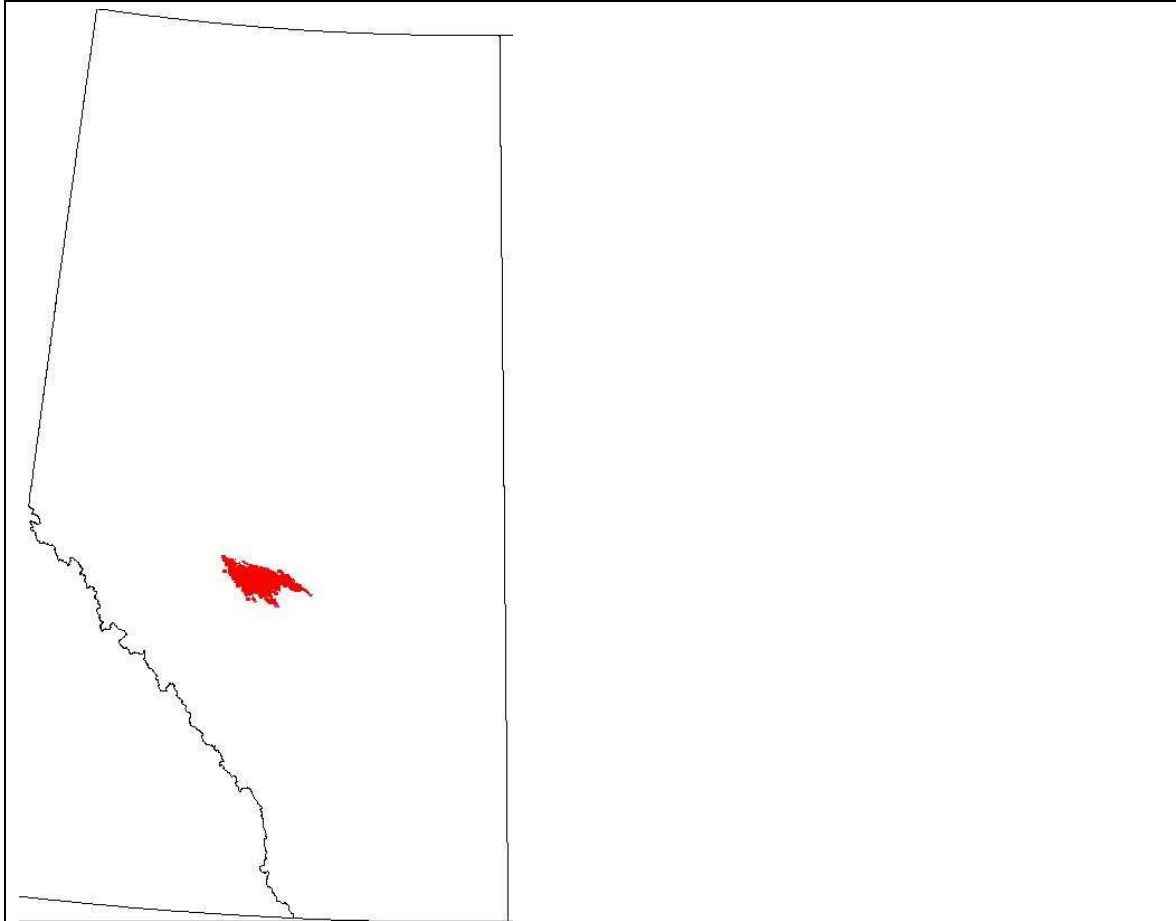


Figure 30. Map of Alberta with the Location of the Pembina Oilfield

Separator samples (oil and gas) were obtained from the Cardium well 100/12-24-047-10W5/0. This well was chosen for sampling because it had a low watercut and a low GOR. A low water cut and low GOR are good indications the well is flowing fresh virgin oil. The production plot shown in Figure 31 indicates that well 12-24 fits these criteria. It currently produces at a low, stable GOR of ~ 300 scf/bbl, and produces almost no water. Historically, the well produced at a high GOR (from 4,000 scf/bbl increasing to $\sim 10,000$ scf/bbl), after being placed on production in 2002, due to lack of waterflood support in the area causing the pressure to drop below bubble-point. Two new horizontal injectors on each side of 12-24 were placed on water injection while the well was shut-in. When the well was placed back on production in 2010, it produced at a much lower GOR (~ 300 scf/bbl), showing the positive effects of the offset injection and re-pressurization.

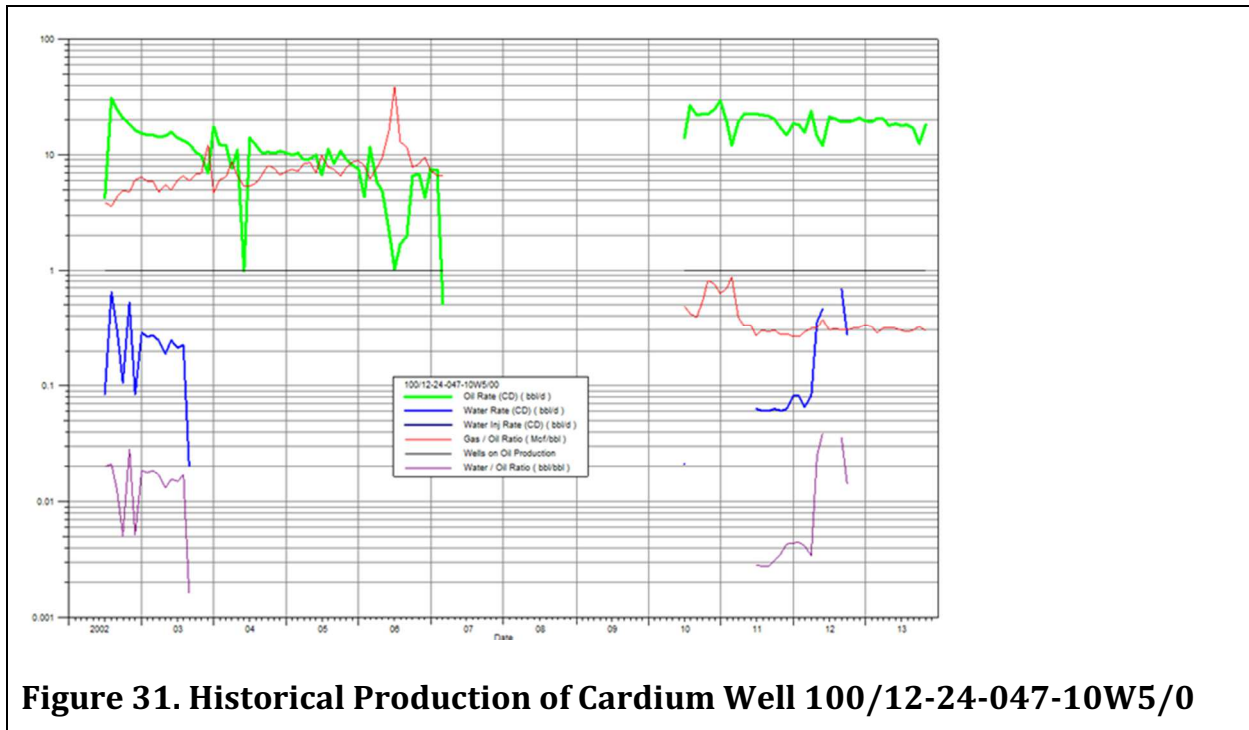


Figure 31. Historical Production of Cardium Well 100/12-24-047-10W5/0

Fluid Sampling

Per the fluid sampling guidelines, all chemical and methanol use was stopped prior to sampling to ensure clean oil samples. Chemicals used to prevent corrosion or to help with emulsion control can affect certain measurements made with the oil. Separator oil samples were taken in 3.8 litre flow through cylinders, and separator gas samples were flashed into evacuated 500 cc cylinders. The well was produced at stable rates for 24 hours prior to sampling.

Neither the initial nor subsequent GORs were considered representative of the original reservoir fluid. The recombination conditions were determined after examining both GOR and bubble point pressure (BPP) from many PVT analyses in offsetting wells. Consequently, the recombination was carried out at a GOR of 650 scf/bbl, considered more representative of virgin reservoir conditions than the low current producing GOR.

Recombined Oil

The analysis (mole fraction) and physical properties of the recombined oil sample are shown in Table 12. The oil has a bubble point pressure of 2389 psia, and an API gravity of ~ 39 degrees, making it a highly desirable light oil.

Table 12. Physical Properties of the Recombined Oil Sample

| | | |
|--------------|--------------|--|
| Total | 1.000 | |
| N2 | 0.0043 | |
| CO2 | 0.0023 | |
| H2S | 0 | |
| C1 | 0.3775 | |
| C2 | 0.0554 | |
| C3 | 0.063 | |
| i-C4 | 0.0141 | |
| n-C4 | 0.042 | |
| i-C5 | 0.0221 | |
| n-C5 | 0.0264 | |
| C6 | 0.0341 | |
| C7 | 0.0293 | |
| C8 | 0.0307 | |
| C9 | 0.0262 | |
| C10 | 0.022 | |
| C11 | 0.0208 | |
| C12 | 0.0179 | |
| C13 | 0.0178 | |
| C14 | 0.0145 | |
| C15 | 0.0122 | |
| C16 | 0.01 | |
| C17 | 0.0089 | |
| C18 | 0.0092 | |
| C19 | 0.0082 | |
| C20 | 0.0069 | |
| C21 | 0.0061 | |
| C22 | 0.0057 | |
| C23 | 0.0053 | |

| C7+ Fraction | |
|---------------------|--------|
| Molecular Weight | 226.81 |
| Mole Fraction | 0.343 |
| Density (g/cc0 | 0.8659 |

| C12+ Fraction | |
|----------------------|--------|
| Molecular Weight | 326.26 |
| Mole Fraction | 0.1877 |
| Density (g/cc0 | 0.903 |

| C30+ Fraction | |
|----------------------|--------|
| Molecular Weight | 619.81 |
| Mole Fraction | 0.0407 |
| Density (g/cc0 | 0.9882 |

| Oil Characteristics | |
|----------------------------|----------|
| BPP | 2389 psi |
| API Gravity | 39.35 |
| Reservoir Temp | 52°C |

| | |
|-----------|--------|
| C24 | 0.0049 |
| C25 | 0.0045 |
| C26 | 0.0042 |
| C27 | 0.0037 |
| C28 | 0.0037 |
| C29 | 0.0034 |
| C30+ | 0.0407 |
| Napthenes | 0.0264 |
| Aromatics | 0.0158 |

4.4.2. Compositional Comparison to Other Cardium Wells

The composition of the recombined oil was compared to a selection of other Cardium wells, all with PVT analyses from the 1950's, representing reservoir fluid compositions at the time of discovery. The wells were chosen from a wide geographical area, but in general, have reservoir temperatures and pressures similar to the 12-24 well.

A compositional comparison of C1 and C7+ is shown in Figure 32. It clearly indicates that the 12-24 recombined oil is higher in C1 and lower in C7+ than the original Cardium analyses. A comparison of BPP is shown in Figure 33. The BPP of the recombined 12-24 oil is much higher than the BPP of the original Cardium analyses.

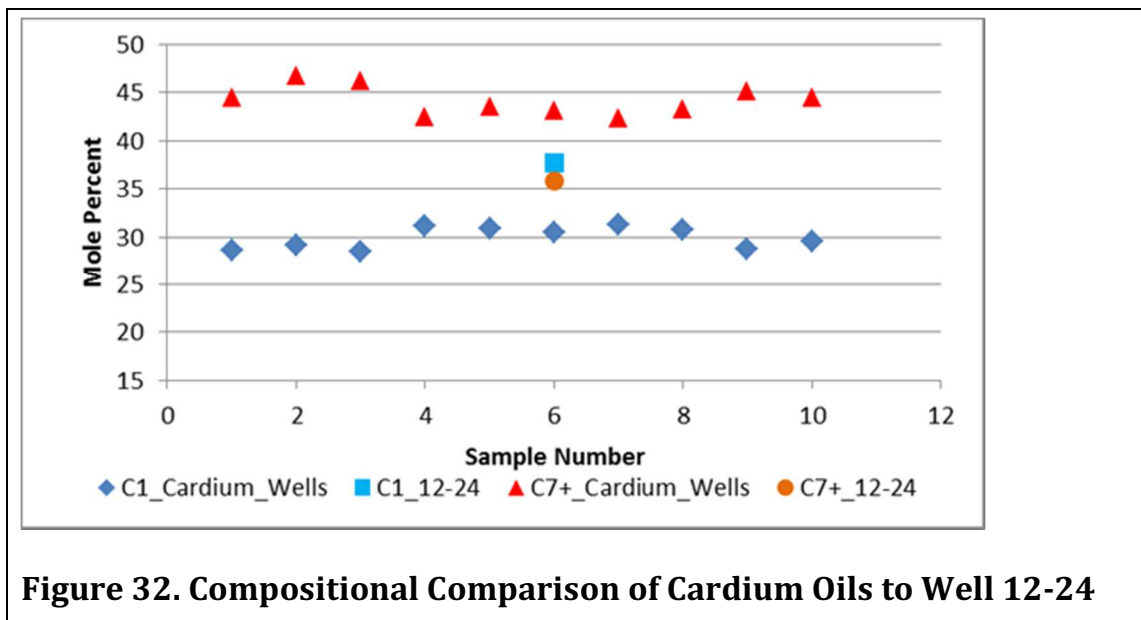


Figure 32. Compositional Comparison of Cardium Oils to Well 12-24

There are a number of possible reasons for these discrepancies. First, the PVT analyses from the 1950's were conducted on samples obtained at essentially virgin reservoir conditions. The 12-24 well has followed a more complex compositional path, beginning production with reservoir pressure below the BPP, as evidenced by the very high GOR during the first five years of production. The well was then shut-in for a number of years with off-setting injection to restore reservoir pressure. When the well was returned to production, the GOR was very low, indicating the injection had been successful in raising reservoir pressure above the BPP. However, the reservoir oil composition at this point will certainly be different than what it was to begin with. Second, the recombination was carried out at a GOR higher than the producing GOR (650 scf/bbl vs 300 scf/bbl), although it was considered more representative of the original reservoir fluid based on offsetting well production. This would likely account for the high methane content in the recombined oil from well 12-24. Third, the composition of the gas used in the recombination may not be consistent with the GOR that was used in the recombination.

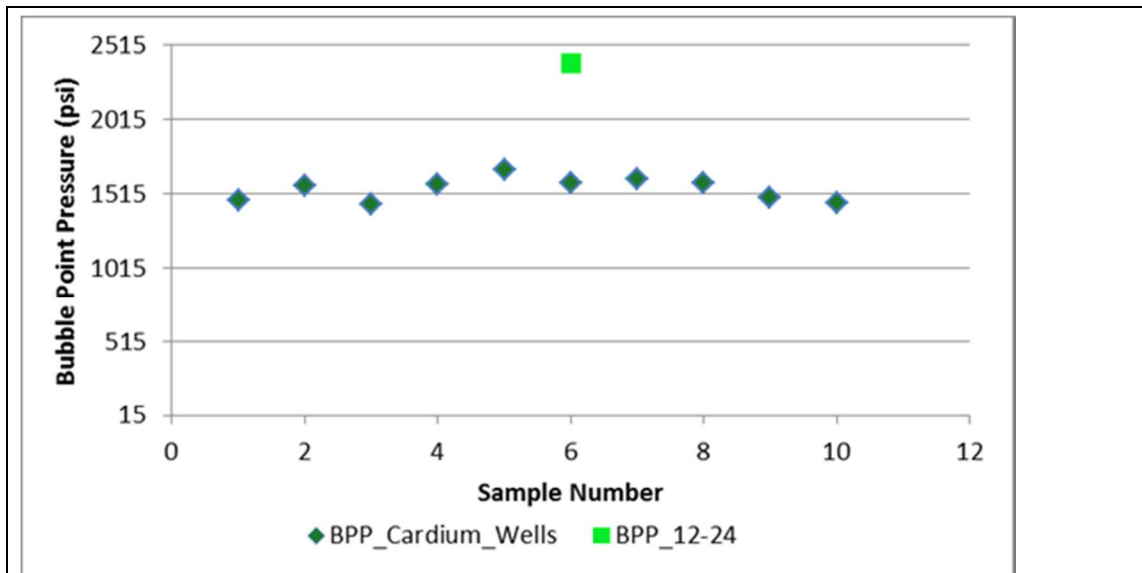


Figure 33. Bubble Point Pressure Comparison of Cardium Oils to Well 12-24

To conclude, the composition of Well 12-24 recombined oil may not be representative of other Cardium oils, and direct results should be extrapolated to the Cardium with caution. However, the same caution must be exercised in the application of this study to any reservoir, without having the benefit of the full laboratory program detailed in Section 4.4. The main use of the experimental data has been in the validation of the correlation, and it is expected that this will still have broad application.

4.4.3. Experimental Apparatus

The MMP is usually evaluated in the laboratory using one of two different experiments: Rising Bubble Apparatus (RBA) or slimtube. The two pieces of equipment are described below in more detail.

Rising Bubble Apparatus

The Rising Bubble Apparatus involves injection of CO₂ into a sample of reservoir oil at reservoir temperature and at various pressures. The behaviour of the CO₂ bubble is observed through a sight glass. The MMP is determined from the mixing behaviour of the CO₂ and oil at increasing pressure. At pressures below the MMP the CO₂ rises through the oil as a distinct bubble, as shown in Figure 34. A well-formed bubble results when there is surface tension between the oil and CO₂, indicating that immiscible conditions are present.

At pressures at or above the MMP the CO₂ instantly mixes with the reservoir oil to form a miscible mixture. There is no distinct bubble, and the CO₂ disperses immediately in the oil, as shown in Figure 35.

2613 psia

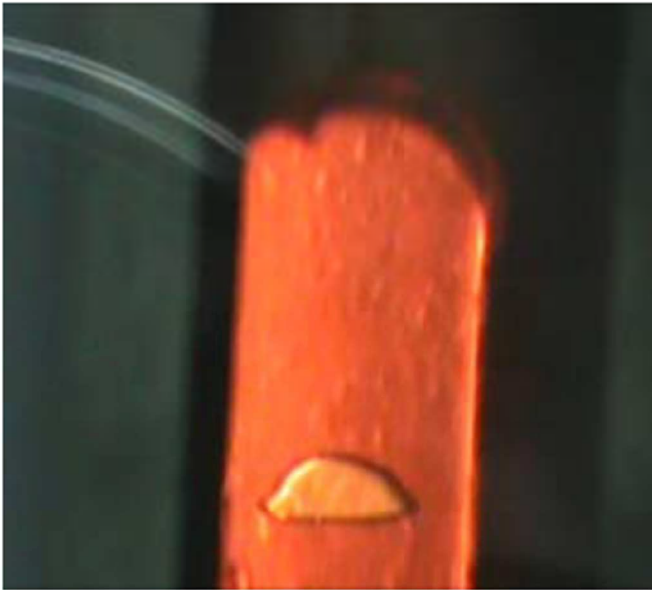


Figure 34. Rising Bubble of CO₂ in Reservoir Oil in an RBA - Immiscible Conditions

3413 psia

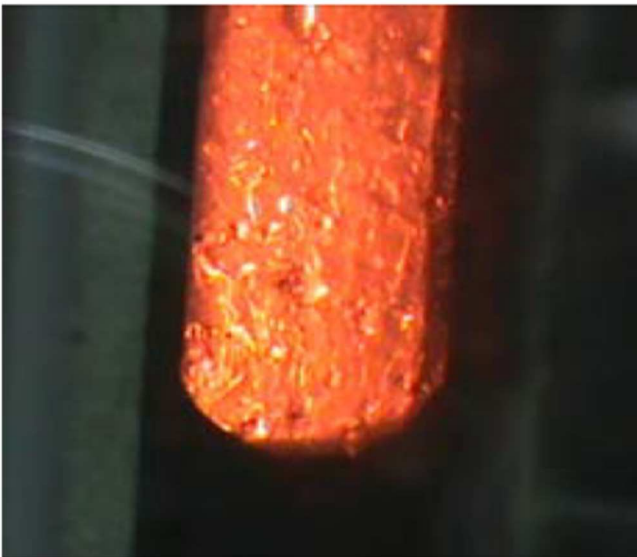


Figure 35. Streaming CO₂ in Reservoir Oil in an RBA - Miscible Conditions

Slimtube

A slimtube is a metal tube of approximately 10 or 15 meters of length which is packed with a high permeability sand. A photograph of a slimtube is shown in Figure 36.

The slimtube is saturated with reservoir oil at reservoir temperature. The gas is injected at the top of the apparatus, and the oil is produced from the other end of the tube. A constant pressure is maintained in the apparatus. Several pore volumes of gas are typically injected, and the recovery factor is usually calculated at 1.2 pore volumes of gas injected.



Figure 36. Photograph of a Slimtube Apparatus

The use of slimtubes to determine the MMP of a given gas mixture is typically performed in the following manner. Four runs are made, two of the runs will be at pressures below the MMP, and two will be at pressures above the MMP. This is illustrated in Figure 37, where the green diamonds represent the recovery factor using pure CO₂. The intersection of the yellow line drawn through the two points below the MMP with the line drawn through the 2 points above the MMP intersects at the MMP. This is the point shown inside the black circle. The measurement of recovery for an impure CO₂ stream is shown by the blue triangles, with the corresponding MMP shown by the intersection of the red line with the yellow line inside the grey circle. The MMP for pure CO₂ (the two yellow lines inside the black circle) occurs at 1785 psi. The MMP for the impure CO₂ stream (intersection of the red line and the yellow line inside the grey circle) occurs at 2150 psi. Based on these pressures, the ratio of the MMP_{impure} to MMP_{pure} is 2150/1785 ~ 1.2.

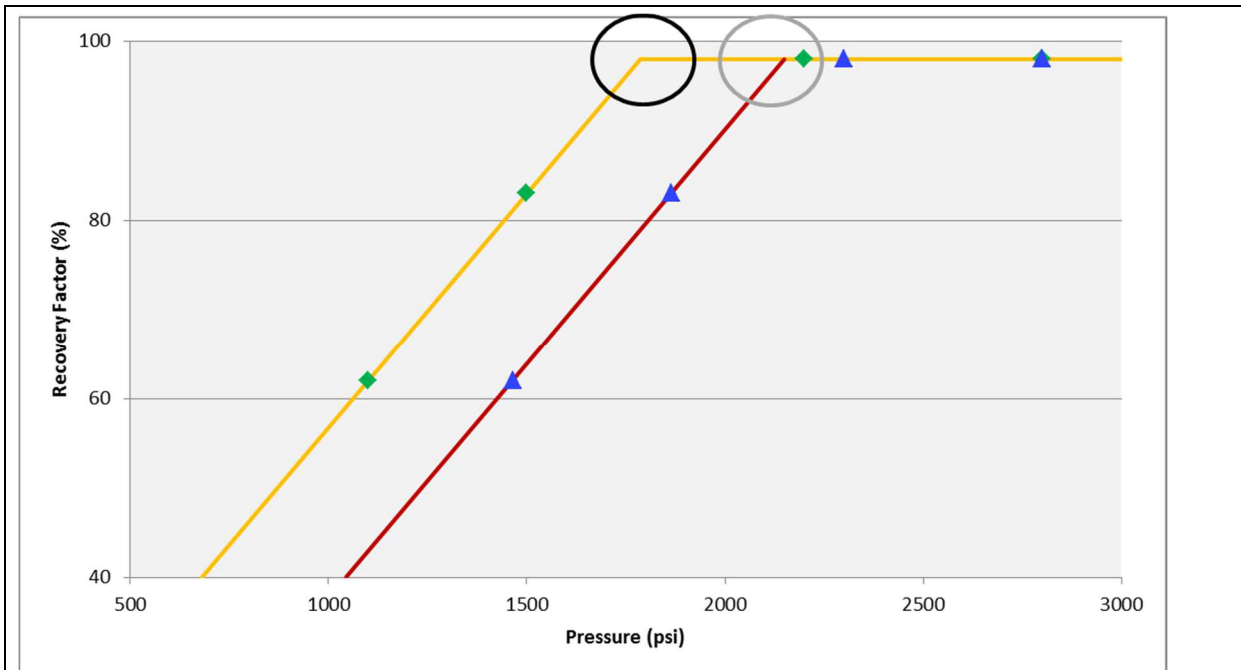


Figure 37. Schematic Showing the Process of Calculating MMP

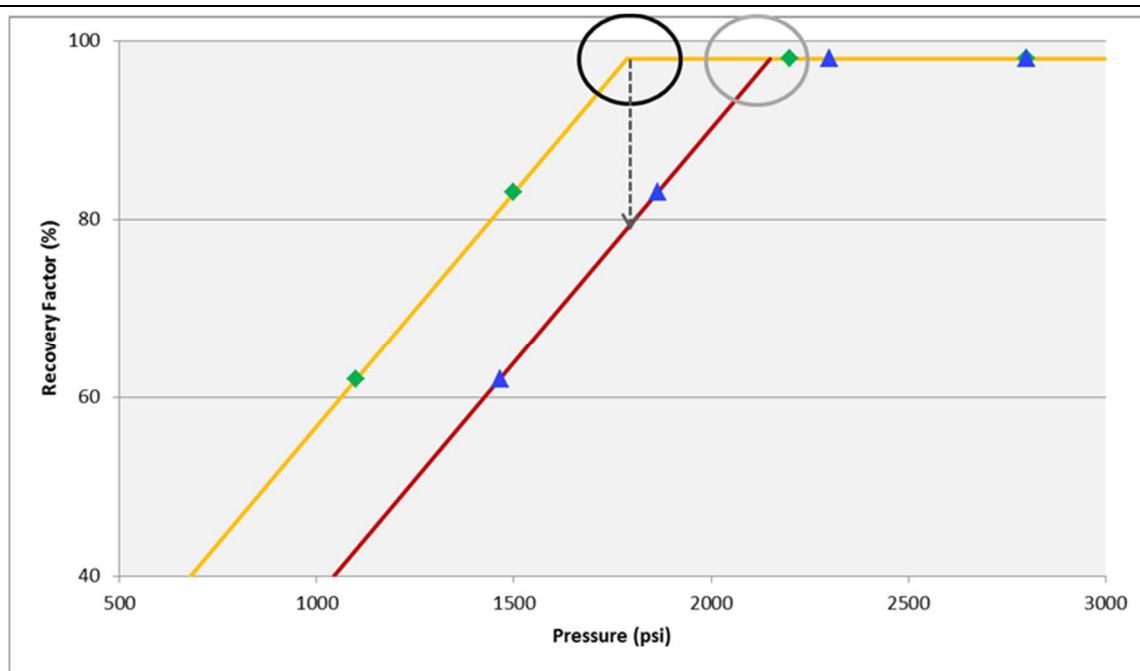


Figure 38. Schematic for Calculating the Decrease in Recovery with Impure CO₂

An estimate of the reduction in recovery due to injection of impure CO₂ is made using the following procedure. A vertical line is drawn at the MMP for pure CO₂, which has been assumed

as the maximum reservoir pressure allowed. Where this line intersects the recovery curve for the impure CO₂ mixture indicates the expected recovery factor for the impure CO₂ mixture. This is shown schematically in Figure 38. In this example, the recovery factor is estimated graphically at ~ 80%.

If the slope of the red line (what is referred to in following sections as the recovery factor slope for impure CO₂) is known, then this method can be easily programmed mathematically. This, in fact, is how the method has been implemented in the technical/economic model.

For example, the recovery factor slope of the red line in this example is 0.0525 percent/psi. The calculated recovery for impure CO₂ at 1785 psi (MMP of pure CO₂) is:

$$RF_{\text{impure}} = 98\% + (1785 - 2150) * .0525 = 78.8\%$$

The experimental data and verification of the correlation for predicting the increase in MMP is expanded upon in the next section.

4.5. Experimental Results

4.5.1. RBA Program

The original lab program, laid out in Figure 39, envisioned conducting RBAs to measure the MMP of various binary gas mixtures. The slimtube tests were to measure the recovery factor slope, measure the MMP with more than one impurity, and confirm that the correlation accurately predicted the increase in MMP for multicomponent impurity mixtures.

| Experiment | Components | Mole Fr | Cum days | Cum Cost | 5 | 10 | 15 | 20 | 25 | 30 | 30 | 35 | 40 | 45 | 45 | 45 | 45 | 45 | 9 weeks |
|------------------------------|--------------|------------|----------------------------|----------|---|----|----|----|----|----|----|----|----|----|----|----|----|----|---------|
| | | | | | 5 | 10 | 15 | 20 | 25 | 30 | 30 | 35 | 40 | 45 | 45 | 45 | 45 | 45 | \$ |
| | | | | | 1 | 1 | 1 | 1 | 1 | 1 | 0 | 1 | 1 | 1 | 0 | 0 | 0 | 0 | |
| RBA1 | CO2 | 100/0 | | | 1 | | | | | | | | | | | | | | |
| RBA2 | co2/n2 | 95/5 | | | | 1 | | | | | | | | | | | | | |
| RBA3 | co2/n2 | 97.5/2.5 | | | | | 1 | | | | | | | | | | | | |
| RBA4 | co2/o2 | 95/5 | | | | | | 1 | | | | | | | | | | | |
| RBA5 | co2/o2 | 97.5/2.5 | | | | | | | 1 | | | | | | | | | | |
| RBA6 | co2/c1 | 97.5/2.5 | | | | | | | | 1 | | | | | | | | | |
| RBA7 | co2/ar | 95/5 | maybe skip this one | | | | | | | | 0 | | | | | | | | |
| RBA8 | co2/ar | 97.5/2.5 | | | | | | | | | | 1 | | | | | | | |
| RBA9 | co2/ar | 92.5/7.5 | | | | | | | | | | | 1 | | | | | | |
| RBA10 | co2/h2 | 95/5 | | | | | | | | | | | | 1 | | | | | |
| RBA11 | co2/n2/o2 | 92.5/2.5/5 | not reqd if doing slimtube | | | | | | | | | | | | 0 | | | | |
| RBA12 | co2/n2/o2 | | | | | | | | | | | | | | | 0 | | | |
| RBA13 | co2/n2/o2/ar | 90/2/3/5 | not reqd if doing slimtube | | | | | | | | | | | | | | 0 | | |
| RBA14 (may scale to 90% co2) | | | | | | | | | | | | | | | | | | | 0 |

Figure 39. Original RBA Program

However, only five RBA tests were conducted. The program was cut short when it became apparent that the RBAs were not doing a good job of estimating the MMP. For example, an MMP for pure CO₂ of 3313 psi was estimated from the RBA. This was much higher than the value of

1844 psi predicted by correlations. At this point, it was decided to stop further RBA testing and proceed exclusively with slimtube tests.

The MMP results for the 5 RBAs are presented in Table 13. The ratio of the MMP of impure CO₂ to the MMP of pure CO₂ is also presented based on the experimental results, and compared to the value calculated from the correlation. It is interesting that, although the absolute values of MMP do not appear valid, the ratios of MMP_{impure}/MMP_{pure} appear reasonable for N₂ and O₂, less so for Ar, and seem completely at odds with the correlation for H₂.

| | Pure CO ₂ | CO ₂ with 5% N ₂ | CO ₂ with 5% O ₂ | CO ₂ with 5% Ar | CO ₂ with 5% H ₂ |
|---|----------------------|--|--|----------------------------|--|
| MMP (psi) | 3313 | 4063 | 4163 | 3700 | 4050 |
| MMP _{impure} /MMP _{pure} | | 1.23 | 1.26 | 1.12 | 1.22 |
| MMP _{impure} /MMP _{pure} from correlation | | 1.21 | 1.19 | 1.28 | 0.98 |

Due to budget and fluid constraints, it was not possible to conduct further work to determine the reason for the discrepancy between the RBA tests and slimtube results. However, one possible reason relates to how miscibility is being developed between CO₂ and this Cardium oil. It is possible that miscibility is developed through a combined “forward/backward” contact mechanism that is handled in the slimtube apparatus, but is not modelled in the RBA. The RBA, by virtue of how the experiment is conducted, models a forward contact process only.

4.5.2. Slimtube Program

The original slimtube program is shown in Figure 40. Each “experiment” was assumed to consist of 5 runs at different pressures, mainly on multi-component mixtures.

| Experiment | Components | Mole Fr | Cum days | 28 | 56 | 84 | 112 | 112 | 224 |
|------------|--------------|--------------|----------|----|----|----|-----|-----|------------|
| | | | Cum Cost | 25 | 50 | 75 | 100 | 100 | \$ 100,000 |
| | | | | | 1 | 1 | 1 | 1 | 0 |
| Slimtube1 | CO2 | 100/0 | | 1 | | | | | |
| Slimtube2 | CO2/N2/o2 | 92.5/2.5/5 | | | 1 | | | | |
| Slimtube3 | co2/n2/o2/ar | 90/2/3/5 | | | | 1 | | | |
| Slimtube4 | co2/n2/o2/c1 | 94/1.5/1.5/3 | | | | | 1 | | |
| Slimtube5 | | | | | | | | 0 | |

Figure 40. Original Slimtube Program

However, the actual slimtube program was conducted entirely on binary mixtures. No multi-component impurity mixtures were tested using slimtubes because:

- Slimtube runs were carried out to measure the MMP for binary mixtures, which originally was planned to do with RBA measurements.
- Financial constraints.

The slimtube program and results are summarized in Table 14.

| Table 14. Summary of Slimtube Results | |
|---|-----------------|
| Experiment Parameters | Recovery |
| Pure CO₂ | |
| Slimtube at 2400 psi with 100% CO ₂ | 100% |
| Slimtube at 1800 psi with 100% CO ₂ | 100% |
| Slimtube at 1300 psi with 100% CO ₂ (suspect data, subsequently ignored) | 95% |
| Slimtube at 1100 psi with 100% CO ₂ | 76% |
| Slimtube at 900 psi with 100% CO ₂ | 68% |
| Slimtube at 500 psi with 100% CO ₂ | 54% |
| CO₂ with 5% N₂ | |
| Slimtube at 2900 psi with Gas (5% N ₂ /95% CO ₂) | 100% |
| Slimtube at 2400 psi with Gas (5% N ₂ /95% CO ₂) | 100% |
| Slimtube at 1800 psi with Gas (5% N ₂ /95% CO ₂) | 97% |
| Slimtube at 1300 psi with Gas (5% N ₂ /95% CO ₂) | 91% |
| CO₂ with 5% O₂ | |
| Slimtube at 2400 psi with Gas (95% CO ₂ /5% O ₂) | 100% |
| Slimtube at 1800 psi with Gas (95% CO ₂ /5% Ar) | 94.1% |
| Slimtube at 1300 psi with Gas (95% CO ₂ /5% H ₂) | 80% |
| CO₂ with 5% Ar | |

| | |
|---|-------|
| Slimtube at 2400 psi with Gas (95% CO ₂ /5% O ₂) | 100% |
| Slimtube at 1800 psi with Gas (95% CO ₂ /5% Ar) | 94.8% |
| Slimtube at 1300 psi with Gas (95% CO ₂ /5% H ₂) | 88.5% |
| CO₂ with 5% H₂ | |
| Slimtube at 2400 psi with Gas (95% CO ₂ /5% O ₂) | 100% |
| Slimtube at 1750 psi with Gas (95% CO ₂ /5% Ar) | 94.2% |

It is worth noting that most of the slimtube runs were completed at pressures below the BPP of the oil (2389 psi). When pressures are dropped below the BPP, gas evolves from the oil and two hydrocarbon phases are present. However, the procedure followed in the lab was to remove all of the evolved gas, so that a saturated oil sample was used in the slimtube run. This is considered a better procedure than to run the slimtube with both a gas and oil phase present in the slimtube.

The estimated MMPs for each of the gas mixtures, as well as the slope of the recovery factor slope below the MMP, are given in Table 15.

| Table 15. Summary of MMP and Recovery Slopes | | |
|---|-------------------|---|
| Gas Mixture | MMP (psi) | Recovery Factor Slope (% recovery/psi) |
| Pure CO₂ | 1755 | 0.0367 |
| CO₂/ N₂ | 2050 | 0.0120 |
| CO₂/ O₂ | 2009 | 0.0282 |
| CO₂/ Ar | 2213 | 0.0126 |
| CO₂/ H₂ | 2145 ¹ | 0.0147 |

¹ The MMP for the CO₂/H₂ mixture could not be estimated from the slimtube data alone, as was done for all other mixtures. It was estimated using a combination of RBA results (the ratio of MMP_{impure}/MMP_{pure}) and the MMP for pure CO₂. The recovery slope was calculated from a line drawn through the MMP CO₂/H₂ and the single slimtube run below the MMP.

The full comparison of MMP increases for the RBA results, slimtube results, and predicted by the correlations are shown in Table 16. Note that the correlation value for N₂ was estimated using a value for MF_i of 1.0 as explained below, rather than the default value shown by Emera and Sarma. The increase in MMP predicted by the correlation is within 5% to that measured from the slimtubes for all gases except H₂. The MF_i of H₂ was also adjusted as noted below to fit the experimental results.

| Table 16. Comparison of MMP increases | | | | | |
|--|----------------------------|---|---|----------------------------------|---|
| | Pure CO₂ | CO₂ with 5% N₂ | CO₂ with 5% O₂ | CO₂ with 5% Ar | CO₂ with 5% H₂ |
| MMP _{impure} /MMP _{pure} RBA | 1.0 | 1.23 | 1.26 | 1.12 | 1.22 |
| MMP _{impure} /MMP _{pure} Slimtube | 1.0 | 1.17 | 1.14 | 1.26 | |
| MMP _{impure} /MMP _{pure} from correlation | 1.0 | 1.21 | 1.2 | 1.28 | 0.99 |

No experimental data were gathered for methane, as there was not enough time, nor resources, to include methane in the experimental program. In the absence of experimental data, the defaults in the correlation were accepted for methane, and the same recovery slope as pure CO₂ was assumed.

4.6. Technical/Economic Model

All reservoirs are unique with respect to gas injection. There are many factors involved, including:

- oil composition;
- pressure;
- temperature;
- depth;
- aquifer and geomechanical limitations to increase pressure.

Due to the uniqueness of each reservoir a standard process is typically followed to conduct a technical and economic evaluation of CO₂ flooding. However, this process must be duplicated on almost every reservoir because of its unique properties and characteristics. It is detailed, extensive, and expensive, and includes the following steps:

1. Laboratory evaluation to determine the oil/CO₂ properties and the MMP;

2. Reservoir characterization and geo model construction;
3. Reservoir simulation to establish a production profile. This includes amount of oil produced, volumes of CO₂ injected and recycled, and the effects of the impurities on recovery. Ideally, this work is carried out in a compositional reservoir simulator which is able to rigorously account for compositional effects between the injected gas and oil.
4. An economic analysis based on cash flows, which accounts for capital outlays, production and injection profiles, operating costs, and prices.

Such a study entails months or years of work.

A simpler, and more general, approach to evaluate the economic impact of impurities in the CO₂ stream was required for this study. The steps involved in this general method are detailed below.

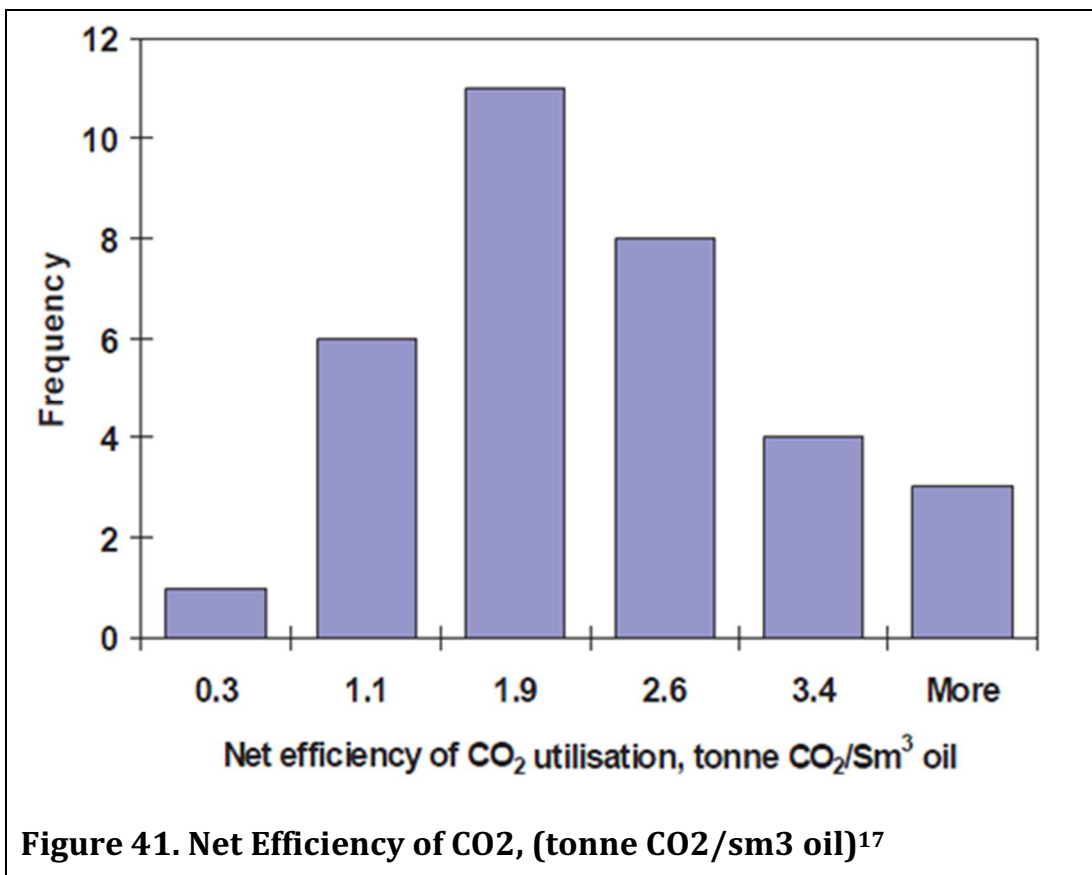
1. **MMP for pure CO₂.** Determine the MMP for pure CO₂. This is a user-defined variable with a default value of 1755 psi based on the MMP of the crude oil used in the experimental program.
2. **Change in MMP.** Determine the ratio of the MMP for the impure CO₂ stream compared to the MMP of pure CO₂ using the correlation of Emera and Sarma, and calculate the MMP_{impure} knowing the value for MMP_{pure}. However, based on the experimental program, certain modifications to the correlation were required. The method of Emera and Sarma includes a critical temperature Modification Factor, MF_i, for each component. Their default factors fit the experimental results well with the following exceptions:
 - N₂: the value of MF was changed to 1.0, from the default value of 1.9
 - H₂: the value of MF was changed to 10 to fit the increase in MMP with 5% H₂ in the CO₂ stream. The default value was 1.0. Theoretically, H₂ should have little to no effect on MMP because it is such a light molecule, and the correlations are based on weight percent of impurities. However, the experimental results from this study indicate it has a much larger impact than that predicted by theory.
3. **Change in recovery factor.** The recovery slopes determined from the slimtube experiments were included in a lookup table, so an impurity-weighted average value of recovery factor slope could be calculated from the user-specified rates for each industrial process. In the absence of data to say otherwise, this was considered a reasonable method to calculate a recovery slope for a multi-component mixture.

Calculate the recovery factor for impure CO₂ by calculating the intersection of the impurity-weighted average recovery factor slope and the MMP of pure CO₂. This process was previously shown schematically in Figure 38.
4. **Loss in reserves.** First, the reserves to be recovered through the injection of pure CO₂ must be estimated. The amount of CO₂ used for EOR over the life of the project and incremental oil volumes are linked in this analysis through a net CO₂ utilization factor. The net CO₂ utilization factor is the net volume of CO₂ injected in the reservoir divided by the

incremental barrels of oil recovered. Knowing the total volume of CO₂ injected over the life of the project, incremental oil volumes can be estimated using the net CO₂ utilization factor.

Two sources of statistical CO₂ utilization are shown in **Error! Reference source not found.** and Figure 42. The first is data based on experience mainly from the Permian Basin.¹⁷ The peak utilization frequency of 1.9 tonnes CO₂/bbl converts to 5.7 mcf/bbl.

Utilization factors were also calculated from data presented by Shaw and Bachu.¹⁸ The utilization data are presented in Figure 42 and show a 50% percentile value based on estimates for 10 Alberta reservoirs of 5.8 mcf/bbl, and an average of 6.3 mcf/bbl. This compares closely to the data from the Permian Basin.



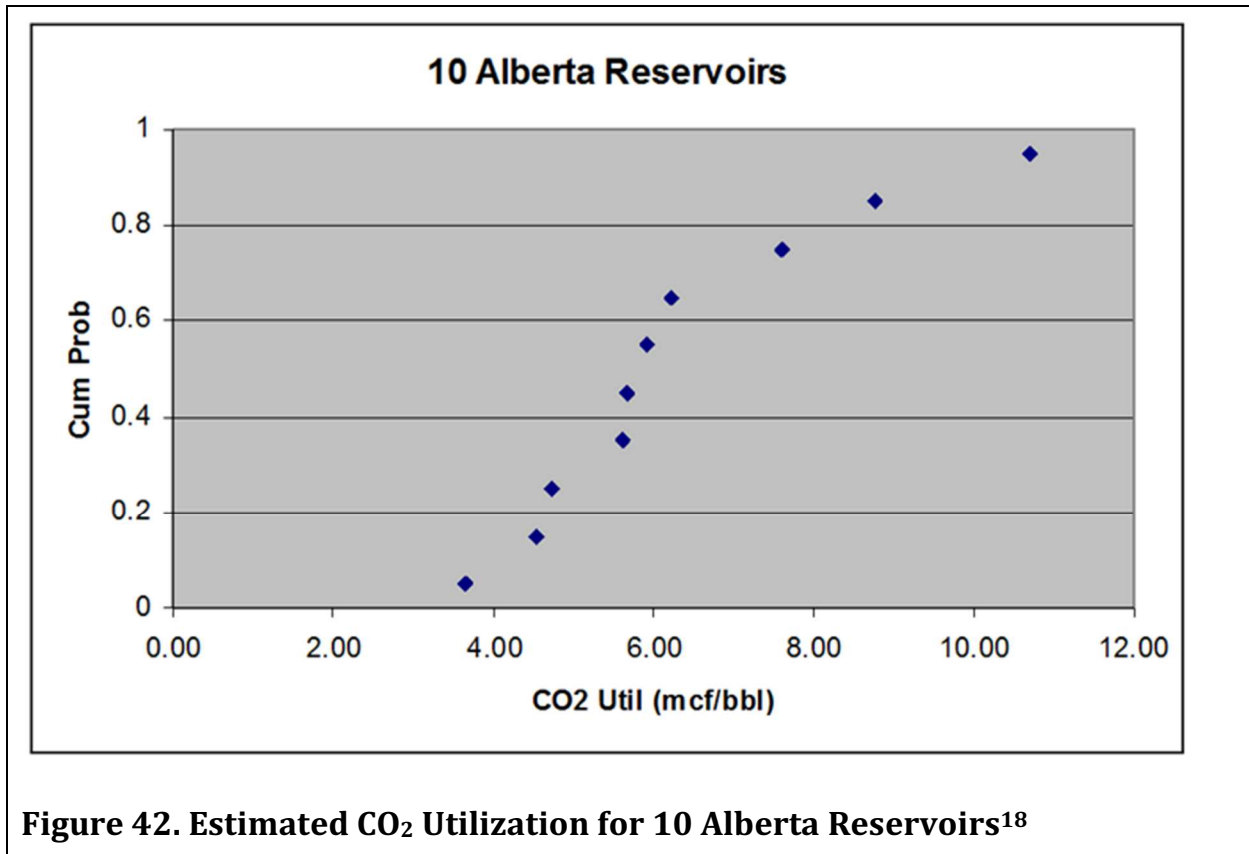


Figure 42. Estimated CO₂ Utilization for 10 Alberta Reservoirs¹⁸

A CO₂ utilization factor of 6 mcf/bbl was set as the default value in the Project technical economic model

The recovery factor for impure CO₂ injection is applied against the volumes of incremental oil to be recovered by injection of pure CO₂ to calculate the volumes of incremental oil recovered under injection of impure CO₂.

5. **Economic Impact.** Evaluate the economic impact of impurities on oil recovery through a user input profitability. Ideally, this would be based on a full technical and economic analysis, and would be a discounted profit, either before tax or after tax, divided by the incremental barrels of oil recovered by the project. Thus, for example, if a project has a discounted cash flow before tax of \$150 million and the incremental oil recovery due to the CO₂ project is 10 million barrels, the profitability would be \$15/bbl. This is the default value used in the Project technical-economic model.

Example calculations of the full methodology are shown in the following section.

4.6.1. Example Calculations of Economic Impact

The economic impact on recovery of injecting impure CO₂ stream is estimated as follows:

1. **Set CO₂ injection volumes.** The volume of injected gas is calculated based on the user-specified emissions coming from each industrial source, the user-specified fraction directed to EOR, and the default project life of 20 years. The volumes of pure CO₂ injected are assumed to be equal to the volumes coming from the industrial sources.
2. **CO₂ utilization factor.** The default CO₂ utilization factor is 6 mcf/bbl.
3. **Incremental oil volume (Pure CO₂).** Divide the injected CO₂ volume by the utilization factor to estimate the incremental oil recovery under injection of pure CO₂.
4. **Incremental oil volume (Impure CO₂).** The incremental recovery under impure CO₂ is equal to the ratio of the $RF_{\text{impure}} / RF_{\text{pure}}$. In the graphical example shown in Section 4.4.3, Figure 38, this is $78.8/98 = 0.804$. Thus, the incremental oil volume recovered under impure CO₂ is $0.804 * \text{the volume recovered under pure CO}_2$. The default recovery factor for pure CO₂ is assumed to be 1.0 in the technical/economic model.
5. **Loss in NPV.** Multiply the difference in incremental oil volumes by the profit/bbl to estimate the loss in NPV by injecting impure CO₂.

Example calculations using the recovery factors based on Figure 38 are shown below. Assumptions include:

- CO₂ injection rates of 100 million scf/d for 20 years (~ 1.9 MT per year)
- 6 mcf/bbl CO₂ utilization
- \$15 Discounted NPV per bbl of incremental oil
- All CO₂ directed to EOR

Oil Recovery under pure CO₂:

- Injected volume in 20 years = 100 million scf/d * 365 * 20 = 730 billion scf
- Incremental oil recovery = 730 billion scf / 6000 scf/bbl = 121.7 million bbl

Oil Recovery under impure CO₂

- 121.7 million bbl * $78.8/98 = 97.8$ million bbl

Loss in Value due to injection of impure CO₂

- $(121.7 - 97.8)$ million bbl * \$15 = \$358 million

4.7. Conclusions

1. A generalized approach was developed to estimate the economic impact on EOR projects of impurities in the CO₂ stream.
2. The MMP of pure CO₂ was estimated at 1755 psi for the Cardium oil used in this study.
3. The MMP measured for pure CO₂ using the RBA (3313 psia) was much higher than that predicted by correlations (average value of 1841 psi) and that measured from slimtube runs (1755 psi). The reasons for this are unknown, and further work would be required to

determine the reasons. The MMP measured from slimtube runs was taken as the definitive value.

4. MMP was measured on 4 out of the 6 impurities considered in the Alberta CO₂ Purity Project. Those tested were N₂, Ar, O₂, and H₂. Neither CO nor C₁ were tested. CO is a minor contaminant. C₁ is a common contaminant and well characterized, so it was assumed that the correlation would accurately predict its effects. Therefore, efforts were concentrated on the less studied contaminants.
5. The correlation proposed by Emera and Sarma was validated for the Cardium oil, but with the following changes to component Modification Factors (MF_i): N₂ from 1.9 to 1.0, H₂ from 1.0 to 10.0.
6. The effect of H₂ on MMP was much greater than that predicted by the correlation. The correlation is based on weight fractions of the individual components in the mixture, and because H₂ is such a light molecule, its effect is predicted to be negligible. However, 5% H₂ in the CO₂ was found by the RBA tests to increase the MMP by 22%.
7. The experimental findings have been included in the technical/economic model.
8. Future work should be directed towards obtaining experimental data for C₁, obtaining more data on H₂, and obtaining data on CO₂ with multiple impurities.

5. CO₂ Sequestration in Deep Saline Aquifers

(Edited summary)

Section author: Jean-Philippe Nicot, University of Texas

5.1.Phase 1 Outcomes

Despite some early work¹⁹²⁰, a literature review determined that very little experimental work and limited modeling work had been done to gauge the impact of impurities on geological systems. The potential impacts are of two types: (1) impacts on flow behavior of the CO₂ plume as described by Nicot et al.²¹ and controlling the whole system including the far field, and (2) near-field impacts because of geochemical reactions if reactive impurities, such as O₂, are injected (for example, Lu et al.²² It was also quickly determined that, unlike the pipeline transportation group, water is always a major component of the subsurface system and an unavoidable component of the gas phase. A similar reasoning led to the addition of methane that will also always be a component of the gas phase in most subsurface contexts. Favorable storage reservoir targets are found in large sedimentary basins that also host major hydrocarbon accumulations, translating into significant dissolved methane in the formation brines even miles away from the closest oil/gas reservoir (see for example, Buckley et al.²³)

5.2.Phase 2 Research Needs

Although there is a comfortable body of operational and field data on the modified behavior of a CO₂ stream with impurities, little systematic research has been done to strictly quantify the impacts of impurities, particularly because these CO₂ streams whose fate is geological sequestration either do not currently exist or are still uncommon. From a flow dynamic standpoint, the issue is rendered more complex by the fact that gas mixture behavior is non-linear and that multicomponent mixture behavior cannot be extrapolated from single-component or binary mixtures. There is a need to obtain experimental PVT data of binary and ternary mixtures at subsurface conditions (that is, typically at temperatures and pressures higher than that typical of pipe lines) to ensure that the generally complex fluid property modules used in compositional numerical models are somewhat accurate. A second need is to understand CO₂ plume behavior in the subsurface, plume size is a function of the gas composition and it impacts cost of sequestration. A third need is to assess the impact of reactive gases on the mineral grains (non-reactive gases such as N₂ and Ar impact only the flow dynamics), in particular O₂, which is not typically injected in the subsurface unlike some other reactive gases such as H₂S or SO₂.

5.3.Research Program

The research built on previous work done for the CCP3 program by Nicot and Solano²⁴, and by Nicot et al²⁵ that investigated the same issues. This report documents the general results delivered by the CCP3-funded project complemented by results from companion tasks specifically performed for ACPP. The overall tasks consisted in:

(1) Conducting a parametric study on impact of impurities on plume dynamics and rate and extent of trapping mechanisms in saline aquifers. The task was mostly a desktop numerical study performed with synthetic simplified cases and generalized models of actual reservoirs (Frio reservoir, Texas; Cranfield reservoir, Mississippi; and University of Calgary's WASP project (<http://www.ucalgary.ca/wasp/>)).

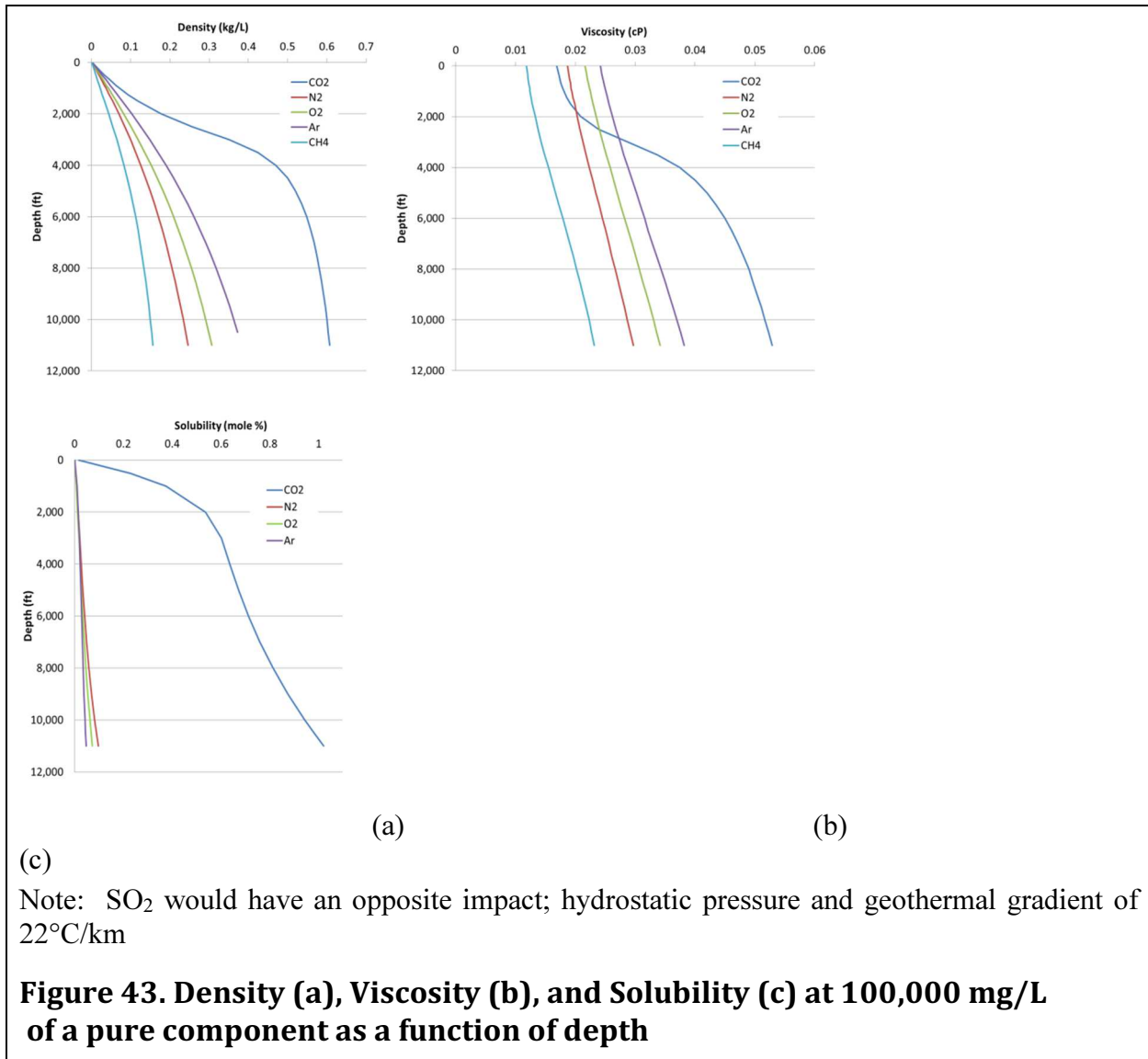
(2) Conducting rock-fluid interaction studies, including modeling and autoclave experiments. Experiments were done with samples from siliciclastic rocks (Offshore Miocene, Texas; Cranfield reservoir Tuscaloosa Formation, Mississippi; and Pembina Cardium Sands, Alberta) and from carbonates (Pembina Leduc carbonate, Alberta);

5.4. Research Outcomes

5.4.1. Plume Dynamics

Summary of Flow Dynamics Findings

The goal of this part of the study was to understand the impact of impurities (N_2 , O_2 , and Ar, to which was added CH_4 , ubiquitous in the subsurface in hydrocarbon provinces, often prime candidates for geological storage) on CO_2 plume dynamics, injectivity, and capacity. The study considered up to 15% volume for N_2 , 5% volume for O_2 , and 5% volume for Ar. Other gases such as CO, H_2 , and SOx, which could have non-negligible mole fractions, are not considered in this part of the study. The problem was approached through an extended desktop study using the numerical modeling tool (multiphase flow code CMG-GEM). In order to work with accurate PVT data (Peng-Robinson EOS), laboratory experiments were performed early in the study to access viscosity and density of the mixtures. CMG-GEM relies on many empirical mixing rules for density and viscosity calculations that need to be calibrated and tuned (Figure 43). In parallel, a comprehensive literature survey was undertaken to collect information on solubility of those various mixture components into the aqueous phase under various subsurface pressure, temperature, and salinity conditions. The differential partitioning of gas components in the aqueous phase impacts the gas phase composition. The work presented in this section does not include geochemical impact of impurities (reactivity of gas components with other components and with minerals). Overall, geochemical processes could affect near-field properties such as injectivity and well integrity whereas larger-scale regional impacts on plume dynamics are likely only an issue with significant mole fractions of non-condensable gases (including O_2). An important observation integral to understanding plume dynamics associated with impurities is that viscosity and density of mixtures are lower than that of neat CO_2 at the same temperature and pressure. Equally important to note, viscosity and density contrasts between mixtures and neat CO_2 decreases with depth.



The numerical models used grow in complexity from simple box-like generic models, to which heterogeneity is added in a second step, to more realistic models constructed from actual North-American locations. The objective was to reproduce end-members of aquifer architecture such as (1) clean homogeneous, medium permeability sand; (2) homogeneous sand/clay, and (3) heterogeneous sand with discontinuous shale partings and continuous baffles. Progressively more complex gas systems, binary, ternary, and beyond, were investigated. The results, normalized by results of the corresponding neat CO₂ case, draw on two metrics, time to hit the top and maximum longitudinal extent. These are contrasted for two depths “shallow” (~5,000 ft, ~60°C, 2500 psi, 100,000 mg/L) and “deep” (~10,000 ft, 125°C, 4500 psi, 180,000 mg/L). Because O₂, N₂, and Ar have similar properties and behavior, they impact the CO₂-dominated mixtures in a similar way, particularly at the concentration level of a couple percent molar and they can be merged in one

unique component with properties of N₂. However, the approximation deviates too much from the “truth” beyond a few percentage points.

Impurities impact density and viscosity of the CO₂-rich mixture. A lower density impacts CO₂ capacity not only because of the smaller fraction injected and space needed for storing impurities but also because of the generally lower density of the impurities at the same conditions. An approximate proxy for capacity change owing to impurities is given by the density ratio. The loss in capacity can be as high as >50% at very shallow depths (~3000 ft, CO₂ and 15% molar N₂) but the difference quickly decreases with depth. Similarly, mass injectivity, which can be represented by the proxy metric of density over viscosity ratio, also shows a decreased value at very shallow depths that quickly recovers with increasing depth.

In terms of plume shape and extent, the impact of impurities is again more marked at shallow depth where the contrast in density and viscosity with neat CO₂ is the largest. It decreases with depth. For example, about 4% mole fraction in a binary system suffices to increase plume length in “shallow” low-dip sloping layers by 25% whereas 9 to 15%, depending on the component, would be the case in a “deep” system. In all cases, plume extent is greater with impurities, however residual trapping occurs faster. This relationship holds for most systems regardless of heterogeneity and complexity. The contrast is most extreme in very simple systems whereas heterogeneity (assuming adequate operational choices) seems to dampen impacts of impurities. This presumably occurs because heterogeneity creates multiple tongues that attenuate the impact of impurities. It also suggests a trade-off between plume extent (area of review with risk of CO₂ leakage) and decreased risk owing to faster trapping. A larger plume translates into a larger area to inspect for leakage pathways such as faults and abandoned wells but a faster trapping translates into a shorter period of time to monitor the site.

Illustration of Key Flow Dynamics Findings

The general approach consisted of a parametric study and sensitivity analyses of a generic case and of three previously studied sites (two on the U.S. Gulf Coast and one in Alberta, Canada), modified slightly to meet the objectives of the study. Gas composition and range were estimated from various sources and before consensus was reached at ACPP (Table 17); see Nicot and Solano²⁴. Because of the lack of accurate data on viscosity and density, we performed 10 experiments (through an external vendor based in Houston, Texas) to tune EOS parameters for various CO₂ mixtures (incorporating CO₂, N₂, O₂, and Ar) at various temperatures (60, 80, and 100°C) and pressures (13.8, 27.6, and 41.4 MPa). We also developed binary interaction coefficients between components under a range of pressure (10–50 MPa), temperature (30–120°C), and salinity (0–200,000 mg/L) conditions through a comprehensive literature audit so as to model dissolution of the mixtures into the brine. We initially used a simple dual generic model: a shallow model reproducing conditions present at the Frio site (southeastern Texas) and a deep model reproducing conditions prevailing at Cranfield (western Mississippi). Both sites are in the U.S. Gulf Coast region and broadly representative of subsurface conditions elsewhere, but for analysis they were stripped of specific geometric properties, retaining only environmental

conditions: pressure, temperature, and salinity (Table 18). In order to focus on the processes of interest and not on specificities associated with an actual site, we developed a generic sloping aquifer and compared results of runs carried out using various CO₂ mixtures. Runs were performed using the CMG-GEM and CMG-WINPROP software packages. GEM is a compositional multiphase flow code that can accommodate multiple gas components and their interaction with a liquid phase. WINPROP is an allied module useful in determining and tuning equations of state.

| Table 17. Molar Composition of Base Cases | | | | |
|--|----------------------------|-----------------|-----------------|--|
| Component (mol %) | Neat CO₂ | Stream A | Stream C | Single component density at 1 atm and 21°C (kg/m³) |
| CO ₂ | 100 | 96 | 92 | 1.834 |
| N ₂ | — | 0.2 | 1 | 1.161 |
| O ₂ | — | 2.1 | 6.5 | 1.327 |
| Ar | — | 1.7 | 0.5 | 1.654 |
| CO | — | — | — | 1.162 |

| Table 18. Characteristics of Shallow and Deep Generic Models | | |
|---|------------------------------------|-------------------------------|
| Reservoir Property | Shallow Reservoir Case | Deep Reservoir Case |
| Model dimensions | 11,000 × 4660 × 300 m ³ | same |
| Number of cells x × y × z | 120 × 51 × 20 | same |
| Cell dimensions | 90 × 90 × 15 m ³ | same |
| Dip in x direction | 2° | same |
| Permeability /kv/kh / porosity | 300 md / 0.01 / 0.25 | same |
| Depth at top downdip | 1675 m | 3040 m |
| Initial pressure (equilibrium at time 0) | V.E. ~17.6 MPa at top downdip | V.E. ~32.4 MPa at top downdip |
| Temperature | 135°F | 257°F |
| Injection rate and period | 8.5 m ³ /s for 30 years | same |
| Maximum res. saturation | 0.30 | same |
| Boundary | No flow except updip (hydrostatic) | |
| Formation water TDS | ~100,000 mg/L | ~170,000 mg/L |
| Simulation period | 100 yr | same |

The only trapping mechanisms simulated in the model were dissolution and residual-phase mechanisms. Mineral-phase trapping on a meaningful scale is generally understood to require at least hundreds or thousands of years. Structural trapping—that is, trapping of CO₂ as would occur in oil and gas accumulations—was not included in the design of the generic model because structural trapping would be of negligible utility in explaining the interplay of all processes and is site specific. The generic model was large enough (11 km) for the CO₂ mixtures to be fully trapped as residual saturation before reaching the updip boundary, assuming an injection rate of 0.5 million tons of pure CO₂ or CO₂ mixture for 30 years and an additional stabilization time of 70 years (100 years total). Injection occurred at the downdip section of the lower third of the 300-m-thick reservoir (Figure 44). Results are to be understood relative to one another, in particular relative to the base cases, because of numerical and gridding issues. For example, in homogeneous models, plume extent is a function partly of cell size but mostly of cell height (Thibeau and Dutin²⁶); these authors investigated the largest cell thickness that would model CO₂ dissolution correctly in their model and concluded that it is <0.1 m). Scaling the plume extent from various runs to the pure CO₂ base case minimizes this effect.

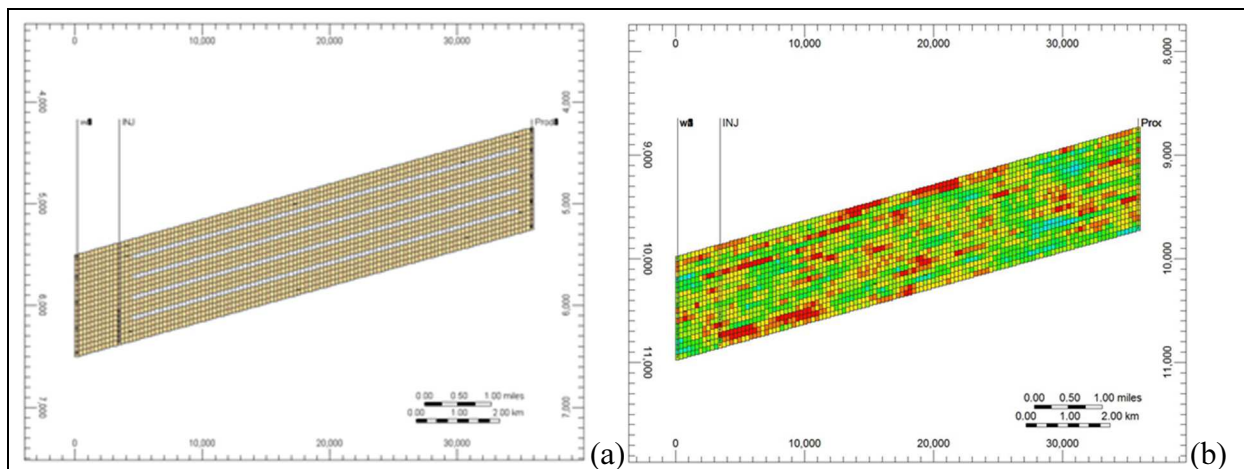


Figure 44. Cross Section of Generic Model Displaying Homogeneous Field with baffles (a) and heterogeneous permeability field (b).

The metrics used to measure impact on storage consisted of (1) time for the plume to reach the top and, more important, (2) extent of the plume at a given time or when all of the injected CO₂ mixture had been immobilized, and (3) time until all CO₂ mixture was immobilized (Figure 46). After treating the homogeneous case, we developed reservoir models encompassing a range of heterogeneity: (1) we handled heterogeneity in a simplistic way by adding four baffles with no porosity, parallel to the formation top and bottom, just upstream of the injection well and short of a few cells, all the way up to the updip boundary and across the whole width of the model (Figure

44a); (2) we obtained multiple heterogeneous fields through permeability generators (Figure 44b); and (3) we used models from actual sites.

First, we estimated static capacity, which is especially relevant to the case of structural traps because it relates to the volume occupied by the mixture in the subsurface. Comparison of densities as a function of depth allows for a first-order comparison of capacities. Second, we examined dynamic capacity. Results are consistent with that of a previous IEAGHG study^{19 20}. These documents addressed topics very similar to those discussed here. They focused on the capacity issues and reported that non-condensables such as N₂, O₂, and Ar impact capacity and that the impact is maximal at a certain pressure under a given temperature. Impurities impact static capacity by causing variations in density and viscosity of the CO₂-rich mixture. A lower density impacts CO₂ capacity not only because of the smaller fraction of CO₂ that can be injected and space taken up by impurities, but also because of the generally lower density of the impurities under the same conditions. An approximate proxy for capacity change owing to impurities is provided by the density ratio. The loss of capacity can be >50% at shallow depths (~3000 ft, CO₂ and 15% molar N₂) (Figure 45), but the difference quickly decreases with depth. Similarly, mass injectivity, which measures how much CO₂ can be injected (and which can be represented by the proxy metric of the density:viscosity ratio), also exhibits a value that decreases at shallow depths but recovers with increasing depth.

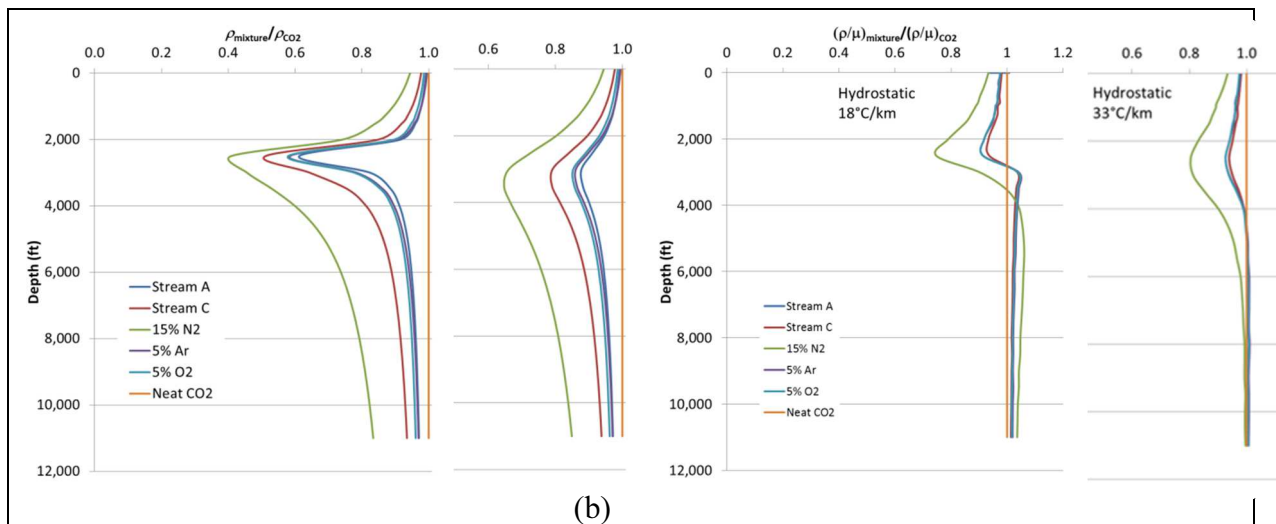


Figure 45. Mixture Density (a) and Density to Viscosity Relative to Neat CO₂ (b) as a function of depth; hydrostatic conditions and geothermal gradient of 18°C/km and 33°C/km

Dynamic reservoir simulations revealed that, following the pattern of static capacity and for the same reasons, impurities impact CO₂ plume shape (rate of vertical ascent and lateral extent) more

markedly at shallow depths where the contrast in density and viscosity with pure CO₂ is at its largest. For example, a 4% mole fraction impurity in a binary system is sufficient to increase plume length in ‘shallow’ low-dip sloping layers by 25%, whereas a mole fraction of 9 to 15%, depending on the component, is needed to create the same impact in a ‘deep’ system (Figure 47). Note that pure-CO₂ plume extent is larger at depth than in the shallow case, but that the difference between streams of pure CO₂ and CO₂ with impurities is smaller in the deep model.

In all cases, plume extent is greater when impurities are present, although residual trapping occurs more rapidly. This is generally the case regardless of reservoir heterogeneity and complexity, although heterogeneity tends to moderate the impact of impurities on plume extent because of the multiplicity of smaller plumes (Table 19, see Nicot and Solano²⁴ for details). Note that heterogeneity tends to increase plume extent because although CO₂ favors higher-permeability streaks, the contrast between pure CO₂ and CO₂ with impurities is smaller. Overall, a trade-off occurs between larger plume lateral extent owing to the presence of impurities and decreased risk owing to faster trapping (pressure management).

| Table 19. Comparison of Stream A, Stream C, and Neat CO₂ Plume Extent (base case) in various conditions of heterogeneity (shallow case) | | | | | | | |
|---|----------------|-----------------------|---------------|---------------|---------------|----------------|----------------|
| (ft) | Uniform | w/ Baffles | Real#7 | Real#8 | Real#9 | Real#10 | Real#13 |
| Neat CO ₂ | 9,300 | 8,400 | 10,500 | 6,900 | 5,100 | 5,100 | 7,200 |
| Stream A | 11,400 | 9,300 | 15,300 | 7,200 | 5,400 | 5,100 | 7,800 |
| Stream C | 14,400 | 10,800 | 19,800 | 7,500 | 5,400 | 6,900 | 7,800 |
| A / neat ratio | 1.23 | 1.11 | 1.46 | 1.04 | 1.06 | 1.00 | 1.08 |
| C / neat ratio | 1.55 | 1.29 | 1.89 | 1.09 | 1.06 | 1.35 | 1.08 |

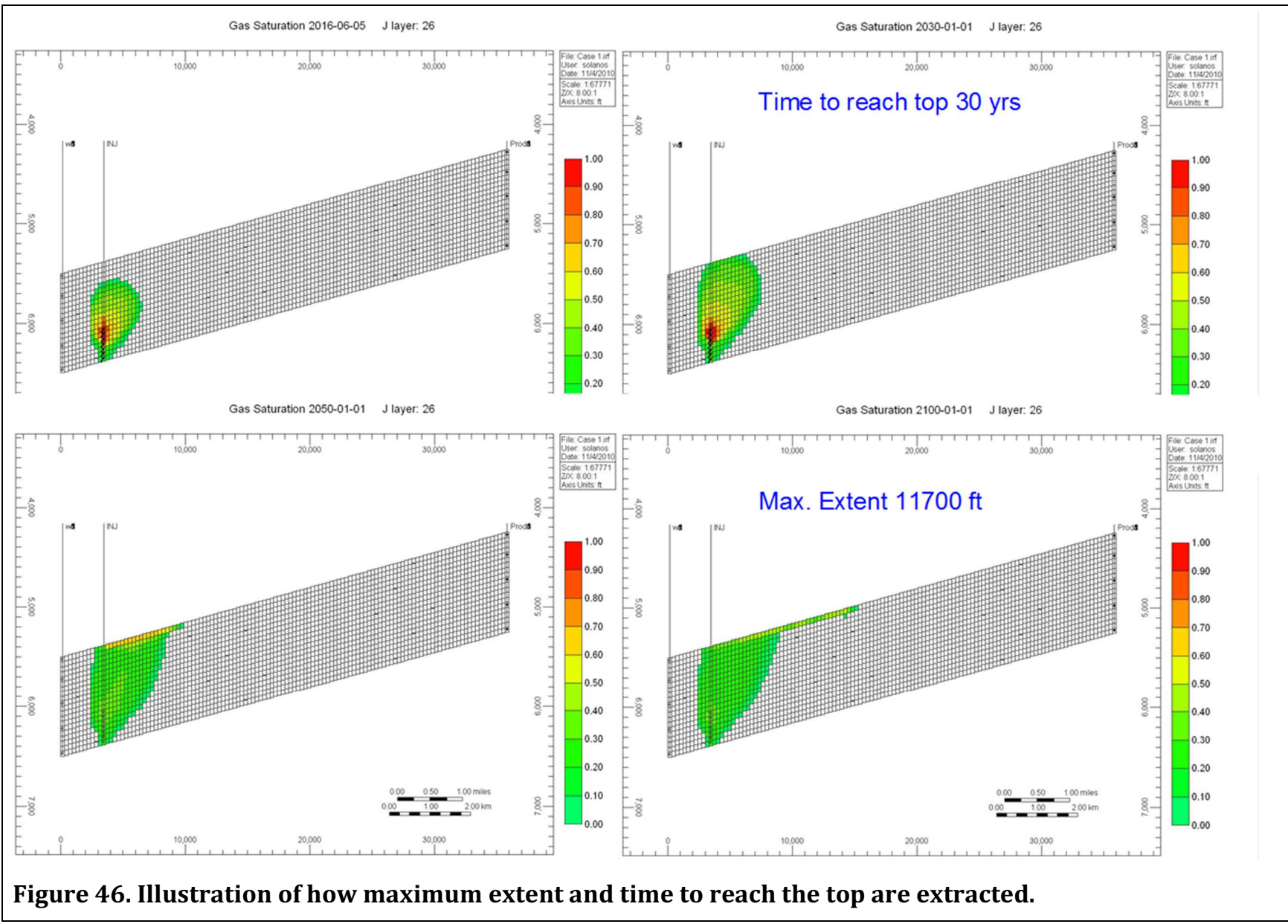
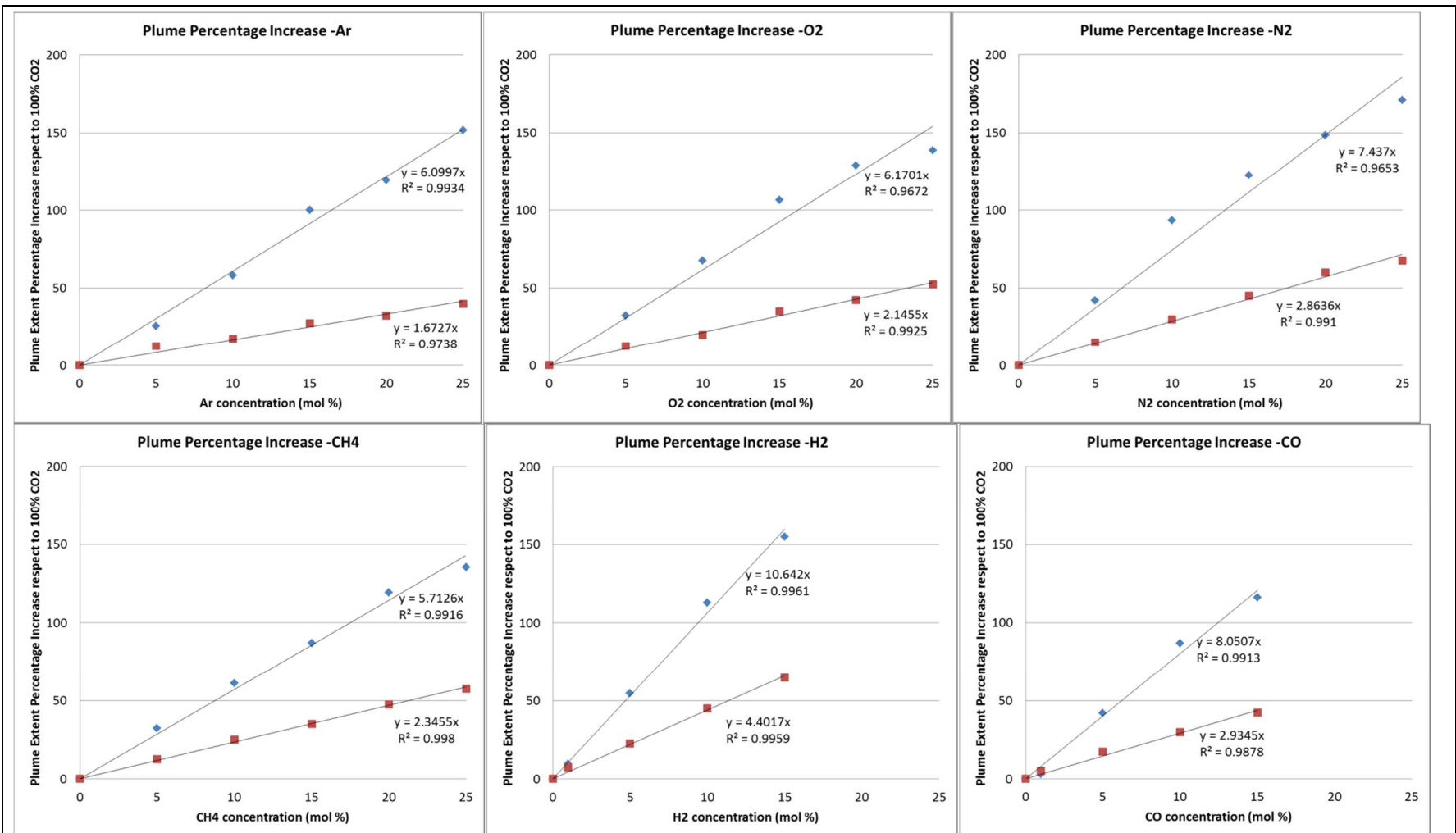


Figure 46. Illustration of how maximum extent and time to reach the top are extracted.



Note: Vertical axis displays additional extent; that is, 100% means a doubling of plume length. Linear fitting by forcing straight line through origin.

Figure 47. Plume-Extent-Increase for Binary CO₂ Systems vs. Pure CO₂ Plume Extent 100 years after start of injection for N₂, Ar, O₂, CH₄, CO, and H₂. Horizontal axis represents impurity molar-fraction range (0–25%)

Wabamun Area, Alberta Case Study

In this section, we describe one of the models used in the simulations to derive the results presented earlier. It was developed within the framework of the WASP project (<http://www.ucalgary.ca/wasp/>). All information about the site was downloaded from a data repository located at the University of Calgary, Alberta, Canada. The focus is on the saline aquifer of the Nisku formation of Devonian age. The Nisku aquifer is located in the Wabamun Lake Area, part of the Western Canada Sedimentary Basin. The formation is a gently dipping carbonate ramp belonging to the Devonian Winterburn Group. The succession consists of mainly carbonate and evaporitic strata with few intervening shales (Bennion and Bachu²⁷). Grid distribution was exported from Petrel as well as three permeability and porosity realizations. Additional reservoir and fluid properties were taken from the initial Eclipse 100 files with corresponding modifications to convert the Eclipse black oil model into a GEM compositional model. Table 20 contains a description of the current Nisku aquifer reservoir model. Figure 48 shows a 3D view of reservoir depth while Figure 49 shows cross-sections of permeability and rock types. For consistency with the other models, the number of injector wells in the modified Nisku/carbonate compositional model has been reduced to one down-dip injector with an injection rate equivalent to 1 Mton/yr of CO₂. Boundary conditions are no-flow in all directions. The total injection time is 30 years and monitoring takes place for 1000 years.

| Table 20. Base-case characteristics of the Canadian Carbonate model | |
|--|---|
| Property | Value |
| Model length | 96,000 m (315,000 ft) |
| Model width | 60,500 m (198,500 ft) |
| Model thickness | variable |
| Number of cells x × y × z | 122x193x30 |
| Average dip | 0.6° |
| Average permeability | 28 mD |
| Average porosity | 5 % |
| Rock compressibility | $6.9 \times 10^{-7} \text{ kPa}^{-1}$ ($2.1 \times 10^{-5} \text{ psi}^{-1}$) |
| Vertical permeability anisotropy (kv/kh) | 0.1 |
| Origin (cell 1,1,1) | Top southernmost cell |
| Max and min depth | 1,884 and 823 m (6181 and 2700 ft) |
| Fracture pressure | 40,000 kPa (5800 psi) |
| Initial pressure | 10,000 kPa (1450 psi) |
| Temperature | 60 °C (140°F) |
| Injection rate | 1.5 MMSCMD |
| Hysteresis | on |
| Formation water TDS | ~190,000 mg/L |
| Maximum res. saturation | $0.2 < S_{grmax} < 0.35$ |
| Injection period | 30 yr |
| Simulation period | 1000 yr |

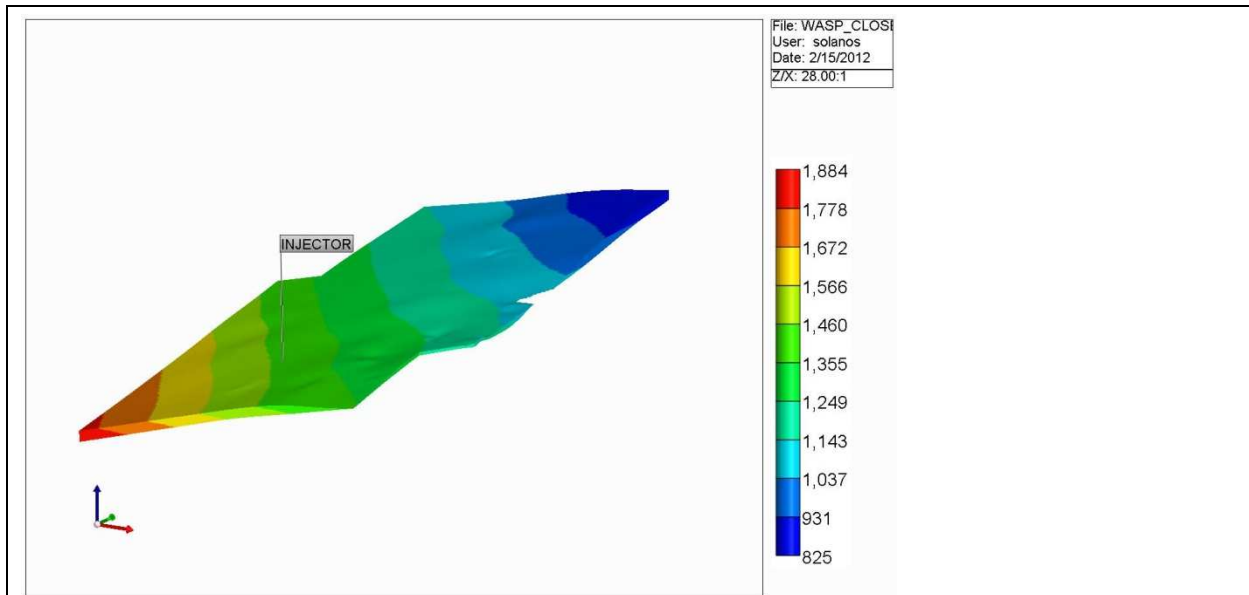


Figure 48. 3D view of the Carbonate Reservoir Model Showing Cell Depth

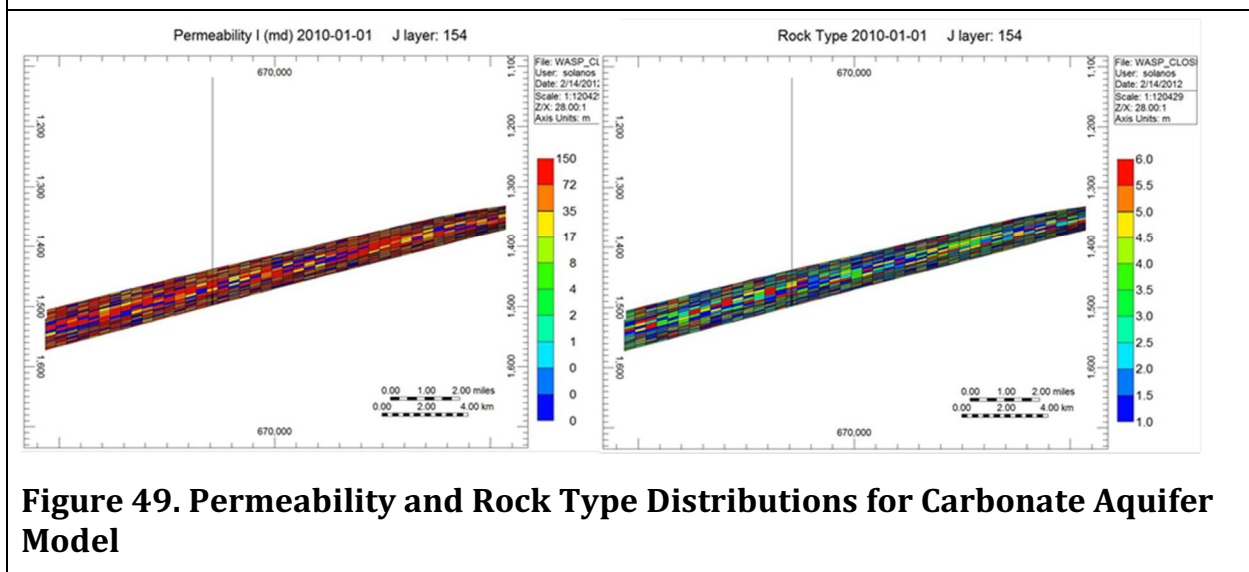
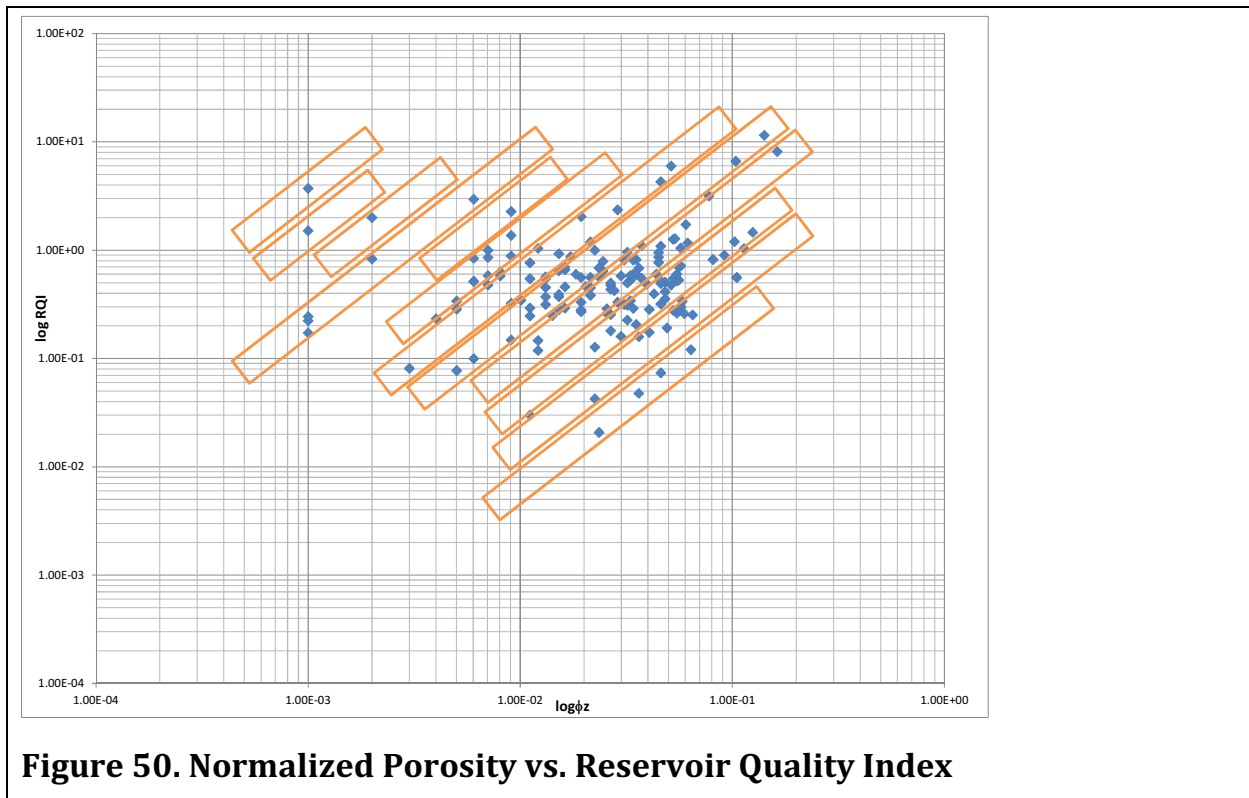


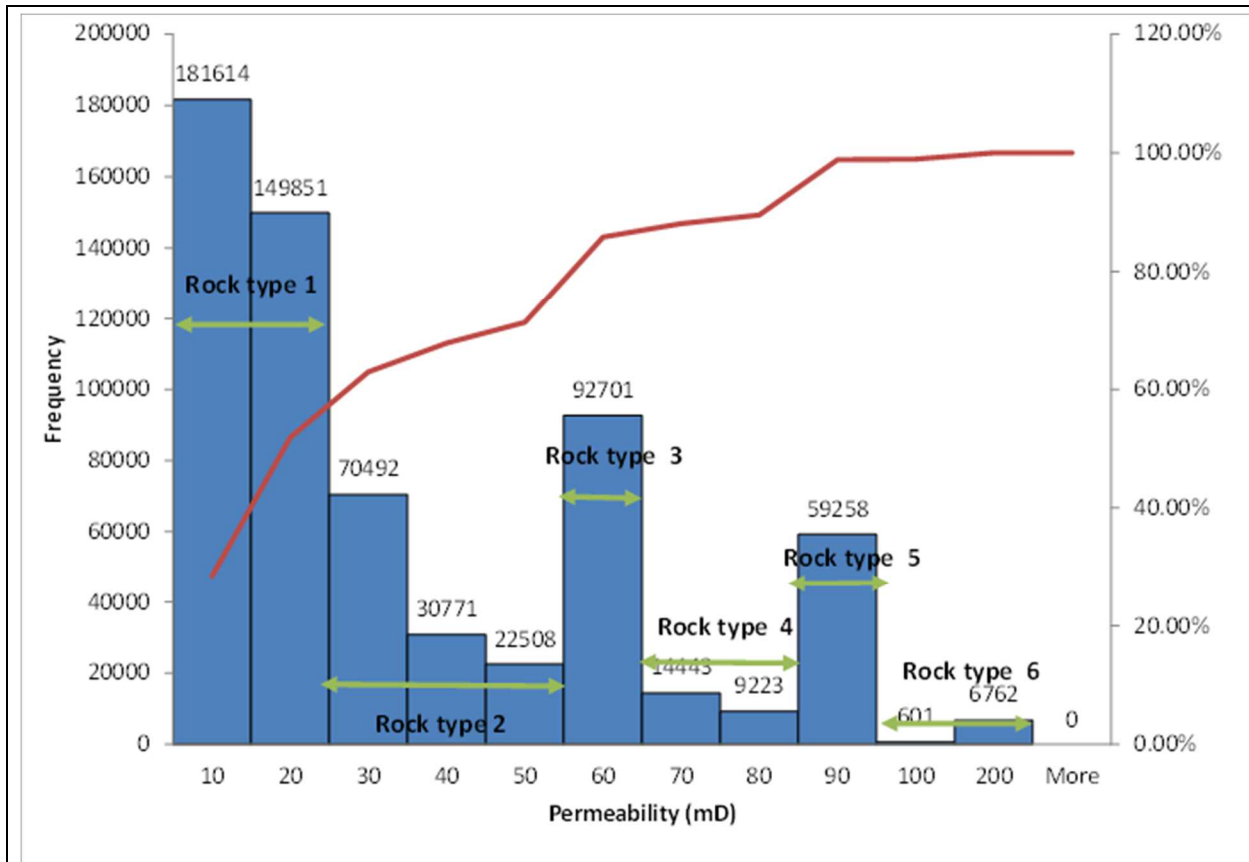
Figure 49. Permeability and Rock Type Distributions for Carbonate Aquifer Model

A major interest to this study was to investigate the impact of heterogeneity on behavior of plume of impure CO₂. In this Alberta model we add an additional level of complexity by considering multiple rock types, each with their own relative permeability characteristics. At least 12 rock types can be identified from the normalized porosity (ϕ_z) vs. reservoir quality index (RQI) plot (Figure 50). The equation below yields a straight line on a log-log plot of RQI vs. ϕ_z with a unit slope. Samples with different flow zone indicator (FZI) values lie on other parallel lines while samples lying on the same straight line have similar pore throat characteristics and, therefore, represent a flow unit (Tiab and Donaldson²⁸) or areas with similar flow properties.

$$\log RQI = \log \phi_z + \log FZI$$

According to Tiab and Donaldson²⁸ straight lines with slopes equal to unity are to be expected primarily in clean sandstones. Because of the similarity in distribution and movement of fluids within clastic and carbonate rock having intercrystalline-intergranular porosity, this zoning process can be directly applied to these reservoir systems. This process is, however, not applicable to carbonate reservoirs with vugular solution channels and/or fractures. Choice of the number of rock types to be used in the model is guided by (1) the flow unit analysis, and (2) permeability and porosity distributions from the initial Petrel model. Based on the permeability frequency distribution observed in realization #1 (Figure 51), a total of six rock types were identified within the following permeability ranges: <20 mD, 20-60 mD, 60-70 mD, 70-90 mD, 90-100 mD and > 100 mD. Because of the importance of accurate relative permeability curves to precisely model the process of CO₂ residual trapping, a literature review on carbonate rocks saturation functions and rock properties was conducted for different carbonate formations to ensure that results are representative of carbonate rocks. The purpose of the rock-type analysis and relative permeability literature review was to collect enough information to accurately account for reservoir heterogeneity typical of carbonate formations in the simulation model. PVT data input for this model was modified from the Frio formation model taking into account Nisku's salinity of 190,000 mg/L.





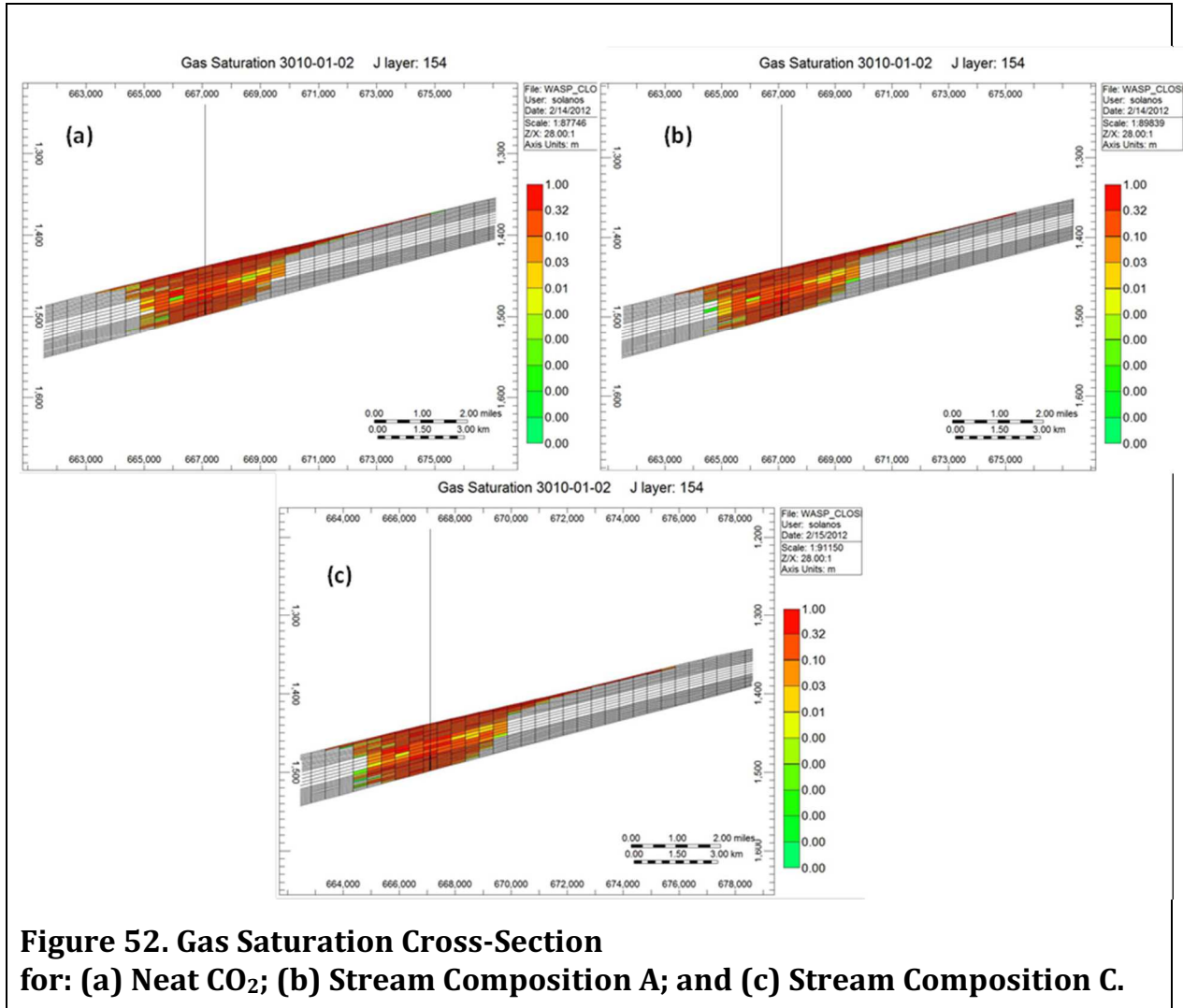
Note: Realization #1 from the WASP dataset, 706,380 gridblocks

Figure 51. Permeability Histogram from Downloaded Petrel Model for Carbonate Aquifer

The three different stream compositions are considered: neat CO₂, stream A (CO₂-96%; N₂-0.2%; O₂-2.1%; Ar-1.7%) and stream C (CO₂-92%, N₂-1%, O₂-6.5%, Ar-0.5%) (see Table 17). Gas saturation cross-sectional views for these three cases after 1000 yr are shown in Figure 52. As observed in previous results, the plume migrates a larger distance in the case of injection stream C whereas the neat CO₂ and stream A cases show similar results. Plume extent in the stream C case exhibits a 6.25% increase after 1000 yr. respect to the neat CO₂ and stream A cases (Figure 53b). Time to hit the top for the neat CO₂, stream A and stream C cases has the same value of 1.5 yr (Figure 53c).

In addition to the results for stream compositions A and C, Figure 54, Figure 55 and Figure 56 show the effect of increasing mole fraction for a single component on plume extent and time to hit the top. Impurity composition varies from 5% to 25% mole fraction. As observed in previous studies, the smaller impurity concentration (5%) displays a small change in plume extent relative to the neat CO₂ base case. At low impurity concentration, time to hit the top remains the same for all instances. As the impurity concentration increases, the divergence of the neat CO₂ case in both

metrics becomes more significant especially for the CO₂-N₂ and CO₂-O₂ cases. This behavior is entirely consistent with the results observed in the generic models and the Frio and Cranfield models.



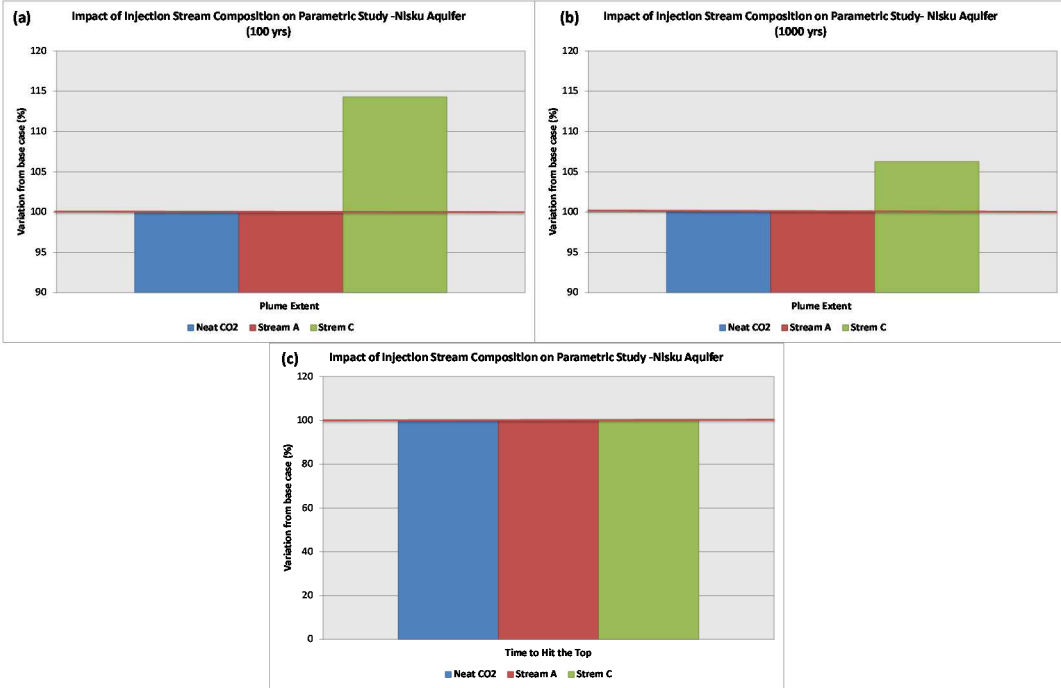


Figure 53. Impact on Injection Stream Composition on Parametric Study for Nisku Aquifer
(a) plume extent at 100 yr; (b) plume extent at 1000 yr; and (c) time to hit the top

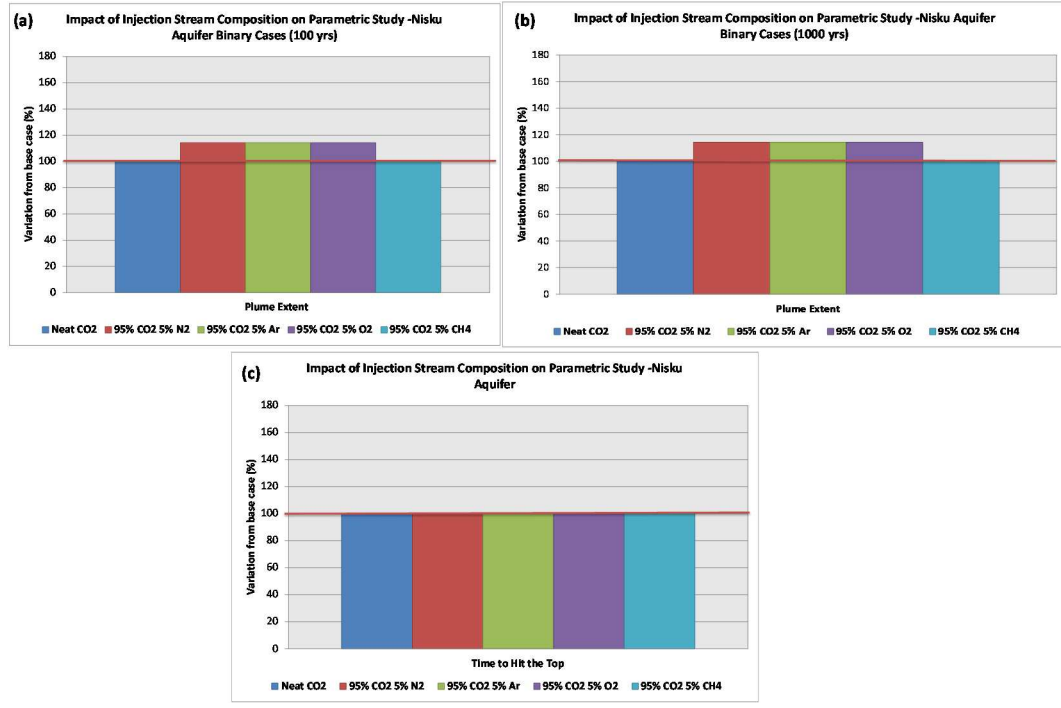


Figure 54. Impact on Injection Stream Composition (95% CO₂) for Carbonate Aquifer
(a) plume extent at 100 yr; (b) plume extent at 1000 yr; and (c) time to hit the top

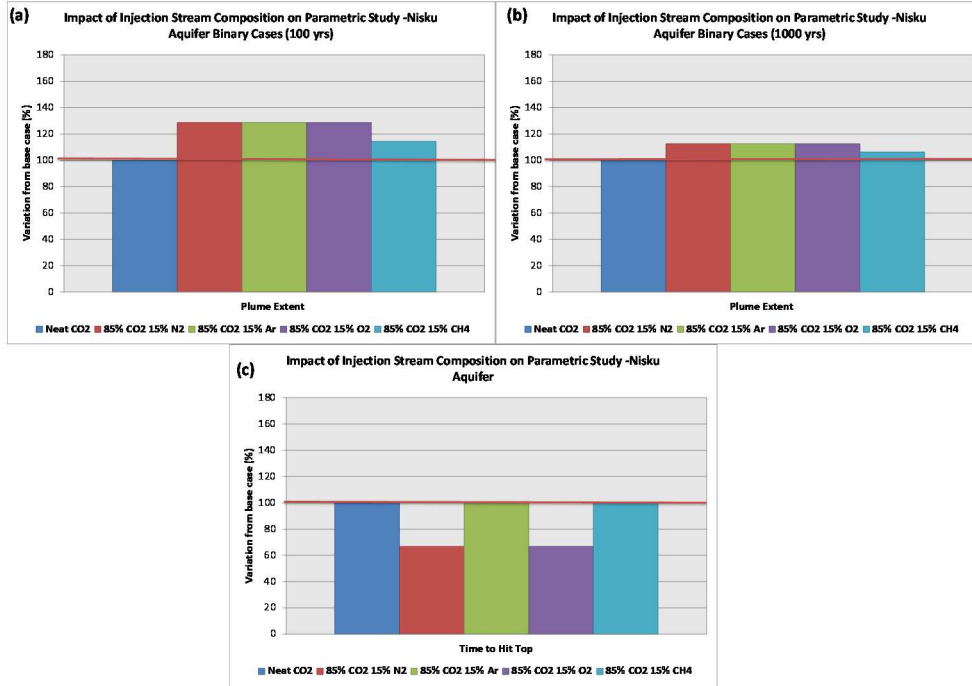


Figure 55. Impact on Injection Stream Composition (85% CO₂) for Carbonate Aquifer
(a) plume extent at 100 yr; (b) plume extent at 1000 yr; and (c) time to hit the top

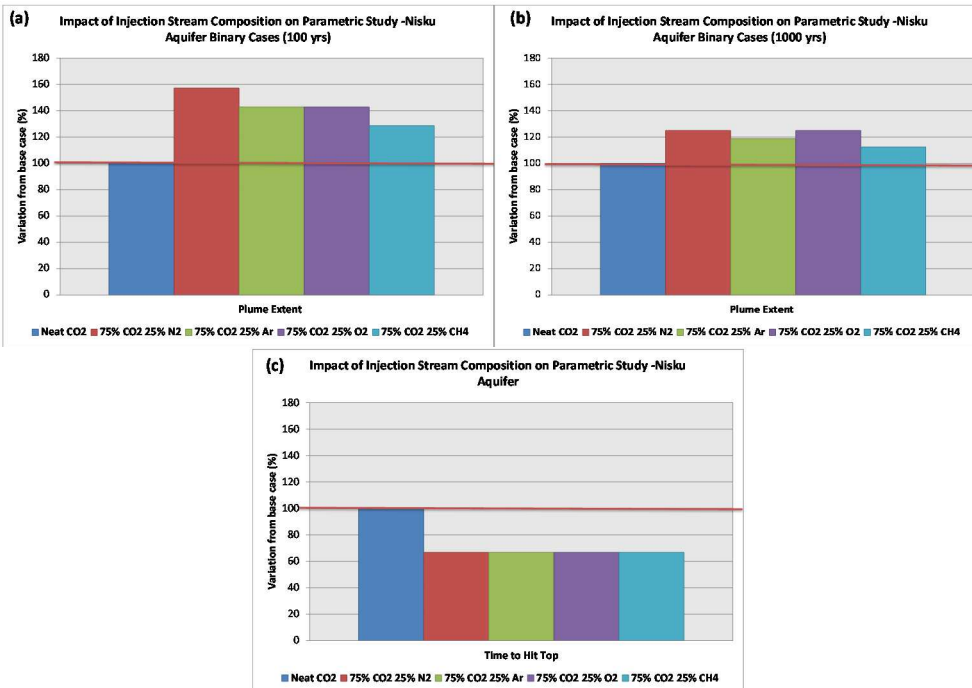


Figure 56. Impact on Injection Stream Composition (75% CO₂) for Carbonate Aquifer
(a) plume extent at 100 yr; (b) plume extent at 1000 yr; and (c) time to hit the top

5.4.2. Geochemistry

The following sections presents (1) a summary of the geochemical analysis of siliclastic rocks with a detailed analysis of the results related to the Cardium samples, (2) a summary of geochemical analysis of carbonate rocks, and (3) a summary of the acid species desktop study.

The geochemical issue is approached through laboratory autoclave experiments coupled with geochemical numerical modeling. The autoclave consists of a 250-ml reactor able to sustain temperatures as high as 150°C and pressures as high as 400 bars, that is, conditions seen in reservoirs up to a depth of 12,000 ft. A computer automatically regulates pressure and temperature and the system also allows for water sampling during the experiments. Typically 10 to 15 samples of the solution were taken during the 10-to-15 day course of each of the experiments. Rock samples were exposed to a supercritical mixture of CO₂ and O₂ (in general 3.5% molar) or to pure supercritical CO₂ that filled about half of the reactor cell. The other half consisted in a single core fragment or a few large fragments (~8g total) submerged into ~140 ml of synthetic brine (~1.88 mol NaCl corresponding to a TDS of 100,000-110,000 mg/L).

Summary of Geochemistry Findings – Siliclastic Rocks

The study analyzed three clastic rock samples: (1) a “dirty sandstone” of Miocene age from a deep well in the shallow offshore off the Texas coast; (2) a relatively clean sandstone from the Cardium Formation of Cretaceous age from Alberta; (3) a chlorite-rich sandstone from the Tuscaloosa Formation in Mississippi originating from the Cranfield reservoir. Composition of the samples is presented in Table 21. More details are provided in Lu et al²².

| Table 21. Summary of Sample Mineralogical Composition | | | |
|--|---|---|---|
| | Offshore Miocene, TX Well OCS-G-3733 Depth 9205 ft | Cardium Sands, AB Well 14-13-048-07W5 Depth 1,458-62 m | Cranfield, MS Tuscaloosa Formation Well CFU31F-3 Depth 10,476.6 ft |
| Quartz | 43.5% | 75.5% | 66.9% |
| Calcite | 11.8% | | |
| Siderite | | 1% | |
| Microcline | 15.2% | 4.2% | |
| Albite | 18.4% | 2.5% | 1.8% |
| Chlorite | | | 20.2% |
| Kaolinite | 6.2% | 10.4% | 7.3% |

| | | | |
|---------|---------|----------|----------------|
| Illite | 5.0% | 6.5% | 2.0% |
| Pyrite | Trace++ | Trace+++ | Trace (barely) |
| Anatase | | | 1.8% |
| Total | 100.1% | 100.1% | 100% |

In addition to quartz, the Miocene sample is dominated by calcite (11.8%) and feldspars (31.6%), the Cardium sample is dominated by clays (16.9%) with some feldspar (6.7%) and siderite (~1%), and the Cranfield sample is dominated by chlorite (20.2%) with some clays (9.3%). Both the Miocene and Cardium samples show evidence of not uncommon pyrite. The “dirty sandstone” Miocene sample allows for investigating carbonate behavior with and without O₂ whereas the relatively clean and non-reactive Cardium sample is a good candidate to investigate feldspar behavior without the overprint of carbonates. The Cranfield sample with abundant clay minerals dominated by chlorite is even less reactive vis-à-vis CO₂. Minerals sensitive to the presence of O₂ are pyrite (present in the Miocene and Cardium samples), siderite (present in the Cardium sample), and chlorite (abundant in the Cranfield sample). They all contain ferrous iron-bearing minerals.

We performed 19 autoclave experiments varying some parameters but only 10 are thoroughly described. They are displayed in the matrix of Table 22. Core segments with pre- and post- reaction rocks were submitted to petrographic analyses (X-ray diffraction –XRD, scanning electron microscope –SEM, and energy dispersive X-ray spectroscopy –EDS) and chemical analyses (TDS, anions, cations, trace elements).

| Table 22. Summary of Geochemical Runs | | | | |
|--|----------------------------------|-------------|----------------------------|--------------|
| | | 70°C | 100°C | 130°C |
| Offshore Miocene | CO ₂ | √ D | √ L (B) | √ H |
| | CO ₂ + O ₂ | √ R | √ S | |
| Cardium Sands | CO ₂ | √ K | √ J | |
| | CO ₂ + O ₂ | √ N | | |
| Cranfield | CO ₂ | √ P | | |
| | CO ₂ + O ₂ | √ O | | |

Note: Letters correspond to individual runs.

The offshore Miocene samples showed dissolution of carbonate (Ca and Mg increase) as well as of feldspars (Ca and K increase, Na concentrations are irrelevant because experiments are done with a NaCl brine). Feldspar dissolution is more intense when O₂ is present. Kaolinite is presumed

to form in both cases. The Cardium samples displayed deep attack of carbonates and of some feldspars with kaolinite formation and perhaps very minor authigenic illite. Pyrite and siderite are degraded when O₂ is added and FeOx species precipitate. The Cranfield samples have limited reactivity when exposed to pure CO₂ as they contain little carbonates. When O₂ is added, some chlorite is degraded and FeOx deposits can be observed as well as formation of some authigenic clays. Those qualitative observations were confirmed by geochemical modeling which was able to reproduce them.

In terms of release rates, results confirmed well-known results and delivered new observations. In pure-CO₂ cases carbonates were observed to dissolve quickly with a sharp increase in Ca, Mg, and other elements typically present in calcite. Calcite solubility was also observed to decrease with increasing temperature (i.e., reverse solubility). As expected, feldspars showed an increase in solubility with increasing temperature whereas clays, including chlorite, remained unreacted. Adding O₂, however, brought in interesting observations, pyrite framboids were clearly degraded, and thus added H⁺ ions to the system with consequent increased carbonate dissolution. The siderite (Cardium sample) is another source of ferrous iron. Both pyrite and siderite attack led to deposition of FeOx on mineral surfaces. Chlorite could also be an important source of ferrous iron but it is mostly stable unless pH drops very low. Such a case could happen if pyrite is present at a few percent level and lack of pH-buffering capacity through carbonates. Some chlorite alteration was seen in the Cranfield sample. Feldspar dissolution is enhanced in the presence of O₂ but in an indirect way, though pyrite oxidation and drop in pH. Overall the additional impact of a few percent O₂ when comparing samples reacted with pure CO₂ and with a CO₂+ O₂ mixture is limited.

Although the following results need to be confirmed by column (coreflood or flow) experiments, the reactive transport modeling suggests that porosity changes due to mineral reactions in siliciclastic material is minor and that mineral precipitation is unlikely to impact fluid flow. Overall, it does not seem that a few percent O₂ in the CO₂ stream has much impact beyond the impact of neat CO₂. The analysis focuses on the differences between pure CO₂ and CO₂+O₂ mixtures systems at different temperatures. An increase in temperature, with no surprise, led to an observed increase in release rates from silicates. O₂ has an impact if there is (1) redox-sensitive mineral species and (2) ferrous iron-bearing minerals (pyrite, chlorite, siderite, ankerite, ferroan dolomite or calcite, maybe glauconite which contains mostly ferric Fe but some ferrous Fe too). The pH drop attending CO₂ injection may be mitigated or reduced by buffering species, such as carbonates or to a lesser extent through dissolution of other species such as feldspars. Once reduced species have been mobilized and are in solution, O₂ can oxidize them. A clear example is siderite or pyrite dissolution with iron hydroxides and allied species (FeOx) precipitating. Overall the release rates, although variable, are very fast with asymptotic behavior reached in a few days. Clearly this is related to the experimental setup, columns experiments or field observations will likely reveal a much longer time frame for completion of the reactions. Batch experiments are typically rate-controlled but reactions taking place in column, and especially, field tests are generally diffusion-controlled, a much slower control.

Summary of Geochemistry Findings – Carbonate Rocks

This section focuses on a single carbonate rock coming from the Pembina oil field in Alberta: the Redwater Leduc limestone. The limestone is dominated by calcite (98.8%) and only contains small amounts of other minerals, such as dolomite (0.5%), quartz (0.4%) and illite (0.3%). The study follows the same methodology as described for siliciclastic rocks. Core segments with pre- and post-reaction rocks were submitted to petrographic analyses (X-ray diffraction – XRD, scanning electron microscope – SEM, and energy dispersive X-ray spectroscopy – EDS) and chemical analyses (TDS, anions, cations, and trace elements). We performed three autoclave experiments, all of them at 200 bars: two consisted in exposing the core fragments to pure CO₂ at 70°C and at 100°C and a third one exposed the core fragments to a CO₂ + O₂ (3.5%) mixture at 70°C.

SEM observations of unreacted and reacted samples with CO₂ showed that the carbonate grains dissolved unevenly with rough grain surfaces and breakage areas being the preferred dissolution sites. The addition of O₂ does not change the overall results, only that it somewhat altered the details of the dissolution pattern. This particular sample did not contain pyrite or another reduced mineral such as siderite (iron carbonate).

Summary of Geochemistry Findings – Acid Species

A desktop analysis investigated the impact on CO₂ sequestration processes of trace and minor reactive acid species not dealt with in the laboratory autoclave experiments. In particular, we characterized the concentration threshold below which the species can be neglected by performing numerical geochemical simulations and in particular the concentrations at which they would have an impact on the pH of the solution. Species included HCl, SO₂, NO, and NO₂ present in the waste stream of oxyfuel power plants. Results suggest that ~1000 ppm for the Frio setting (depth of ~5,000 ft, ~60°C) and ~100 ppm for the deeper Cranfield setting (depth of ~10,000 ft, ~125°C) are the threshold values beyond which the pH starts dropping significantly beyond that of CO₂ alone if no buffering capacity is available. No impact on pH was observed in the numerical experiments if buffering capacity was adequate. In the former case, trace impurities seem to have a bigger impact at depth than in shallower zones because carbonates, if present would dissolve more slowly at higher temperature. Typical concentrations of HCl and NO_x species are likely below the threshold values but SO₂ concentration is likely higher in effluent streams. When considering only the pair CO₂ + trace gas, redox conditions can also change becoming more reducing with SO₂ in the CO₂ stream and more oxidizing with NO_x. This aspect has not been studied in this work but literature exists (see Nicot et al.²¹).

5.5. Conclusion

An important observation controlling all study results was that viscosity and density of the mixtures considered are lower than those of pure CO₂ at the same temperatures and pressures. It follows that a plume of CO₂ with impurities, moving updip with no barrier, will therefore migrate farther from the point of injection but will be trapped through residual saturation sooner than will a plume of pure CO₂ and possibly enhance dissolution, primarily because it is exposed to more

rock / brine volume. A larger plume, however, means that a larger area must be defined and monitored for leakage pathways, such as faults and wells, but the faster trapping translates into a shorter monitoring period. Equally important is that contrasts of viscosity and density between pure CO₂ and a CO₂ mixture decrease with depth, suggesting that differences in flow behavior and storage capacity are proportionally reduced with depth. In terms of plume shape and extent, the impact of impurities is more marked at shallow depths, where the contrast in density and viscosity with neat CO₂ is the largest. This density contrast diminishes considerably at depth. The results also suggest a trade-off between plume extent (area of review with risk of CO₂ leakage) and decreased risk owing to faster trapping. A larger plume translates into a larger area to inspect for leakage pathways, such as faults and abandoned wells, but a faster trapping translates into a shorter period of time to monitor the site. Heterogeneities seem to dampen the impact of impurities, but not in all cases.

Whereas flow behavior may impact the larger storage venue reservoir and seal rocks, geochemical impacts are more likely to be restricted to the well-bore environment and adjacent proximal reservoir. Detrimental reactions occurring close to the wellbore could be handled by established operational approaches if their origin and symptoms are understood. Batch experiments conducted in high-pressure, high-temperature autoclaves with siliciclastic (that is, quartz-rich) rocks immersed in synthetic brine and exposed to supercritical CO₂ with and without admixed O₂ show that O₂ is likely to alter the geochemistry of subsurface systems in ways that the pure CO₂ case does not, in particular when ferrous-iron bearing minerals are present. For example, pyrite (FeS₂) is quickly oxidized by O₂ and pH can drop significantly if the system has little or no buffering capacity leading to deeper degradation of feldspars (here, mostly K and Na silicate). Iron-bearing carbonates (e.g., ferroan calcite, siderite, ankerite) are degraded formation of carbonic acid with CO₂ addition. This mobilizes ferrous Fe which then precipitates as iron oxides when contacted by O₂. Iron-bearing chlorite is also mildly attacked by O₂ with subsequent iron oxide precipitation. In all of the autoclave experiments runs, mineral precipitation remained minor because the precursor minerals that supply component ions are not abundant. This suggests that as long as a precursor reactive mineral fraction is a small portion of the rock, O₂ will not have a large geochemical effect on mineral precipitation and therefore on rock stability or fluid flow. To have an impact on permeability by obstructing pores, redox-sensitive minerals must be abundant enough with sufficient oxidizing material (O₂) to impact the system. Results from the Cardium sandstones, Alberta show that little material precipitates compared to the pore volume. Permeability change is very sensitive to the exact location in the pore of the authigenic mineral deposits (i.e., pore throats as opposed to pore bodies) but past field experience, such as at the Rouse Field, France or injecting air or flue gas, do not point to this being a major issue.

In addition, a desktop study investigated the impact on CO₂ sequestration processes of trace and minor reactive acid species (HCl, SO₂, NO, and NO₂) not dealt with in the laboratory autoclave experiments. In particular, we characterized the concentration threshold below which the species can be neglected by performing numerical geochemical simulations or below which they would have limited impact on the pH of the solution. Results suggest that ~1000 ppm for the “shallow”

Frio setting and ~100 ppm for the deeper Cranfield setting are the threshold values beyond which the pH starts dropping significantly beyond that of CO₂ alone (if no buffering capacity – if buffering capacity, no impact). In this case, trace impurities seem to have a bigger impact at depth than in shallower zones. Typical concentrations of HCl and NO_x species are likely below the threshold values but typical SO₂ concentration is possibly higher. When considering only the pair CO₂ + trace gas, redox conditions can also change becoming more reducing with SO₂ in the CO₂ stream and more oxidizing with NO_x.

6. Phase 3 Quantifying Economic Implications with the Cost Optimization Model

(Edited summary)

Section author: Andrew McGoey-Smith, WorleyParsons

6.1. Model Scope

This section describes the ACPPE techno-economic model (TEM) from its inception to final form, which is a user interface dashboard which accepts different input parameters and displays the associated outputs. The dashboard is made available to the general user who can explore CCS design decisions in a plug-and-play manner.

The development of the TEM followed a systematic model development methodology which has proven effective on many modelling projects over the years and has been adopted by such organizations as the US Department of Energy. In this methodology, development of the model occurs in a series of well-defined stages which are:

1. Objectives and performance measures
2. Conceptual model: feature, events and processes
3. Mathematical mode: equations and algorithmic rules
4. Data, including uncertain data which are modelled as probability distributions
5. Implementation in software
6. Results and analysis
7. Conclusions

6.2. Model Objectives

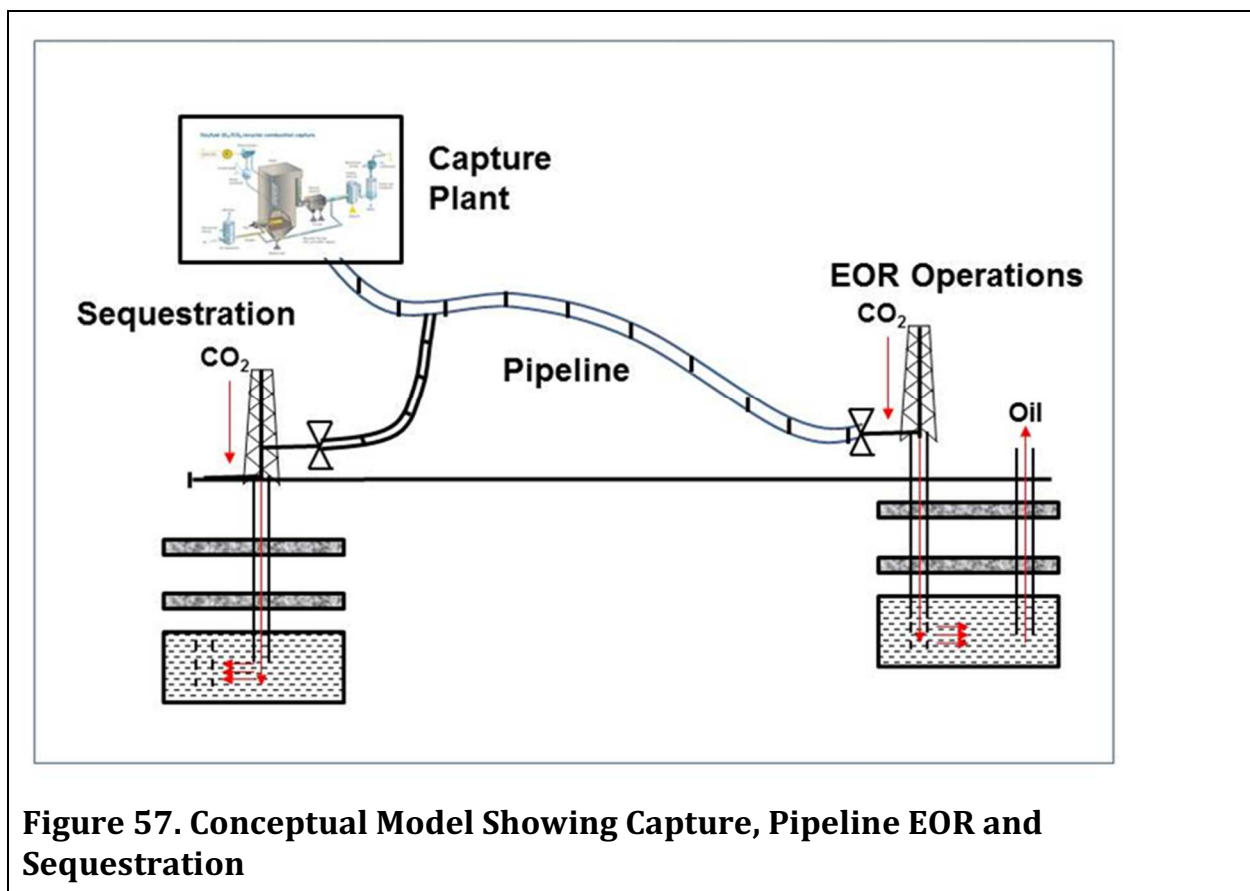
The objectives of the TEM were as follows:

- Compute the overall cost of developing a CCS facility in Canada using Alberta the physical location) within Canada since it is close to large CO₂ sources and large CO₂ sinks) as a function of the purity of the CO₂ stream as defined by 6 different capture technologies (See Table 2):
 - Heavy Amine Post-combustion (taken as the “pure” CO₂ case)
 - Heavy Fuel, Oxy
 - Natural Gas Oxy
 - Heavy Fuel, IGCC Partial Shift
 - Various Natural Gas Processing Plant
 - Natural Gas Steam Methane Reforming (SMR)

- Explore the relative contribution to the overall cost among the 4 CCS sub-components:
 - Capture,
 - Transport (Pipeline),
 - EOR and
 - Geologic Sequestration (GS);
- Act a system integration tool for making design decisions such as trade-offs between purity, and other input parameters, and costs.

6.3. Conceptual Model

The conceptual model for the TEM is modular. The cost associated with each sub-component model is treated individually and the overall cost is just a straight linear summation of the individual costs. The conceptual model for each sub-component is described below. A schematic showing the inter-connection between capture, pipeline and EOR is shown in Figure 57.



6.3.1. Conceptual Model for Capture

This conceptual model is the simplest of the TEM sub-component models and is treated as a “black box” because capture is the least known and understood technology as of 2014. CO₂ capture systems are not a mature technology and are currently being developed around the world. Some are proprietary and their details are not public. Because of the uncertainties associated with these costs and the fact that some are proprietary, probability distribution functions of cost were developed by ConocoPhillips and supplied to the ACPP team.

6.3.2. Conceptual Model for Pipelines

The conceptual model is based on the work of ICO₂N²⁹ and on previous analysis of pipeline cost data by Herdman which is turn is based upon CO₂ pipeline models developed by WorleyParsons and MIT^{30 and 31}. These models were developed for a pure CO₂ stream. Cost is calculated in terms of dollars per km of length and diameter in inches. Pipeline diameter in turn is calculated as a function of:

- Mass flow rate of CO₂;
- Pressure drop across the length of pipeline
- CO₂ density at the midpoint of the pipeline which is in turn dependent on pipeline, temperature and chemical composition of the (impure) CO₂ stream at the pipeline midpoint.

Diameter is then rounded to nearest realizable standard diameter used in pipeline construction.

In addition to the indirect impact of impurities on cost through density which affects diameter, in the specific case of the presence of hydrogen in the stream, the model adds a multiplicative factor to pipeline cost. This is because hydrogen is a light gas and can induce longitudinal cracking of the pipeline and therefore requires braces to be added to the pipeline to mitigate against spills. In addition because hydrogen is explosive when exposed to air, it requires additional material strength to mitigate against spills. The impact of the presence of hydrogen gas in the CO₂ stream on cost was highlighted during discussions with Enhance Energy³².

6.3.3. Conceptual Model Enhanced Oil Recovery

EOR is the only revenue-producing component of the four CCS subsystems. The conceptual model for EOR cost is based up the assumption that the volume of oil recovered from an EOR reservoir is directly proportional to the volume of CO₂ injected into the reservoir formation over the CCS operable lifetime which is taken to be 20 years for this system. The model was described earlier in Section 4 of this report. Figure 57 showed earlier that CO₂ is injected into a reservoir containing trapped oil and the oil is recovered at the surface.

The revenue recovered from the EOR process is directly proportional to the volume of oil recovered as expressed as a Net Present Value (NPV). The ratio of oil recovered to CO₂ injected into the formation is a function of the thermodynamic properties of the chemical impurity constituents.

6.3.4. Conceptual Model for Geologic Sequestration

For geologic sequestration, the sources of cost of sequestration in the Alberta Sedimentary Basin are threefold:

- Construction and maintenance of injection wells;
- Well monitoring of underground plume, both CAPEX and OPEX;
- Seismic monitoring of the caprock (aquitar) which confines the CO₂ to the storage reservoir; and
- Completion (mitigation) of leaky abandoned wells which penetrate the storage formation and intersect the surface projection of underground CO₂ plume.

Figure 58 shows the projection of the underground plume onto the ground surface and the locations of abandoned wells which penetrate the storage reservoir.

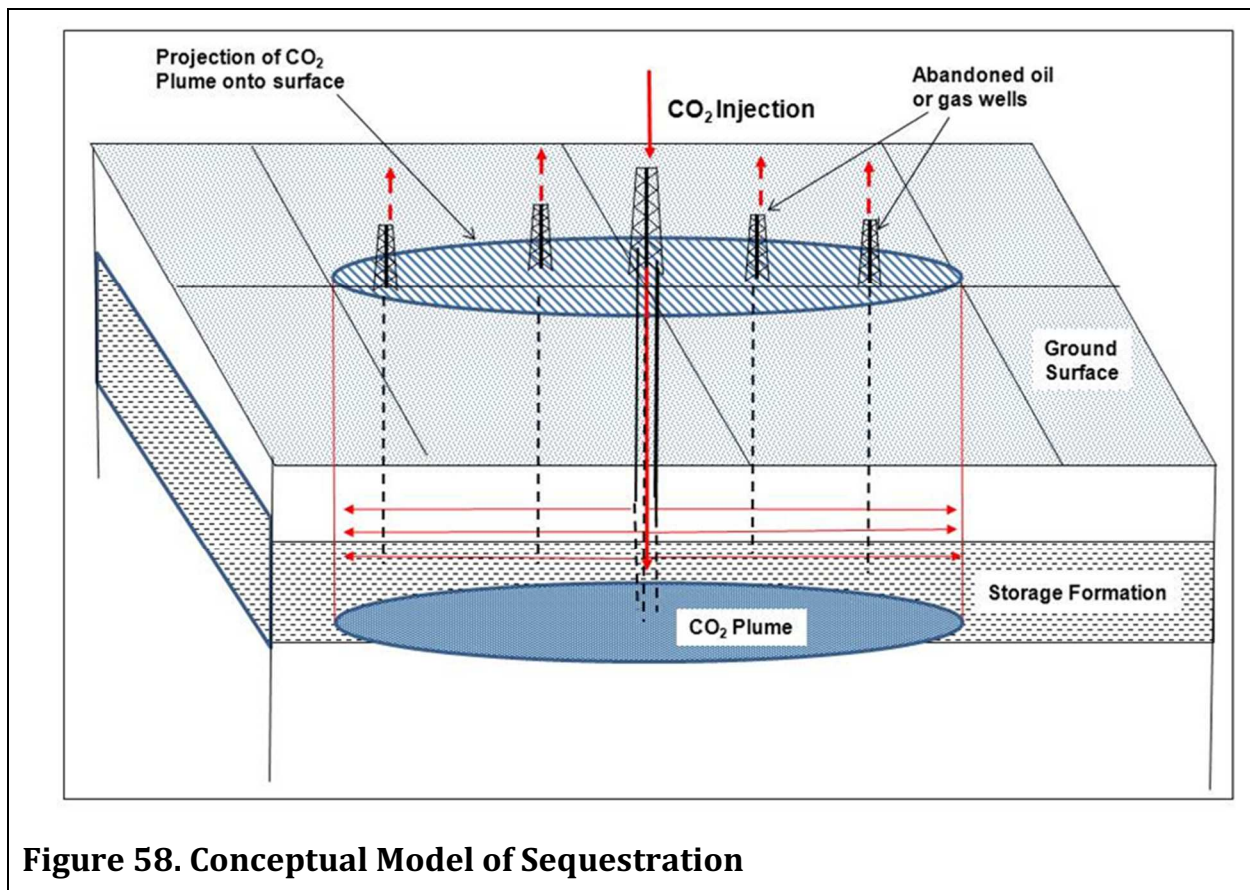


Figure 58. Conceptual Model of Sequestration

The cost of construction and maintenance of injection wells has been estimated by Nygaard and Lavoie as part of the WASP Project³³ on a well-by-well basis for CO₂ storage in Alberta. The overall cost of well construction and maintenance therefore depends on the number of injection wells required which can be estimated from the well pumping equation (Nordbotten³⁴). This is

dependent on the mass of CO₂ to be sequestered, the density and viscosity of the impure CO₂ stream in the formation, the radius of the injection wells and the geologic properties of the storage formation.

The cost of seismic monitoring depends on the area of the underground plume. Costs of monitoring were developed for the WASP project by Nygaard and Lavoie³³. For ACP, the costs of seismic monitoring were estimated based on the size of the plume relative to the size of the WASP plume.

Finally, the cost of mitigating abandoned wells which have penetrated the underground CO₂ plume and therefore can leak CO₂ to the surface depends on the density of wells penetrating oil and gas formations in the region of Alberta where CO₂ can be stored, the fraction of those wells which are incomplete and the area of the underground plume. The well density and fraction of wells which are leaky has been investigated by Watson and Bachu³⁵. A risk-based model for predicting the volume of leakage from direct and indirect pathways was developed by the section author as part of WASP³⁶.

The area of the underground CO₂ plume for an arbitrary combination of chemical impurities was estimated from plume area calculations performed by the University of Texas, Bureau of Engineering Geology using Computer Modelling Group's GEM software³⁷. The plume area is taken to be the estimated size of the plume after 100 years. The calculations were conducted for specific binary combinations (CO₂+impurity). The underlying assumption is that the plume area for multiple impurities is the linear sum of CO₂ plus single impurities which is assumed to be sufficiently accurate for this high level study because the concentration of impurities is less than 8%.

6.4. Mathematical Model

The overall cost of implementing a CCS system is simply the linear sum of the costs associated with each individual sub-component which is written as

$$C_{\text{tot}}(Q_1, Q_2, \dots, Q_6) = C_{\text{tot}}(Q) = C_{\text{Capt}}(Q) + C_{\text{Pipe}}(Q) - C_{\text{EOR}}(Q) + C_{\text{GS}}(Q) \quad (1)$$

where the word subscripts are self-explanatory, Q_j are the mass flow rates in units of megatonne/yr for each of the 6 capture technologies (j=1,2,...,6) using the naming convention described in the Introduction. Equation (1) makes use of vector notation for six flow rates for compactness, where we have introduced the vector

$$Q = \begin{pmatrix} Q_1 \\ Q_2 \\ Q_3 \\ Q_4 \\ Q_5 \\ Q_6 \end{pmatrix} \quad (2)$$

The effect of purity of the CO₂ stream is not calculated explicitly in the capture model. Rather, purity is accounted for indirectly in terms of the chemical compositions of the 6 realizable capture

technologies. The model converts a combined stream into mole fractions of pure CO₂ and mole fractions of up to six impurity components.

6.4.1. Chemical Composition of Impure Stream

Costs for Pipeline, EOR and Geological Sequestration subsystems are calculated on the chemical composition of the CO₂ stream. For pipelines, cost depends on stream density which is calculated internally in the TEM using an approximation to the GERG 2008 equation of state³⁸.

The relationship between component mole fractions and the 6 capture technology types was shown earlier in Table 2. Each type of capture technology is associated with a physically realizable capture plant which has an associated standard mass flow rate Q_n^s as per equations (1) and (2) for each of the 6 capture technologies ($n=1, \dots, 6$). The standard mass flow rates shown in Table 23 were estimated from the range of project scales in the capture data provided to the ACPP and correspond closely to the project scales forming the basis of the capture cost data. They are further informed and calibrated by publically available data.

| Table 23. Standard Mass Flow Rates Q_j^s for each Capture Technology | | | | | | |
|--|------------------------------|------------------------------|-------------------------------|-------------|------------------------------|-------------------------------|
| | Amine Post Combustion | Oxy Fuel (heavy fuel) | Oxy Fuel (natural gas) | IGCC | Natural Gas (Various) | SMR (physical solvent) |
| Composition Number | 1 | 2 | 3 | 4 | 5 | 6 |
| Q (Mt/year) | 1.0 | 1.4 | 1.0 | 5.7 | 1.02 | 0.58 |

The TEM is flexible with regard to mass flow rates and allows the user to change the mass flow rate to Q_j^{input} for each capture technology.

Therefore the purity of the captured CO₂ stream for transport and storage can vary substantially and is defined by the set of chemical components c_i where $i=0, 1, \dots, 6$ and c_i are expressed in mole fraction in percent. These components are CO₂, N₂, O₂, Ar, CO, H₂ and CH₄ and are denoted by the indices 0 to 6 respectively.

The vector of chemical components for the combined stream is related to the set (6x7 matrix) of mole fractions in Table 2.

$$c_i = \sum_{j=1}^6 f_j \chi_{i,j} \quad i = 0, 2, \dots, 6 \quad (3)$$

where the fraction f_j is the normalized ratio of input capture flow rate to standard capture flow rate defined by the 2 equations below:

$$f_j = \frac{r_j}{\sum_{j=1}^6 r_j} \quad (4)$$

and

$$r_j = Q_j^{input} / Q_j^s. \quad (5)$$

r_j is the ratio of capture flow rate in *Mt/yr* input by the user to standard flow rate from Table 23 also in *Mt/yr*.

The chemical composition of the captured stream influences cost of pipeline, EOR and geological sequestration. For pipelines, cost is a function of the combined stream density. Combined stream density is calculated from the first order Taylor series expansion the GERG 2008 model as extracted by Botros³⁹ which estimates density for binary CO₂ gas mixtures and is considered state-of-the-art in the gas industry. The main result of these calculations is:

$$\rho(\chi_1, \chi_2, \chi_3, \chi_4, \chi_5, \chi_6) \approx \rho_0 + \sum_{i=1}^6 m_i \chi_i \quad (6)$$

Where ρ_0 refers to the density of pure CO₂ and m_i is the gradient of density with respect to the i^{th} chemical component, estimated using linear approximation between the density of impure CO₂ containing the maximum concentration for the i^{th} component in the set of capture streams (with the other contaminants set to zero), and the density of pure CO₂ divided by the maximum concentration difference.

In the GERG 2008 model, temperature and pressure at the mid-point of the pipeline were used as inputs and density was the output.

6.4.2. Mathematical Model for Capture

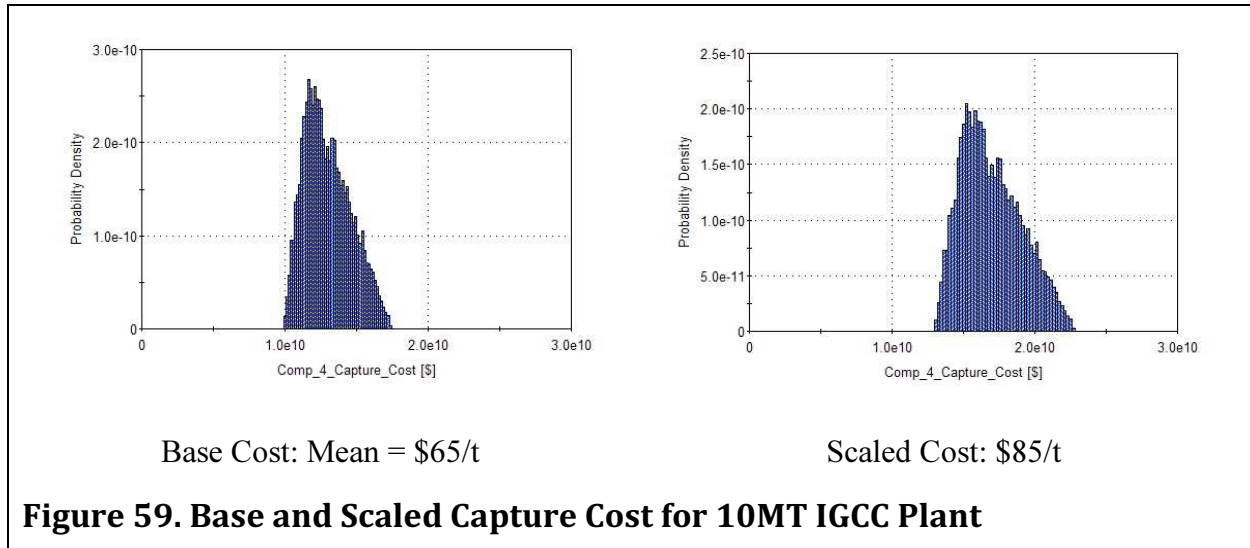
The base costs for capture are defined in terms of triangular distribution functions with 3 values: L_B , ML_B and H_B which correspond to *lowest*, *most likely* and *highest* value respectively. Because the mean cost of capture could change as the capture technologies mature over time, the TEM allows the mean capture cost to be changed to a scaled value while preserving the original spread of cost of the base. If the lowest, highest and most likely base cost values are denoted as L_B , H_B and ML_B , then the *scaled* cost distribution C_S takes the form:

$$C_S \sim \left(\frac{\mu_S}{\mu_B} \right) tri(L_B, ML_B, H_B) \quad (8)$$

Where μ_B is the mean value of the *base* cost, μ_S is the mean value of the inputs scaled cost, $tri(..)$ denotes the triangular distribution function and the symbol \sim denotes ‘is sampled from’. Note that the mean value of the triangular distribution is readily calculated from the lowest, most likely and highest values using the well-known expression from Wolfram⁴⁰

$$\mu_B = \frac{1}{3}(L_B + ML_B + H_B) \quad (9)$$

The effect of scaling of cost on the capture cost probability density function is shown in Figure 59. Note the shape of the base and scaled cost distribution is the same.



6.4.3. Mathematical Model for Transport

Pipeline cost is calculated using the model supplied by ICO₂N²⁹ which uses a simple cost rate of \$64,356 per km of length and inch of standard diameter (Alberta 2012). The \$64,356 number accounts for the agglomeration of the cost of materials, labour, right of way and miscellaneous cost factors. Pipeline length is defined by the model user and refers to the length of the backbone. Although in practice a CCS system would comprise a network of both backbone lines and distribution (feeder) lines, the distribution lines can be neglected at this level of detail.

The standard pipeline diameter is calculated internally in the TEM. It taken from the set of realizable industry standard pipeline diameters which can be determined by calculating the nominal diameter d_{MIT} as a function of system variables using fluid mechanics as discussed in the next paragraph and then rounding up to the nearest standard diameter which is taken from the following set {8, 10, 12, 16, 20, 24, 28, 30, 32, 36, 40, 42} in units of inches. The nominal pipeline diameter is calculated using the formula from MIT^{31 and 41}

$$d_{MIT} = \left(\frac{32 \cdot F_F \cdot Q_m^2 \cdot L \cdot 1000}{\pi^2 \rho_{CO_2}} \right)^{1/5} \quad (10)$$

where

d_{MIT} is in units of inches and

F_F is the Fanning Friction factor⁴²

Q_m is the mass flow rate in the pipeline in kg/s

L is the pipeline length in km

E is pipe surface roughness in mm ; and

ρ_{CO_2} is the density of impure CO₂ stream in kg/m^3 of the combined stream

The Fanning Friction factor is calculated using the formula

$$f_F = \left\{ 4 \log_{10} \left[2.28 + \frac{2.54 \cdot 10 \cdot d_{WP}}{E} \right] \right\}^{-2} \quad (11)$$

Where d_{WP} is the diameter given by the WorleyParsons formula³⁰

$$d_{WP} = (7.7 + 0.009 \cdot L_{mi}) \cdot Q_M^{0.38} \quad (12)$$

Where

Q_M is mass flow rate in *megatonne/yr* for the *combined stream*; and

L_{mi} is pipeline length in *miles*.

To account for uncertainty in actual pipeline costs, the base pipelines was scaled by an uncertainty of up to $\pm 20\%$ about the mean value given by a triangular distribution so that the final cost function is

$$C_{Pipe}(\mathbf{Q}) = C_{km-in} \cdot d_{MIT}(\mathbf{Q}) \cdot L \cdot tri(0.8, 1.0, 1.2) \quad (13)$$

Where C_{km-in} is the cost of pipeline per *km* of length and *inch* of diameter. This formula needs to be modified in the case of the presence of H_2 . Hydrogen poses additional costs because it can lead to longitudinal fracturing along the pipe which is mitigated by adding braces. In addition, hydrogen is an explosive gas when exposed to air in the event of an accidental spill which is mitigated by using special grade of steel. The additional costs are modelled as a 15 to 20% increase in cost for the maximum H_2 concentration which is 4% (in the case of IGCC). For concentrations of H_2 which are greater than zero and less than 4%, a linear scaling is applied. Thus for *non-zero hydrogen* concentration in the combined stream, the pipeline cost is scaled by the factor f_{Hyd} given by

$$f_{Hyd} = \frac{[1 + \chi_{Hyd} U(0.15, 0.2)]}{0.04} \quad (14)$$

For an IGCC stream which contains 4% hydrogen, the pipeline cost is an additional 15 to 20% on top of the cost of a pure CO₂ stream. In equation (14), χ_{Hyd} is the mole fraction of hydrogen in percent for the combined stream and $U(\cdot)$ denotes the uniform probability distribution function.

6.4.4. Mathematical Model for EOR

The model was developed by Edwards based on the work of Emera and Sarma as described in Section 4 of this report.⁴³ From the conceptual model described in Section 6.3.3, the cost recovery for the EOR process depends on the volume of oil recovered. For the pure case, oil recovered depends on the volume of CO₂ injected over the lifetime of the project scaled by a utilization factor which is simply the volume of CO₂ required to release a barrel of oil.

The decrease in cost of oil recovered ΔC_{EOR} in \$ for the impure CO₂ stream, relative to the pure CO₂ stream is simply given by

$$\Delta C_{EOR} = (VOR_{imp} - VOR_{pure}) \cdot NPV_{oil} \quad (15)$$

where

| | |
|--------------------|--|
| VOR_{imp} | volume of oil recovered in \$ for an impure CO ₂ stream |
| VOR_{pure} | volume oil recovered in \$ for pure a CO ₂ stream; and |
| NPV_{oil} \$/bbl | NPV of oil in \$/bbl amortized over the lifetime of the project |

As per the previous discussion the volume of oil recovered for the pure CO₂ stream is given by

$$OR_{pure} = \frac{T \cdot Q_{pure} \cdot 365}{1,000 \cdot U_{EOR}} \quad (16)$$

Where 365 refers to the number of days per year and

| | |
|------------------------|--|
| T (yr) | Is the lifetime of the CCS project, |
| $Q_{P,VI}$ (mm scf/d) | Is the flow rate in imperial units for the EOR component which was captured for the CO ₂ stream, and |
| U_{EOR} (mm scf/bbl) | Is the utilization factor relating the volume (mm scf or 1000ft ³) of CO ₂ required to release one barrel (bbl) of oil during the EOR process. The nominal (deterministic) value is 6 mm scf/bbl. |

The utilization factor is variable and is modelled as a triangular function centred at 6,000 scf/day per bbl with upper and lower values of 4,000 and 8,000 mmscf/day per bbl respectively.

$$U_{EOR} \sim tri(4000,6000,8000) \quad (17)$$

The volume of oil recovered for the impure stream is much more complicated to compute. However, it is done so using a simple scaling calculation

$$OR_{impure} = OR_{pure} \cdot f_{IR} \quad (18)$$

where

f_{IR} is the fraction of impure recovery.

This impure fraction is computed using a thermodynamic model based on the work of Emera and Sarma⁴⁴ which is described below and is related to the difference between the slim tube recovery factor (f_{STR}) and the fractional decrease in recovery of the impure stream (f_{DRI}).

$$f_{IR} = f_{STR} - f_{DRI} \quad (19)$$

The slim tube recovery factor is usually one and fractional decrease in recovery is calculated using the following relationship

$$f_{DRI} = f_{PR} \cdot (MMP_{imp} - MMP_{pure}) \quad (20)$$

where

f_{PR} is pressure recovery factor;
 MMP_{imp} (psi) is the maximum miscible pressure of the impure stream; and
 MMP_{pure} (psi) is the maximum miscible pressure of the pure stream.

The pressure recovery factor is a weighted sum of the of the impure mole fractions

$$f_{PR} = \frac{\sum_{i=1}^6 w_{PR}(i) \cdot \chi_i}{\sum_{i=1}^6 \chi_i} \quad (21)$$

Where the summation over the index i begins at $i=1$ because $i=0$ corresponds to the pure CO₂ mole fraction and the coefficients $w_{PR}(i)$ are small numbers. Maximum miscible pressure for the pure input stream is a constant and is input via the dashboard with default value of 1,841 psi.

The maximum miscible pressure for the impure stream is related to maximum miscible pressure for pure CO₂ by the linear relationship

$$MMP_{imp} = R_{MMP} \cdot MMP_{pure} \quad (22)$$

where R_{MMP} is the MMP ratio computed using the thermodynamic model of Emera and Sarma which is a polynomial function of the critical pressures and critical temperatures of the impure stream components.

$$R_{MMP} = G \cdot \sum_{i=1}^6 w_{Str}(i) \cdot P_c(i) / P_c(CO_2) \quad (23)$$

Where G is a sum of polynomials related to critical temperature of each stream component, $P_c(i)$ denotes critical pressure of the i^{th} component with the index $i=0$ corresponding to pure CO₂, and $w_{Str}(i)$ is a weighting coefficient given by

$$w_{Str}(i) = \frac{MW_i \cdot \chi_i}{\sum_{i=0}^6 MW_i \cdot \chi_i}$$

First we define the polynomial expansion factors

$$G = 6.606 + \sum_{k=1}^6 \frac{g_k(1.8 \cdot T_c^{SA} + 32)}{[1.8 \cdot T_c(CO_2) + 32]^k} \quad (24)$$

Where T_c^{SA} is the stream critical temperature, averaged over the molecular weight of each stream component and a factor term:

$$T_c^{SA} = \sum_{i=0}^6 MF_i \cdot MW_i \cdot \chi_i \cdot T_c(i) / \sum_{i=0}^6 MW_i \cdot \chi_i \quad (25)$$

where MF_i is a factor term which ranges from 1.0 to 1.6.

6.4.5. Mathematical Model for Geologic Sequestration

From the conceptual model, the main driver of cost is associated with the presence of the underground CO₂ plume in the reservoir. The area of this plume is influenced by the type and quantity of impurities. Two types of cost are incurred in connection with the plume: seismic

monitoring of CO₂ containment and remediating any abandoned oil and gas wells which intersect the plume. Another cost contributing to sequestration is the number of wells required for injection.

The plume area was calculated as the area at 100 years as a function of concentration of impurities by Nicot³⁷ by running CMG GEM reservoir simulation software for CO₂ plus a single impurity. The presence of each impurity increases the plume area in an almost linear fashion. Because the maximum concentration of impurity of 4% (for H₂ in the case of an IGCC capture plant), it is assumed that adding successive impurities to the CO₂ stream increases the overall plume area linearly and additively.

$$A(\chi_1, \chi_2, \chi_3, \chi_4, \chi_5, \chi_6) = A_0 + \sum_{i=1}^6 m_i \chi_i \quad (26)$$

Where m_i is the appropriate partial derivative estimated from binary combinations (CO₂ plus single contaminant) at maximum concentration in all capture streams (e.g. 4% for H₂, 3.9% for Ar, etc.) Note: although this is only an approximation, at this level of detail and low impurity mole fractions (maximum 4%), this seems reasonable.

For a given the plume area, Watson and Bachu³⁵ have estimated the spatial density of intersecting oil and gas wells d_{AW} in the central Alberta region in units of number of wells per area in km^2 . For the WASP project, which was concerned with the feasibility and cost of storing up to a \$1GT of CO₂ in central Alberta, the cost of remediating a single abandoned well was estimated by Nygaard and Lavoie which we denote C_{AW}^{WASP} . Therefore the cost of remediating abandoned wells intersecting the CO₂ plume for this system is obtained by multiplication of the plume area, spatial well density and cost of remediation per well:

$$C_{AW} = A(\chi_1, \chi_2, \chi_3, \chi_4, \chi_5, \chi_6) \cdot d_{AW} \cdot C_{AW}^{WASP} \quad (27)$$

Similarly, for WASP, the cost seismic monitoring of the underground plume was also estimated by Nygaard and Lavoie. Using this value, the cost of seismic monitoring for the TEM can be estimated as

$$C_{SM} = C_{SM}^{WASP} \cdot A(\chi_1, \chi_2, \chi_3, \chi_4, \chi_5, \chi_6) / A_{WASP} \quad (28)$$

Finally, the cost of injection is estimated using the cost of drilling a well and the number of wells required to inject a certain volume of CO₂. The number of injection wells n_{inj} is estimated to be as follows based on Nicot⁴⁵

$$n_{inj} = \frac{Q \cdot \mu_{CO_2}}{6000D \cdot 4\pi \cdot k \cdot k_{rCO_2} \cdot \rho_{CO_2}} \ln \left(\frac{2.25 \cdot k \cdot k_{rCO_2} \cdot T}{\varphi \cdot c_{sys} \cdot \mu_{CO_2} \cdot r_w^2} \right) \quad (29)$$

Where:

Q is the volume of CO₂ injected over the lifetime of the project (usually assumed to be 20 years),

μ is the viscosity of CO₂ in the reservoir,

k and k_{rCO_2} are the permeability and relative permeability of the storage formation rock to CO₂

ρ is the density of CO₂ in the formation

T is project lifetime

ϕ is rock porosity to CO_2

c is the compressibility of the rock- CO_2 system; and

r_w is the injection well radius.

The injection cost can therefore be estimated using

$$C_{inj} = n_{inj} \cdot C_{inj}^{WASP} \quad (30)$$

where the cost of injection for a single well in Alberta is denoted C_{inj}^{WASP} as was estimated for WASP³³. Note, the equation for the number of injection wells assumes single phase flow for simplicity. In actuality, brine will be present in the formation which means there is really two phase flow. Given that injection cost is not the largest contributor to overall cost in the project, the single phase flow is adequate at this stage in the project.

The total cost for geologic sequestration is the sum:

$$C_{seq} = C_{inj} + C_{AW} + C_{SM}$$

6.5. Input Data

In this section the definition of input data for the TEM, including uncertainty variables (defined as probability distribution functions) is given.

6.5.1. Capture Input Data

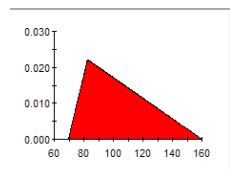
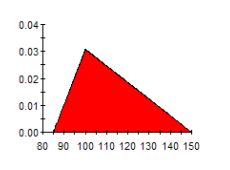
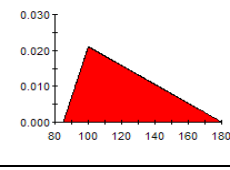
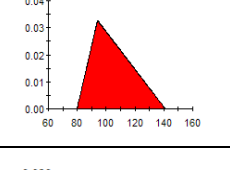
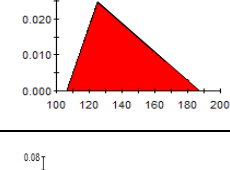
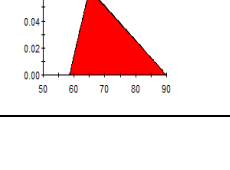
The base costs of capture are given in terms of the 10th, 50th, and 90th percentiles of a log-normal probability distribution function as estimated from the capture cost data provided to the ACPP as well as from publically available data. These three values can be interpreted as a lowest value, most likely value and highest values and are modelled as triangular distributions in the model as shown in Table 24.

6.5.2. Pipeline Input Data

The data input for the pipeline model are given in the Table 25.

6.5.3. Enhanced Oil Recovery Input Data

The EOR model makes use of critical temperature and pressures. Some of these are documented on p49 of Mohitpour⁴⁶ and a complete list is given below in Table 27. Other parameters related to oil recovery cost and the MMP ratio are shown in Table 26. Table 28 shows the polynomial coefficients g_k in equation (24) and the pressure MF factors are shown in Table 29.

| Table 24. Base Cost Values for Capture | | | | |
|---|--------------------|-------------------------|---------------------|---|
| Capture Technology | Lowest (\$) | Most Likely (\$) | Highest (\$) | Prob. Distribution Function (\$) |
| Heavy Post-combustion | 70 | 80 | 160 |  |
| Heavy Fuel, IGCC | 85 | 100 | 150 |  |
| Heavy Fuel, Oxy Partial Shift | 85 | 100 | 180 |  |
| Gas SMR | 79.9 | 94 | 141 |  |
| Gas Oxy | 106.25 | 125 | 187.5 |  |
| Gas Processing Plant | 58.5 | 65 | 90 |  |

| Table 25. Pipeline Model Input Parameters | |
|--|--------------|
| Quantity | Value |
| Surface roughness | 372 mm |
| Base cost per km-inch | \$64,356 |

| Table 26. EOR Model Parameters | |
|---------------------------------------|---------------------------|
| Quantity | Value |
| MMP Pure | 1755 (Nominal value) |
| Slim tube recovery | 1 (Nominal value) |
| NPV Oil | 15 \$/bbl (Nominal value) |

| Table 27. Critical Parameters for Components | | |
|---|----------------------------------|--------------------------------|
| Component | Critical Temperature (°C) | Critical Pressure (MPa) |
| CO ₂ | 30.85 | 7.38 |
| N ₂ | -147.15 | 3.4 |
| O ₂ | -118.15 | 5.0 |
| H ₂ | -240.15 | 1.3 |
| Ar | -122.15 | 4.9 |
| CO | -140.3 | 3.5 |
| CH ₄ | -82.15 | 4.61 |

| Table 28. Coefficients in Polynomial Expansions | |
|--|--------------|
| Coefficient | Value |
| g ₁ | -29.69 |
| g ₂ | 109.5 |
| g ₃ | -213.363 |
| g ₄ | 208.366 |
| g ₅ | -98.46 |
| g ₆ | 18.009 |

| Table 29. Pressure Recovery and MF Factors | | |
|---|---------------------------------|------------------|
| Component | Pressure Recovery Factor | MF Factor |
| CO ₂ | - | 1.0 |
| CH ₄ | 0.000 367 | 1.6 |
| N ₂ | 0.000120 | 1.0 |
| O ₂ | 0.000 282 | 1.0 |
| CO | 0.000 367 | 1.0 |
| H ₂ | 0.000 147 | 10.0 |
| Ar | 0.000126 | 1.0 |

6.5.4. Geological Sequestration Input Data

The major inputs to the sequestration model are the plume areas at 100 years of injection which are calculated from the plume extents supplied by Nicot³⁷. The plume areas a function of binary impurities are shown from Table 30 to Table 35.

Other parameters in the Sequestration model pertain to abandoned well remediation, seismic monitoring and injection well costs and are shown in Table 15.

| Table 30. Plume Areas for CO₂ plus N₂ | | | | | | | |
|--|----------------|----------------------------|-------------------------------|-----------------|----------------|-----------------------------|-------------------------------|
| Shallow | | | | Deep | | | |
| CO ₂ | N ₂ | Plume Extent @ 100 yrs(ft) | Plume Area (km ²) | CO ₂ | N ₂ | Plume Extent @ 100 yrs (ft) | Plume Area (km ²) |
| 100 | 0 | 9300 | 8.035184 | 100 | 0 | 12000 | 13.37804 |
| 95 | 5 | 13200 | 16.18743 | 95 | 5 | 13800 | 17.69245 |
| 90 | 10 | 18000 | 30.10058 | 90 | 10 | 15600 | 22.60888 |
| 85 | 15 | 20700 | 39.80802 | 85 | 15 | 17400 | 28.12732 |
| 80 | 20 | 23100 | 49.57399 | 80 | 20 | 19200 | 34.24778 |
| 75 | 25 | 25200 | 58.99715 | 75 | 25 | 20100 | 37.53376 |

| Table 31. Plume Areas for CO₂ plus Ar | | | | | | | |
|---|----|--------------------------|-------------------------------|-----------------|----|--------------------------|-------------------------------|
| Shallow | | | | Deep | | | |
| CO ₂ | Ar | Plume Extent @ 100 years | Plume Area (km ²) | CO ₂ | Ar | Plume Extent @ 100 years | Plume Area (km ²) |
| 100 | 0 | 9300 | 8.035184 | 100 | 0 | 12000 | 13.37804 |
| 95 | 5 | 11700 | 12.7175 | 95 | 5 | 13500 | 16.93158 |
| 90 | 10 | 14700 | 20.07542 | 90 | 10 | 14100 | 18.47005 |
| 85 | 15 | 18600 | 32.14074 | 85 | 15 | 15300 | 21.74767 |
| 80 | 20 | 20400 | 38.66253 | 80 | 20 | 15900 | 23.48682 |
| 75 | 25 | 23400 | 50.86999 | 75 | 25 | 16800 | 26.22095 |

| Table 32. Plume Areas for CO₂ plus O₂ | | | | | | | |
|--|----------------|--------------------------|-------------------------------|-----------------|----------------|--------------------------|-------------------------------|
| Shallow | | | | Deep | | | |
| CO ₂ | O ₂ | Plume Extent @ 100 years | Plume Area (km ²) | CO ₂ | O ₂ | Plume Extent @ 100 years | Plume Area (km ²) |
| 100 | 0 | 9300 | 8.035184 | 100 | 0 | 12000 | 13.37804 |
| 95 | 5 | 12300 | 14.0553 | 95 | 5 | 13500 | 16.93158 |
| 90 | 10 | 15600 | 22.60888 | 90 | 10 | 14400 | 19.26437 |
| 85 | 15 | 19200 | 34.24778 | 85 | 15 | 16200 | 24.38147 |
| 80 | 20 | 21300 | 42.14918 | 80 | 20 | 17100 | 27.16578 |
| 75 | 25 | 22200 | 45.78633 | 75 | 25 | 18300 | 31.1123 |

| Table 33. Plume Areas for CO₂ plus CH₄ | | | | | | | |
|---|-----------------|--------------------------|-----------------|-----------------|-----------------|--------------------------|-------------------------------|
| Shallow | | | | Deep | | | |
| CO ₂ | CH ₄ | Plume Extent @ 100 years | CO ₂ | CO ₂ | CH ₄ | Plume Extent @ 100 years | Plume Area (km ²) |
| 100 | 0 | 9300 | 100 | 100 | 0 | 12000 | 13.37804 |
| 95 | 5 | 12300 | 95 | 95 | 5 | 13500 | 16.93158 |
| 90 | 10 | 15000 | 90 | 90 | 10 | 15000 | 20.90318 |
| 85 | 15 | 17400 | 85 | 85 | 15 | 16200 | 24.38147 |
| 80 | 20 | 20400 | 80 | 80 | 20 | 17700 | 29.10559 |
| 75 | 25 | 21900 | 75 | 75 | 25 | 18900 | 33.18589 |

| Table 34. Plume Areas for CO₂ plus H₂ | | | | | | | |
|--|----------------|--------------------------|-------------------------------|-----------------|----------------|--------------------------|-------------------------------|
| Shallow | | | | Deep | | | |
| CO ₂ | H ₂ | Plume Extent @ 100 years | Plume Area (km ²) | CO ₂ | H ₂ | Plume Extent @ 100 years | Plume Area (km ²) |
| 100 | 0 | 9300 | 8.035184 | 100 | 0 | 12000 | 13.37804 |
| 99 | 1 | 10200 | 9.665632 | 99 | 1 | 12900 | 15.45999 |
| 95 | 5 | 14400 | 19.26437 | 95 | 5 | 14700 | 20.07542 |
| 90 | 10 | 19800 | 36.42171 | 90 | 10 | 17400 | 28.12732 |
| 85 | 15 | 23700 | 52.18271 | 85 | 15 | 19800 | 36.42171 |

| Table 35. Plume Areas for CO₂ plus CO | | | | | | | |
|---|----|--------------------------|-------------------------------|-----------------|----|--------------------------|-------------------------------|
| Shallow | | | | Deep | | | |
| CO ₂ | CO | Plume Extent @ 100 years | Plume Area (km ²) | CO ₂ | CO | Plume Extent @ 100 years | Plume Area (km ²) |
| 100 | 0 | 9300 | 8.035184 | 100 | 0 | 12000 | 13.37804 |
| 99 | 1 | 9600 | 8.561944 | 99 | 1 | 12600 | 14.74929 |
| 95 | 5 | 13200 | 16.18743 | 95 | 5 | 14100 | 18.47005 |
| 90 | 10 | 17400 | 28.12732 | 90 | 10 | 15600 | 22.60888 |
| 85 | 15 | 20100 | 37.53376 | 85 | 15 | 17100 | 27.16578 |

| Table 36. Well and Monitoring Costs | |
|---|--|
| Quantity | Value |
| Single well injection cost | Uniform Distribution U(\$1.19M, \$3.2M) |
| Annual seismic monitoring cost (for WASP area) | Triangular Distribution tri(\$480K, \$611K, \$741K) |
| WASP Surface Area | 2,700 km ² |
| Single abandoned well plug removal Cost | Triangular Distribution tri(\$109,355, \$218,711, \$437,422) |
| Single well monitoring cost (CAPEX) | Triangular Distribution tri(\$87,993, \$124,167, \$170,340) |
| Single well monitoring cost (OPEX) per Lifetime of 20 years | Triangular Distribution tri(\$599,900, 683,600, 787,300) |

Finally spatial well densities from Watson and Bachu³⁵ are shown in Table 37.

| Table 37. Abandoned Well Spatial Densities in Central Alberta | |
|--|---|
| Type | Value |
| High Density | Triangular Distribution tri(45, 216, 721) wells/km ² |
| Medium Density | Triangular Distribution tri(8, 61, 144) wells/km ² |
| Low Density | Triangular Distribution tri(0, 11, 130) wells/km ² |
| Overall | (Low+Medium+High)/3 |

6.6. Software Implementation

The TEM was implemented in GoldSim version 10.5, a probabilistic modelling software environment (i.e. tool) designed for performance assessment of engineered systems such as mines, geological storage and chemical processing plants. It has been used by Los Alamos National Laboratory in their CO₂ PENS Model⁴⁷.

GoldSim is a graphically based tool and comprises a series of elements (shown as icons) which contain data, equations and results. One particular type of element is a container which groups together large sub-components of the model such as a major subsystem like Capture or EOR. The model is of medium complexity and comprises 850 elements. Each element is linked to another element via a series of influences denoted as arrows. GoldSim is also hierarchical and is therefore “top-down”. Figure 60 shows the top level system diagram which comprises the 4 major subsystem containers and also containers which house common data.

Figure 61 shows the Capture Model which comprises cost calculation for the purest capture plant and the other 5 capture plants.

Figure 62 shows the Pipeline Model which comprises a container for the pipeline diameter calculation using the MIT method which is shown in Figure 63. Note that the diameter calculation contains the density calculation which contains the approximation to the GERG 2008 equation of state.

Figure 64 shows the top level model for EOR. The bulk of the calculations are concerned with impure recovery and in particular the MMP ratio calculation which is shown in Figure 65.

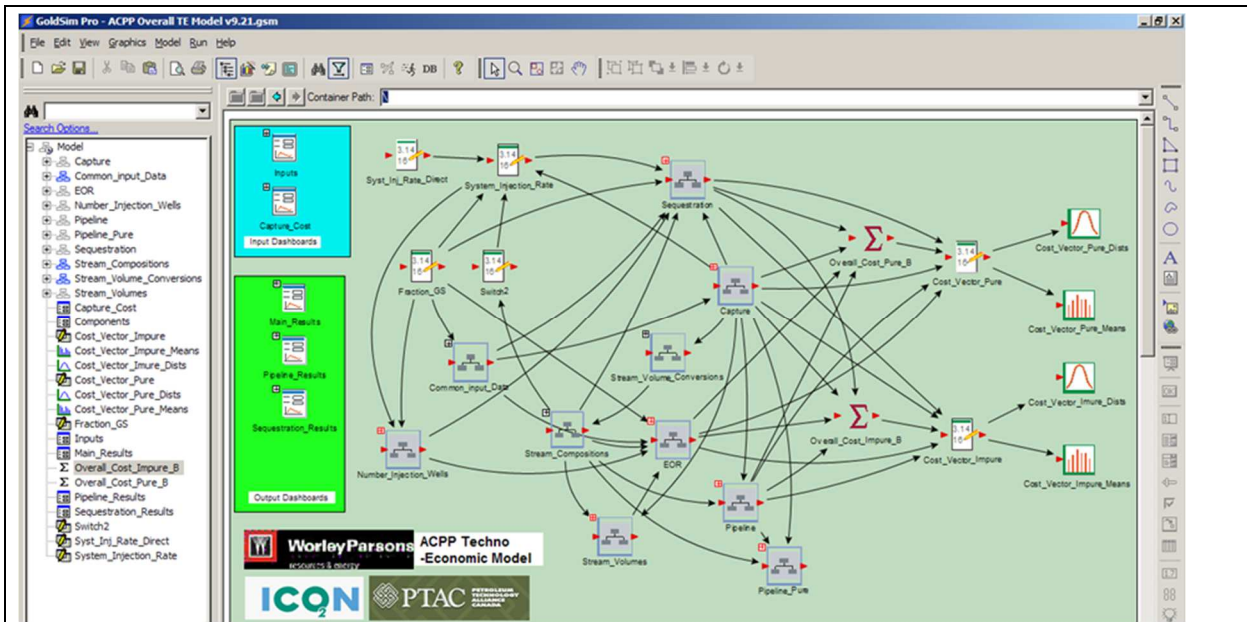


Figure 60. Top level System Model

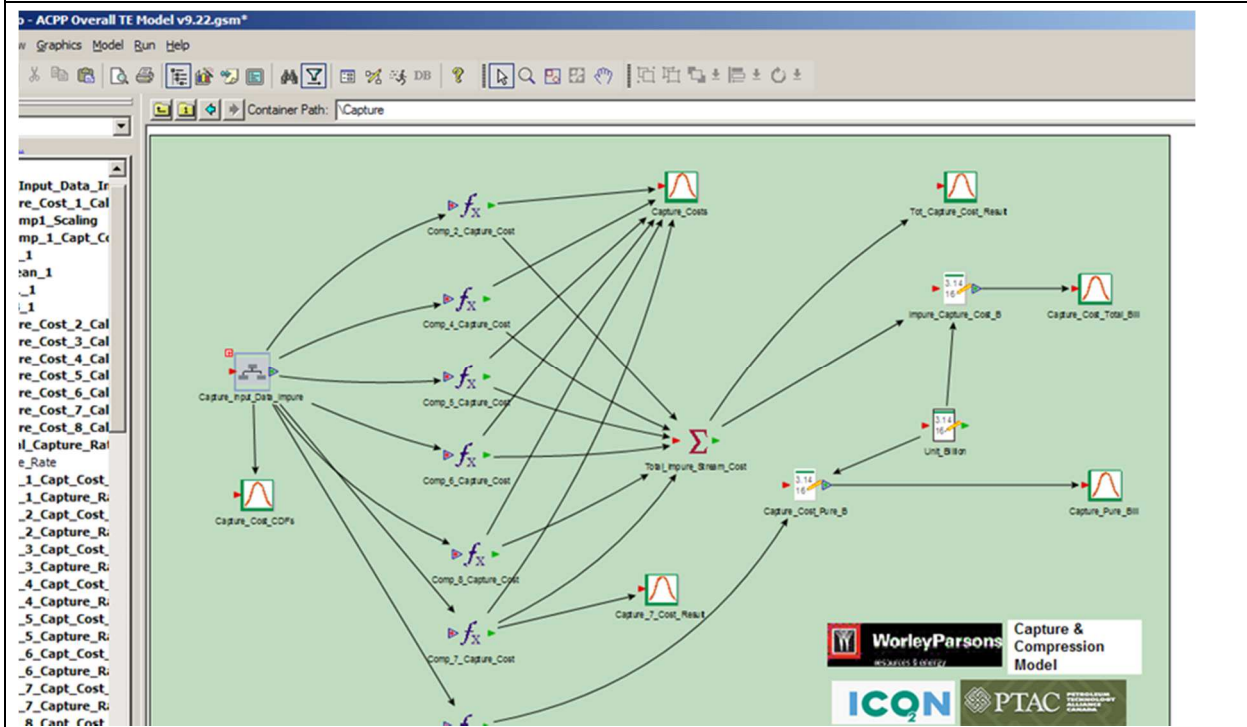


Figure 61. Capture Model

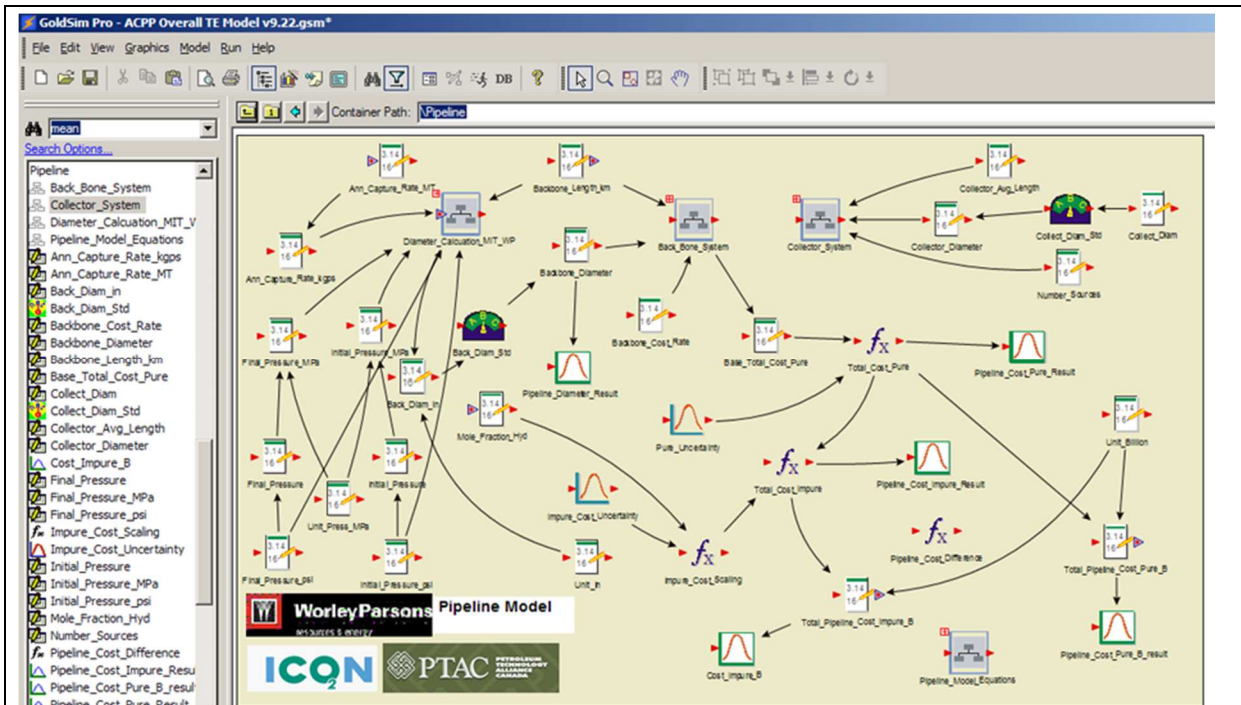


Figure 62. Pipeline Model

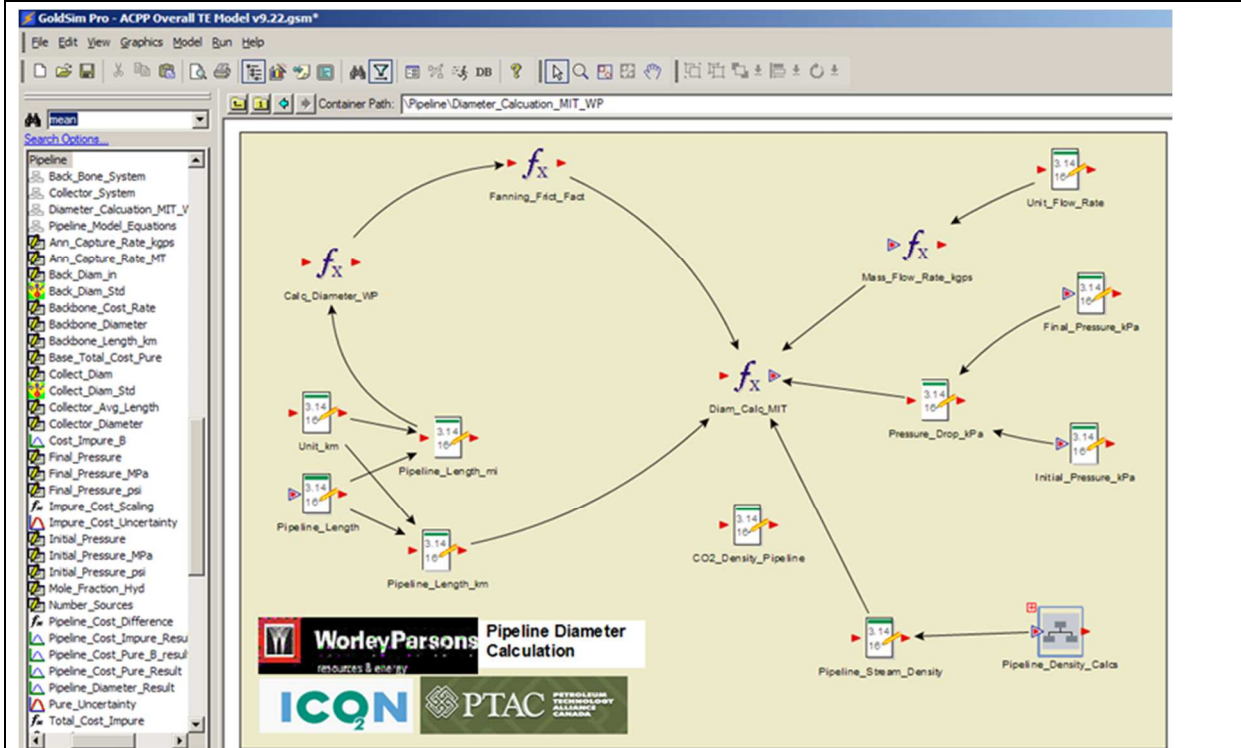


Figure 63. Pipeline Diameter Calculations

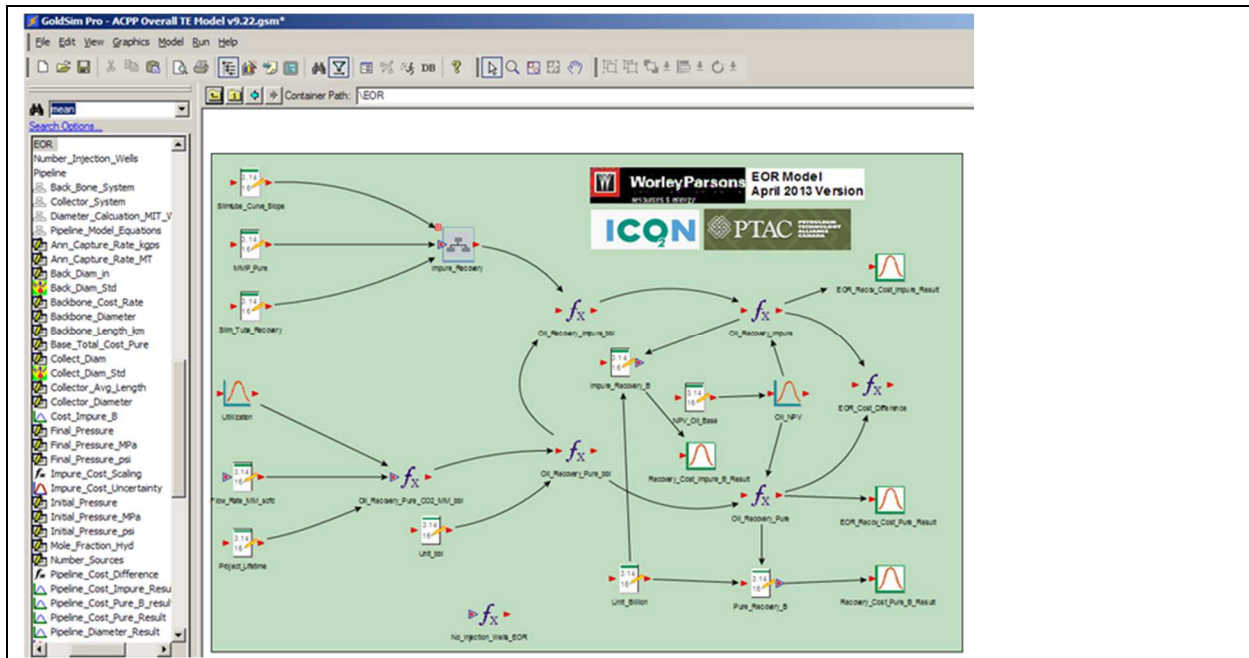


Figure 64. Enhanced Oil Recovery Model

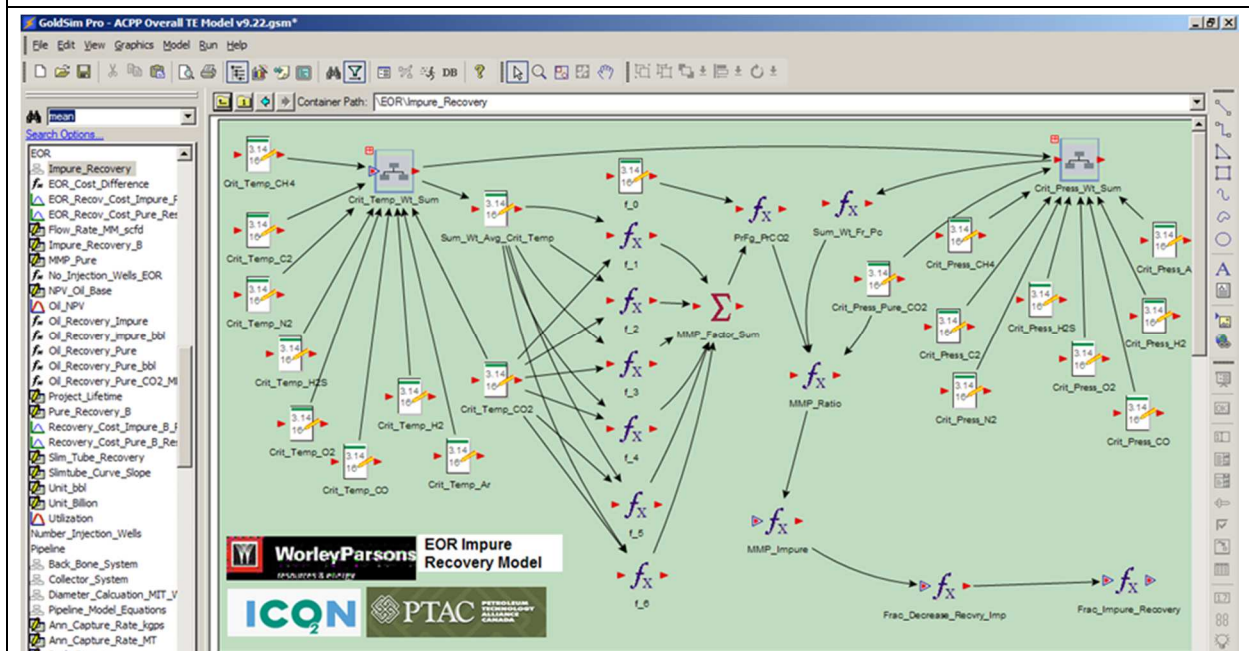


Figure 65. EOR Software: Impure Recovery

The impure recovery model involves calculations involving critical temperatures and critical pressures which are shown in Figure 66 and Figure 67 respectively.

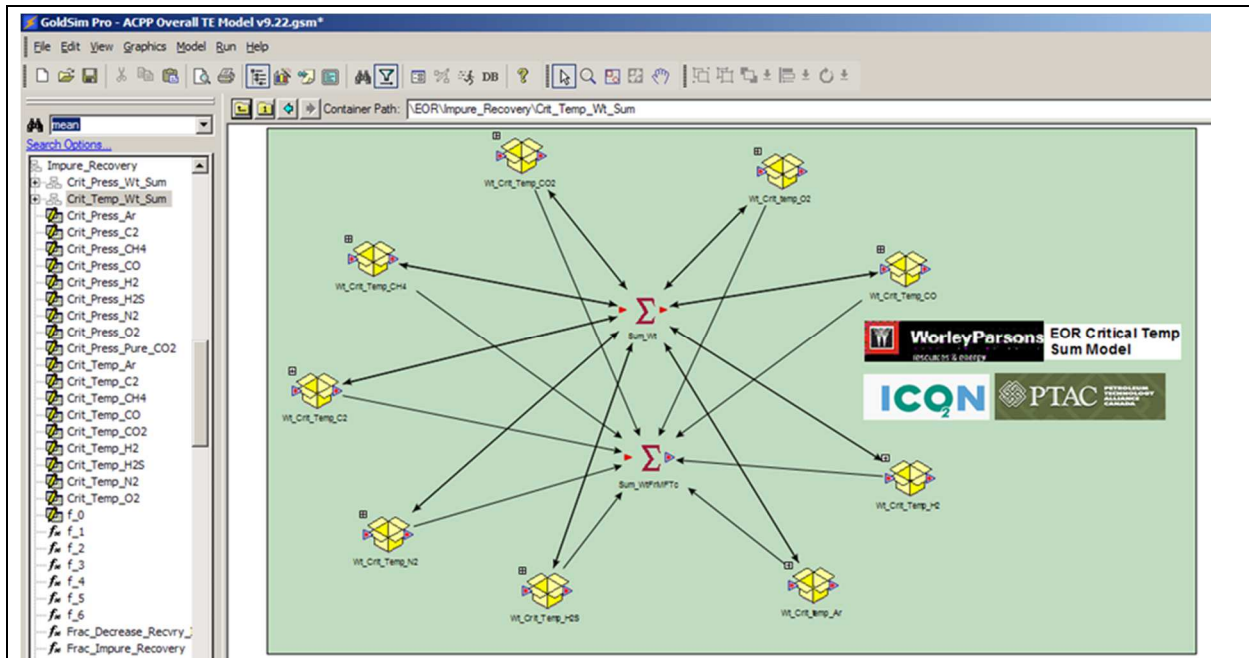


Figure 66. Calculations involving Critical Temperatures

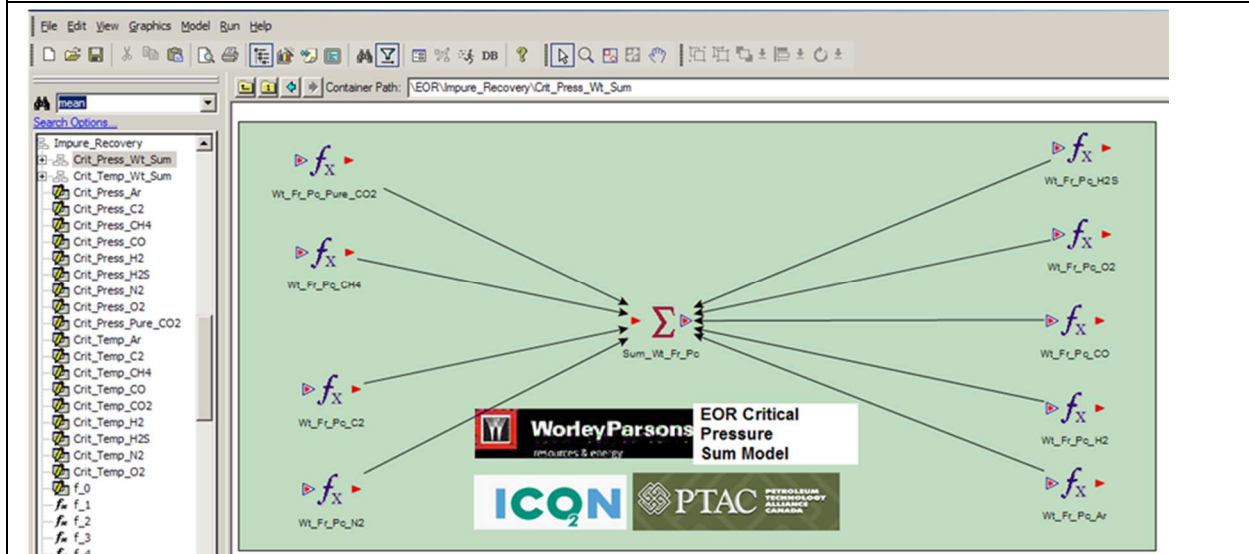


Figure 67. Calculations involving Critical Pressures

Figure 68 shows the top level model for sequestration. This is divided into the plume area calculation for deep and shallow reservoirs shown in Figure 69 and spatial well density calculation in Figure 70. The number of injection wells calculation is shown in Figure 71 and the overall cost for sequestration calculation is shown in Figure 72.

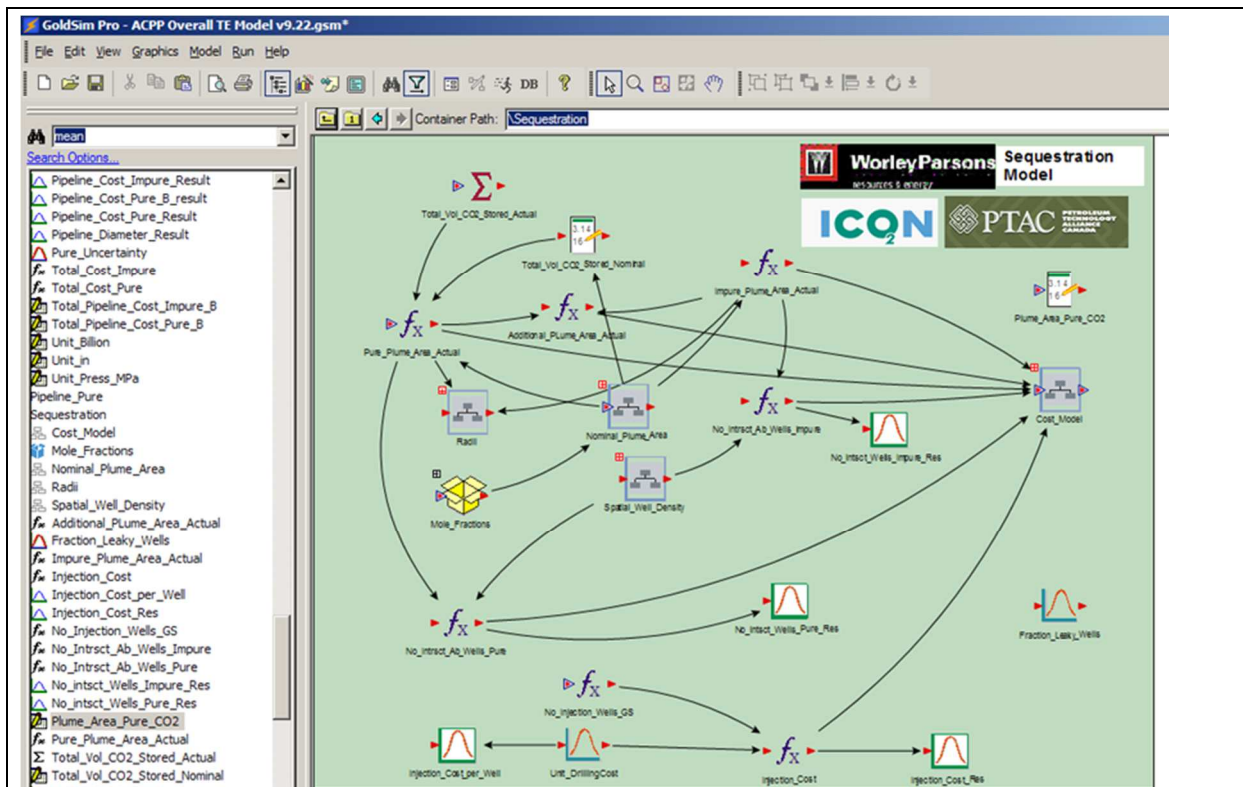


Figure 68. Sequestration Model

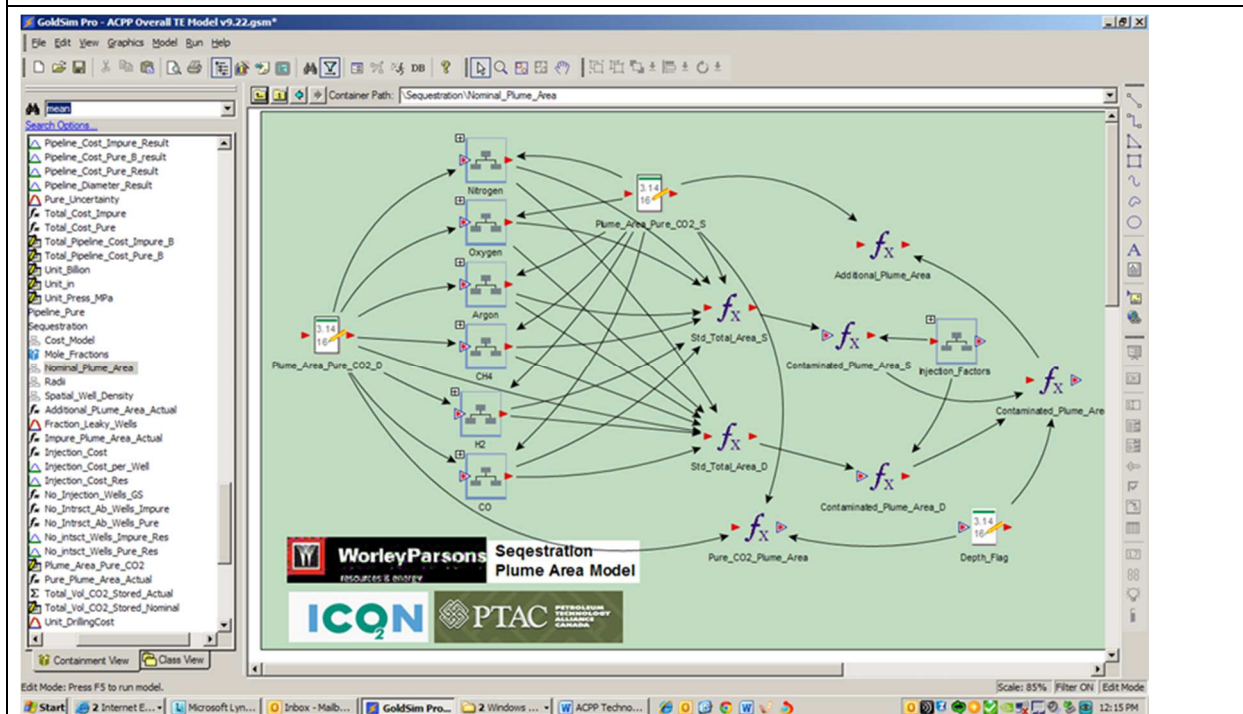


Figure 69. Plume Area Calculations

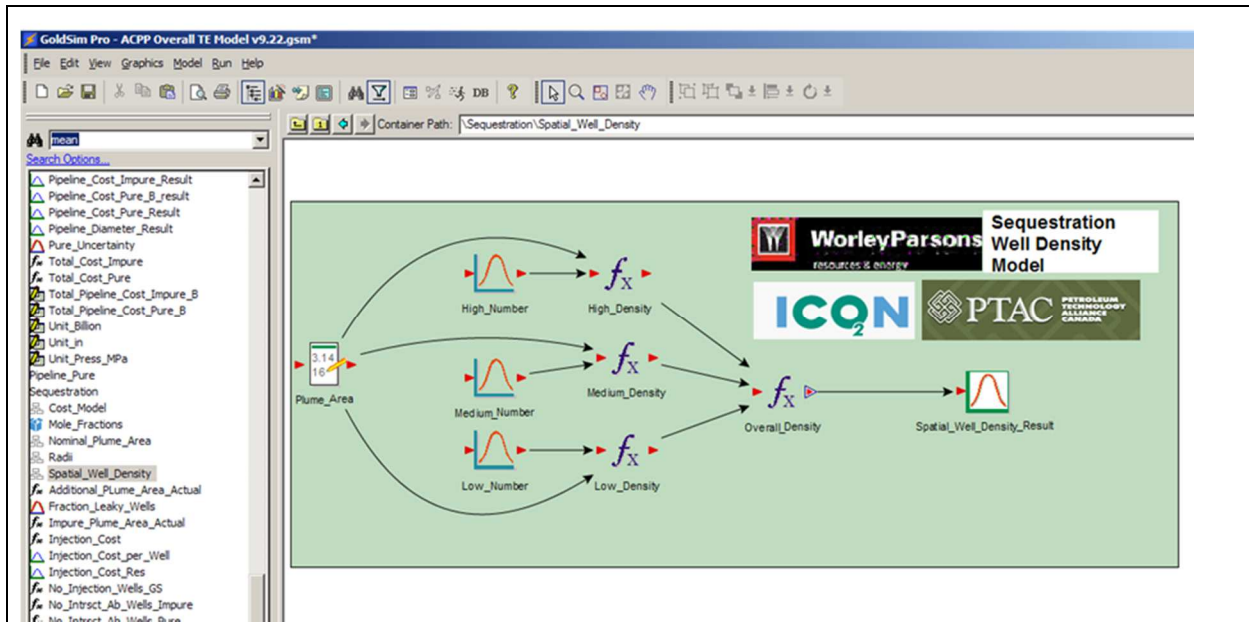


Figure 70. Spatial Well Density Calculations

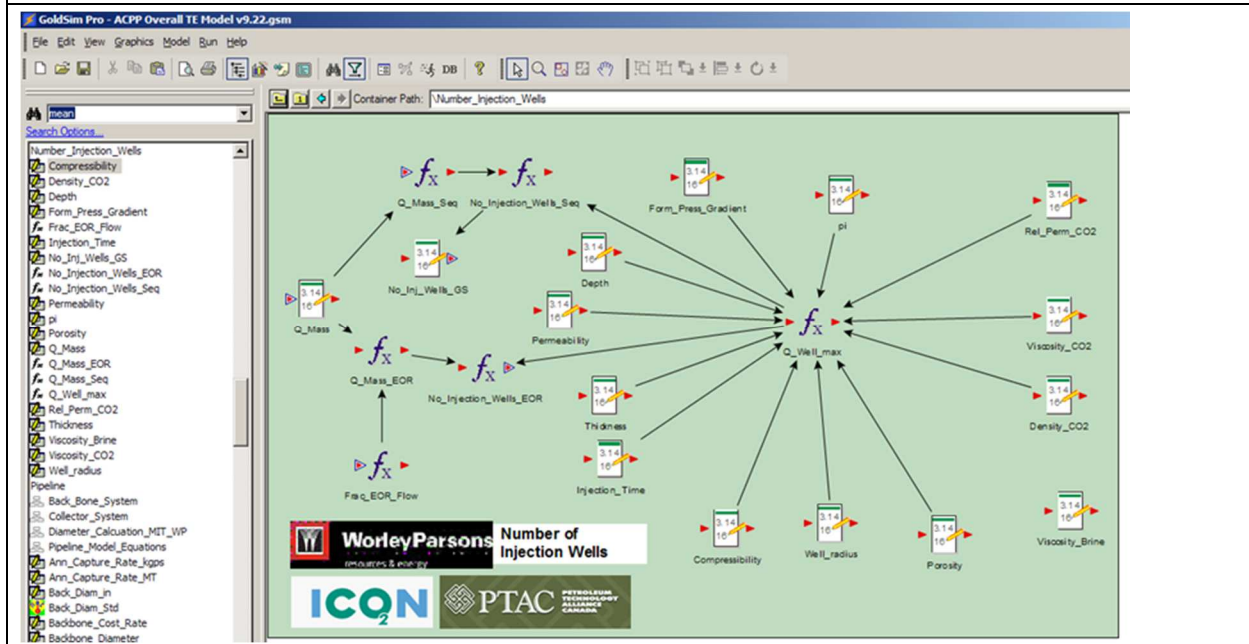


Figure 71. Number of Injection Wells Calculations

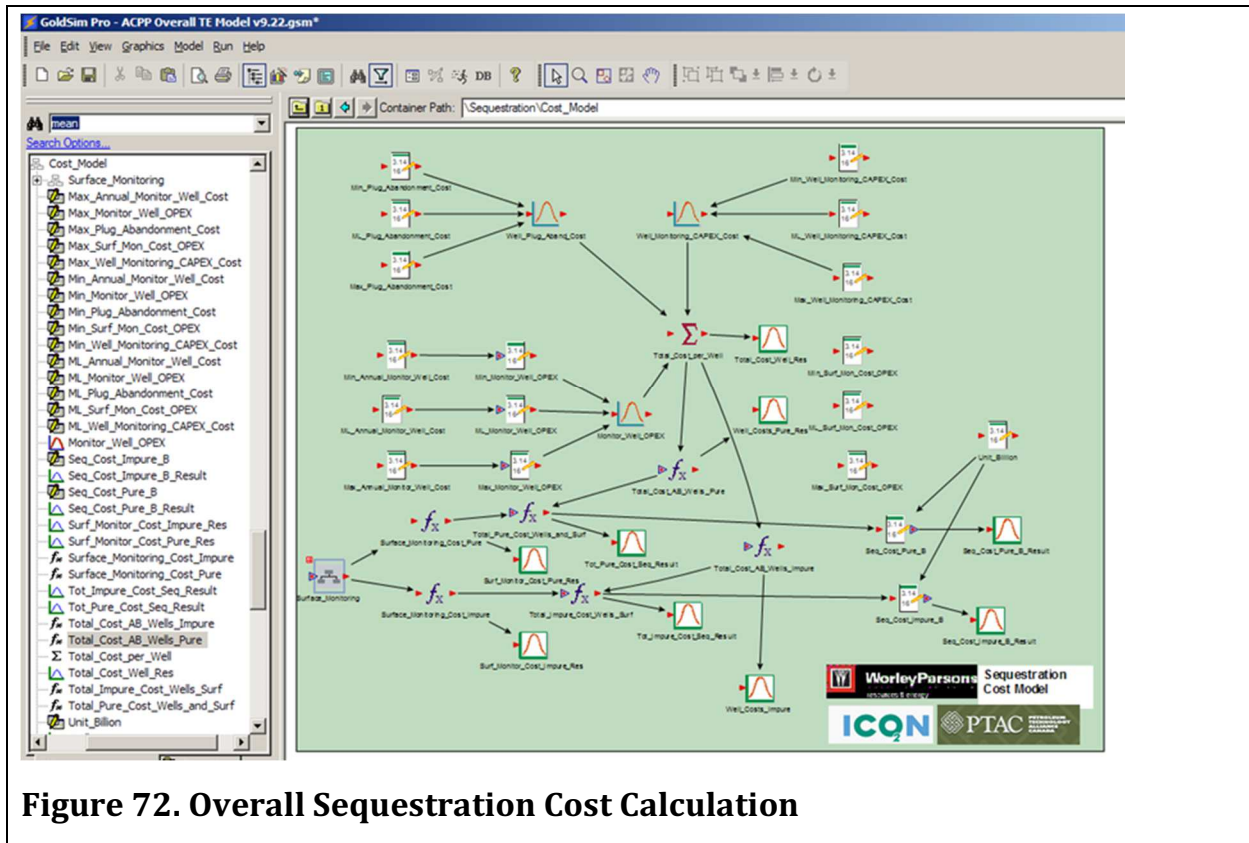


Figure 72. Overall Sequestration Cost Calculation

6.7. Results

One advantage of using GoldSim is that it provides user-interface dashboards for displaying inputs and outputs to and from the model. Figure 73 shows the input dashboard for the Techno-economic Model and Figure 74 shows the output dashboard. Inputs are self-explanatory and are described in detail in Sections 6.3 and 6.4.

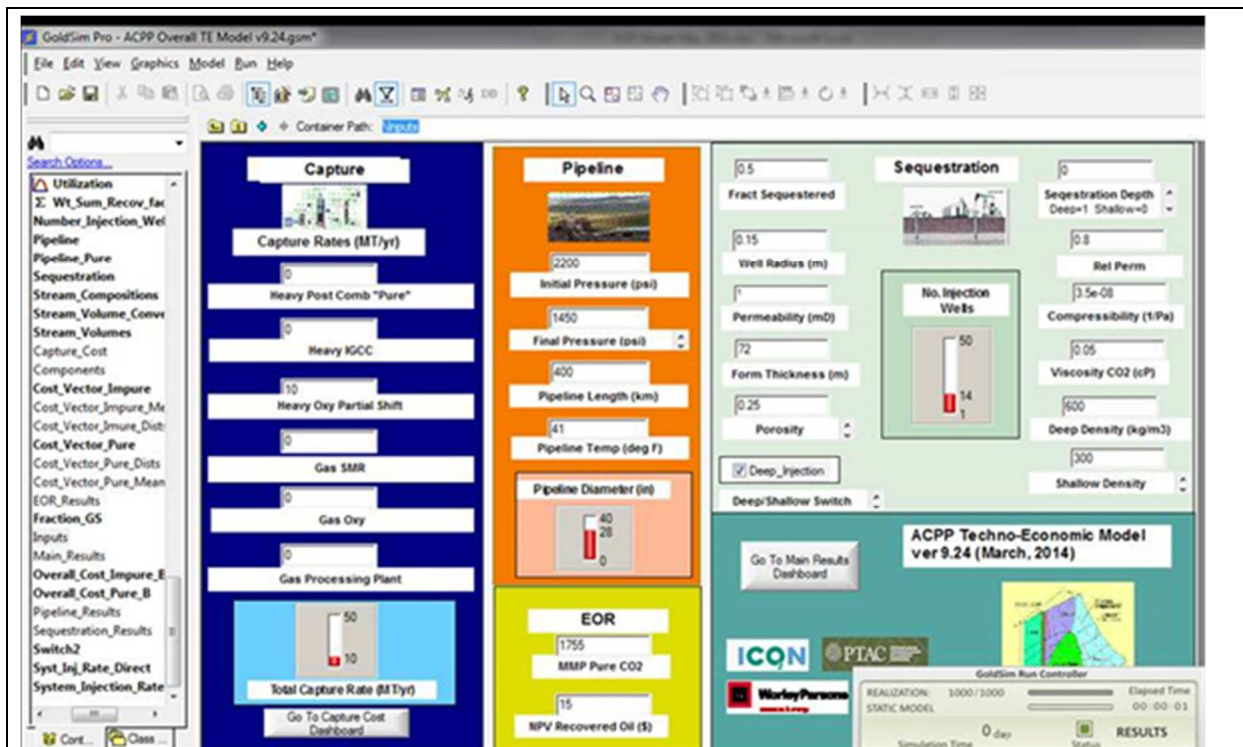


Figure 73. Input Dashboard for Techno-economic Model

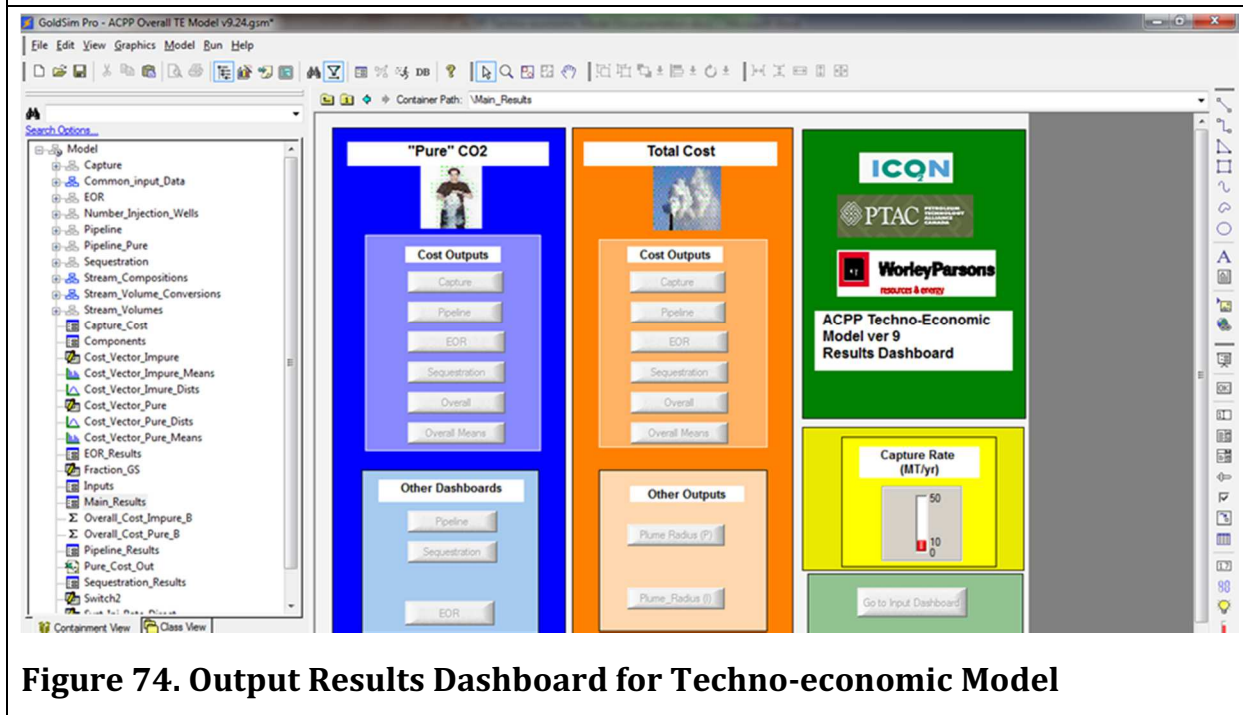


Figure 74. Output Results Dashboard for Techno-economic Model

Many different outputs can be displayed. The main outputs are cost for each subsystem for both pure CO₂ and impure CO₂. These are in the form of cumulative distribution functions (CDFs) as shown in Figure 75 to Figure 80 for 10 MT of CO₂ captured from each type of capture plant.

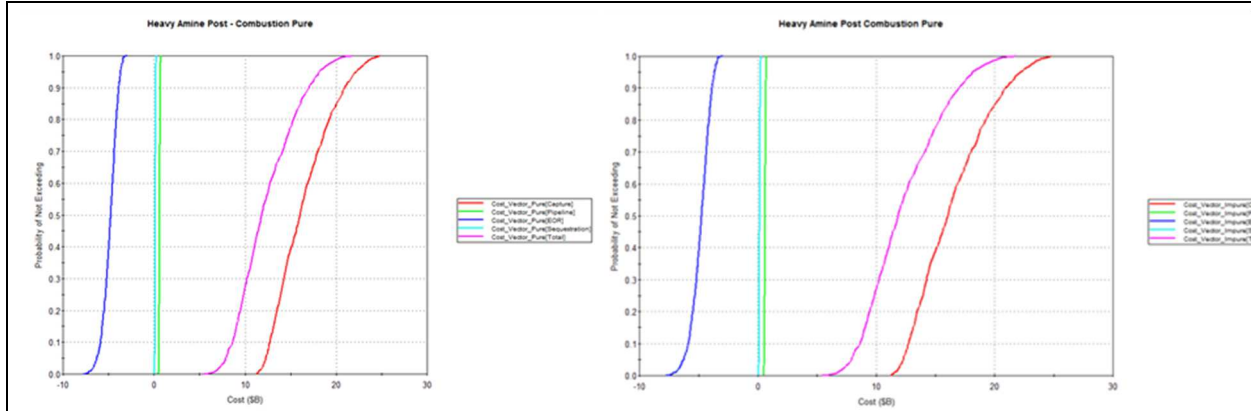


Figure 75. 10MT Heavy Amine Post - combustion

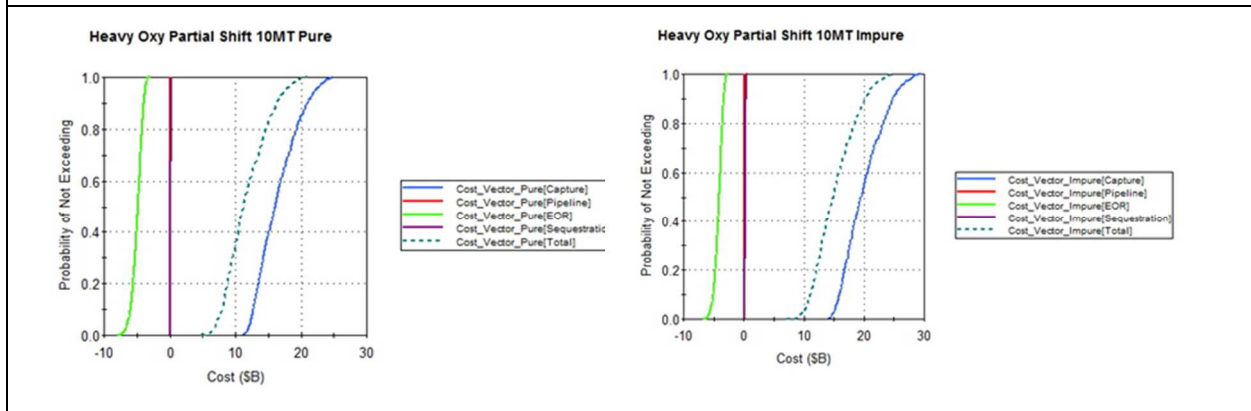


Figure 76. 10MT Heavy Oxy

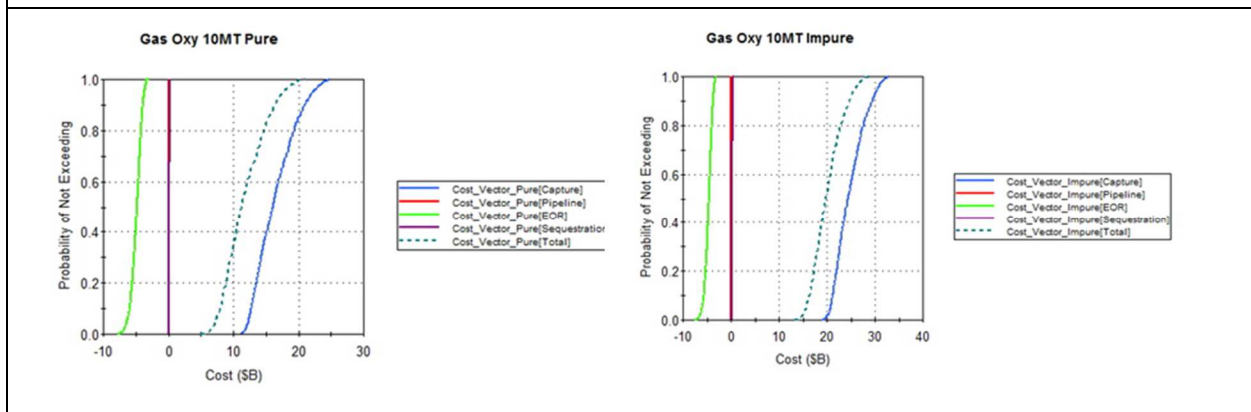


Figure 77. 10MT Natural Gas Oxy

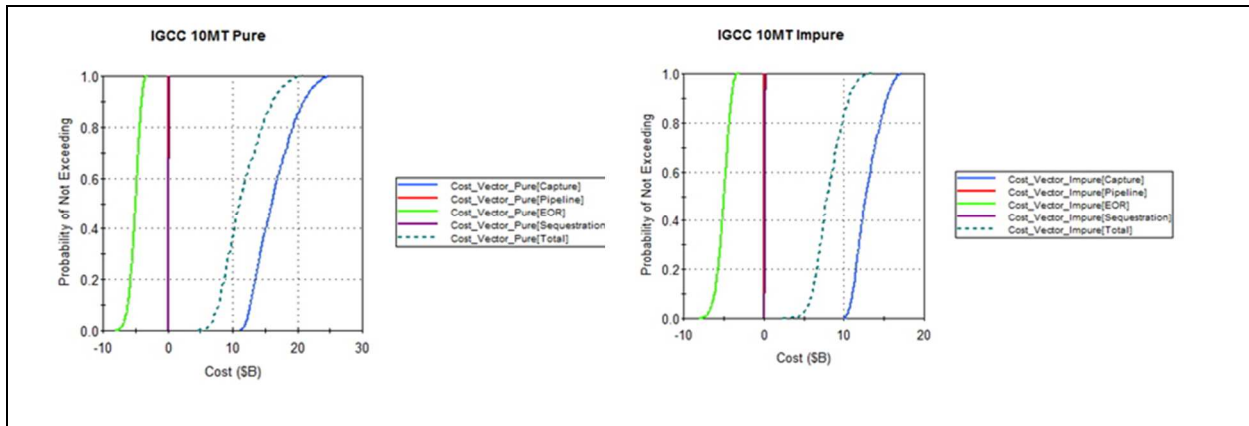


Figure 78. 10MT IGCC Partial Shift

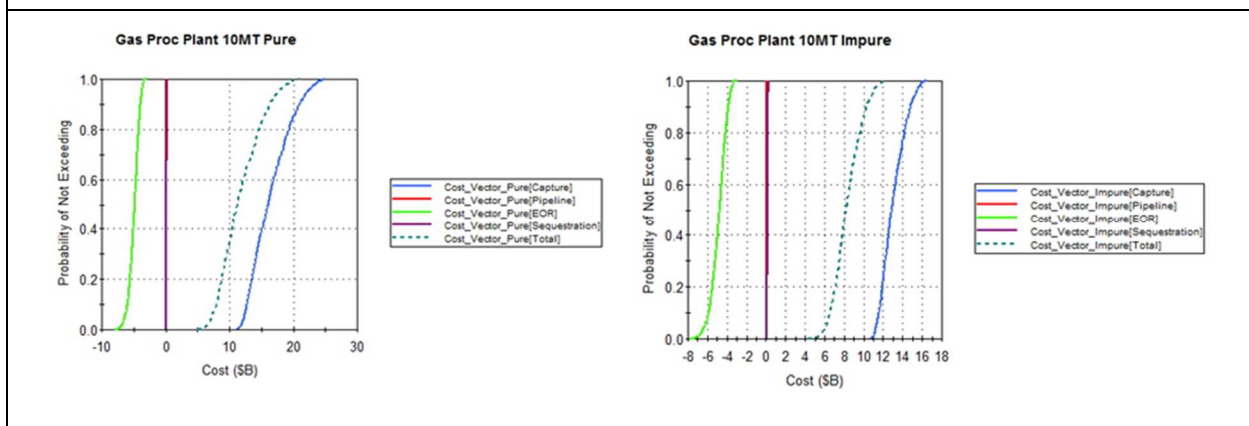


Figure 79. 10MT Various Natural Gas Processing Plant

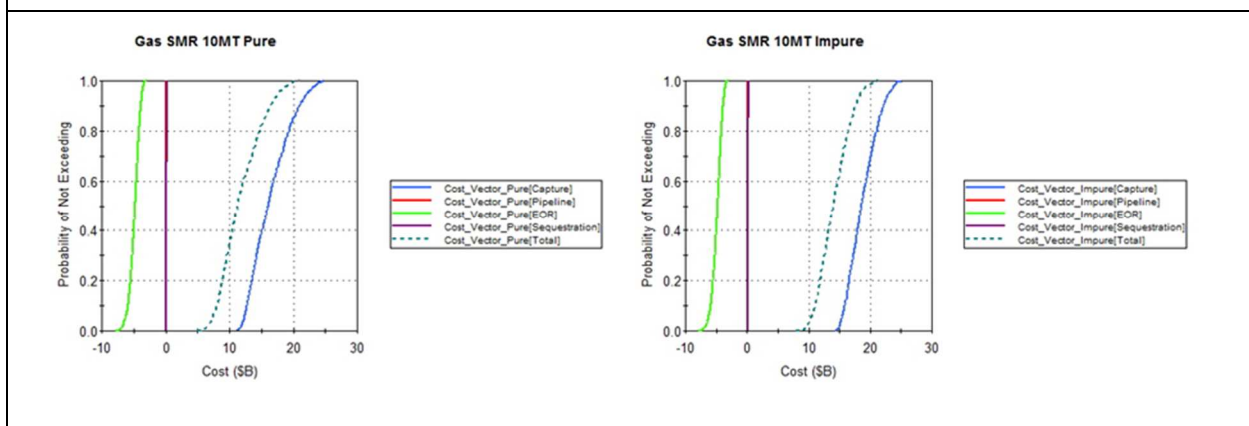


Figure 80. 10MT Natural Gas Steam Methane Reforming (SMR)

Figure 81 shows the mean values for each subsystem plotted on a single graph for pure CO₂, using the Heavy Oxy Partial Shift capture technology as the example. Figure 82 shows the same type of plot, but for impure CO₂. In both cases the costs of implementing CCS increase with increasing capture rate where 50% of the CO₂ is used for EOR and 50% is sequestered. For this particular

capture technology, the costs of an impure stream are greater than for a corresponding pure stream but this is not always the case. Note these plots were developed in Microsoft Excel from extracting the results table for all Monte Carlo realizations by clicking on the Overall buttons (pure and impure buttons), clicking on the GoldSim results icon (looks like a table) and pasting into Excel.

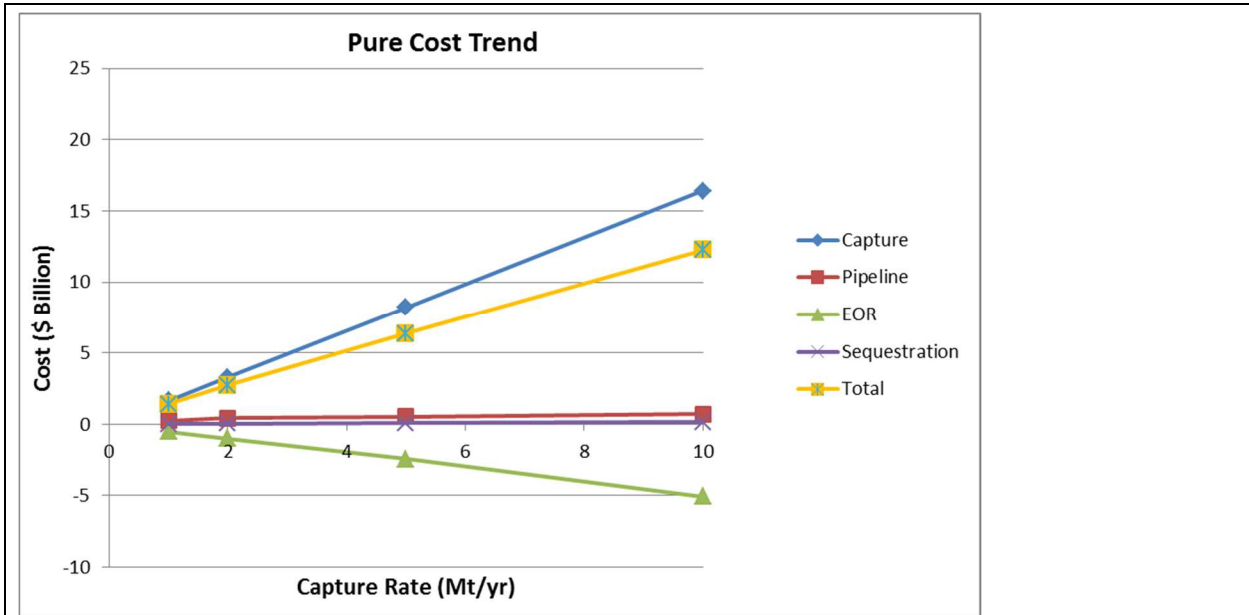


Figure 81. All Costs vs. Capture Rate: Pure CO₂

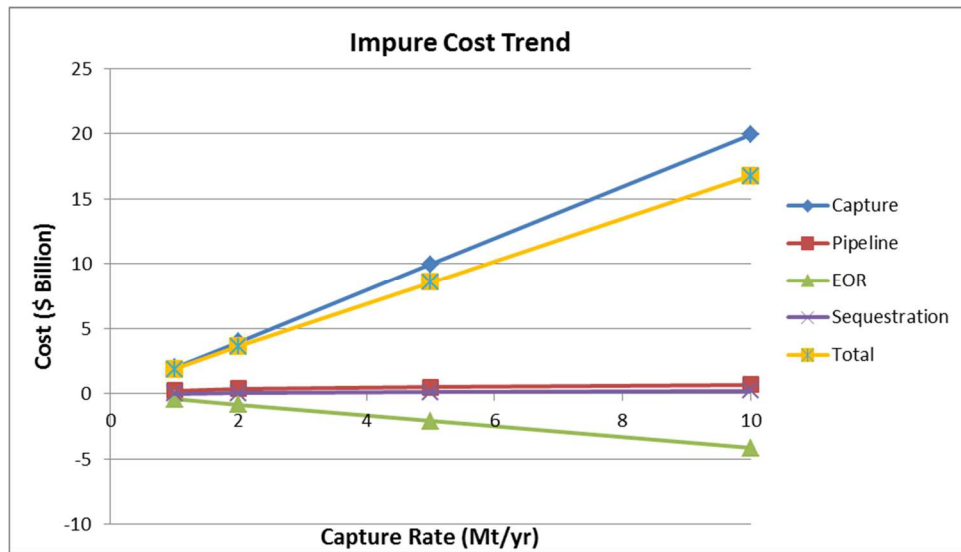


Figure 82. All Costs vs. Capture Rate: Impure CO₂

Figure 81 and Figure 82 show that all costs increase as a function of capture flow rate, except EOR which decreases as expected. The overall cost for pure CO₂ is higher than for impure CO₂, again as expected because capture cost dominates.

Note also that dashboards were developed for Pipeline, EOR and Sequestration intermediate calculations. These allow such intermediate calculations as pipeline diameter and realizable pipeline diameter to be explored as a function of capture rate, capture composition (as set by capture plant types), pressure drop across the pipeline, temperature at the midpoint and pipeline length to be displayed. These outputs are useful for pipeline design as well all have an impact on pipeline cost. The dashboards are shown in Figure 83 to Figure 85.

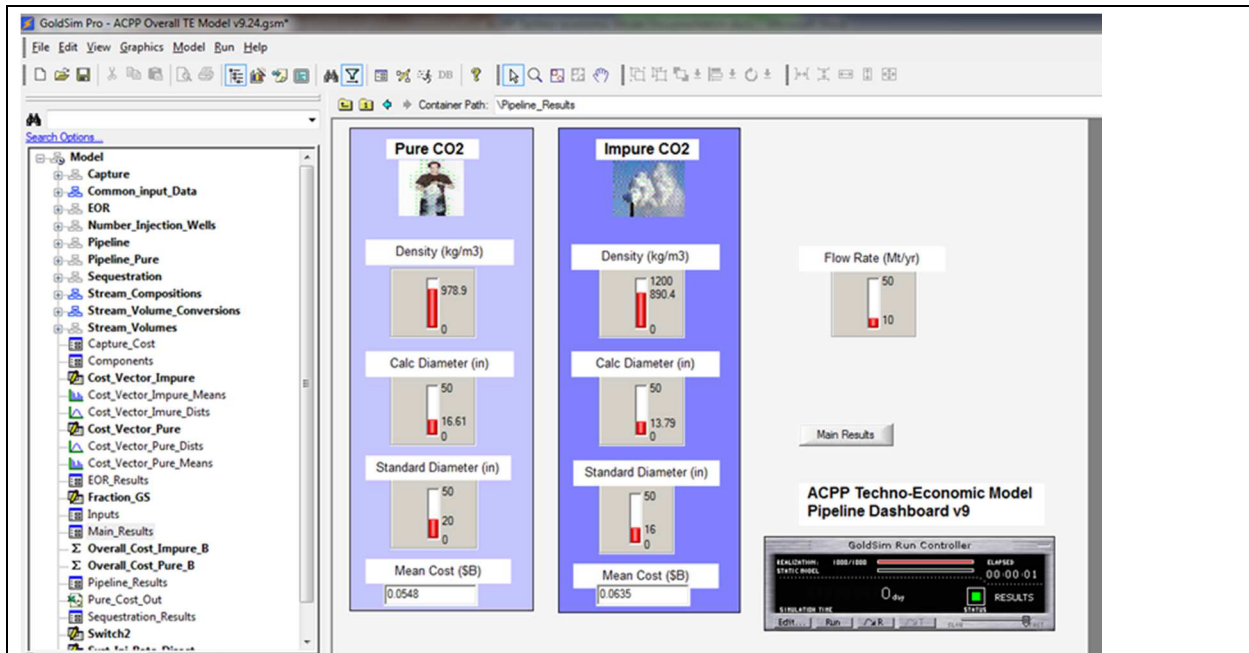


Figure 83. Pipeline Dashboard

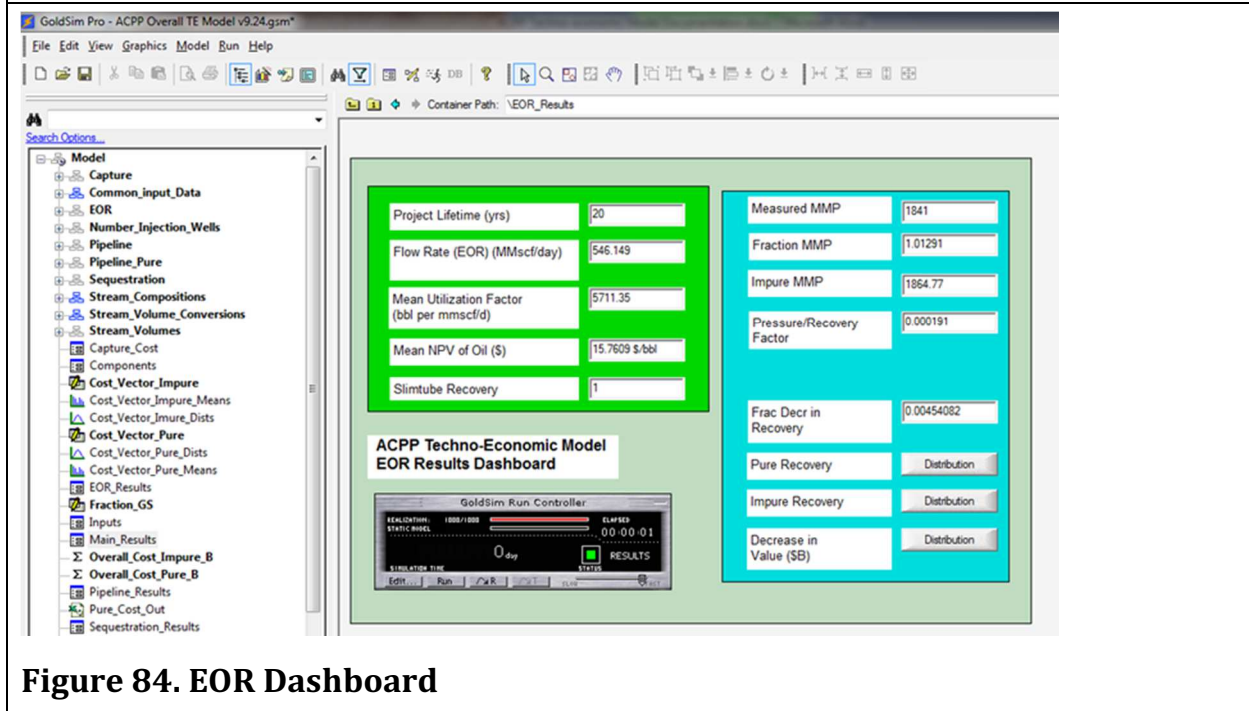


Figure 84. EOR Dashboard

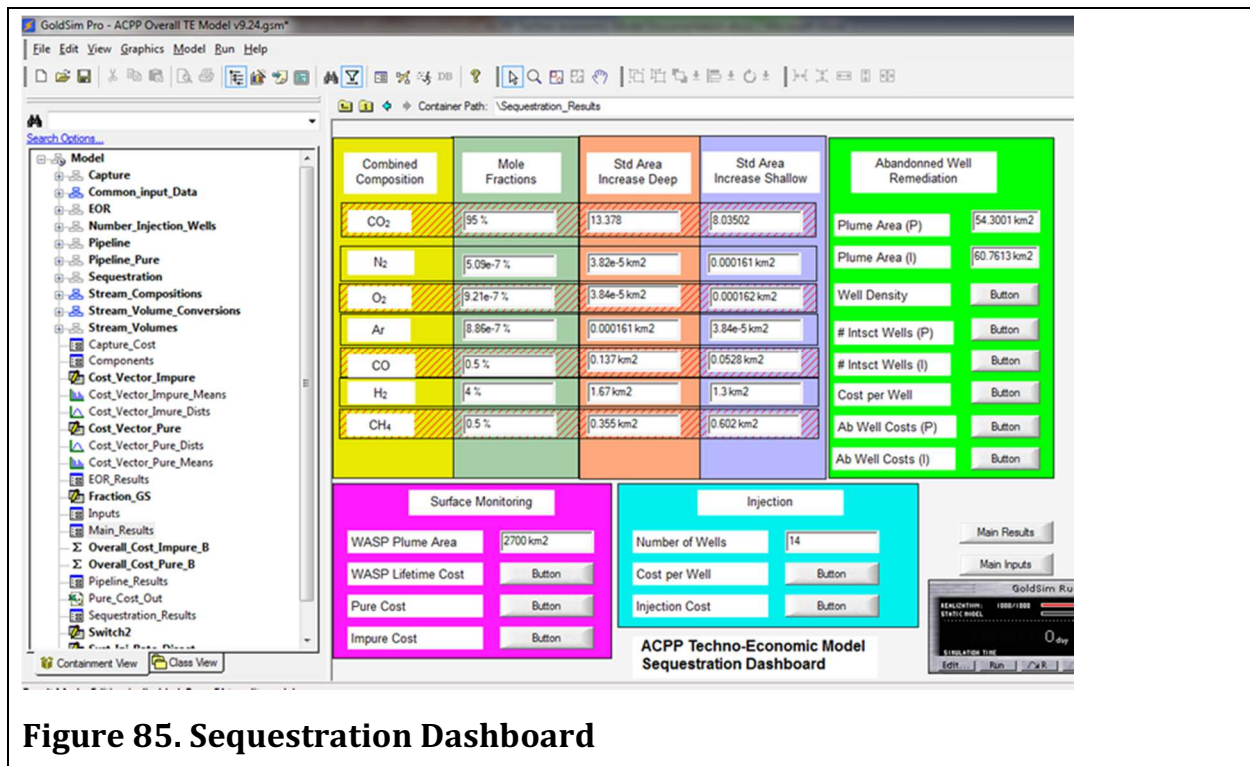


Figure 85. Sequestration Dashboard

6.8. Conclusions

A techno-economic model was developed and implemented in GoldSim, a probabilistic system modelling software environment. This allows the user to plug-and-play and change many system inputs pertaining to the following inputs:

- Capture plant type and annual volume of CO₂ captured each year
- Pipeline input parameters
- EOR input parameters
- Sequestration inputs parameters

Probability distribution functions (probability density function and cumulative distribution function) and properties of those distributions (mean and percentile values) are output from the model for Capture, Pipeline, EOR and Sequestration.

Dashboards for Pipeline, EOR and Sequestration allow the user to show intermediate calculations which contribute to cost.

A system top-down approach to modelling was utilized exploiting the object-oriented and diagrammatic features of GoldSim. Inputs from the ACPPTechno-Economic Model managers for each subsystem were implemented in to the model. These were at different levels of complexity to reflect the relative technical maturity of each subsystem.

This model was developed for use as a planning tool and can be used to provide information for high level decision-making. In particular, it provides information about the effect of CO₂ purity and volume captured on the costs of Capture, Pipeline, EOR and Sequestration. It can be used to made design decisions for making trade-offs as is necessary in the design of any complex system.

7. Phase 4 – Preparing and Sharing Project Outcomes

The purpose of Phase 4 is knowledge mobilization and it is now taking place with the publication of this ACPP Final Report, the distribution of the techno-economic model to ACPP participants, and presentations at selected industry and academic gatherings.

For examples, key findings of this work are to be presented at the Carbon Management Annual Conference in May 2014.

The techno-economic model will be used by individual companies and government departments to apply proprietary or regional data in reaching conclusions relevant to their industrial opportunity or policy need.

8. Conclusion

The ACPP Project examined the technical and cost impact of impurities on each of the four elements of the CCS value chain:

- Capture of CO₂ emissions from large industrial facilities;
- Transportation of the CO₂ through pipelines; and
- Permanent storage of the CO₂ in deep underground formations:
 - Oil reservoirs where CO₂ is utilized for EOR;
 - Deep saline aquifers (sequestration).

As the world moves to capture and utilize anthropogenic CO₂, current industrial experience with geologic CO₂ is not sufficient. With anthropogenic CO₂, the number of potential contaminants increases, including compounds that are poorly understood from the point of view of their impact on CCS. The amount and properties of these impurities will impact differently the elements of the CCS value chain and the purity specification that would optimize performance and cost throughout the CCS value chain is not obvious.

During Phase 1, ACPP conducted a number of literature searches and consultations with industry and academics in order to understand the current state of knowledge. This led to the identification of knowledge gaps in each of the 4 CCS value chain elements with respect to the impact of impure CO₂ compositions that are mostly likely to become industrially relevant in Canada. It also led to the realisation that it is unlikely that there would be a single “made in Alberta” purity specification, and ACPP decided to develop a techno-economic model that could be used to find the optimum purity for any particular project.

Phase 2 was composed of a number of laboratory and numerical modeling work packages aimed at filling specific knowledge gaps:

- The impact of anthropogenic impurities was investigated on the dew point of supercritical CO₂. Results indicate that if water content is at or below the industrially important concentration of 500 ppm, the presence of typical anthropogenic impurity compositions is not likely to result in the dew point occurring within typical industrial pressure and temperature conditions.
- The presence of anthropogenic impurities, particularly low molecular weight compounds such as H₂, was found to reduce pipeline flow transportation capacity. The extent of such reduction will depend of the nature and the amount of the impurities.
- The impact of natural and anthropogenic impurities of the performance of EOR was quantified in laboratory experiments. All anthropogenic impurities are expected to negatively impact EOR performance.
- Impurities were also found to reduce the viscosity and density of CO₂ stored in deep saline aquifers, resulting in a larger aerial extent of the stored CO₂ plume. The impacts are to

increase the scale of regional monitoring infrastructure but to reduce the time of such monitoring. The presence of oxygen could alter the geochemistry of the host rock, in particular when ferrous-iron bearing minerals are present

The information analysed in Phase 1 and generated in Phase 2 was integrated into the ACP model techno-economic model during Phase 3. The ACP model allows the user to specify the characteristics of the CCS value chain under study and inquire as to the cost impact of various impurity compositions, as compared to industrially pure CO₂. The flexibility of the model will allow individual companies and government jurisdiction to model the impact of CO₂ purification decisions in order to arrive at the optimum design for each situation.

9. References

- 1 Wiebe, R. & Gaddy, V. L. Vapor Phase Composition of Carbon Dioxide-Water Mixtures at Various Temperatures and at Pressures up to 700 Atmospheres. *J. Am. Chem. Soc.* **63**, 475–477 (1941).
- 2 Wiebe, R. & Gaddy, V. L. The Solubility of Carbon Dioxide in Water at Various Temperatures from 12 to 40° and at Pressures to 500 Atmospheres. Critical Phenomena*. *J. Am. Chem. Soc.* **62**, 815–817 (1940).
- 3 Song, K. Y. & Kobayashi, R. Water Content of CO₂ in Equilibrium With Liquid Water and/or Hydrates. *SPE Form. Eval.* **2**, 500–508 (1987).
- 4 Coan, C. . R. & King, A. D. J. Solubility of water in compressed carbon dioxide, nitrous oxide, and ethane. Evidence for hydration of carbon dioxide and nitrous oxide in the gas phase. *J. Am. Chem. Soc.* **93**, 1857–1862 (1971).
- 5 Bamberger, a., Sieder, G. & Maurer, G. High-pressure (vapor+liquid) equilibrium in binary mixtures of (carbon dioxide+water or acetic acid) at temperatures from 313 to 353 K. *J. Supercrit. Fluids* **17**, 97–110 (2000).
- 6 Briones, J. A., Mullins, J. C., Thies, M. C. & Kim, B.-U. Ternary phase equilibria for acetic acid-water mixtures with supercritical carbon dioxide. *Fluid Phase Equilib.* **36**, 235–246 (1987).
- 7 Dohrn, R., Bünz, A. P., Devlieghere, F. & Thelen, D. Experimental measurements of phase equilibria for ternary and quaternary systems of glucose, water, CO₂ and ethanol with a novel apparatus. *Fluid Phase Equilib.* **83**, 149–158 (1993).
- 8 Tödheide, K. & Franck, E. U. Das Zweiphasengebiet und die kritische Kurve im System Kohlendioxid–Wasser bis zu Drucken von 3500 bar. *Z. Phys. Chemie, Neue Folge* **37**, 387–401 (1963).
- 9 D'Souza, R., Patrick, J. R. & Teja, A. S. High Pressure Phase Equilibria in the Carbon Dioxide - n-Hexadecane and Carbon Dioxide-Water Systems. *Can. J. Chem. Eng.* **66**, 319–323 (1988).
- 10 Jackson, K., Bowman, L. E. & Fulton, J. L. Water Solubility Measurements In Supercritical Fluids and High-Pressure Liquids Using Near-Infrared Spectroscopy. *Anal. Chem.* **67**, 2368–2372 (1995).
- 11 M. Mohitpour, P. Seevam, K.K. Botros, B. Rothwell, C. Ennis: "Pipeline Transportation of Carbon Dioxide Containing Impurities", ASME, in Press.
- 12 O. Kunz, R. Klimeck, W. Wagner, M. Jaeschke, M. "The GERG-2004 Wide-Range Equation of State for Natural Gases and Other Mixtures", Groupe Européen de Recherches Gazières (GERG), Technical Monograph, GERG TM15 (2007).

-
- 13 Botros, K.K., Piazza, M. and Abayarathna, D.: "Tools and Methods for Internal Pipe Coating Evaluation for Gas Transmission Systems", ASME 9th International Pipeline Conference & Exhibition, TELUS Convention Centre, Calgary, Alberta, Canada, September 24-28, 2012.
- 14 C. F. Colebrook, "Turbulent flow in pipes, with particular reference to the transition region between smooth and rough pipe laws," *Journal of the Institution of Civil Engineers (London)*, 1939.
- 15 Rocha, P. S., Alves, D. R., Costa, G. M. N., "Pure and Impure CO₂ Minimum Miscibility Pressure: Comparing Sixteen Correlations", found on website:
http://www.isasf.net/fileadmin/files/Docs/Arcachon/posters/p25-P36_Pure%20and%20ImpureCO2%20Minimum%20Miscibility%20Pressure%20-%20Comparing%20Sixteen.pdf
- 16 Emera, M. K., and H. K. Sarma, "Genetic Algorithm (GA)-Based Correlations Offer More Reliable Prediction of Minimum Miscibility Pressures (MMP) Between Reservoir Oil and CO₂ or Flue Gas, *JCPT*, August 2007, Volume 46, No. 8, Pg 19-25
- 17 EOR and CO₂ disposal – economic and capacity potential in the North Sea, Torleif Holt and Erik Lindeberg, SINTEF Petroleum Research, Trondheim Norway, Presentation to the 4th Trondheim Conference on CO₂ Capture, Transport and Storage, October 16 - 17 2007, Trondheim Norway
- 18 Shaw, J and S. Bachu, "Screening, Evaluation, and Ranking of Oil Reservoirs Suitable for CO₂-Flood EOR and Carbon Dioxide Sequestration", *JCPT*, September 2002, Volume 41, No. 9, Pg 51-61
- 19 IEAGHG, 2011, Effects of Impurities on Geological Storage of CO₂, report 2011/04 prepared by CanmetENERGY, Natural Resources Canada, June, 63 pages + Appendices.
- 20 Wang, J., D. Ryan, E. J. Anthony, N. Wildgust, and T. Aiken, 2011, Effects of impurities on CO₂ transport, injection and storage, *Energy Procedia*, Vol.4, Proceedings of 10th International Conference on Greenhouse Gas Control Technologies GHGT10, September 19–23, Amsterdam, The Netherlands, p. 3071-3078.
- 21 Nicot, J.-P., Lu, C., Mickler, P., Yang, A. L., Romanak, Katherine, and Zhang, T., 2013, Impact of CO₂ impurities on storage performance and assurance; Tasks 3 and 4: Geochemistry: The University of Texas at Austin, Bureau of Economic Geology, contract report prepared for CO₂ Capture Project (CCP) Phase III, 224 p.
- 22 Lu, J., P. J. Mickler, J.-P. Nicot, C. Yang, K. D. Romanak, 2014, Geochemical impact of oxygen on siliciclastic carbon storage reservoirs, *International Journal of Greenhouse Gas Control*, 21, p.214–231, <http://dx.doi.org/10.1016/j.ijggc.2013.12.017>
- 23 Buckley, S. E., C. R. Hocott, and M. S. Taggart Jr., 1958, "Distribution of dissolved hydrocarbons in subsurface waters." *Habitat of oil: Am. Assoc. Petroleum Geologists*: 850-882.

-
- 24 Nicot, J. -P., and Solano, Silvia, 2012, Impact of CO₂ impurities on storage performance and assurance; Tasks 1 and 2: Plume dynamics: The University of Texas at Austin, Bureau of Economic Geology, contract report prepared for CO₂ Capture Project (CCP) Phase III, 155 p.
- 25 Nicot, J. -P., Solano, S., Lu, J., Mickler, P., Romanak, K., Yang, C., and Zhang, X., 2013, Potential subsurface impacts of CO₂ stream impurities on geologic carbon storage: Energy Procedia, v.37, Proceedings of 11th International Conference on Greenhouse Gas Control Technologies GHGT11, November 18-22, Kyoto, Japan, p. 4552-4559.
- 26 Thibeau, S., and A. Dutin, 2012, Large scale CO₂ storage in unstructured aquifers: Modeling study of the ultimate CO₂ migration distance, 11th International Conference on Greenhouse Gas Control Technologies (GHGT11), International Energy Agency Greenhouse Gas R&D programme, Kyoto, Japan, November 18–22, 2012, 8p.
- 27 Bennion, B. and Bachu, S., 2005, Relative permeability characteristics for supercritical CO₂ displacing water in a variety of potential sequestration zones in the western Canada sedimentary basin, SPE95547.
- 28 Tiab, D. and Donaldson, E.C., 2004, Petrophysics Theory and Practice of Measuring Reservoir Rock and Fluid Transport Properties, 2nd edition, p.121-126.
- 29 Butler, 2012. David Butler, ICO2N (private communication), December, 2012
- 30 WorleyParsons, 2009. DRET CCS Task Force Support, Summary of Pipeline Sizing Study, WorleyParsons, 20 August 2009;
<http://www.ret.gov.au/resources/Documents/Programs/cst/WP%20-%20Pipeline%20and%20Injection%20Pumping%20Study.pdf>
- 31 MIT, 2003. The Economics of CO₂ Storage, Gemma Heddle, NETL, August 2003.
http://sequestration.mit.edu/pdf/LFEE_2003-003_RP.pdf
- 32 Enhance Energy, 2012. Enhance Energy, (private communication), December, 2012
- 33 Nygaard and Lavoie, 2010. R Nygaard and R Lavoie, Project Cost Estimate, Wabamun Area CO₂ Sequestration Project Report, University of Calgary Institute for Sustainable Energy, Environment and Economy, January 2010
- 34 Nordbotten 2005. Nordbotten J. M., M. A. Celia, S. Bachu, H. K. Dahle (2005), Semi-Analytical Solution for CO₂ Leakage through an Abandoned Well, Environmental Science & Technology, 39(2), 602-611
- 35 Watson and Bachu, 2007. TL Watson and S Bachu, Evaluation of the Potential for Gas and CO₂ Leakage along Wellbores. Society of Petroleum Engineers E&P Environmental and Safety Conference, Galveston, Texas, USA, March 2007
- 36 McGoey-Smith, 2010. AD McGoey-Smith, Risk-based Leakage Model, Wabamun Area CO₂ Sequestration Project Report, University of Calgary Institute for Sustainable Energy, Environment and Economy, January 2010,
<http://www.ucalgary.ca/wasp/RiskBasedLeakageModel.pdf>

-
- 37 Nicot, 2012. J-P Nicot, (private communication), July, 2012
- 38 GERG, 2008. O Kunz and W anger, The GERG-2008 Wide-range Equation of State for Natural Gases and Other Mixtures, J Chem & Eng Data, Vol 57 (11), pp 3032–3091, October, 2012
- 39 Botros, 2014. K Botros (private communication), March, 2014
- 40 Wolfram, 2014. Wolfram Mathworld, Triangular Distribution, <http://mathworld.wolfram.com/TriangularDistribution.html>
- 41 MIT, 2008. Carbon Management GIS: CO2 Pipeline Transport Cost Estimation, MIT, June 2009; http://sequestration.mit.edu/energylab/uploads/MIT/Transport_June_2009.doc
- 42 Perry, 2007. DW Green and RH Perry, Perry’s Chemical Engineering Handbook, 8th Edition, McGraw-Hill, 2007.
- 43 Edwards, 2012. Kelly Edwards, (private communication), April, 2012
- 44 Emera, 2006. MK Emera, Modelling of CO2 and Green-house Gases (GHG) Miscibility and Interactions with Oil to Enhance The Oil Recovery in Gas Flooding Processes, PhD Thesis, University of Adelaide, March, 2006.
- 45 Nicot, 2013. J-P Nicot, (private communication), December, 2013
- 46 Mohitpour, 2012. Pipeline Transportation of Carbon Dioxide Containing Impurities, M Mohitpour, S Seevam, KM Botros, B Rothwell and C Ennis, ASME Press, USA, 2012
- 47 GoldSim, 2014. GoldSim: Monte Carlo Simulation Software for Decision and Risk Analysis, www.goldsim.com, 2014